UCRL-LR-125352

X-Ray Ablation Measurements and Modeling for ICF Applications

Andrew T. Anderson
(Ph.D Thesis)

September 1996

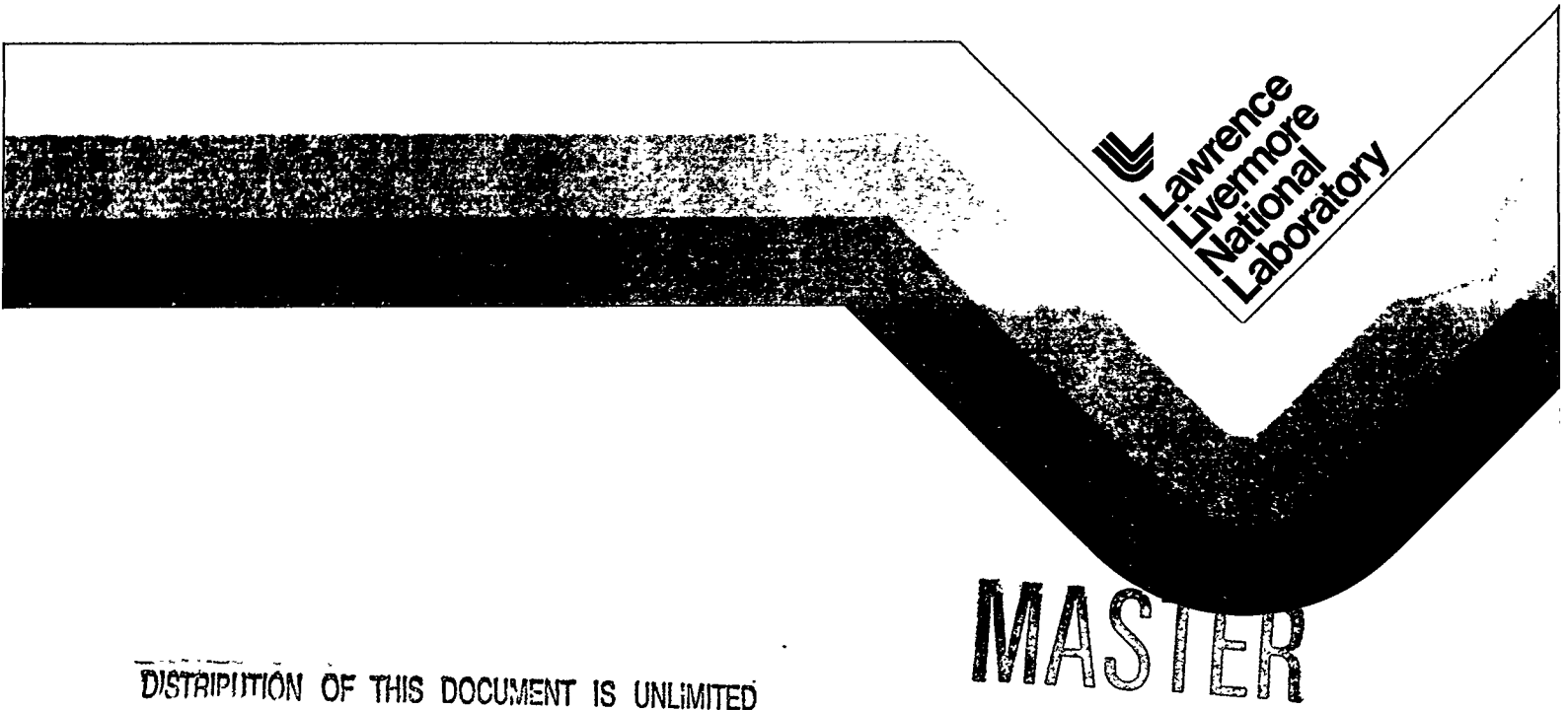

DISCLAIMER

This report has been reproduced
directly from the best available copy.

Available to DOE and DOE contractors from the
Office of Scientific and Technical Information
P.O. Box 62, Oak Ridge, TN 37831
Prices available from (615) 576-8401, FTS 626-8401

Available to the public from the
National Technical Information Service
U.S. Department of Commerce
5285 Port Royal Rd.,
Springfield, VA 22161

Work performed under the auspices of the U.S. Department of Energy by Lawrence Livermore National Laboratory under Contract W-7405-ENG-48.

UCRL-LR-125352
Distribution Category UC-700

X-Ray Ablation Measurements and Modeling for ICF Applications

Andrew T. Anderson
(Ph.D Thesis)

September 1996

LAWRENCE LIVERMORE NATIONAL LABORATORY
University of California • Livermore, California • 94551

X-Ray Ablation Measurements and Modeling for ICF Applications

by

Andrew Thomas Anderson

B.S. (Rensselaer Polytechnic Institute) 1982
M.S. (Rensselaer Polytechnic Institute) 1985

A dissertation submitted in partial satisfaction of the

requirements for the degree of

Doctor of Philosophy

in

Engineering – Mechanical Engineering

in the

GRADUATE DIVISION

of the

UNIVERSITY of CALIFORNIA, BERKELEY

Committee in charge:

Professor Per F. Peterson, Co-Chair
Professor Phillip Colella, Co-Chair
Professor Costas P. Grigoropoulos
Professor T. Kenneth Fowler

1996

The dissertation of Andrew Thomas Anderson is approved:

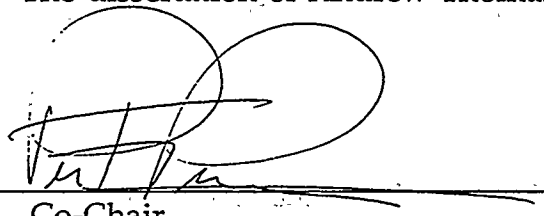

8/29/96

Co-Chair Date

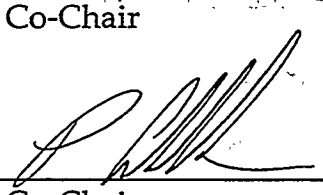

8/29/96

Co-Chair Date

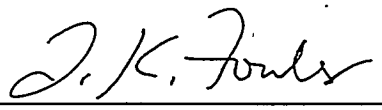

Aug. 20, 1996

Date

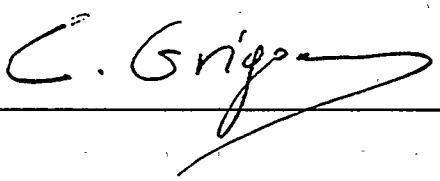

8/29/96

Date

University of California, Berkeley

1996

Abstract

X-Ray Ablation Measurements and
Modeling for ICF Applications

by

Andrew Thomas Anderson

Doctor of Philosophy in Mechanical Engineering

University of California, Berkeley

Professor Per F. Peterson, Co-Chair
Professor Phillip Colella, Co-Chair

X-ray ablation of material from the first wall and other components of an ICF (Inertial Confinement Fusion) chamber is a major threat to the laser final optics. Material condensing on these optics after a shot may cause damage with subsequent laser shots. To ensure the successful operation of the ICF facility, removal rates must be predicted accurately. The goal for this dissertation is to develop an experimentally validated x-ray response model, with particular application to the National Ignition Facility (NIF).

Accurate knowledge of the x-ray and debris emissions from ICF targets is a critical first step in the process of predicting the performance of the target chamber system. A number of 1-D numerical simulations of NIF targets have been run to characterize target output in terms of energy, angular distribution, spectrum, and pulse shape. Scaling of output characteristics with variations of both target yield and hohlraum wall thickness are also described.

Experiments have been conducted at the Nova laser facility in Livermore on the effects of relevant x-ray fluences on various materials. The response was diagnosed using post-shot examinations of the surfaces with scanning electron microscope (SEM) and atomic force microscope (AFM) instruments. On the basis of these observations, judgments were made about the dominant removal mechanisms for each material. Measurements of removal depths were also made to provide vital benchmark data for the modeling.

The finite difference ablation code developed here (ABLATOR) combines the thermomechanical response of materials to x rays with models of various removal mechanisms. The former aspect refers to energy deposition in such small characteristic depths (on the order of a micron) that thermal conduction and hydrodynamic motion are significant effects on the nanosecond time scale. The material removal models use the resulting time histories of temperature and pressure profiles, along with ancillary local conditions, to predict rates of surface vaporization and the onset of conditions that would lead to spallation.

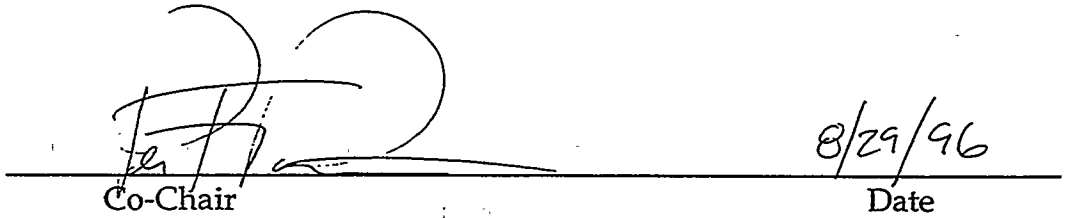

Co-Chair 8/29/96 Date

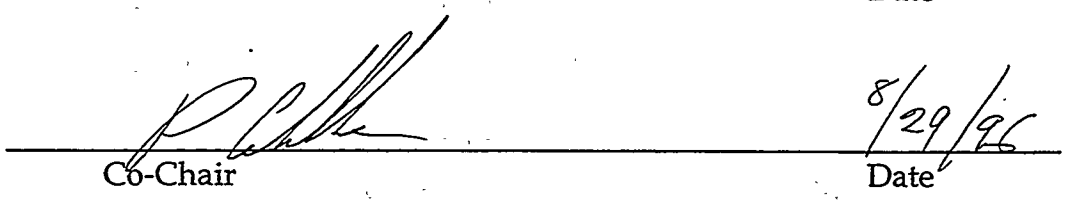

Co-Chair 8/29/96 Date

TABLE OF CONTENTS

LIST OF FIGURES

Chapter 1

Chapter 2

Chapter 3

Chapter 4

Chapter 5

Chapter 6

LIST OF TABLES

Chapter 1

Chapter 2

Chapter 4

Chapter 5

Chapter 6

NOMENCLATURE

α	thermal diffusivity; thermal expansion coefficient
a,b,c,d,t_o	double exponential fit parameters for x-ray pulses
a_j	acceleration of node j
BB, BBT	blackbody temperature (equivalent x-ray spectrum)
DT	deuterium/tritium
E	internal energy per unit mass
E	Young's modulus
f_1,f_2	equation of state parameters
Γ	Grüneisen coefficient
h	heat flux due to conduction
ICF	Inertial Confinement Fusion
IFE	Inertial Fusion Energy
I_o	incident photon energy
J	bubble nucleation rate ($1/m^3s$)
κ	thermal conductivity
λ	photon mean free path
LEH	hohlraum laser entrance holes
ν	Poisson's ratio
NIF	National Ignition Facility
NNE	Non-Neutron Energy
p	pressure or normal stress
P_d	rate of deviatoric stress work
P_{sat}	equilibrium vapor pressure at a given temperature
q	viscous stress (artificial)
Q_{in}	heat added per unit time and mass
ρ	mass density
r*	critical radius for bubble nucleation
σ	stress; surface tension
σ_j	normal stress in zone j
SIM	Six-Inch-Manipulator (for Nova sample emplacement)
u_j	velocity of node j
x_j	location of node j
Δt	time step size
Δx	finite difference grid size

ACKNOWLEDGMENTS

I would like to thank my primary research advisor, Prof. Per Peterson, for providing invaluable guidance throughout the course of this effort. I also greatly appreciate the help and advice of Prof. Phil Colella.

This dissertation would not have been possible without the technical help and advice of many colleagues at LLNL. Rob Managan provided me an education in the use of the LASNEX code. Alan Burnham was instrumental in conducting and analyzing the Nova experiments. I benefited greatly from numerous discussions of ablation thermodynamics with Gerry Wilemski.

Another key component of the LLNL contributions was on the management side. The Mechanical Engineering Department's half-time financial support, initiated by Ron Carr and continued by Bill Ruvalcaba, was absolutely critical. Continued support from the ICF Program, through Bill Hogan, John Woodworth, and Mike Tobin, provided a productive environment in which to pursue my research.

Finally, I wish to acknowledge the sacrifices of my family during the long hours of studying and research work. I could not have completed this work without their loving support.

DEDICATION

To the memory of
my father
Richard Anderson

1. Introduction to ICF Chamber Dynamics

1.1 Background

This dissertation investigates and explains the x-ray ablation process for a variety of materials under conditions generated by Inertial Confinement Fusion (ICF). The motivation for this study is the need to design ICF facilities to withstand the intense energy release from the driver and target thermonuclear yield without a degradation in performance. ICF chamber dynamics is the description of the events within a target chamber from the initiation of the driver pulse to final condensation of ablated materials.

Controlled thermonuclear fusion of deuterium and tritium atoms (DT fusion) requires some minimum combination of ion temperature, ion density, and confinement time. The two common approaches to achieving the necessary conditions are magnetic confinement and inertial confinement. Magnetic Fusion Energy (MFE) experiments aim for a rather large plasma at 15 keV, densities well below solid density, and long confinement times (seconds to steady state). The ICF approach utilizes discrete fuel pellets that are compressed to very high densities, high temperatures (about 10 keV for ignition), but very short confinement times (sub-nanosecond).

The target for the National Ignition Facility (NIF) can be used to illustrate the sequence of events in obtaining inertial fusion yield. Figure 1-1 shows the baseline NIF target design, which is based on the indirect drive concept. The fuel capsule is contained with a gold radiation case, or hohlraum. Intense laser beams enter the hohlraum through the holes in the end plates and deposit their energy on the interior walls of the hohlraum. This energy is efficiently converted to x rays by the hot gold plasma. (Some ICF reactor

designs envision deposition of ion beam, rather than laser, energy into special radiators, producing the same x-ray effect). With the x-ray energy largely contained within the radiation case, the capsule receives a uniform energy flux over its entire surface. Energy deposition in the outer layers of the capsule cause them to ablate outward at high velocity. In a rocket-like reaction, the inner fuel layers of the capsule are driven to rapid convergence at the center. Stagnation of the fuel kinetic energy brings the material to very high temperatures and densities. Thermonuclear burn initiated under these conditions can continue until hydrodynamic re-expansion drops the capsule density significantly, a process that takes less than a nanosecond.

An ICF chamber environment encompasses the threats from target emission and system response to these threats. Again the National Ignition Facility design will be used to illustrate these concepts. Figure 1-2 gives a simplified view of the NIF target chamber with some of the major components indicated. The chamber itself is a 10-m diameter aluminum sphere with numerous penetrations for laser beam and diagnostic access. To minimize the generation of vapor and particulates from x-ray ablation, the aluminum chamber wall is protected by panels of refractory material (boron carbide). Final optics assemblies support a vacuum window, frequency conversion crystals, focusing lens, phase plate, and finally a debris shield to permit entrance of the 1.06 μm laser light, convert it to 0.35 μm light, and focus this light at chamber center. The purpose of the debris shield is to protect the more expensive optics behind it from x rays and debris generated in the target chamber. Because the frequency conversion is only 60% efficient, some 1.06 μm and 0.53 μm laser light enters the chamber along with the

0.35 μm light. The unconverted light from each beam is absorbed in a dump on the far side of the target chamber from the entrance point.

A chronology of source and response terms for each system of interest in the chamber will enable the proper integration of responses to each threat over the wide variety of time scales, from nanoseconds to milliseconds. Figure 1-3 shows a representative graph of the threat chronology to the NIF chamber wall and final optics, while Table 1-1 provides a more detailed descriptions of these events. Laser light initiates the process and drives x-ray production, both of which occur in nanoseconds to tens of nanoseconds. Thermonuclear burn starts near the end of the laser pulse and lasts only about 100 psec. All of the energy in alpha particles (20% of the total) is deposited in the capsule material, as is 5-10% of the neutron energy. The remaining neutron energy escapes the target and passes through the chamber wall about 100 ns later. After disassembly of the target due to the rapid post-burn expansion, vaporized target debris is the next energy source, arriving at the first wall on the microsecond to millisecond time scales. The last threat to the target chamber is the shrapnel from fragmented supports and shields originally near the target, which reaches the chamber wall in a few milliseconds.

Chamber dynamics concerns the interaction of driver and target emissions with all materials within an ICF target chamber. The first stage in the analysis is to define the energy source terms in the problem, including the driver (e.g. laser light), x rays, target debris, and shrapnel. The second part is to determine the response of the structures in the chamber to each of these emissions. For x rays, the response frequently involves ablation of a thin surface layer from

target-facing surfaces. The materials response calculations produce two key results. The depth of material removed is of primary importance, as this will give the total mass of material released into the chamber. The velocity and form (vapor, liquid droplets) of this material must be known to determine how it will be transported in the chamber. Evaluation of the transport and eventual deposition of these ablated or fragmented materials is the third step in the analysis. Finally, the performance degradation, if any, of each component (e.g. laser debris shields) is determined to ensure that the target chamber will perform acceptably on subsequent shots.

Chamber dynamics analysis requires validated models that allow prediction of conditions within ICF target chambers. A major part of this effort is the development of sufficient understanding of each step in the chronology outlined above. This understanding can then be incorporated into computer models in a suite of codes. Predictions from these codes can be validated with experimental data, primarily from the Nova facility at Lawrence Livermore National Laboratory. The codes can then be used to predict chamber environments and responses for the design of the NIF (National Ignition Facility) and future IFE (Inertial Fusion Energy) target chambers.

Specific needs of the ICF program drive the chamber dynamics development effort. In the near-term, the use of updated models will permit optimization of the National Ignition Facility target chamber design. The relevant systems include the target inserter, first wall protection, and final optics protection. The National Ignition Facility will be the next major step in the development of inertial confinement fusion. Ignition of a fusion target is

the primary goal, meaning that more energy is produced in thermonuclear yield than required in laser driver energy. Other goals include investigation of high energy density physics issues and IFE development. The laser system will produce over 1.8 MJ (500 TW peak power) of ultraviolet energy with 192 beamlines. These will be directed into a 10-m diameter target chamber designed hold the final optics, target, and diagnostics, and contain the effects of the laser deposition and yield (up to 20 MJ).

In a somewhat longer-term view, chamber dynamics must be used in the advanced design and operational phases of NIF to evaluate the impact on chamber survival (primarily optics damage) from the use of equipment in the target chamber. The goal is to restrict the placement of diagnostics and the use of various targets and target shields, or at least to fully understand the consequences of their use. Proposed experiments by various NIF user groups will be similarly evaluated. In the long term are IFE uses for chamber dynamics analysis. Many IFE credibility issues will be resolved with NIF experiments, and chamber dynamics calculations will be necessary to field and understand these experiments. These validated chamber dynamics models will then be used for post-NIF facilities and reactor chamber designs.

1.2 X-ray Ablation Physics

The short duration, high intensity x rays produced in an ICF target can damage exposed surfaces. In a fusion reactor, ablated vapor is a concern because the recondensation time for this material may limit the shot rate. In the NIF, condensing vapors and spalled liquid droplets or solid particulates can obscure optical surfaces, lowering laser damage thresholds and transmitted beam quality. The x rays may also deposit sufficient energy to

damage these optical surfaces directly. The ablation process must be well understood to permit successful design of ICF target chambers.

The interaction of the various x-ray energy source terms typically takes place in a very thin layer on the surface of a material. For example, most of the energy from sub-keV x rays will deposit in just a few microns, even in low-Z (low atomic number) materials. Another feature of these source terms is a very short time scale during which the energy is deposited, typically a few nanoseconds for most ICF x-ray sources. Because materials can not conduct a significant amount of energy away from the surface layers in this time, surfaces may be driven past their melt or vaporization points. An accompanying pressure rise will occur in the heated material, driving shock waves into the bulk material and possibly ejecting the melted material from the surface. This section addresses the complex hydrodynamic and thermodynamic processes during x-ray ablation.

X-ray ablation is governed by four physical phenomena. The first is the *energy deposition* from the x rays through the thin surface layers of material. *Transient thermal conduction* allows this energy to move within the material, which is particularly important near the strongly heated surface layers. Heating causes thermal expansion, which raises pressures and causes *hydrodynamic motion* as the pressures release from the surface. The fourth process is the removal of material through *vaporization and/or spall.*

The x-ray deposition calculation is generally straightforward, in that published tables of photon cross-sections[1] can be used at most fluences of interest (less than 10 J/cm^2). The given input spectrum is divided into

numerous groups (50-100), and the energy absorption for each group is tracked through the material. The total energy at any depth is just the sum over all energy groups. Deposition of incident energies in excess of 10 J/cm^2 over a few nanoseconds involves more complex physics. A plasma may be generated, so that the atomic physics processes must be modeled. These include ionization, differing electron and ion transport, and bleaching.

Laser ablation of materials is a closely related topic that has been studied extensively. Dabby and Paek[2] provided an analytical description 25 years ago. More recent work includes Kelly et al[3] and Ho, Grigoropoulos, and Humphrey.[4] X-ray deposition generally produces different types of material response than does corresponding levels of laser energy deposition. The primary distinction is the depth of deposition, which is generally on the order of microns for x-ray energy and tens of Angstroms with laser energy. One result of the difference in deposition length scales is that models of heat transfer in the two cases are based on different assumptions. In the laser deposition problem, heating is often considered as a surface flux that eventually melts and vaporizes the target material on two moving fronts. Conversely, for x-ray deposition (at least without surface vaporization) the front surface can be thought of as thermally insulated on the typical short, sub-μsec time scales. As interior material is raised in temperature, a substantial layer of two-phase (solid/liquid) material can be created, a phenomenon not usually observed in surface-heating laser ablation work.

The second result of the longer (x-ray) energy deposition distances is the importance of the hydrodynamics of the interior material. The rapid increase in internal energy due to x-ray deposition creates high pressures within the

material, according to its density and equation of state. This pressure drives expansion (hydrodynamic motion) from the surface layers away from the bulk of the material. As the expansion stops at the end of the x-ray pulse, rarefaction waves (tensile stresses) propagate from the surface into the bulk of the material. Such tensile stresses can be very important as mechanisms for ablation of heated material.

Three distinct material removal mechanisms have been identified: surface vaporization, thermal shock/spall, and liquid ejection. *Vaporization* is the flux of atoms or molecules leaving the surface of a strongly heated solid or liquid. Brittle materials are subject to *thermal shock/spall* when cracks initiate after initial melting due to thermal stress and are propagated to failure by tensile waves on subsequent x-ray exposure. *Melt layer ejection* can be caused by several processes, including sub-surface boiling and Rayleigh-Taylor instabilities. From combinations of these removal mechanisms, ablated material can exist in a variety of forms, from vapor to liquid droplets or solid particulates.

Thermodynamics and heat and mass transfer rates will determine the state of the ablated material that moves about the chamber. Whether this material exists as a vapor or as condensed droplets is one major aspect of material state. Material initially in the vapor state may partially condense during its expansion and cooling, through a homogeneous nucleation process. Conversely, liquid ablated from a surface may rapidly evaporate as the local pressure drops, as has been observed in short-pulse laser ablation experiments.[5] The final state will depend on the relative rates of heat and mass transfer in the nanosecond-to microsecond time immediately following

ablation. The chemical kinetics of recombination for any molecular, rather than elemental, material may also have a significant impact on the final material state, as noted in Chen.[6]

Another possible damage mechanism is spall within the bulk solid material. Ablation pressures experienced in these materials will generate shock waves that will propagate into the bulk solid material. The rapid expansion of the material on the new front surface will subsequently launch a rarefaction wave directly behind the shock. This combination of shock and rarefaction waves may cause spall in the bulk material or debonding of a thin coating layer. Particularly large tensions are possible at locations where a rarefaction wave reflects off the rear surface of a thin material layer. Thicker material layers (generally more than a few millimeters) are not at risk from shock damage, as the rarefaction wave quickly overtakes the shock, greatly reducing the amplitude of the propagating stress pulse. Analysis of the failure process must include rates of void nucleation and crack growth, because the stress pulse duration is on the order of nanoseconds.

1.3 Overview

The objective of this dissertation is to observe, understand, and model x-ray ablation, particularly in those materials likely to be used in NIF. The first step is the determination of what the x-ray threat will be on NIF, to obtain the best possible simulation with experiments. The second step is experimentation on the materials of interest to determine their response to x rays. The third step is the development of models of the ablation process. In particular, the models of removal mechanisms are refined and benchmarked with the experimental data. The end result is an analytical tool for prediction of

material removal for the NIF and other ICF facilities. This will determine the mass loading of ablated material in the target chamber and will serve to initialize the codes that calculate material motion within the chamber. This section describes the major results of the dissertation toward meeting its objective.

A major improvement in the modeling of x-ray emissions from ICF targets has been achieved with newly available computational tools. The primary target of interest for NIF response calculations is the baseline indirect drive design for 20-MJ yield with 1.8-MJ, 500-TW input laser energy. This target provides the worst case loadings on the NIF chamber components. Chapter 2 gives detailed descriptions of x-ray outputs, including fluences, spectra, and pulse shapes. With this information as a starting point, other calculations determine the source term variations caused by changes in hohlraum wall thickness, hohlraum size, and target yield. Other targets of interest for NIF include gold disks, or other specialized types. Another important set of modeling runs discussed in Chapter 2 focuses on output from Nova targets, to provide for benchmarking of code results against experimental data. These techniques can potentially be extended to determine the emissions from targets relevant to inertial fusion energy reactors.

The x-ray emission predictions are important in development of response models because they provide a necessary understanding of x-ray conditions relevant to NIF. The NIF output predictions also serve as a basis for selection of the proper range of experimental conditions. Finally, these x-ray emissions

are needed for the most immediate use of the response models developed here, the extension of the Nova test data to NIF conditions.

Experimental investigation of the ablation process comprises the second stage in this study. The Nova laser facility at Lawrence Livermore National Laboratory was used to expose a variety of materials to x-ray fluences from 1 to 3.5 J/cm^2. Chapter 4 describes a significant amount of new data on material removal depths as a function of x-ray fluence that was generated with this unique facility. Detailed examinations of exposed surfaces with a range of microscopy techniques provided the key to determination of likely mechanisms of removal. The three mechanisms identified were vaporization, thermal shock/spall of solid material, and liquid expulsion. Knowledge of removal mechanisms guided model development and provided benchmark data for the completed codes.

The final objective is development of validated models that capture the essential physics of ablation process. A new code, called ABLATOR (Ablation By LAgrangian Transient One-D Response), is the result of this development effort. Chapter 3 presents the components of the numerical model, including x-ray deposition, heat conduction, and hydrodynamics. An important feature of the model is the treatments of the individual removal mechanisms identified, which are also described in Chapter 3. Application of these models to the results of the experimental work helped to determine the relative importance of various removal mechanisms in a particular material. Chapter 5 details this modeling for each of the materials examined in Chapter 4. Particularly good agreement was found between experiments and predictions for materials that ablate by surface vaporization.

Chapter 6 discusses applications of the ABLATOR code beyond matching the Nova experimental data. The new models are used to extend experimental results for tested materials from Nova to NIF x-ray conditions. Another application for the code is to determine likely material removal mechanisms and ablation depths for untested materials. Chapter 6 evaluates the performance of each removal model to assess the code's predictive ability in these applications. It is determined that minimum ablation losses (from vaporization) can now be quantified, and removal depths due to other mechanisms can also be estimated.

References

1) Cullen D.F., et. al., "Tables and Graphs of Photo-Interaction Cross Sections from 10 eV to 100 GeV Derived from the LLNL Evaluated Photon Data Library (EPDL)", UCRL-50400-V 6, Oct 1989.

2) Dabby FW, Paek U., "High-Intensity Laser-Induced Vaporization and Explosion of Solid Material" IEEE J Quant Elec, Vol QE-8, N2, p106-111, Feb 1972.

3) Kelly R, Miotello A, Braren B, Gupta A, Casey K., "Primary and Secondary Mechanisms in Laser-Pulse Sputtering", Nucl Inst & Meth, B65 p187-199, 1992.

4) Ho JR, Grigoropoulos CP, Humphrey JAC., "Computational Study of Heat Transfer and Gas Dynamics in the Pulsed Laser Evaporation of Metals", J Appl Phys V78 N7, p4696-4709, Oct 1995.

5) Downer M.C., et. al.., "Femtosecond Imaging of Melting and Evaporation at a Photoexcited Silicon Surface", J. Opt. Soc. Am. B, Vol. 2, No. 4, April 1985.

6) Chen X.M., Peterson P.F., and Schrock V.E., "The Calculation of Kinetic Rate Constants for LiF and BeF2," Fusion Technology, Vol. 21, pp. 1537-1540, 1992.

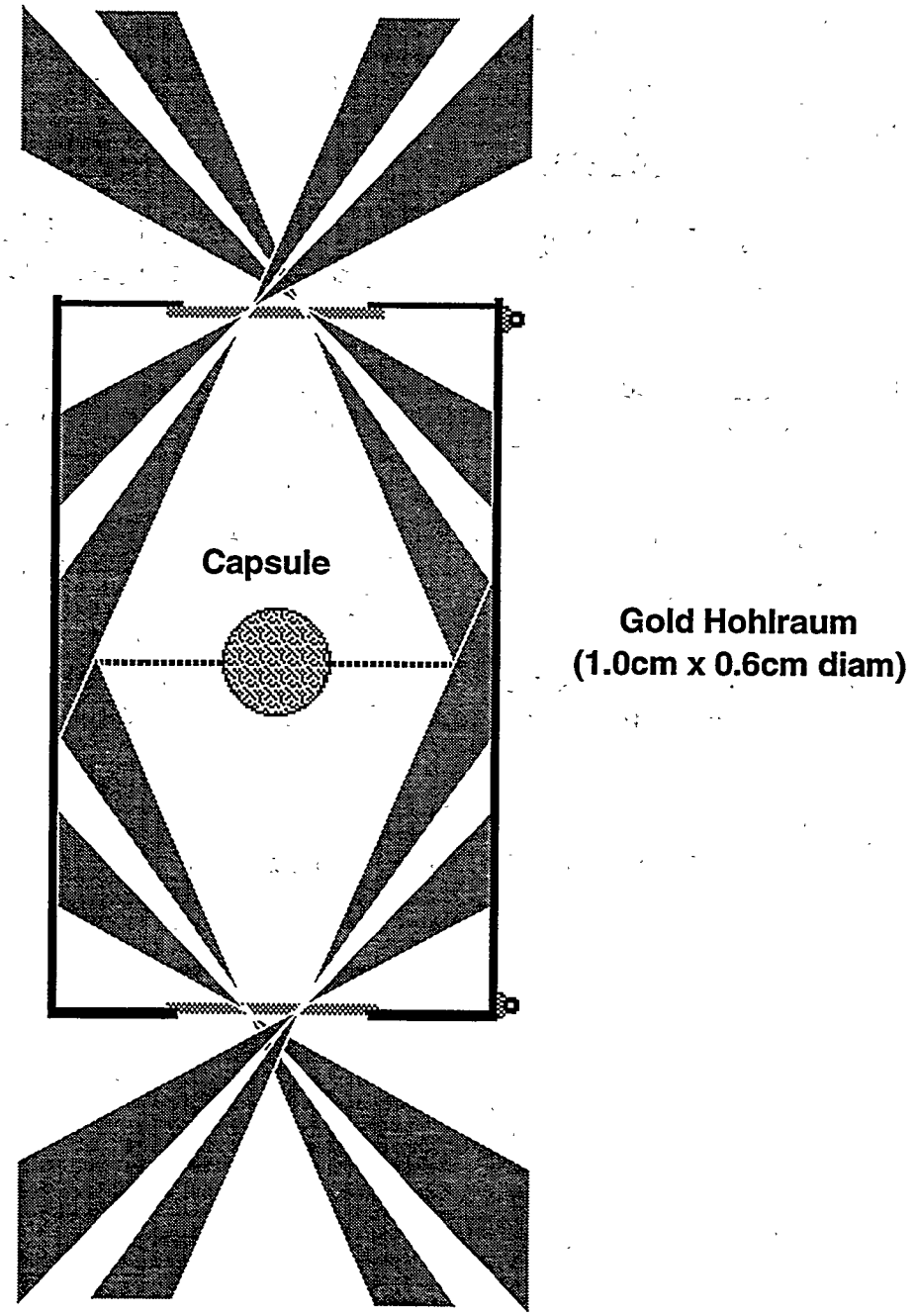

Figure 1-1: Indirect drive NIF target design showing entrance of laser beams. Beams are arranged in two axially symmetric cones at angles of about 25° and 47° from the hohlraum axis. Indirect drive refers to lasers generating x rays, which then drive the capsule implosion.

Unconverted light absorbers

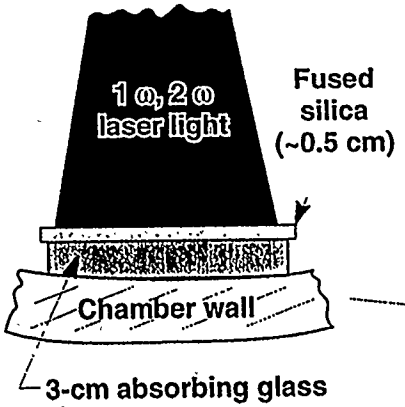

Final Optics Assembly

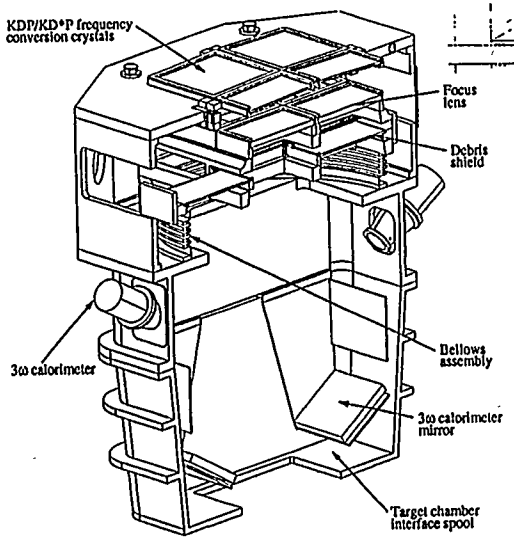

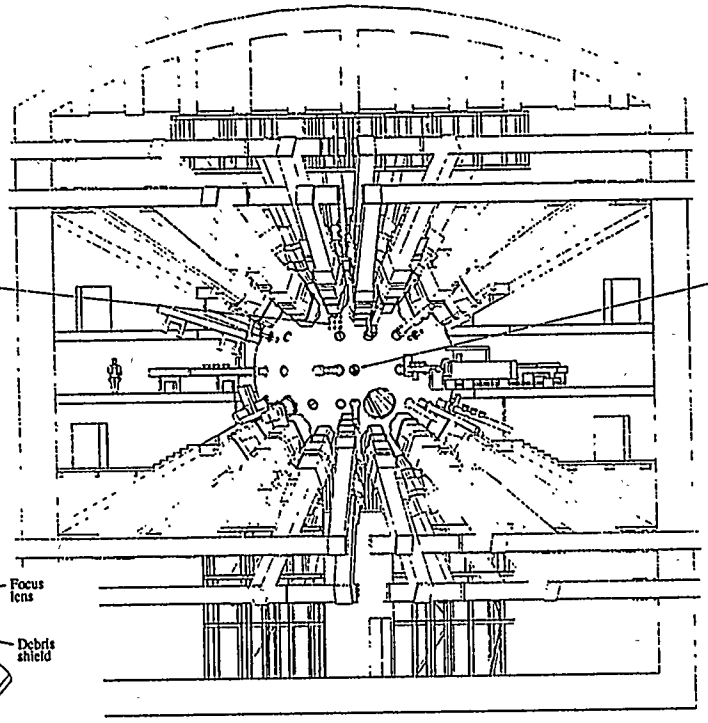

Chamber wall x-ray protection:

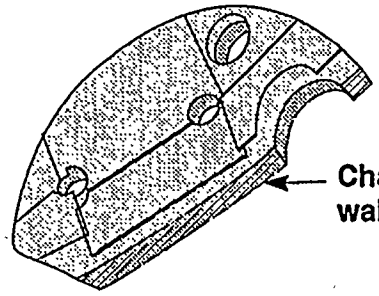

Mounted aluminum plates with a plasma-sprayed or hot-pressed coating (e.g., B_4C) [~300 m^2 total]

Figure 1-2: NIF target chamber is a 10 m diameter sphere with 192 beams (grouped in 2x2 arrays). Details show first wall protection, beam dump for unconverted light, and debris shield location in optics assembly.

Table 1-1: Approximate Source Term Chronology (20 MJ Yield)

Start Time	End Time	Event
-20 ns	0 ns	laser beams enter hohlraum
0	100 ps	thermonuclear burn
2 ns	2.1 ns	neutrons reach target positioner
3 ns	-	hohlraum wall burnthrough (30 μm wall)
20 ns	85 ns	x rays hit first wall (0% - 90% of energy)
95 ns	100 ns	neutrons reach first wall (0% - 90% dose)
130 ns	135 ns	neutrons reach debris shields (0% - 90% dose)
10 μs	60 μs	hohlraum wall material reaches first wall
250 μs	1 ms	ablated target positioner material reaches 1st wall
1.9 ms	10 ms	target support & shield shrapnel reaches first wall
-	100 ms	ablated materials fully condensed

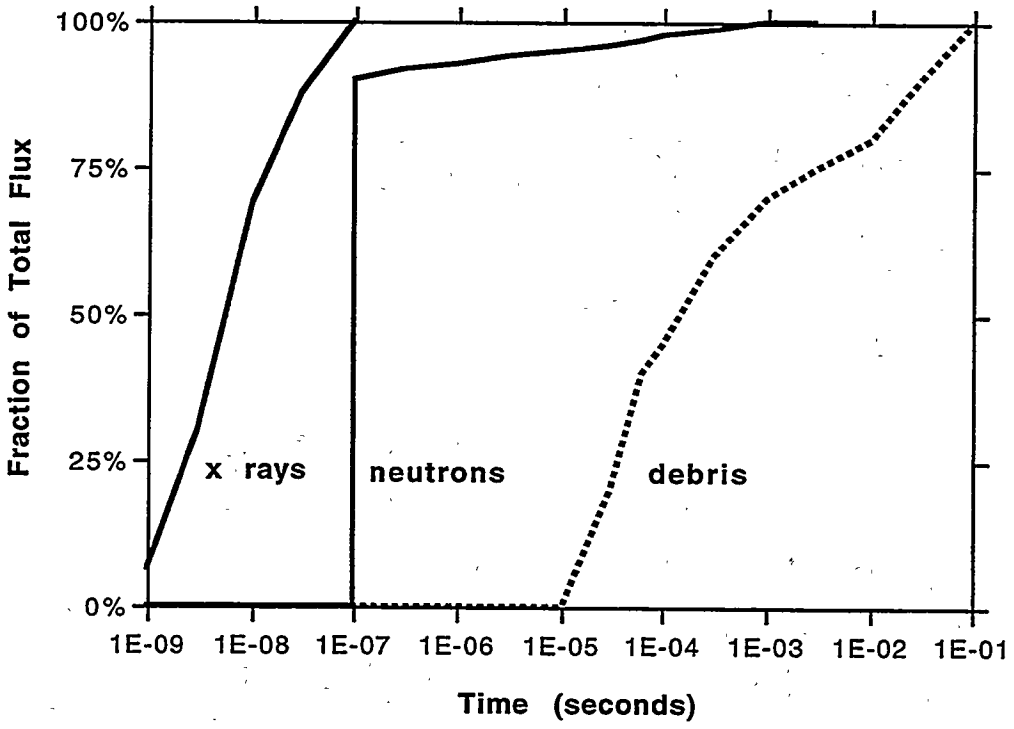

Figure 1-3: Approximate chronology of x-ray, neutron, and debris deposition at NIF first wall. Fusion burn at t = 0.

2. X-ray Source Description

2.1 Introduction

Target chamber designs for ICF (Inertial Confinement Fusion) facilities must ensure that all performance requirements are met. For example, survival of the final optics is the primary goal for the NIF (National Ignition Facility). The threat to final optics from direct (target x-rays and debris) and indirect (debris from ablation of chamber components) sources must be evaluated. Accurate knowledge of the x-ray emissions from NIF targets is a critical first step in this process.

Calculation of x-ray emission from an ICF target requires complex treatment of many physics processes. LASNEX[1], an LLNL 2-D radiation-hydrodynamics code with an extensive history of ICF development and experimental validation, incorporates detailed models for these processes and thus is currently considered the most accurate tool for simulating ignition and burn of ICF targets. The x-ray emission from targets depends primarily on the configuration and temperature of the target material before and following ignition. Because LASNEX currently provides the best available information on transient target-material configurations and temperature, here LASNEX has been used to predict x-ray emission for a variety of ICF targets. I compare these predictions with experimental measurements of x-ray emission from hohlraums fielded on the Nova laser, to validate LASNEX's predictive capability for numerical experiments studying ICF target x-ray emission.

This chapter describes the calculations and details the current NIF x-ray source term predictions. The predictions presented here are based on a

number of 1-D simulations. These have been run out to late times to characterize target output variations with both target yield and hohlraum wall thickness. Validating data from some preliminary 2-D simulations[2] are also given.

2.2 Model Description

The baseline NIF target design is based on the indirect drive concept[3,4]. The DT fuel capsule is surrounded by a cylindrical gold hohlraum. Laser beams enter the hohlraum through holes in the end faces and strike the inner surface of the gold walls. The laser pulse is 20 ns long, with 80% of the energy coming in the last 3-4 ns. The laser energy is efficiently converted to x rays, which provide uniform illumination of the capsule. The x rays drive the compression of the solid DT fuel shell by ablating the outer CH layer of the capsule. Figure 2-1 shows the baseline target and the 1-D model approximation. Table 2-1 contains some of the key parameters for the target and model.

The model used for this study is a 1-D spherical approximation to the NIF target design. The spherical capsule is modeled well in this case, except that no nonuniformities, instabilities, or mixing of layers is possible. In this respect, the 1-D model will produce the upper limit for yield in any given target design (30 MJ in this case). A more realistic limit is about 20 MJ yield. The surface area of hohlraum wall in the model matches that of the NIF target by appropriate choice of the inner radius of the gold shell.

To approximate the effect of the laser entrance holes (LEH), radiation is permitted to leave the interior of the gold sphere directly by using a "leak

Table 2-1: Specifications for modeled NIF indirect drive target design.

Yield	30 MJ (Max)
Laser Energy	1.8 MJ
Peak Laser Power	500 TW
Laser Pulse Shape	16ns foot, 4 ns peak
DT Mass	326 μg
DT Temperature	0.01 eV
Capsule Inside Radius	0.0995 cm
Capsule Outside Radius	DT 0.109 cm / ablator 0.127 cm
Hohlraum Length	1.0 cm (inside)
Hohlraum Diameter	0.6 cm (inside)
Hohlraum Wall Thickness	30 μm
Hohlraum LEH Diameter	0.3 cm
Hohlraum Liner	none
H/He Gas Mix	20%/80%
H/He Temperature	0.01 eV
H/He Density	0.001 g/cc
Window Thickness	1.0 μm (not modeled)
Window Material	Kapton (rho = 1.425) (not modeled)
Cryo System Copper Mass (g)	~ 200 mg (not modeled)
Cryo System SS Mass (g)	~ 10 mg (not modeled)

source". The model applies this leak source (actually an energy sink in this case) to the H/He region between the capsule and the gold interior. The leak rate is 1/4 times the particle velocity times the hole area divided by the total volume of all zones in the leak region, which gives the fraction of photons leaked out per unit time. This equation is based on the relation from kinetic theory that the number of molecules striking a surface per unit area per unit time is 1/4 times the particle density times their velocity. Gold vapor expanding from the interior walls may partially or completely close the LEH openings. Resolution of this issue will require 2-D calculations and some experimentation. Until these data are available, two limiting scenarios will serve to bound the problem. One models a quickly closing LEH, while the

other leaves the entrance holes open for the duration of the simulation. These models are shown in Figure 2-2.

One parameter of the target design that can be modified without significantly affecting the capsule yield is the thickness of the gold hohlraum wall, provided some minimum value is maintained. With a wall that is thicker than nominal, it is expected that x-ray output would be reduced at the expense of increased debris generation. A thinner wall would conversely move the x-ray/debris split in the opposite direction. Simulations were performed at different hohlraum wall thicknesses, using the same inside radius as the baseline model. All runs used the nominal 30 MJ yield capsule design.

This study also determined target output with a range of capsule yields. The parameter used to give different yields was the DT gas density inside the fuel shell. The mechanism of capsule yield reduction with increased gas density will be discussed in the next section. Seven different gas densities gave a range of yields from the baseline 30 MJ down to 1/2 MJ.

All runs used the same driving energy source. In the H/He region between the capsule and the inside of the hohlraum, the radiation field was specified as a function of frequency and time. This source is based on the results of more complex calculations of radiation-hydrodynamics conditions inside a laser-driven NIF hohlraum.

The simulations were taken out to very long times (for LASNEX runs) of at least 150 ns. The criterion for a minimum stop time was that the internal

energy remaining in the hot gold had to drop to a small part (<5%) of the total non-neutron energy. After this time, x-ray emission is negligible and the remaining energy is in debris kinetic energy.

2.3 Physics of Hohlraum Disassembly

The hohlraum functions as an enclosure for x-ray radiation, providing uniform illumination of the spherical fuel capsule. Laser beams initiate the process with efficient conversion to x-ray energy through interaction with the interior wall material of the hohlraum. Except for losses out the laser entrance holes, this emitted energy is essentially trapped within the hohlraum. The x rays are continually absorbed and reemitted by the wall material, which drives the whole interior of the hohlraum to a uniformly high temperature (~300 eV). As the wall material is heated strongly by the x rays, a radiation wave starts to propagate through the thickness of the wall. The balance among the energy input from the lasers, radiation losses out the LEH, and diffusion through the wall, determines the interior temperature of the hohlraum. Because radiative losses decrease and x-ray conversion increases with higher atomic number, materials like gold are used for the hohlraum.

Absorption of x rays by the ablator surrounding the fuel shell heats the material and drives it outward very rapidly. By a rocket-type reaction, the fuel shell is driven radially inward at high velocities. When the fuel stagnates at the center, its kinetic energy is converted into thermal energy. If the temperature and ion density are sufficiently high, a thermonuclear burn will begin and consume a significant fraction of the fuel before capsule disassembles. The energy of the burn is divided 80%/20% between neutrons

which largely escape from the target and alpha particles which are generally absorbed in the capsule material.

While the laser-driven radiation in the hohlraum is important for initiation of fusion burn, the dominant energy source in the hohlraum disassembly comes from the interaction with the post-burn capsule material with the hohlraum wall. LASNEX calculations show that about 75% of the yield energy escapes as neutrons. Since DT fusion gives 80% of its energy in neutrons, a modest fraction is being absorbed in the capsule material. This is possible in spite of the generally low neutron scattering cross sections in the target materials because of their very high ρR (product of density and radial thickness) at burn time. For the 30-MJ yield cases, up to a total of 7 MJ is deposited in the target, compared to the input 1.8 MJ of laser energy. Deposition of the burn particles heats the capsule material strongly and drives a rapid expansion. This high energy material stagnates against the inner wall of the gold hohlraum, creating high temperatures and pressures. Some of this energy is radiated directly out the laser entrance holes and some launches strong shocks and radiation waves into the remaining hohlraum wall material. When these waves break out or burn through, the wall material radiates much of the energy as x rays. The remaining energy goes to the kinetic energy of the hohlraum and capsule expansion.

It was mentioned in the model description section that the gas fill density in the center of the fuel capsule was used to vary the fusion yield. At the baseline gas density, the capsule diameter is reduced by a factor of 35 from its initial value to the value at peak compression. Because work must be done against the central gas, increasing the gas density inside the shell will prevent

the fuel from compressing as far. With a larger minimum diameter in the compressed fuel, the peak density falls and lower yield is achieved. Figure 2-3 shows results of calculations from Haan[4] for a target somewhat smaller than the design considered here.

The baseline target hohlraum described in the previous section is filled with a hydrogen/helium gas mixture. Calculations have shown this gas to be necessary for suppressing the "blow-in" of the wall material until late times. By keeping the material near its original location, the laser beams, which intercept the wall at angles from 23° to 50°, deposit their energy in roughly the same axial and radial locations through the pulse. This helps to maintain x-ray illumination symmetry within the hohlraum. It is the radial motion of gold wall material from the end caps across the LEH openings that cause the hole closure modeled in the simulations (plotted in Figure 2-2).

X-ray emission from the NIF targets can be divided into two components. One source is the radiation escaping directly out of the laser entrance holes from the hot interior of the hohlraum. The bulk of this energy is emitted when the interior is hottest (just after burn), and so it is characterized as having a high effective blackbody temperature and relatively short pulse length, as the material quickly cools from its peak temperature. Because the emission is from a hole in a blackbody enclosure, the radiation has a Lambertian distribution. (This is a cosine law dependence with the angle from the normal to the hole, with a peak of twice the isotropic fluence.) Some reduction is seen within a few degrees of the axis due to the reduced view to the hot hohlraum walls. The Lambertian distribution has been confirmed with 2-D LASNEX runs.[2] Figure 2-4 plots the predicted emission

from these runs as a function of angle from the hohlraum axis, together with a Lambertian distribution curve.

The other x-ray component emitted comes from transmission through and emission from the hohlraum wall. The effective emission temperature from the wall is significantly lower than from the LEH because the energy is distributed over a larger mass. The pulse length is much longer than for the LEH component because the large mass at lower temperature has a lower cooling rate than a small mass at high temperature. Since the emission rate goes as the fourth power of the temperature, more time is required to emit a given amount of energy. Because of the initial geometry, with gold surfaces normal to both the axial and radial directions, it is assumed that the x-ray emission from the wall is isotropically distributed.

2.4 Experimental Validation

2.4.1 Introduction

LASNEX simulations are valuable in predicting the x-ray threat to components inside the NIF target chamber. Models of igniting (and other) targets are run well past burn to determine how the non-neutron energy is eventually partitioned. Emission from and through the gold hohlraum wall is expected to be in long, cold pulses (<100-eV blackbody spectrum, 60 ns). This is not a regime where the code is often used, so there is some question of the accuracy of its predictions. This section describes a Nova experiment to benchmark the low energy, late time performance of the code. A good correlation to the test data will give confidence in using LASNEX to extrapolate to NIF scale target emissions.

The test case target was chosen to be an empty scale 1 Nova hohlraum (2800 μm x 1600 μm diameter) with a 3-μm gold wall thickness. The laser drive was taken to be 28.3 kJ of 3ω (0.35 μm) in pulse shape 22 (2.2 ns long). These conditions allowed the DANTE diagnostic[5] to measure the spectrum and x-ray emission as a function of time.

2.4.2 LASNEX Model Description

A 1-D spherical approximation was made for the hohlraum, based on an existing input deck for a Nova hohlraum. The radius was chosen to give the same surface area of gold as with the actual hohlraum. Energy input came from a laser source depositing on the inner surface of the gold. Losses out the laser entrance holes were simulated with a leak source, which allowed radiation to escape from the interior of the gold. The amount of energy released is in proportion to the fractional open area in the original hohlraum geometry. The simulation was run from start of the laser pulse until 100 ns had elapsed, by which time the x-ray emission had essentially decayed away.

2.4.3 Nova Experiment Description

Two thin-walled hohlraums described in the introduction were built and fitted with copper shields having a large rectangular opening. The hole in the shields measured 1950 μm x 700 μm and so gave the DANTE diagnostic a view of a large area on the outside of the hohlraum wall. (DANTE's view is normal to the cylindrical hohlraum surface.) In addition to DANTE, the FXI (flexible x-ray imager) was used, mounted in SIM 1 (six-inch-manipulator #1). The laser drive came from 9 beams, as one was out of service at the time. By adjusting other beam energies, however, the total laser energy in the hohlraum was very near the goal of 28.3 kJ (about 28.1 kJ). Pulse shape 22 was

used to match to the LASNEX code simulation. Both Nova shots (RET_XEMIT_01 & _02) provided essentially identical results.

2.4.4 Results

One measure of comparison between code and experiment is the spectrum of the x-ray emission as a function of time. From the code, this is obtained from a least-squares fit of a blackbody curve to the instantaneous spectra at several time steps. The Nova result is the curve based on DANTE data reduction that fits area under the measured spectral curves with appropriate blackbody fits. The resulting curves are plotted in Figure 2-5. The peaks in the curves agree very well, both in time (a few tenths of a nanosecond) and in temperature (within 1.5 eV). The rate of decay from the peaks also matches well, providing a key piece of information on the validity of the code simulations. The measured spectrum does rise gradually in earlier times, in contrast to the LASNEX predictions of a more distinct breakout of the radiation wave. The FXI photos show that the areas under the laser spots are quite a bit hotter than the other areas of the hohlraum wall. The early measured emission is likely due to this non-uniform heating effect.

Another way to examine the results is to compare the x-ray fluxes as a function of time. This is shown in Figure 2-6. Here again there is good agreement between DANTE and LASNEX in both the timing of the emission peak and the behavior at late times. The major difference in the curves is that LASNEX does predict quite a bit higher peak emission rate than the measured value. This indicates that the code may be more sensitive to some fine details at breakthrough time than during the long cool-down period. For example, the 0.3 μm (10%) tolerance in hohlraum wall thickness may account

for much of the differences near 2.5 ns. Part of the sensitivity comes because the burnthrough comes just as the laser pulse ends.

Finally, the curves in Figure 2-6 were integrated to give a running sum of the x-ray emission as a function of time. Figure 2-7 gives the resulting plot. A comparison of the curves shows that the LASNEX prediction is higher than the DANTE result by about 1.5 kJ at a time of 4 ns. Because the slopes of the emission fluxes agree at late times, one would therefore expect this difference to remain essentially constant at longer times. The code predicts 11.5 kJ of x-ray emission through the wall after 100 ns have elapsed, so the experiment can be estimated at a total of 10 kJ. Therefore the code prediction is about 15% too high in terms of total emission, due primarily to differences in flux at the time of breakthrough.

2.4.5 Conclusions

The Nova experiments have validated much of the LASNEX prediction for x-ray emission from and through the gold hohlraum wall. Therefore we can have confidence in the code results for the NIF x-ray threat, although refinement in the details of the behavior near the time of radiation breakthrough might improve predictions somewhat.

2.5 Results

Table 2-2 summarizes results for a range of yields with a 30-μm thick hohlraum wall. The target energy that does not escape as neutrons is made up entirely of debris kinetic energy and x-ray emissions. As noted previously, this amounts to about 25% of the yield, plus the laser input energy. The numerical model captured the x-ray emission in two components. First is the

radiation leak source that simulates LEH losses. The other part is a radiation flux contour on the outside surface of the gold for transmission through and emission by the gold hohlraum wall. Shapes of spectral curves for each radiation were fit to blackbody (color) temperature (BBT) curves. A single blackbody curve fit the LEH emission spectrum for any particular run. Two blackbody temperatures were required to match the wall radiation spectra because of cooling during the long output pulse. The table lists the total energy in each component of the total x-ray energy. Pulse lengths were

Table 2-2: Summary of NIF x-ray emissions from gold disks and 30-μm wall indirect drive targets.

Target	Yield MJ	Debris Energy MJ	X-ray Energy MJ	BBT eV	Pulse 10-90% ns	5 meters 10°	Fluence 5 meters 30°	(J/cm^2) 5 meters 50°	5 meters 90°
disk (1 MJ)	-	0.2	**0.70**	200	3	**0.45**	**0.39**	**0.29**	**0.00**
disk (1.8 MJ)	-	0.3	**1.26**	200	3	**0.80**	**0.69**	**0.52**	**0.00**
hohlraum	0.1	0.75	**1.08**			**0.57**	**0.51**	**0.41**	**0.12**
closing			0.70	255	10.0	0.45	0.39	0.29	0.00
LEH			0.23	52	61	0.07	0.07	0.07	0.07
			0.15	12	61	0.05	0.05	0.05	0.05
hohlraum	5	1.15	**1.87**			**0.90**	**0.82**	**0.68**	**0.30**
closing			0.94	290	9.0	0.60	0.52	0.39	0.00
LEH			0.78	75	60	0.25	0.25	0.25	0.25
			0.15	18	60	0.05	0.05	0.05	0.05
hohlraum	5	0.87	**2.15**			**1.23**	**1.08**	**0.84**	**0.14**
open			1.70	240	19	1.08	0.94	0.70	0.00
LEH			0.29	58	175	0.09	0.09	0.09	0.09
			0.16	13	175	0.05	0.05	0.05	0.05
hohlraum	20	2.05	**4.54**			**2.03**	**1.87**	**1.61**	**0.86**
closing			1.84	400	6.3	1.17	1.01	0.75	0.00
LEH			2.50	89	49	0.79	0.79	0.79	0.79
			0.20	18	49	0.06	0.06	0.06	0.06
hohlraum	20	1.65	**4.94**			**2.64**	**2.35**	**1.88**	**0.51**
open			3.35	320	13	2.13	1.85	1.37	0.00
LEH			1.38	81	67	0.44	0.44	0.44	0.44
			0.21	15	67	0.07	0.07	0.07	0.07

determined from the time history plots of each component as the time for emission of from 10% to 90% of the total energy.

Predicted outputs from disk shots are also shown in the table, to give a more complete set of possible x-ray source terms. The disk target predictions are based on experience with similar targets in Nova, with a 70% x-ray conversion efficiency assumed for the 0.35 μm laser irradiation. The blackbody temperatures of 200 eV should be a conservative estimate for these sources.

Table 2-2 also gives x-ray fluences at the first wall (5 meters from the target) at various angles from the hohlraum axis. For these calculations, the assumed angular distributions are isotropic emission for wall radiation and Lambertian distribution (cosine law) for x rays emitted from the LEH. Disk shot emission is assumed to be fully Lambertian.

A curve-fitting technique was used to approximate the x-ray output pulses obtained from the 1-D simulations to permit implementation in the x-ray response code. Wall and LEH emissions are curve-fit separately. The form of the curve fit is a double exponential. The four-parameter curve-fit equation is:

$$\text{Power} = a*\left[e^{-b*(t-t_o)} - e^{-c*(t-t_o)}\right] \quad \text{for } t>t_o \tag{1}$$

$$\text{Energy} = \left(\frac{a}{b}\right)*\left[1-e^{-b*(t-t_o)}\right] - \left(\frac{a}{c}\right)*\left[1-e^{-c*(t-t_o)}\right] \tag{2}$$

The parameters have the following interpretations:

a - scaling to obtain the correct energy
b - time constant of decaying output pulse
c - time constant for pulse rise time
t_o - fit to starting time of pulse relative to some reference

The double exponential fit is well suited to describing the x-ray pulse shapes. The (usually) rapid "turn on" of the LEH and wall emissions can be captured, as can the slow decay. The decay in the LEH x rays comes from the gradual hole closure and the cooling of the hohlraum interior. The wall emission decays with its temperature as energy is lost radiatively and as the material expands into the vacuum. Table 2-3 contains the fit parameters for the 30-μm wall hohlraums at various yields. As examples, Figures 2-8 and 2-9 show the x-ray pulses for 20 MJ and 100 kJ shots with a 30 μm hohlraum wall.

Table 2-3: Double exponential curve-fit parameters (see equations 2 & 3) for x-ray pulses from 30-μm wall NIF hohlraums. All times are referenced to the start of a 20 ns laser pulse.

Yield MJ	LEH model	a-LEH MJ/ns	b-LEH ns^{-1}	c-LEH ns^{-1}	to-LEH ns	a-Wall MJ/ns	b-Wall ns^{-1}	c-Wall ns^{-1}	to-Wall ns
0.1	closing	0.611	0.301	0.466	15.94	0.0109	0.0230	0.153	68.71
5	closing	0.739	0.287	0.450	16.27	0.0429	0.0347	0.147	43.91
5	open	0.236	0.133	3.578	16.76	0.0078	0.0173	1.568	53.30
20	closing	0.741	0.368	4.332	20.51	0.1477	0.0503	0.641	22.33
20	open	1.354	0.289	1.021	19.07	0.0867	0.0446	0.241	20.50

Emission from the LEH starts sooner (has a lower t_0) for the 100-kJ shot than for the 20-MJ shot. This brings out the fact that there are two sources of the target energy with different timing. First is the laser energy, which peaks several nanoseconds before the thermonuclear burn occurs. In the low energy shots, the laser energy dominates, so the bulk of the emission occurs sooner. In the high yield shots, the capsule energy is significantly greater than the laser energy, as discussed in section 2.3. Thus for the high yields, the curve fit to pulse shape primarily follows the burn emission.

The x-ray energy predictions reported in Table 2-2 were scaled up from the 1.0 MJ radiation source used in the simulations to the full 1.8 MJ laser energy baseline case. This was done to provide a more conservative estimate of the target output for each run. For scaling each run, total x-ray energy was maintained at the same fraction of non-neutron energy as calculated in the run. Similarly, the run's x-ray energy partition between LEH and wall components was used to distribute the increased x-ray energy. Blackbody temperature fits were not adjusted for the increased target energy because the spectra change slowly with energy. Ignoring this small correction gives a slightly more conservative source prediction. Pulse lengths also were not corrected for the increased target energy, so that the only change to the pulse shape parameters given above was to modify "a" to produce the proper integrated x-ray energy.

2.6 Discussion

2.6.1 General

Until this detailed study was undertaken to examine the specific target designs envisioned for the NIF, the predictions for x-ray output were based on general trends developed for a variety of target types. In particular, it was assumed that the non-neutron energy (the laser energy plus 20% of the yield) was evenly divided among x rays and target debris. The results obtained with this series of LASNEX simulations indicate an x-ray fraction of 60 - 75% of the non-neutron energy, rather than 50%. This represents a considerable improvement in the prediction for the NIF target chamber. In a similar way, Inertial Fusion Energy (IFE) studies could benefit from the more detailed predictive capability now available. For example, the HYLIFE II reactor design

is based on the assumption of a 50/50 split between x rays and debris of the non-neutron energy (one-third of the total target energy)[6].

Uncertainty in the rate of laser entrance hole closure required the calculation of two bounding cases. The open LEH model gives a total x-ray energy emitted of about 10 - 15% higher than with the closing LEH model. This is a modest change compared to the difference in the way the x-ray energy is divided between LEH and wall emissions in the two cases. For example, the Table 2-2 data show that in the closing LEH scenario, the wall x-ray emissions are 50% and 60% of the total for the 5-MJ and 20-MJ yields, respectively. The open LEH model gives the wall emission 21% and 32% of the total for these two cases. The "open" model gives a wall emission about half that of the "closing" model. This is because the internal hohlraum energy escapes quickly and is not able to couple into the wall material in the open case.

The question of which of the two LEH closure models produces the most severe x-ray threat to the chamber is a complex one that depends on the surface material and chamber location of interest. For a material that damages according to the maximum melt depth (as the NIF first wall coating of boron carbide is thought to), the open LEH model emissions near the hohlraum axis are the most stressing. For materials whose damage is more associated with peak surface temperature (e.g., the fused silica beam dumps on NIF), having more energy in the colder spectrum of the wall emission may make the closing LEH the worst case. The reason for presenting both open and closing LEH model results is to allow response calculations to determine the more damaging scenario for a given set of conditions.

The x-ray emission from the wall requires a composite of two blackbody curves to accurately fit the time-integrated LASNEX spectrum. This is necessary because the wall material cools significantly due to radiation losses and expansion into vacuum. Emission in the higher photon energy bins (above a few hundred eV) falls off rather rapidly, while the lower energy bins continue to emit throughout most of the simulation.

The laser entrance hole spectrum (closing LEH model) can be fit with a single blackbody curve because closure of the entrance holes occurs before the temperature on the hohlraum interior can fall significantly. With the open LEH assumption, a single blackbody fit also serves at high yields because the strong pulse of emission near the times of burn and collision of the capsule material with the wall dominates the later time emission after the interior has cooled. In the no-yield case, where the LEH output comes solely from the laser pulse, the closure of the LEH happens late enough that there is little difference between the open and closing LEH cases.

2.6.2 Variations with yield

Higher energy shots drive up the temperatures of both the hohlraum interior and the bulk hohlraum wall material. Radiated power is directly proportional to the fourth power of temperature, so the higher energy targets will emit more energy than lower energy targets. The fraction of the non-neutron energy in x rays should therefore increase with yield. As shown in Figure 2-10, the x-ray fraction of non-neutron energy with the closing LEH model increases from just below 60% to 72% as the yield increases from 0.45 MJ up to 30 MJ. The open LEH results show a variation from 70% to 77% with yield.

Figure 2-11 shows the variation in the fraction of total x-ray energy emitted out the LEH. At the low yields, there is much less energy available to heat the hohlraum wall material sufficiently to radiate significant energy, which lowers the relative contribution of the wall emission. This explains why the LEH fraction of x-ray emission is highest at low yields.

Examination of Table 2-2 shows that the effective blackbody temperature of the LEH emission is nearly a linear function of yield. This is expected since the kinetic energy and temperature of a gas (plasma) are related by $E = 3/2\,kT$. The hohlraum is a good radiation case to maintain this temperature for the duration of the x-ray output pulse. The data in the Table 2-2 show that higher yields also cause higher emission temperatures in the wall component. The varying energy fractions in the two-BBT fit to the wall output make a more complex relation between temperature and yield than for the LEH emission.

The pulse lengths, defined as the time for 10% to 90% of the energy emission to occur, are plotted against yield in Figure 2-12. Shorter pulse lengths at higher yields are the result of higher emission rates at the higher temperatures. Although energy is still emitted as the high-yield targets cool, the integrated energy is dominated by what came off at the highest temperatures.

2.6.3 Variations with wall thickness

One goal for the wall thickness parameter study was to determine how much the thickness could be reduced before the internal radiation environment was affected. The method of driving the target with a radiation source guaranteed that capsule yield would not be degraded by extra losses

through the hohlraum wall. Since yield was invariant, the wall effect on radiation drive can best be seen by plotting the input energy required to supply the specified radiation field against hohlraum wall thickness. Figure 2-13 shows this for the closing LEH model runs. At wall thicknesses of 30 μm and above, the input energy was constant. Below 30 μm, the input energy begins to increase, though only by 7% with a 10-μm wall. The one run made with a 5-μm wall thickness showed more than a 30% increase in required input energy. Since this case violated the assumption that the radiation drive used in the simulation was what would have been generated by the standard laser drive, this case is not included in any of the other results presented here. If the threshold for minimum wall thickness must be accurately determined, further simulations will be required using the actual laser drive (as opposed to a fixed radiation drive) over the 10 - 40 μm wall thickness range.

The other motivation for studying wall thickness effects (besides determining the minimum wall thickness) was to examine possible trade-offs between x-ray and debris energy. Figure 2-14 plots the changing energy split for the two LEH closure assumptions. It is also important to determine the contribution of the LEH and wall components in specifying the x-ray source term, because of the differences in effective temperature, pulse length, and spatial distribution. Figure 2-15 presents a plot of the emitted energy in the LEH component as a function of wall thickness. Because the thinner walls do not retain the yield energy as well as the thick walls do, the LEH energy falls off below about 30 μm. The wall emission, in contrast, increases quickly with lesser wall thicknesses. The radiation wave burns through the thin walls soon after bang time, so the material is quite hot and radiates effectively. The thicker walls require more time to burn through and have much more mass

to heat up. This reduces the radiated energy at the expense of increased kinetic energy in the debris.

These variations give the opportunity to tailor the x-ray emission to minimize damage to the target chamber, provided a minimum thickness is maintained to prevent burn-through. A thin wall would make the x-ray energy distribution more isotropic and would decrease the mass of target debris. But more energy would come in the colder, generally more damaging, spectrum of the wall emission. An increase in wall thickness would greatly reduce the isotropic wall component. This might be a benefit for the target positioner, for example, which has very little direct view of the LEH. Trade-offs will have to be evaluated based on an integrated analysis of the target chamber response to a particular target design.

References

1) LASNEX and Atomic Theory, LLNL Laser Program Annual Report, 1980, Vol 2, UCRL-50021-80.

2) R.R.Peterson, P.Wang, J.J.MacFarlane, G.A. Moses, "Off axis X-Ray Emission from the Hohlraum Case of Ignited NIF Indirect Drive Targets", presented at 37th Meeting of Division of Plasma Physics, Louisville KY, Nov 6-10, 1995.

3) Lindl, J., "Development Of The Indirect-Drive Approach To Inertial Confinement Fusion And The Target Physics Basis For Ignition And Gain", Physics Of Plasmas, 1995 Nov, V2 N11:3933-4024.

4) Haan SW, et. al., "Design and Modeling of Ignition Targets for the National Ignition Facility", Phys Plasmas **2** (6), June 1995.

5) Kornblum, H.N., Kauffman, R.L., and Smith, J.A., "Measurement of 0.1-3 keV X Rays From Laser Plasmas," Review of Scientific Instruments, V57, No.8, pages 2179-2181, August, 1986.

6) Moir RW, Bieri RL, Chen XM, Dolan TJ, Hoffman MA, House PA, Leber RL, Lee JD, Lee YT, Liu JC, Longhurst GR, Meier WR, Peterson PF, Petzoldt RW, Schrock VE, Tobin MT, Williams WH, "HYLIFE-II - A Molten-Salt Inertial Fusion Energy Power Plant Design - Final Report", Fusion Technology, 1994 Jan, V25 N1:5-25.

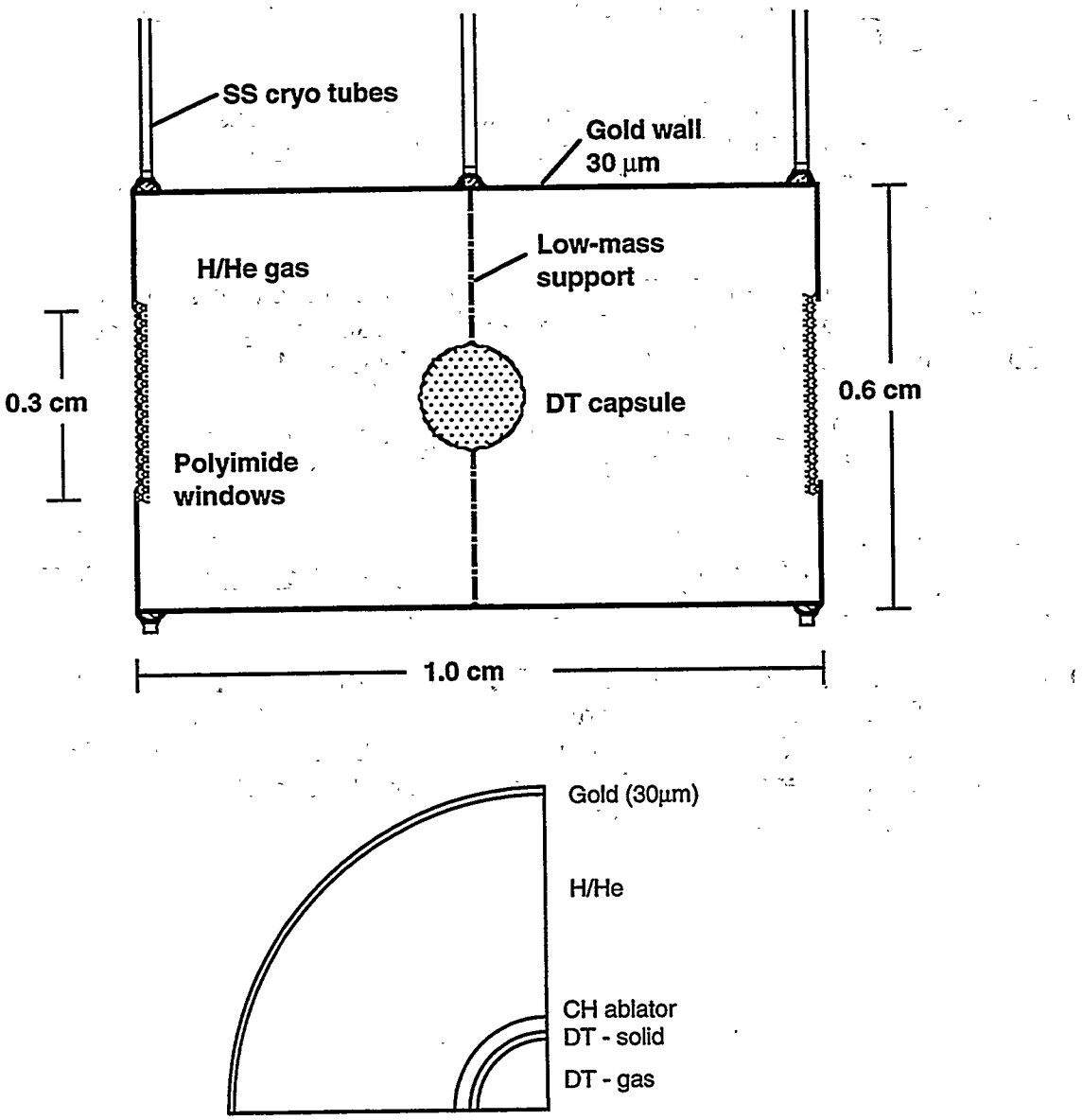

Figure 2-1: Baseline NIF target design and 1-D model approximation

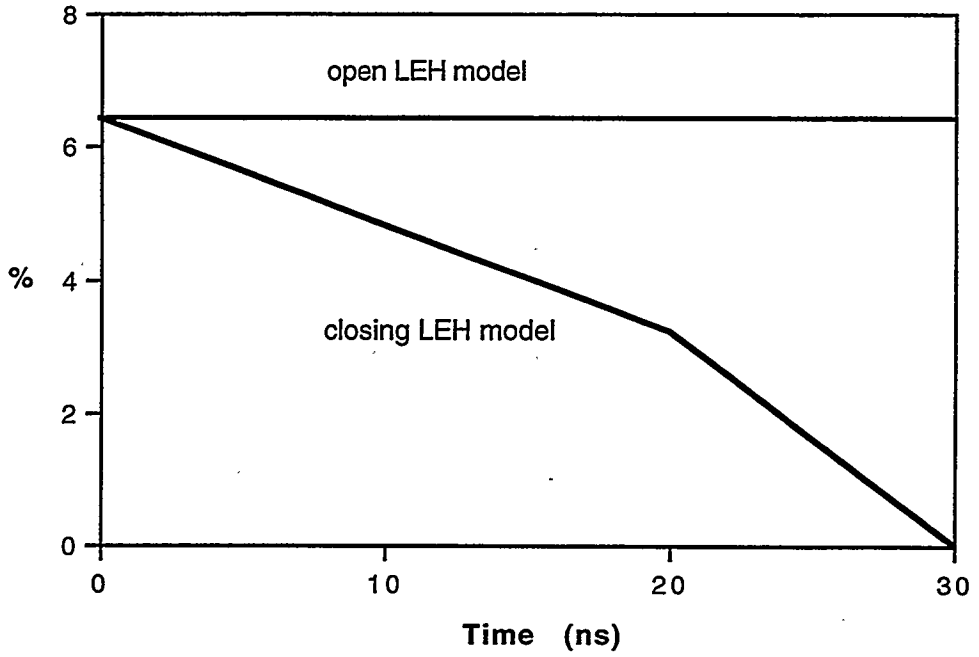

Figure 2-2: Fraction of 1-D surface area free to radiate directly from hohlraum interior. Laser pulse runs from t = 0 to 20 ns.

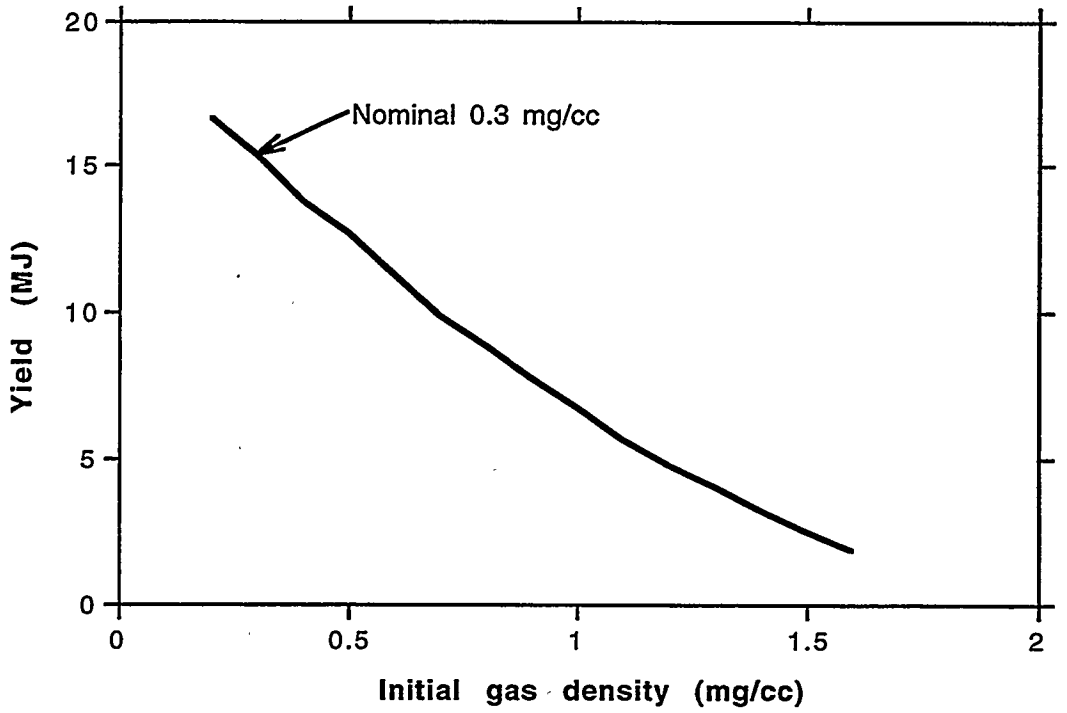

Figure 2-3: Effect of internal gas density on capsule performance. Based on a smaller capsule design than considered here.

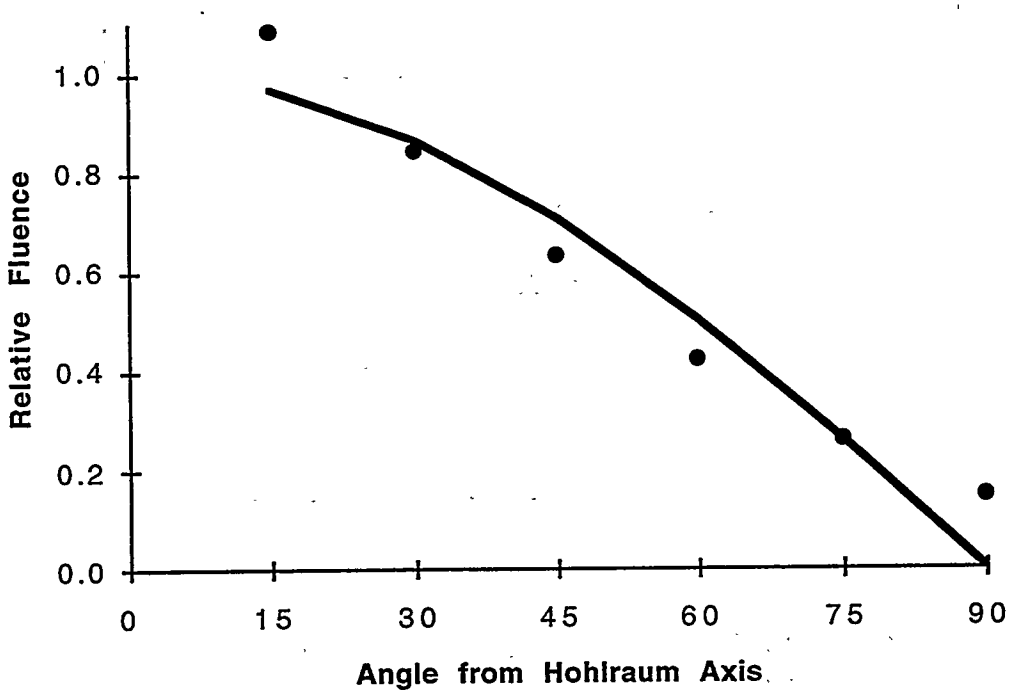

Figure 2-4: Angular dependence of LEH x-ray emission predicted by a 2-D simulation[2]. Comparison with a best-fit Lambertian distribution shows good agreement. Results for a 10-MJ yield indirect drive target.

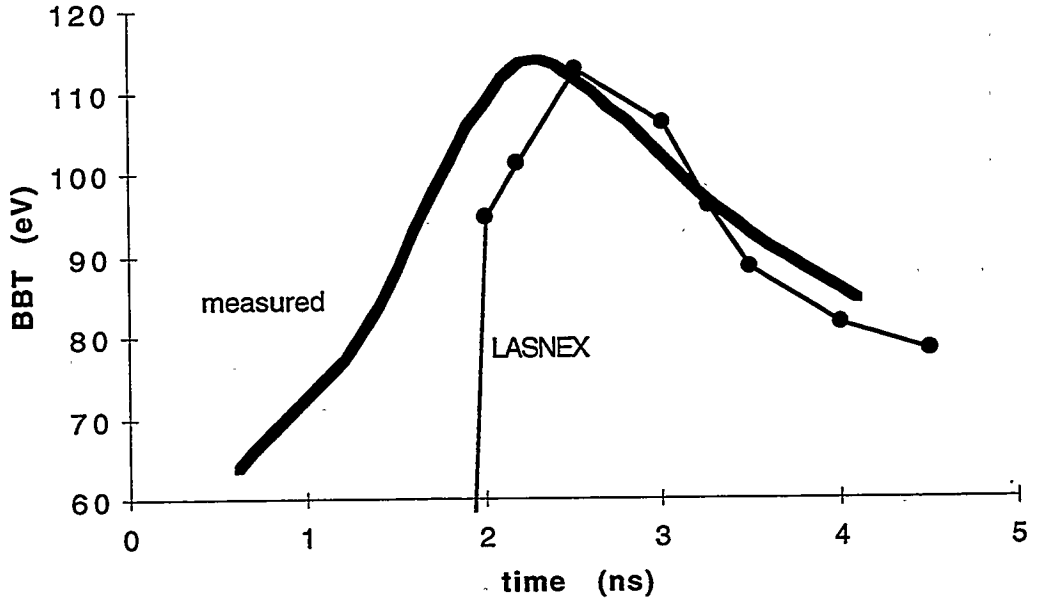

Figure 2-5: Comparison of spectral fits to wall x-ray output of 3-μm wall Nova hohlraum driven by 28 kJ of laser energy.

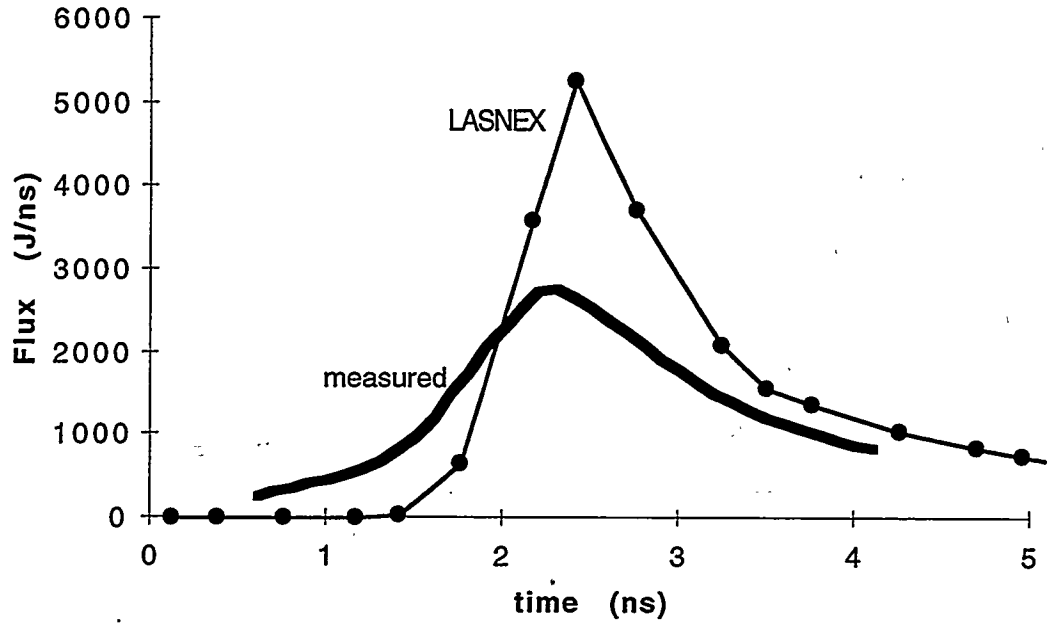

Figure 2-6: X-ray flux from/through 3-μm Nova hohlraum wall. Late time emission rates agree well.

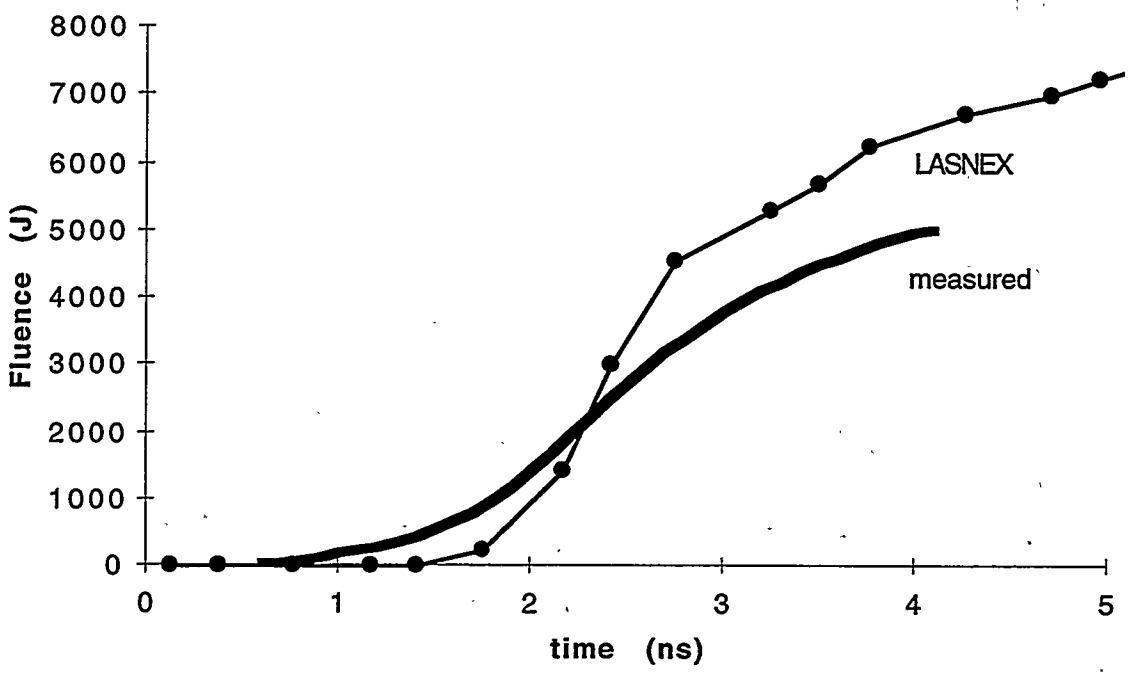

Figure 2-7: Running sums of x-ray fluence through 3-μm hohlraum wall.

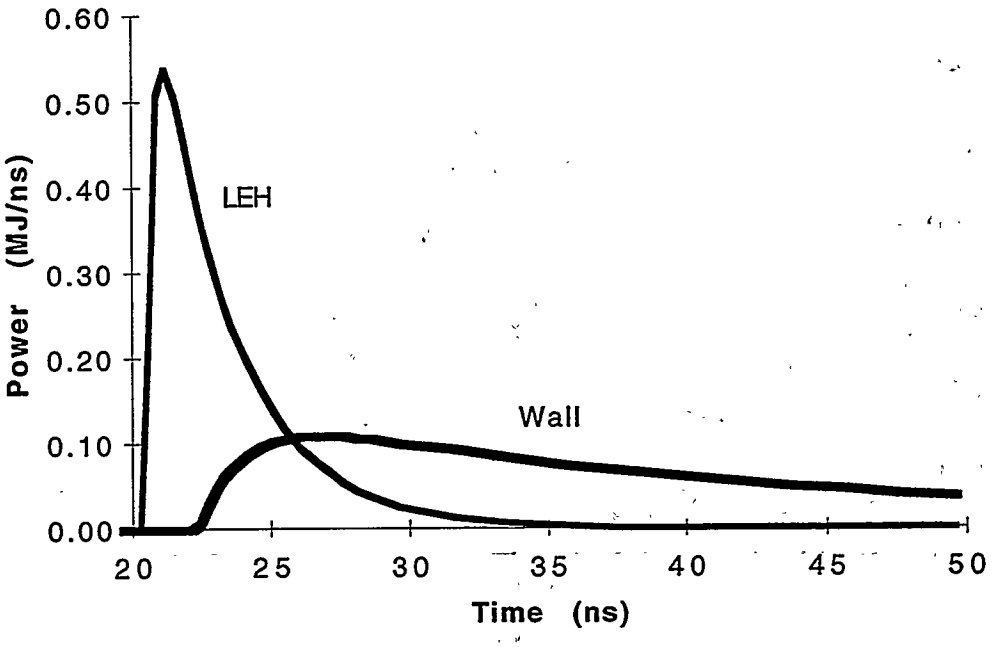

Figure 2-8: 20 MJ x-ray output pulses (30-μm wall, closing LEH model).

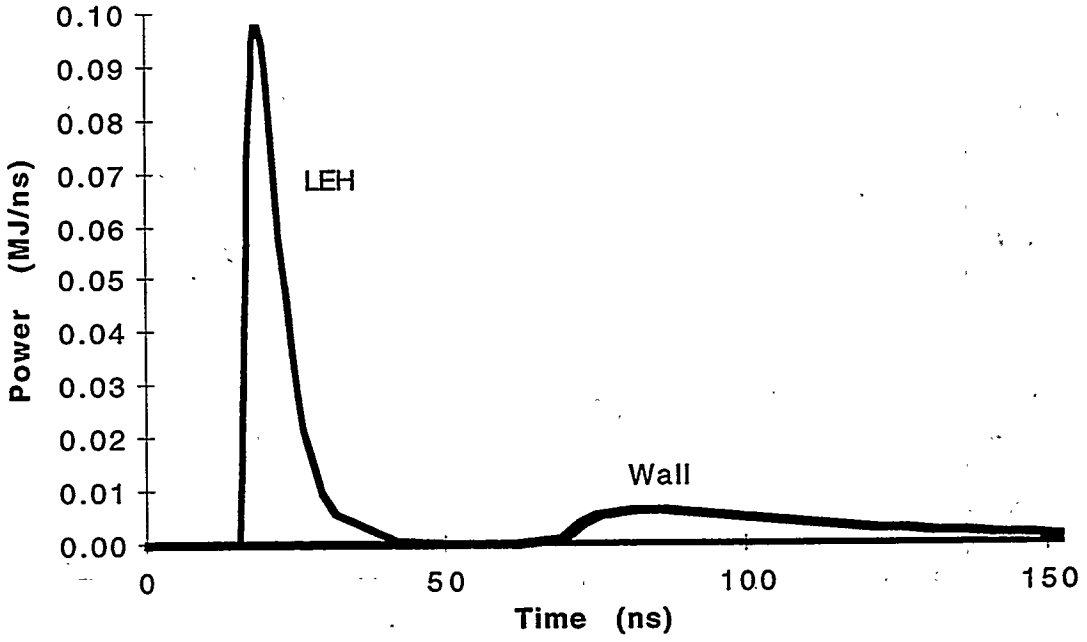

Figure 2-9: 100-kJ shot x-ray output pulses for 30-μm wall thickness.

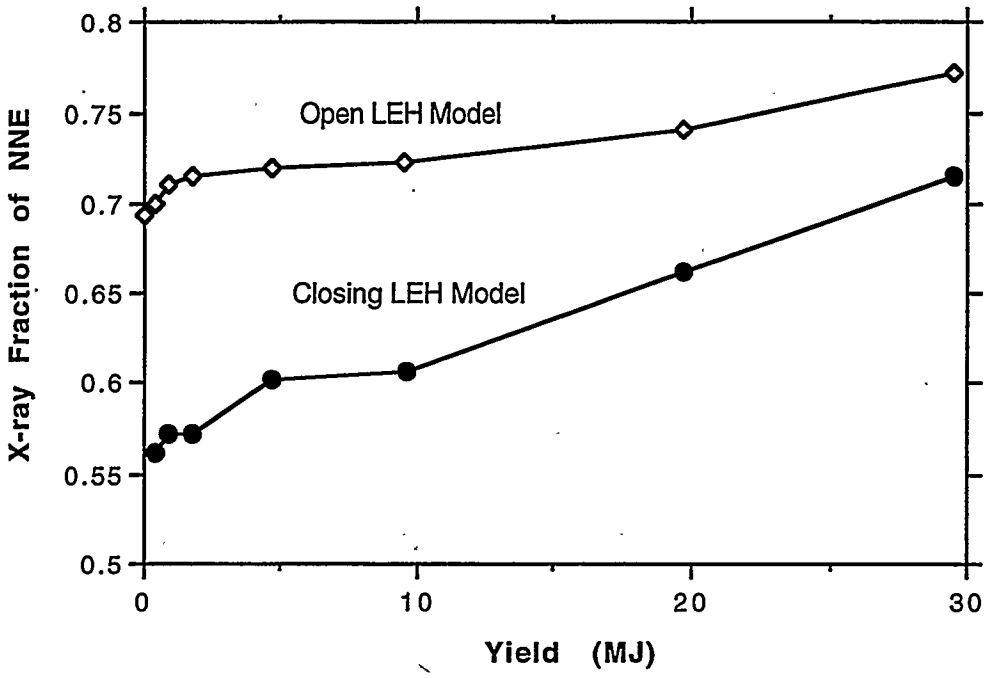

Figure 2-10: Fraction of non-neutron output energies (NNE) as a function of yield for 30-μm wall hohlraum. NNE is a relatively constant 25% of yield.

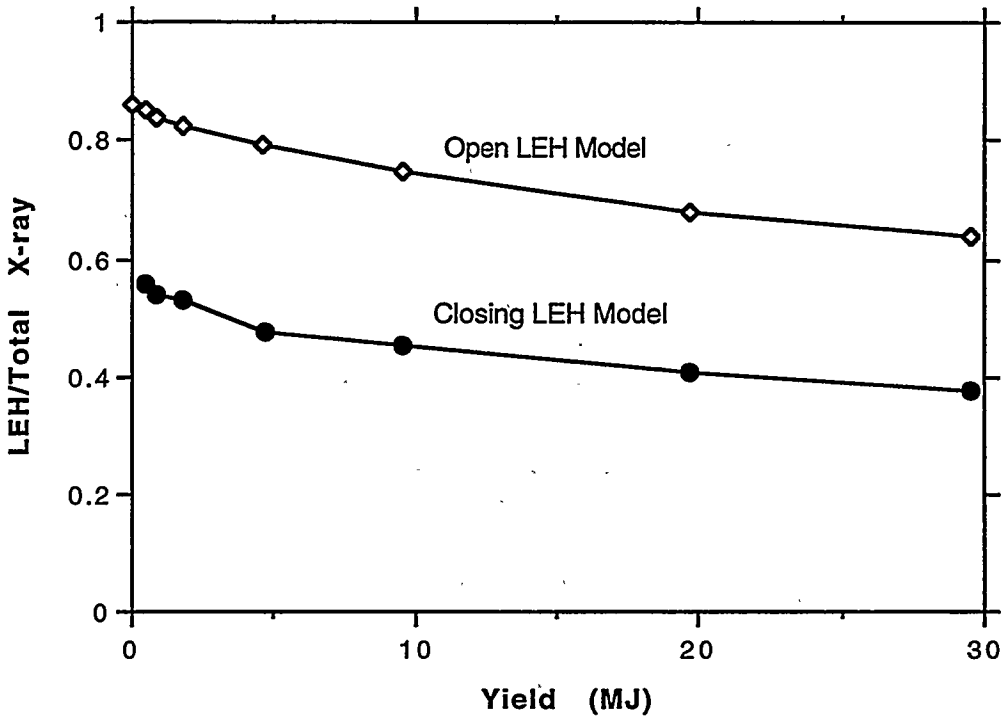

Figure 2-11: Fraction of total x-ray energy emitted from LEH as a function of yield for 30-μm wall hohlraum.

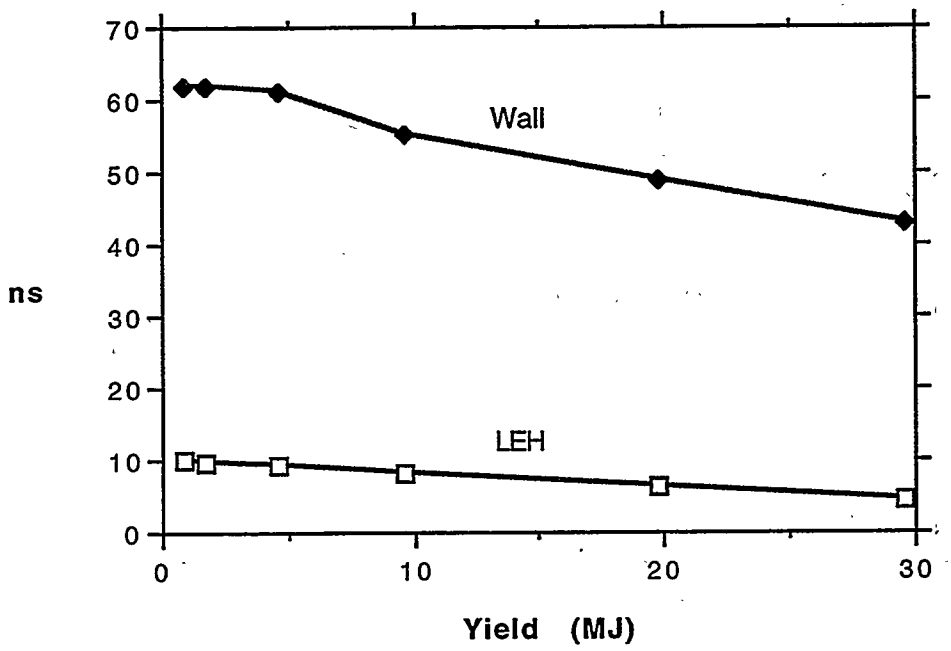

Figure 2-12: X-ray output pulse lengths as a function of yield.

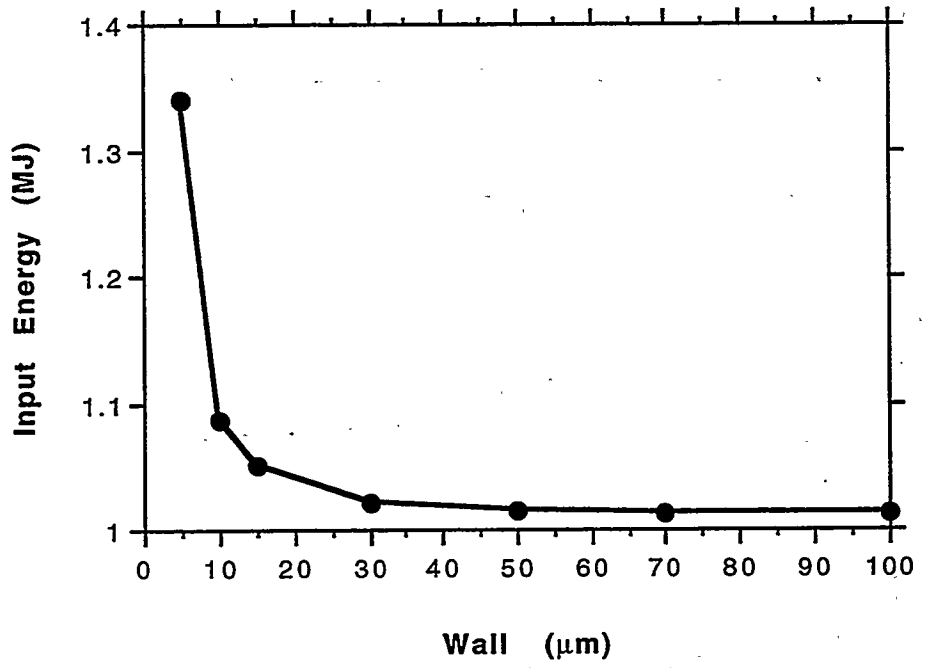

Figure 2-13: Required source energy to maintain radiation drive conditions inside hohlraum. Losses through the wall become significant below 15 μm.

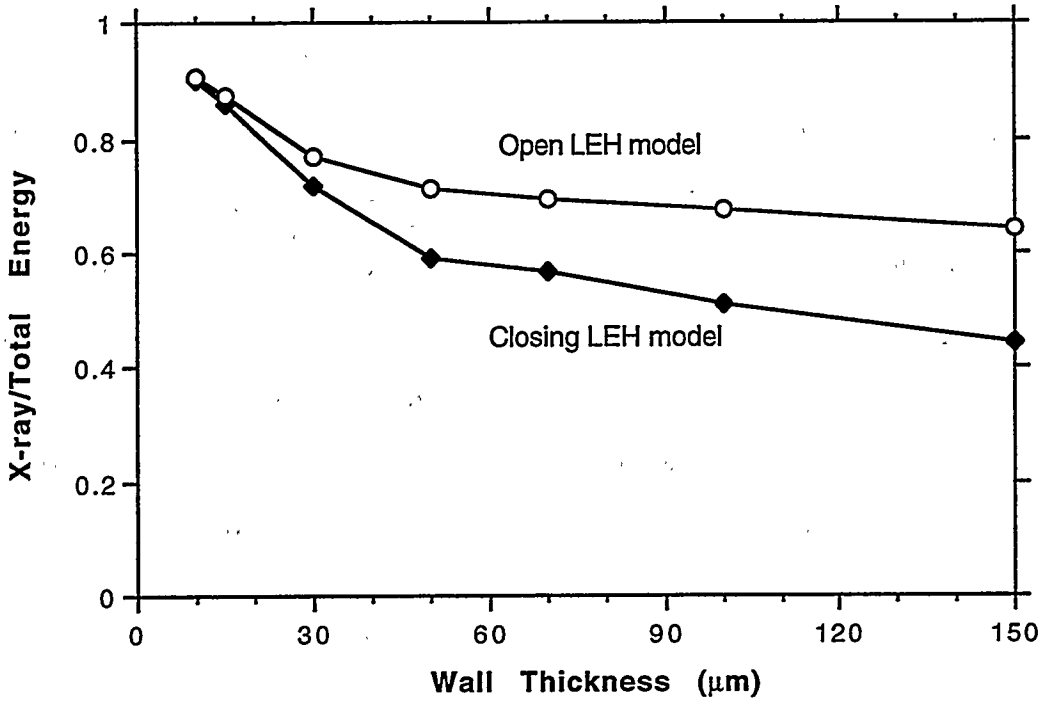

Figure 2-14: Fraction of non-neutron energy emitted as x rays as a function of hohlraum wall thickness. Non-neutron energy is relatively constant at 25% of yield.

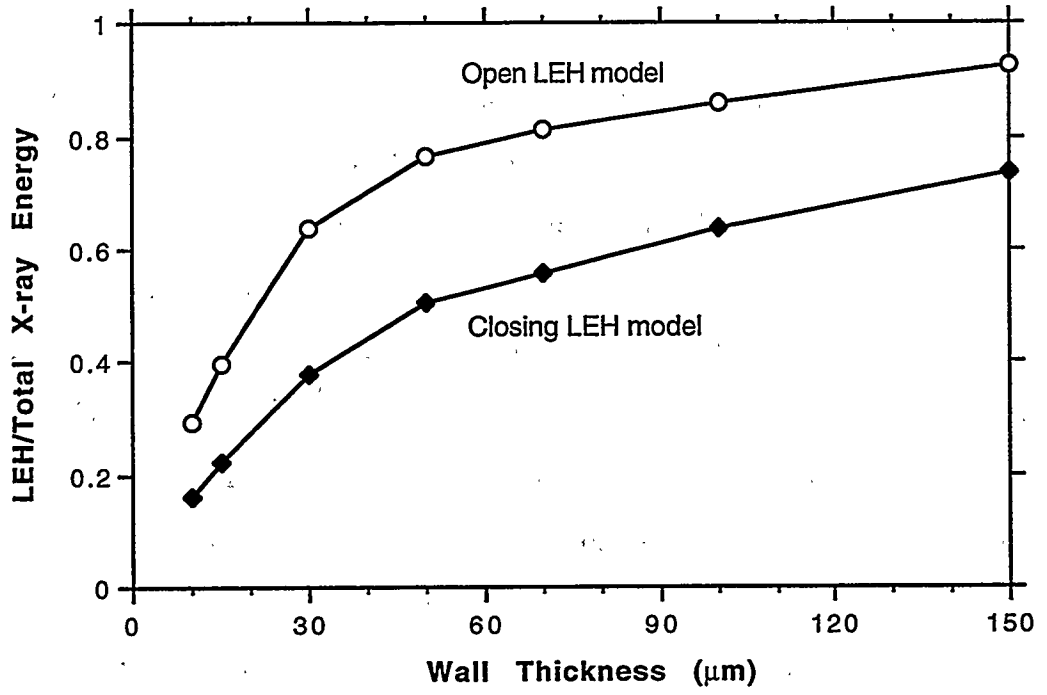

Figure 2-15: Fraction of total x-ray energy emitted from LEH as a function of hohlraum wall thickness.

3. ABLATOR Transient Ablation Model

3.1 Introduction

X-ray emissions from targets can be sufficiently energetic to ablate material from exposed surfaces in ICF target chambers. Of particular interest is the first wall of the National Ignition Facility (NIF) chamber, which will receive x-ray fluences up to about 2.6 J/cm^2. This is a pulsed situation, with energy released over a few to a few tens of nanoseconds in shots occurring every few hours. Energy deposition occurs in such a small characteristic depth (on the order of a micrometer), that thermal conduction and hydrodynamic motion significantly affect the material response during these short pulses.

The transient ablation modeling has two goals. The first is to predict the amount of material removed by the x rays (the ablation depth). The second goal is to determine the state of the ablated material after it leaves the surface. This includes information on velocity and temperature and whether the material is vapor, liquid droplets or solid particulates. The primary goal is to determine total amount and form of any material in the chamber that may deposit on the optics and cause damage during subsequent laser shots.

Four processes are included in the ablation model to accomplish these goals. The first process is the energy deposition from the x rays through the thin surface layers of material. A transient thermal conduction model allows this energy to move between zones, which is particularly important in the strongly heated surface material. Heating causes rapid thermal expansion, which raises pressures and causes hydrodynamic motion as the pressures release from the surface. The fourth part of the model describes the removal of material through surface vaporization and various spall processes.

3.2 General Description

The ABLATOR code is a new program developed specifically for this x-ray ablation study. It is a one-dimensional Lagrangian finite difference code for the calculation of material response to x rays. The code name is taken from "Ablation By LAgrangian Transient One-dimensional Response". In the Lagrangian scheme, zones and zone boundaries move with the material, as opposed to permitting mass flow between zones in a fixed grid (Eulerian formulation). The Lagrangian form guarantees mass conservation and is well-suited to one-dimensional analyses where a zone can only interact with zones immediately adjacent to it (no mixing).

The code uses an explicit scheme for advancing in time. This means that conditions at the next time step are calculated directly from the state at the current time step, plus any incremental energy input. The advantage of this approach over an implicit method is that rapid and relatively simple calculations suffice to advance the solution in time. The major disadvantage is that numerical stability concerns limit the maximum time step size to a rather small value, so that many more time steps are needed to reach a given stop time.

Some typical run conditions may serve to illustrate the operation of the code. To capture the x-ray deposition and subsequent ablation accurately, many zones are needed near the surface, in the first micrometer or two. One grid arrangement uses 100 zones with geometrically increasing size to cover just over 50 μm depth. The first zone (at the surface) has a thickness of 0.01 μm, and each zone into the material is 1.06 times as thick as the previous zone. Various thermal and hydrodynamic stability limits give a typical time step size of about a

picosecond, with total problem times of a few hundred nanoseconds. A single case will run in a few minutes on a Hewlett-Packard 735 workstation.

The flow chart in Figure 3-1 shows the order of operations in a time step. A loop through each node in the problem occupies most of the cycle. The motion of the zone boundary is first determined from stresses in the adjacent zones. Since zone mass is fixed, the zone density calculation follows directly. New stresses and work terms are then determined from the strains in the zone. Energy inputs from the x-ray source and gains or losses from thermal conduction are next found for the zone. By applying energy conservation, the new zone energy is determined. Equation of state relations are then used to obtain new values for the pressure in the zone. The pressure is combined with the deviatoric stresses already calculated to give the new normal stress in the zone. It is this normal stress that drives the motion on the next time step. After the new state has been determined for all zones, calculations are made for the surface vaporization, which is applied to the zone containing the moving surface on the next time step. After finding the maximum time step size permitted by explicit stability considerations, the problem time is advanced and the cycle through the zones is repeated.

The code models different materials through the use of two external material data files. The first file "matdata" contains thermal conductivity, enthalpy/ temperature relations, EOS (equation of state) data, and some mechanical properties. These data are obtained from reports in the literature. The second file "opacdata" gives the photon energies and corresponding absorption cross-sections for the material.

3.3 X-ray Deposition

X rays of a particular photon energy deposit according to a simple exponential decay. This uses a cross-section based on the cold opacity of the material at that energy. The cross-sections used in the ABLATOR code come from the elemental values given in Cullen, et al[1], appropriately combined on a weight-fraction basis for a particular compound. The photon energy range from 1 eV to 100 keV is divided into a number bins, each of which is treated as a monoenergetic deposition process. Energy is deposited into the zones in each time step according to the given x-ray energy pulse shape. The total energy at any depth is just the sum over all energy groups.

$$e(x) = \sum_{i=1}^{n} \frac{I_o(i)}{\lambda(i)} \exp\left(\frac{-x}{\lambda(i)}\right) \qquad (1)$$

where $I_o(i)$ is the incident energy in group i and λ is the photon mean free path.

The photon energy group approach gives an accurate representation of the edges in the typical opacity curves. Figure 3-2 shows the opacity curve for silicon dioxide (fused silica) as a function of photon energy for the bin structure used in the code. Also shown are two typical blackbody x-ray spectra. Figure 3-3 shows the variation in peak surface temperature for fused silica for several different numbers of photon groups. The conditions were depositions of 1 ns square pulses of: a) 0.5 J/cm^2 of 200 eV blackbody x rays and b) 0.25 J/cm^2 of 100 eV blackbody x rays. Neither case shows much change from the changing group structures, so the choice of either 45 or 90 groups is sufficiently accurate.

The code allows several different ways of specifying the x-ray source energy spectral and temporal characteristics. A menu allows the selection of one of the

NIF hohlraum cases presented in Chapter Two (100 kJ, 5MJ, 20MJ yields, with either open or closing LEH models). These options provide the code with the complex time-varying x-ray energy from multiple blackbody components. Alternatively, the user may choose to supply a single blackbody spectral component in either a square or gaussian pulse shape. Note that the square pulse has a 2% time ramp at the leading and trailing edges of the pulse to reduce the instabilities resulting from an abrupt change in energy input. Finally, a simple exponential deposition may be selected to simulate response to a laser or line x-ray radiation. This energy may be deposited in a square or gaussian pulse of arbitrary length. Specifying the distance from the target and the angle from the hohlraum axis provide the connection from total x-ray power to flux on a surface at a particular location. Note that energy deposited in the square or gaussian pulses is assumed to have a Lambertian distribution (characteristic of a simple disk target for example), while the NIF-specific sources have the distributions discussed in the previous chapter.

The fraction of energy from a particular blackbody emission deposited in each zone is determined once at the start of the simulation. This is possible because cold opacities are used in this Lagrangian code, so the attenuation in a zone at a given photon energy stays constant through the run. The attenuation information is stored in a two-dimensional array EFRAC(zone#, group#). At each step in the run, routines determine the incremental change in input energy during that interval for each of the photon energy groups. The energy deposited in a particular zone is the sum over the photon groups of the product of the energy in a group and the EFRAC fraction for that group.

One result of the treatment of x-ray deposition used in the code is that vapor shielding is an inherent part of the formulation. Vapor shielding is the process by which energy deposited in a surface is reduced by the attenuation of x rays in the vapor which has already blown off the surface. Such a process might be observed with long (several nanoseconds), high energy pulses and low boiling point materials. The phenomenon is particularly important in laser ablation of materials, where a strongly-absorbing plasma can be quickly formed on the irradiated surface. Of course if a plasma is generated during x-ray deposition, the cold-opacity assumption breaks down.

3.4 Energy Transport

The one-dimensional planar equation of energy conservation is:

$$\rho\frac{\partial E}{\partial t} = (p+q)\frac{1}{\rho}\frac{\partial \rho}{\partial t} + P_d + \frac{\partial h}{\partial x} + \rho Q_{in} \qquad (2)$$

E = internal energy per unit mass
p = pressure or normal stress
q = viscous stress (see next section)
P_d = rate of deviatoric stress work (see next section)
h = heat flux due to conduction
Q_{in} = heat added per unit mass and time

This equation equates the rate of change in energy to work terms (pressure, viscous, and deviatoric) plus net heat conduction plus the heat added (from x-ray deposition). The work terms will be discussed in the next section, with the details of the hydrodynamics and stress-wave calculations.

The code treats the internal energy of each Lagrangian zone as the primary quantity for energy conservation, rather than using temperature as a basis. This avoids some of the difficulties encountered in temperature-based methods near

the solid/liquid phase change. These other methods need some means to incorporate the latent heat of melting into the heat capacity formulation for the material. With the energy-based method, there is no difficulty in smoothly increasing the energy in a zone, even though the temperature may remain fixed. However, temperatures are required for two purposes in the code. They are used to calculate the net thermal conduction gain (or loss) for each time step, through the temperature gradient. The zone temperature is also required for determining certain temperature-dependent material properties, in particular the thermal conductivity and yield strength.

Temperature is determined for each phase (solid, liquid, and vapor) as a function of enthalpy (u + pv), based on curve fits to thermodynamic data. The data are generally taken directly from the JANAF tables[2] for the condensed phases and for monatomic vapors. Treatment of polyatomic vapor species depends on pressure, temperature, and the resulting compositional changes in a complex way. Specialized thermodynamic analyses (see Wilemski [3,4] for example) have provided the necessary information in these cases.

Thermal conductivities for the solid and liquid phases of a material are assumed to be temperature dependent. The code accepts fifth-order polynomial fits to whatever data is available in the literature for each phase. The vapor phase thermal conductivity is assumed to follow the form[5]:

$$\kappa = A_v\sqrt{T} = \left[\frac{1}{d^2}\sqrt{\frac{k^3}{\pi^3 M}}\right]\sqrt{T} \qquad (3)$$

d = molecular diameter
k = Boltzman's constant
M = molecular weight
T = temperature

The code uses a single input parameter (A_v) for this relation. This function was derived for a monatomic gas, so if better data are available for the gas species, A_v can be used as a curve fit parameter. However, as a practical matter, the vapor conductivity has little effect on the calculations. Gas conductivity is generally rather low, the distances for conduction are relatively large in the expanded vapor, and the time scales are too short.

Heat conduction between adjacent zones is calculated from the finite difference form of the Fourier heat conduction equation (for planar, 1-D geometry).

$$\frac{Q}{A} \doteq -\kappa \frac{(T_1 - T_2)}{(x_1 - x_2)} \qquad \kappa = \frac{2\kappa_1\kappa_2}{(\kappa_1 + \kappa_2)} \tag{3}$$

The thermal conductivity is temperature dependent, so a geometric mean of κ_1 and κ_2 is used with this equation. The net heat flux for a zone is calculated from the difference between heat flow to the right and to the left.

The steep temperature gradients resulting from the x-ray deposition in a few micrometers of surface material give rise to high heat fluxes. Fluxes on the order of 10 MW/cm^2 have been calculated in various material response simulations. Recent work in the area of laser ablation of materials (Kar et al[6] and Peterlongo[7], for example) raise the issue that in very high heat flux regimes, the thermal wave velocity may become important. The Fourier law assumes an infinite propagation speed of thermal energy, giving rise to the classical parabolic equation for transient heat conduction. Inclusion of the real velocity of the thermal wave changes the problem to a hyperbolic equation. A test for this condition was discussed in reference 7, referring to an earlier paper by

Harrington[8]. Harrington argued that the usual parabolic formulation could be used provided that the difference in thermal gradients between two isothermal planes was well-approximated by the second spatial derivative. That is,

$$\rho c \Delta x \Delta t = \kappa \left(\frac{\partial T}{\partial x_1} - \frac{\partial T}{\partial x_2} \right) \approx \kappa \frac{\partial^2 T}{\partial x^2} \tag{4}$$

A Taylor's series expansion of the first derivatives gives

$$T_1' - T_2' = T_2'' \Delta x + T_2''' \frac{(\Delta x)^2}{2!} + T_2'''' \frac{(\Delta x)^3}{3!} + \ldots \tag{5}$$

Harrington argued that if $T''_2 >> T'''_2 (\Delta x/2)$, then the parabolic form of the heat conduction equation could be used. A typical test case was run to determine which heat transfer regime should govern for these x-ray response calculations. The thermal profile in aluminum exposed to 1.2 J/cm^2 of 160 eV blackbody radiation was determined and curve fit with a fifth order polynomial in ln(x). Derivatives were taken from the curve fit to establish the ratio of the first to second terms on the right side of equation 5. The ratio was between 5 and 9 in the first micrometer of the aluminum material, where the temperature gradients were steepest. This reflects a possible 10 - 20% effect from the non-Fourier heat conduction components. Given that the uncertainties in thermal conductivities at high temperatures are at least this large, the omission of higher-order terms seems reasonable.

The thermal boundary conditions typically used in the code are rather simple. The rear surface is assumed to remain at the bulk temperature throughout the run. For this reason the overall thickness of the mesh should exceed the distance over which conduction will increase local temperatures within the simulation time. A thickness of 50 μm has proven more than adequate for runs up to 1000

ns long. The front boundary (to the left of zone number one) is assumed to be insulated. This reflects the facts that no thermal conduction or convection can occur where there is no material (in ablation into a vacuum), and that the thermal radiation flux is too low to be important. For example, even if the surface remained at 8500 K for an entire 1000 ns run, only 0.03 J/cm^2 would be radiated to a room temperature heat sink.

For an explicit method of time advance as used in the ABLATOR code, the time step size is limited by the stability condition:

$$\Delta t \leq \frac{(\Delta x)^2}{2\alpha} \tag{6}$$

where α is the thermal diffusivity. If this condition is not satisfied, unstable oscillations quickly develop. The minimum step size, called Δt_{heat}, is found by evaluating this criterion for each of the zones in the problem. The time step size used for the next increment is the minimum of this Δt_{heat} and the Δt_{hydro} calculated based on the hydrodynamic stability requirements. This step size may be further reduced if certain limits on maximum temperature change in a zone or in surface vaporization rate are exceeded.

3.5 Mechanical Response Model

3.5.1 General Formulation

A finite-difference hydrodynamic model is implemented to track stress wave and material motion caused by the sudden energy deposition. At each time step, the zone energy and density information, combined with a Grüneisen EOS give the pressure and stress in each zone. These data are used to compute accelerations with F=ma, which in turn gives velocities and zone boundary

locations. With the (constant) zone mass, densities can be determined to continue the cycle.

The formulation used in ABLATOR is based on that used in the Sandia National Laboratory code WONDY V. Kipp and Lawrence's thorough report on the code[9] contained all the necessary finite difference relations for determining mechanical response. This section will present the important points of the WONDY method, with coverage of many details left for the original report.

The structure of the finite difference mesh is that all quantities represent averages over the zone between two adjacent node points. The exception is that the node points themselves carry acceleration, velocity, and position. The following sketch gives the general arrangement. In the current implementation of the code, node 0 corresponds to the left edge of the problem, and is the surface that first intercepts the x-ray energy.

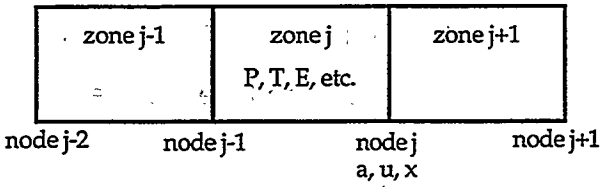

In the time discretization scheme, all quantities are defined at time steps n, n+1, n+2, etc. through the problem run time. The only exceptions are the velocity (u_j) and the time step itself (Δt), which are established on the half time step (n-1/2, n+1/2, and so on).

The one-dimensional, planar equation for conservation of momentum in differential form is:

$$\rho a = -\frac{\partial}{\partial x}(\sigma + q) \tag{7}$$

and in finite difference form:

$$a_j^n = 2\left[\frac{\left(\sigma_{j-1/2}^n + q_{j-1/2}^n\right) - \left(\sigma_{j+1/2}^n + q_{j+1/2}^n\right)}{\rho_{j+1/2}^n\left(x_{j+1}^n - x_j^n\right) + \rho_{j-1/2}^n\left(x_j^n - x_{j-1}^n\right)}\right] \tag{8}$$

where: x = Lagrangian spatial coordinate; ρ = mass density
a = acceleration; q = artificial viscous stress
σ = normal stress in x direction
j = zone or node index (spatial discretization)
n = time index (temporal discretization)

Computation of the acceleration from current stress states starts the time-advancement cycle. From acceleration, velocity and position are directly determined by the following relations. Once the new zone boundary locations are determined, the density comes directly from the known (and unchanging) zone mass and the new zone size.

$$u_j^{n+1/2} = u_j^{n-1/2} + \frac{1}{2}\left(\Delta t^{n+1/2} + \Delta t^{n-1/2}\right) a_j^n$$
$$x_j^{n+1} = x_j^n + \Delta t^{n+1/2}\, u_j^{n+1/2} \tag{9 & 10}$$

The viscous stresses shown in equations (7) and (8) result from the artificial viscosity formulation used in the code. Artificial viscosity was initially developed by von Neumann and Richtmyer[10] for numerical calculation of shock wave propagation. In regions of strong compression characteristic of material near a shock, artificial viscosity acts to spread the shock front over several zones. This serves to stabilize the numerical solution. There are two components of the artificial viscosity, one linear and the other quadratic in the rate of change of density. The quadratic term is most effective near shocks, while the linear term

adds damping over the mesh to minimize numerical oscillations. The viscosity is generally turned off in zones that are expanding, which is the scheme employed in WONDY. The ABLATOR code permits use of either this switch or a more sophisticated one from Moss and White.[11]

Strain rates are determined from the velocity differences between adjacent nodes. These values are used with the material shear modulus (G) to determine a deviatoric stress in the zone. Stress deviators are defined as

$$\sigma_x^d = \sigma_x - (-p) = \sigma_x - \left[\frac{1}{3}\left(\sigma_x + \sigma_y + \sigma_z\right)\right] \tag{11}$$

where the sign convention of stresses positive in tension and pressures positive in compression has been applied. The deviatoric stress is found from

$$\frac{\partial \sigma_x^d}{\partial t} = 2G d_x^d = 2G\left(\frac{\partial u}{\partial x} + \frac{1}{3\rho}\frac{\partial \rho}{\partial t}\right) \quad \Rightarrow \quad \sigma_x^{d(n+1)} = \sigma_x^{d(n)} + \left(\frac{\partial \sigma_x^d}{\partial t}\right)^n \Delta t^{n+1/2} \tag{12}$$

The deviatoric stresses arise from the ability of the material to resist deformation, thus they are limited by the material strength. The stress is taken as the minimum of either the value calculated with equation (12) or two-thirds of the yield strength. The local yield strength is assumed to be temperature dependent, varying linearly from the nominal value at room temperature down to zero at the melt temperature. This ensures a smooth transition to the liquid state where the yield strength vanishes.

The deviatoric stress and strain rates determine the rate of deviatoric stress work. The work term and the corresponding form required for the energy conservation equation are given by

$$P_d = \frac{3}{2}\sigma_x^d d_x^d \qquad \Delta E^d = \frac{4P_d \Delta t^{n+1/2}}{\rho_{j-1}^{n+1} + \rho_j^{n+1} + \rho_{j-1}^n + \rho_j^n} \tag{13}$$

The finite difference form of the energy equation used in the code is

$$E_j^{n+1} = E_j^n + \left(P_j^{n+1} + P_j^n + 2q_j^n\right)\left(\frac{\Delta\rho}{2\rho^2}\right) + \Delta E^d + \Delta Q \tag{14}$$

Here the ΔQ is taken as the net heat addition from x-ray deposition and thermal conduction, as described in the energy transport section. Note that the pressure at the next time step appears in the energy equation. The pressure is determined from the equation of state, which has the general form

$$P^{n+1} = f_1\left(\rho^{n+1}\right) + f_2\left(\rho^{n+1}\right) E^{n+1} \tag{15}$$

Equations (14) and (15) form a set of simultaneous equations for the unknowns P^{n+1} and E^{n+1}. The energy can be solved for explicitly to give

$$E_j^{n+1} = \frac{E_j^n + \left(f_{1j}^{n+1} + P_j^n + 2q_j^n\right)\left(\frac{\Delta\rho}{2\rho^2}\right) + \Delta E^d + \Delta Q}{1 - f_{2j}^{n+1}\left(\frac{\Delta\rho}{2\rho^2}\right)} \tag{16}$$

With the zone energy determined, the code calls the equation of state routines (described in the next section) to determine the pressure in the zone. Knowing the pressure permits the calculation of the normal stress, σ, according to

$$\sigma = -\sigma_x = P - \sigma_x^d \tag{17}$$

This is the stress used in the momentum balance relation of equation (7). Note that σ is taken to be positive in compression (same as the pressure term). The final step for the hydrodynamics is to determine the maximum step size for the next time increment. The usual criterion for an explicit wave propagation code is

$$\Delta t \leq \frac{\Delta x}{c} \tag{18}$$

where c is the local sound speed. The WONDY formulation requires a somewhat modified form of this equation to account for the effects of artificial viscosity. The minimum value of this Δt for any of the zones in the calculation is taken to be Δt_{hydro}. As described earlier, the next time step for the run is determined from this and other stability criteria.

Two different types of boundary conditions are used in ABLATOR for the hydrodynamics calculations. The front surface is handled as a free surface. This involves using the normal equation of motion (equation 7) for node zero with some dummy values for the stress and density of "zone zero". For expansion into a vacuum, both dummy values are set to zero. The rear surface will generally be set to some "large" distance, compared to the heat conduction time scales (about 50 μm). Since the sound speed is on the order of a few μm/ns, a "large" distance for the hydrodynamic calculation would be on the order of 1000 μm. With the smaller distance, using either the free boundary assumption or a fixed boundary ($u_n = 0$, x_n fixed) will result in reverberations of the initial shock throughout the problem run. However, these spurious waves can be largely eliminated from the smaller problem through the use of a non-reflecting boundary condition. The idea is to provide some measure of impedance matching in a special formulation of the equation of motion for the last node point. A finite difference formula giving the velocity of this last node was implemented from the work of Halpern[12]. This technique reduces the reflected wave by better than an order of magnitude, which permits the use of the smaller computational domain, resulting in substantial savings in computational time.

3.5.2 Equations of State

The purpose of an equation of state (EOS) is to determine pressure in a zone, given its density and internal energy. The ABLATOR code uses an equation of state form that is linear in energy, according to equation (15). The functions of density, f_1 and f_2, vary depending on the phase of the zone under consideration. Separate treatments exist in the code for the condensed phase, the vapor phase, and some mixture of the two. Therefore it is implicitly assumed in the code that temperatures are below the critical point, so that such a phase distinction makes sense. Other treatments of the equation of state, such as links to tabulated SESAME[13] data, can allow extension into higher energy regimes.

Determination of which EOS to apply to a particular zone is based on location relative to the current surface of the condensed material. This surface can move through the zones by the advancement of the vaporization front or by some spall process that removes one or more zones of condensed material. Vaporization is discussed in the next section, while the spall mechanisms are covered in the final section of this chapter. If a zone lies to the right (bulk material side) of the front surface of the condensed material, then the condensed phase EOS is applied. Any zone to the left of this surface, in the so-called "spalled" material, uses an EOS routine that permits a mixture of the condensed phase and an ideal gas phase in the zone.

The condensed phase is subject to high pressures (order 1 GPa) during heating by short x-ray pulses. A commonly used EOS for such hot shocked material is the Grüneisen relation. The implementation used in ABLATOR is the same as the DYNA2D EOS #4, which uses a cubic fit to shock velocity – particle velocity data.[14] The pressure is given by the following relations.

$$p = \frac{\rho_o C^2 \mu \left[1 + \left(1 - \frac{\Gamma_o}{2}\right)\mu - \frac{a}{2}\mu^2\right]}{\left[1 - (S_1 - 1)\mu - S_2 \frac{\mu^2}{\mu+1} - S_3 \frac{\mu^3}{(\mu+1)^2}\right]^2} + (\Gamma_o + a\mu) E \qquad \text{for } \mu>0 \qquad (19)$$

$$p = \rho_o C^2 \mu + (\Gamma_o + a\mu) E \qquad \text{for } \mu<0 \qquad (20)$$

where

$$U_s = C + S_1 U_p + S_2 U_p^2 + S_3 U_p^3 \qquad \mu = \frac{\rho}{\rho_o} - 1$$

$$\Gamma_o = \frac{\alpha}{c_v \rho K} = \text{Grüneisen coefficient}$$

α = thermal expansion coefficient K = compressibility

Another format compatible with the assumed linear relation between pressure and energy is the polynomial form (DYNA2D EOS #1).

$$P = C_o + C_1\mu + C_2\bar{\mu}^2 + C_3\mu^3 + \left(C_4 + C_5\mu + C_6\bar{\mu}^2\right) E \qquad (21)$$

where $\bar{\mu} = \text{Max}(\mu, 0)$

The vapor phase equation of state is based on the ideal gas relation

$$P = \rho_{vap} R T \qquad (22)$$

As with the relations for enthalpy and temperature in a vapor, the gas constant is trivial for a monatomic vapor, and a complex function of composition otherwise.

The EOS for "spalled" zones is based on the assumption of instantaneous homogeneous equilibrium between vapor and the condensed phase. As a zone changes from an expanded solid or liquid with the Grüneisen equation of state to a spalled zone, a small amount of vapor is assumed to be generated to permit the liquid portion to relax to its density at positive pressure. The amount and state

of the vapor, presumably in the form of small bubbles, is consistent with the total density and energy in the zone. The solution method is based on iteration of the temperature to produce the proper quality (mass fraction of vapor) values from density and energy considerations. A trial temperature is used to determine liquid and vapor specific enthalpies from inverting the T vs. H relations used in the code. Using the equation

$$H_{total} = X * H_{vapor} + (1-X) * H_{liquid} \tag{23}$$

gives X_H, the quality based on energy considerations. The trial temperature is then applied to the equilibrium saturation equation

$$Log(Psat) = A - B / Tsat \tag{24}$$

to determine the trial pressure. The ideal gas EOS then is used to determine the vapor density under these conditions. Similarly, an application of the condensed material EOS for the liquid gives its density.

$$\rho_{total} = X * \rho_{vapor} + (1-X) * \rho_{liquid} \tag{25}$$

gives the quality from density balance, $X\rho$. Iterations are made on temperature until the two calculated qualities are equal. This routine can accommodate both pure vapor and pure liquid/solid phases. The formulation does not permit negative pressures (tensile forces) in these spalled zones.

3.6 Surface Vaporization Model

Vaporization is assumed to occur only at the free surface. The rate of evaporation is governed by the maximum flux of atoms per unit area that would occur under equilibrium vapor/liquid (or vapor/solid) conditions. The resulting flux, given by

$$\text{flux} = \frac{P_{sat}}{\sqrt{2\pi RT}} \tag{26}$$

increases exponentially with surface temperature, through the saturation vapor pressure term. Therefore no single "boiling temperature" exists and vaporization occurs continuously over a range of temperatures. The mass flux is an upper limit, in that no recondensation is included. This approximation is reasonable for exposures in the Nova and NIF target chambers, which are under vacuum.

The treatment of x-ray ablation in ABLATOR differs from those found in several computer codes relevant to ICF chamber design, including CONRAD[15] from the University of Wisconsin, TSUNAMI[16] from UC Berkeley, and the codes used by SRI, Intl (FSCATT, SRI PUFF)[17]. These models determine x-ray vaporization depths from energy distribution profiles based on typically instantaneous deposition. The vaporized depth is typically taken as the point in the energy profile where the cohesive or sublimation energy is exceeded. Such models do not account for the limitation in surface vapor flux, or for additional vaporization from the remaining hot liquid at just below the cutoff energy. In strongly heated systems, where super-critical conditions allow very hot "fluid" to leave the bulk material without a distinct phase change, these models may be quite reasonable.

Although vaporization is a continuous process, the code is Lagrangian, with mass allocated to discrete zones. This mismatch is reconciled by treating the surface zone with special relations unlike those for the remainder of the mesh. The most important distinction is that the mass fraction of vapor (quality) in the zone is imposed on it. The increase in quality in each time step is determined by the subroutine that computes the evaporation rate. As discussed in the previous

section, other zones that have already vaporized or spalled off use a zone density and energy balance to determine a consistent value for quality.

The surface zone is the one zone that is not treated as a homogeneous material. The concept is that the expanding vapor occupies the free surface side of the zone, while the remaining liquid is in a layer next to the bulk material. Within this one zone there are essentially two zones with different motions and stress responses that must be reconciled into a single density and total energy. The equation of state routine for this special surface zone must then accommodate the two phases in a consistent way. It first uses iteration to determine a split in zone energy between vapor and liquid that gives the same temperature in both phases. This routine then computes the zone pressure based on the equilibrium vapor pressure, which is the most reasonable choice for the effects on the zones in the bulk material.

While the vapor pressure is a good choice for the condensed material in the zone, it is not very accurate for the vaporized part. This material undergoes an unsteady, nearly adiabatic expansion after leaving the vaporizing surface. Since the pressure drops substantially during the expansion, fixing the pressure causes a large error by the time a zone is almost completely vaporized. The artificially high pressure would drive an artificially high velocity at the outer boundary of this zone. To avoid this problem, a different pressure is used in the equation of motion of this outer node. The new pressure is based on an analytical solution to the 1-D unsteady compressible gas dynamics equations. To ensure a smooth transition in node velocity after this zone completely vaporizes, for high qualities the new pressure is made to asymptote to the ideal gas pressure for a zone with its temperature and vapor density.

Ideally the surface temperature (and so the corresponding pressure) should change smoothly over time regardless of the vaporizing front passing from one zone to the next. One obvious requirement is that as the surface zone fully vaporizes, the temperature of the condensed zone adjacent to the surface zone must approach the surface zone temperature. To ensure that this temperature matching occurs, the conduction heat transfer is assumed to occur from the plane of the zone boundary to the vaporizing surface. The heat conduction rate is governed by

$$\frac{Q}{A} = \kappa \frac{\Delta T}{\Delta x} \tag{27}$$

As the distance (Δx) tends to zero, the temperature difference must also, in order to have a heat flux in accordance with the overall energy balance. The difficulty with this approach is in the stability of the numerical heat transfer method. For an explicit method of time advance as used in the ABLATOR code, the time step size must be limited by the stability condition from equation (6):

$$\Delta t \leq \frac{(\Delta x)^2}{2\alpha} \tag{6}$$

Obviously this would require the time step size to go to zero as the surface zone vaporized. To avoid this problem, this one heat conduction component is solved implicitly. The implicit numerical scheme is unconditionally stable for this heat conduction calculation, which means that any time step size will give stable results. Iterations are performed on the heat flux value until equation (27) is satisfied using the temperatures at time step n+1.

3.7 Special Routines

3.7.1 Spall Model

The rapid deposition of the x-ray energy raises the pressure in the surface layers of the wall material. The stress causes movement away from the bulk material to relieve this pressure. The interaction of this pressure relief with the free surface constrained at low pressure generates a negative pressure wave that moves into the material. It is well known that solid materials can withstand a reasonable amount of tensile stress without failure. Surprisingly, this is also true for many liquids, particularly for the short duration tensile pulses typical of x-ray exposures[18]. In order to spall from the bulk, a material must develop voids, which form over a finite period of time. Therefore unless the tensile forces are exceptionally large, even liquids will remain intact. To allow the possibility of this phenomenon occurring, the code sets a tensile limit for fully melted zones. If a liquid zone exceeds this stress, it is declared a "spalled" zone for subsequent time steps. If there are condensed zones above this spalled zone (closer to the surface), they are considered spalled as well.

3.7.2 Rayleigh-Taylor Instability

Another mechanism for the removal of liquid layers apart from the very high tensile stress spall phenomenon is the Rayleigh-Taylor instability. As described in the previous subsection, the liquid layer will be subject to tensile forces as the rapid initial thermal expansion slows or stops, as at the end of the x-ray pulse. The situation is somewhat analogous to a thin layer of liquid on a ceiling, subject to gravitational load, which tends to come down as discrete droplets.

The ABLATOR code has an optional module to investigate Rayleigh-Taylor instability growth in the melt layer caused by x-ray exposure. The model is

based on work by Wolfer and Hassanein for material removal in plasma disruptions in magnetic fusion facilities[19]. They present solutions of a dispersion relation developed by Feldman[20]. The solution relates the critical exponent (κ_c) to the surface Reynolds number (R) and the surface Weber number (W). The critical exponent determines the amplitude growth rate, given by $\exp(\kappa_c t)$, of the most unstable wavelength for some given set of R and W conditions. The nondimensional quantities are defined as follows:

$$R = \frac{\sqrt{f\rho}h^{1.5}}{\eta} \qquad W = \frac{fh^2}{\sigma} \tag{28}$$

where: f = force density = density × acceleration
h = melt layer thickness
η = liquid viscosity (temperature dependent)
σ = surface tension (temperature dependent)

Thus the Reynolds number relates momentum to viscous forces, while the Weber number relates momentum to surface tension.

At each time step in which a melt layer exists, the code computes average densities and accelerations through the melt layer to get the force density. The current surface temperature is used to find the surface tension, while a mass-averaged viscosity is compiled through the melt layer zones. The Reynolds and Weber numbers are then computed and applied to Wolfer and Hassanein's solution to give κ_c. The growth rate quantity $\exp(\kappa_c \Delta t)$ is then applied to a running product (AMP) maintained for the duration of the run. A large final value of AMP indicates a strong possibility of liquid ejection due to Rayleigh-Taylor instabilities.

3.7.3 Sub-Surface Boiling Model

Another form of vaporization is considered for several materials, specifically sub-surface boiling. The motivation for considering this removal mechanism is the observation of very rough surfaces with evidence of droplet ejection on some of the x-ray exposure samples. A sudden sub-surface boiling (or vapor explosion) would generate sufficient pressures to eject much of the over-lying liquid layer. One cause of the sub-surface vaporization is the passage of the rarefaction wave through hot liquid material just after the energy deposition pulse ends. This wave generates sufficient tensile stresses (negative pressures) to cause massive nucleation and growth of vapor bubbles. Paltauf and Schmidt-Kloiber[21] describe an experimental investigation of this process in the case of pulsed laser ablation of liquids for surgical applications. Hassanein and Konkashbaev[22] discuss melt-layer splashing due to bubble growth and explosion in wall materials during tokamak disruptions.

A detailed treatment of the sub-surface boiling process would require sophisticated bubble nucleation and growth-rate models to determine the material velocities and two-phase compositions during ablation. Such an analysis is not attempted here. Instead, a relatively simple nucleation rate model is employed as a test for the existence of conditions that would likely cause sub-surface boiling to occur. The maximum depth at which these conditions exist will serve as the estimate for material removal due to this process.

The nucleation rate equation used in this modeling (from Carey[23]) is:

$$J = N_l \sqrt{\frac{3\sigma}{\pi m}} \exp\left[\frac{-16\pi\sigma^3}{2kT_l\left[\eta P_{sat}(T_l) - P_l\right]^2}\right] \tag{29}$$

where J is the nucleation rate, N_l is the number density of liquid molecules, σ is the surface tension, m is the weight of a molecule, k is the Boltzmann constant, and η is given by

$$\eta = \exp\left(\frac{P_l - P_{sat}(T_l)}{\rho_l R T_l}\right) \tag{30}$$

This relation for nucleation rate requires surface tension as the only new material parameter beyond those already introduced. Equation (29) is the form of Carey's equation that is valid for cavitation situations.

Consideration of the volume fraction of bubbles within a liquid at a particular time requires both the total number of bubbles per unit volume and some estimate of the bubble size. The number of bubbles in a volume is easily calculated as a running sum of the product of nucleation rate and time step size for each zone at each time. One conservative way to estimate the bubble size is to compute the critical bubble radius that will be in equilibrium under give superheat conditions. (The nucleation rate is defined in terms of the number of bubbles that grow to exceed this size per unit time and volume.) Carey's relation for the critical bubble radius is

$$r^* = \frac{2\sigma}{P_{sat}(T_l)\exp\left\{\left[P_l - P_{sat}(T_l)\right]/\rho_l R T_l\right\} - P_l} \tag{31}$$

3.7.4 Thermal Shock/Stress Model

Thermal stress appears to play the major role in the x-ray ablation of several of the brittle refractories tested. The damage process starts as material cools from the peak temperatures. Any material that had melted will be in a stress-free state

at the melt point as it solidifies. Additional material that peaked near the melt temperature will also soften somewhat, leading to a reduced-stress condition. As these surface layers cool, they will be put under tension, because the underlying bulk material constrains any lateral contraction. If the stresses exceed the tensile strength, brittle material will develop thermal stress cracks on the surface. Subsequent x-ray exposures can remove damaged material in two ways. One cause is the shock and rarefaction waves generated by absorbing the x-ray pulse. The other mechanism is thermal stress from additional heating/cooling cycles on the already damaged material.

Thermal stress arises in the 1-D geometry because no thermal expansion or contraction can occur in the lateral (in-the-plane) directions. For a slab geometry, the equation for thermal stress due to a temperature differential normal to the surface is

$$\sigma = \frac{\alpha E \Delta T}{1-\nu} \tag{32}$$

where α is the thermal expansion coefficient, E is the elastic modulus, and ν is Poisson's ratio. For the thermal stresses that develop on cooling, ΔT is the difference between the temperature at which the material is stress-free and room temperature. The stress-free temperature is just the melt temperature for any material that fully melted. Solid material that has been pushed to near, but not over, the melt point is expected to soften substantially and so plastically deform in response to the initial thermal compressive stresses on heating. Therefore this heated solid can be expected to have a modified stress-free temperature compared to the bulk of the sample, which is assumed to be stress free at room temperature.

The thermal stress response of the "softened solid" is treated by assuming some residual compressive stress remains from the initial heating. The resulting equation for thermal stress on cooling is

$$\sigma = \frac{\alpha E(T_{max} - T_o)}{1-\nu} - \text{Min}\left[\sigma_{yield\,@T_{max}}, \frac{\alpha E(T_{max} - T_o)}{1-\nu}\right] \qquad (33)$$

with T_{max} as the peak temperature and T_o as room temperature. The yield strength at T_{max} is computed from the relation used in the ABLATOR code, which is a linear drop from the room temperature value to zero at the melt temperature. (With brittle materials, the compressive strength is used in place of a yield strength.) For the bulk of the material, cooling from the peak temperature will simply bring it back to the original stress-free state.

3.8 Grid Size Effects

The effects of discretization must be investigated in the development of any numerical method. The goal is to choose the best grid size for a given class of problems. This involves a trade off between making the resolution fine enough that no important details are lost, yet as large as possible to minimize run time. Such a study was already presented (in Figure 3-3) for the number of groups used in x-ray spectral representation. The spatial grid size was examined with a similar approach, in which the standard grid size of 0.01 μm (at the front surface) was increased by a factor of five and also decreased by a factor of two. The sample case used in the comparison was exposure of fused silica to 2.5 J/cm^2 of 250-eV blackbody x rays in a 1-ns square pulse. Figure 3-4 shows a plot of temperature profiles for each ABLATOR run at time equals 10 ns. All three cases match very well at the surface and at all depths below 0.5 μm. In this first half-

micron, the five-times-larger grid gives temperatures somewhat below those of the standard and half-size grids. The vaporization depths predicted were 0.111 μm for both the standard and half-size grids, and 0.114 μm for the large grid. Since there is only about a 3% difference with a five-times-larger grid, the standard grid is shown to be a safe size choice for x-ray response calculations.

References

1) Cullen, D E;Chen, M H;Hubbell, J H;Perkins, S T;Plechaty, E F;Rathkopf, J A; Scofield, J H., "Tables and graphs of photon-interaction cross sections from 10 eV to 100 GeV derived from the LLNL evaluated photon data library (EPDL)", LLNL, UCRL-50400-V6-Rev-4, 1989.

2) Stull, DR., Prophet, H., JANAF Thermochemical Tables, USGPO, Washington, D C, 1975.

3) Wilemski, G., "Silica vapor pressure and energy calculations", LLNL Technical Memo, TAT 96-008.2, March 22, 1996.

4) Wilemski, G., "Boron carbide vapor pressure and energy calculations", LLNL Technical Memo, June 1996.

5) Bird RB, Stewart WE, Lightfoot EN, Transport Phenomena, John Wiley and Sons, NY, 1960.

6) Kar, Chan, Mazumder, "Comparative Studies on Nonlinear Hyperbolic and Parabolic Heat Conduction for Various Boundary Conditions: Analytic and Numerical Solutions", ASME J. Heat Transfer, V114, Feb 1992, p 14-20.

7) Peterlongo, Miotello, Kelly, "Laser pulse sputtering of aluminum: Vaporization, boiling, superheating, and gas-dynamic effects", Physical Review E, V50, N6, Dec 1994, p 4716-4727.

8) Harrington, R.E., "Application of the Theory of Heat Conduction to the Absorption of Blackbody Radiation", J. Appl. Phys. V38 N8, July 1967, p 3266.

9) Kipp, M.E., Lawrence, R.J., "WONDY V – A One-Dimensional Finite-Difference Wave Propagation Code", Sandia Natl Lab, SAND81-0930, June 1982.

10) von Neumann J, Richtmyer RD, "A Method for the Numerical Calculation of Hydrodynamical Schocks", J Appl Phys, 21, p 232 (1950).

11) Moss W, White J, "New Physical Criteria for Using Linear Artificial Viscosity", J Comp Phys, 106, 397-399.

12) Halpern L, "Absorbing Boundary Conditions for the Discretization Schemes of the One-Dimensional Wave Equation", Math Comp, V38 N158, April 1982, p 415-429.

13) Holian, KS, T-4 Handbook Of Material Properties Data Bases, Los Alamos National Laboratory, LA-10160-MS, 1984

14) Whirley RG, Engelmann BE, "DYNA2D: A Nonlinear, Explicit, Two-Dimensional Finite Element Code for Solid Mechanics User Manual", LLNL, UCRL-MA-110630. April 1992.

15) Peterson, RR., MacFarlane, JJ., Moses, GA., "CONRAD – A Combined Hydrodynamics–Condensation/Vaporization Computer Code", Univ. Wisc., UWFDM-670, July 1988.

16) Chen, XM., "A Study of Thermal Hydraulic and Kinetic Phenomena in HYLIFE-II – An Inertial Confinement Fusion Reactor", PhD dissertation, UC Berkeley, Jan 1993.

17) Tokheim, RE., Seaman, L., Curran, DR., "Threats from Radiation Effects in the Proposed Nova Upgrade", SRI Intl Final Report for LLNL, Sept, 1992.

18) Rybakov AP, Rybakov IA, "Reaction of Condensed Matter to Extremely Short-Duration and Intense Loading. Strength of Solids and Liquids Under Dynamic Damage", Eur J Mech, B/Fluids, V14 N2, p 197-205, 1995.

19) Wolfer WG, Hassanein AM, "On Melt Layer Stability Following a Plasma Disruption", Univ Wisc, UWFDM-470, May 1982.

20) Feldman S, "On the Instability Theory of the Melted Surface of an Ablating Body When Entering the Atmosphere", J Fluid Mech, 6, p 131-155, 1959.

21) Paltauf G, Schmidt-Kloiber H, "Model Study to Investigate the Contribution of Spallation to Pulsed Laser Ablation of Tissue", Lasers in Surgery and Medicine, **16**:277-287 (1995).

22) Hassanein A, Konkashbaev I., "Erosion of plasma-facing materials during a tokamak disruption", Atomic and Plasma-Material Interaction Data for Fusion, V5:193-224, Dec 1994.

23) Carey VP, Liquid–Vapor Phase–Change Phenomena: An Introduction to the Thermophysics of Vaporization and Condensation Processes in Heat Transfer Equipment, Hemisphere, 1992.

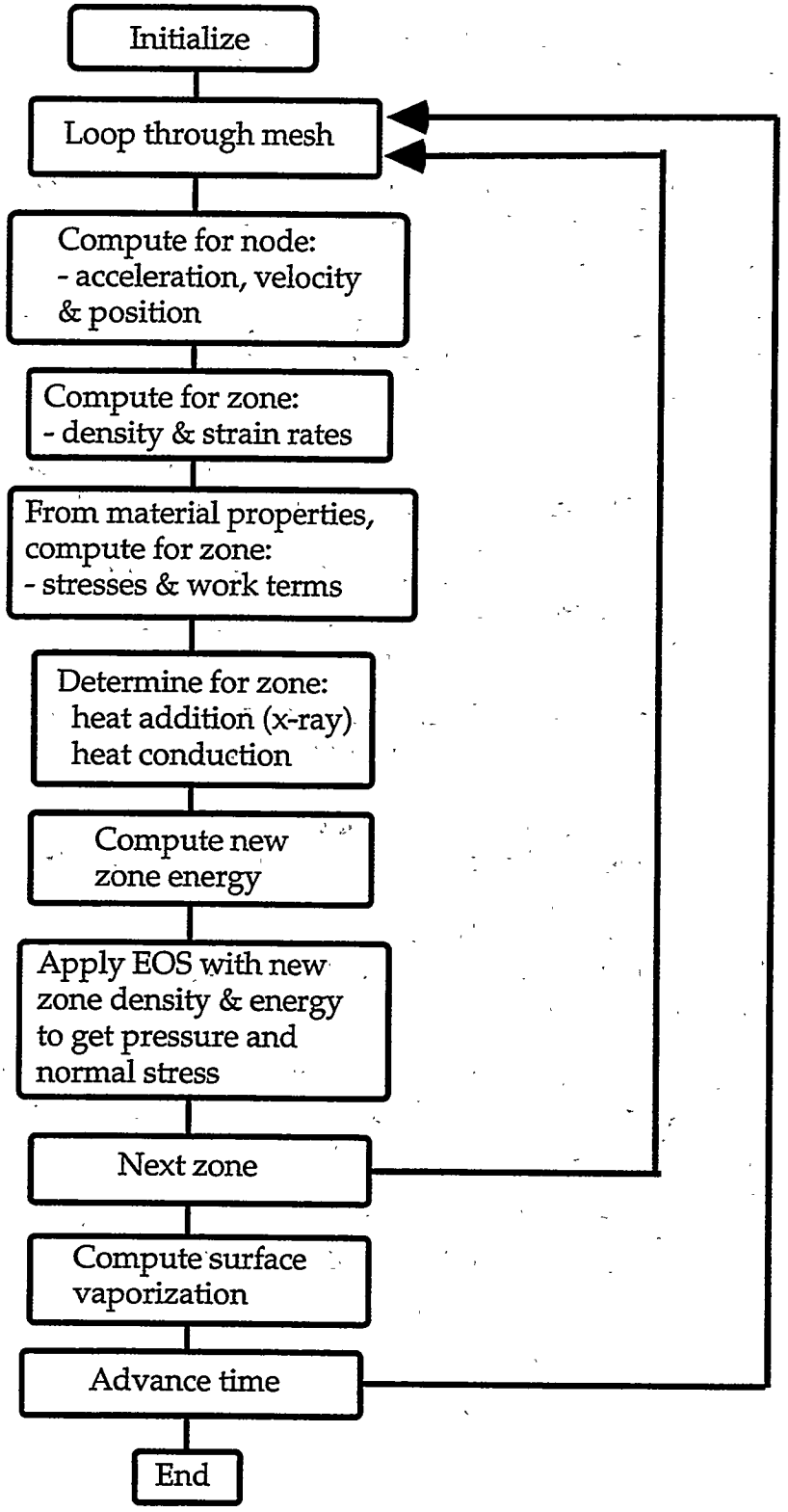

Figure 3-1: Flow chart for ABLATOR calculation.

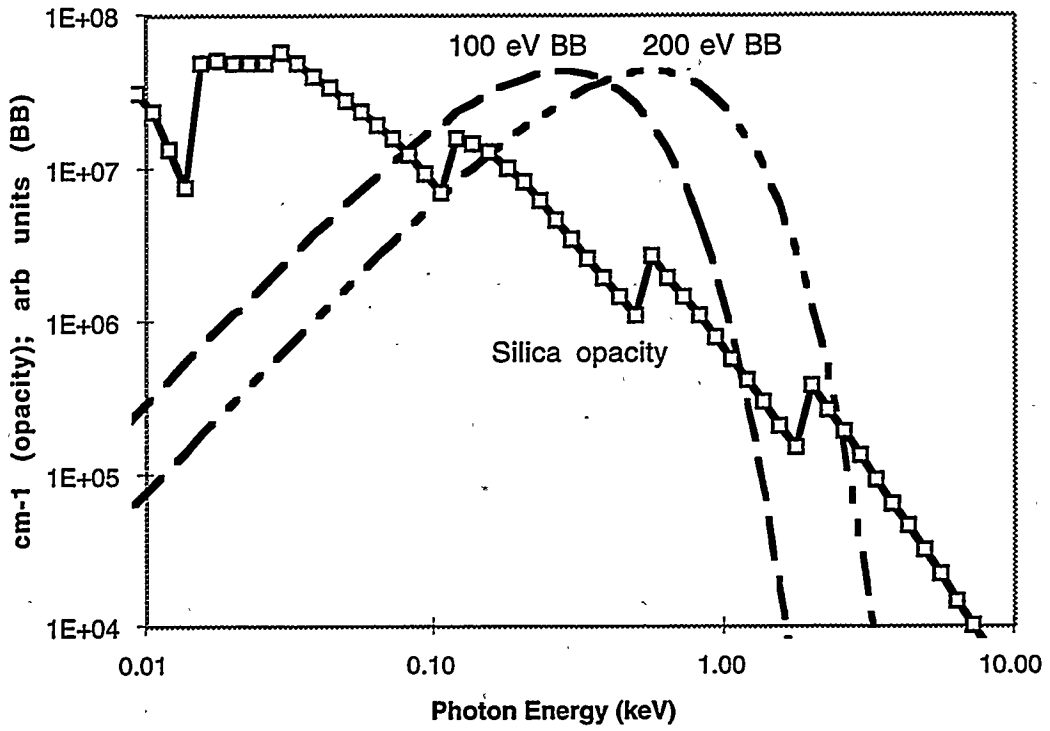

Figure 3-2: Opacity of silica with some typical blackbody x-ray spectra.

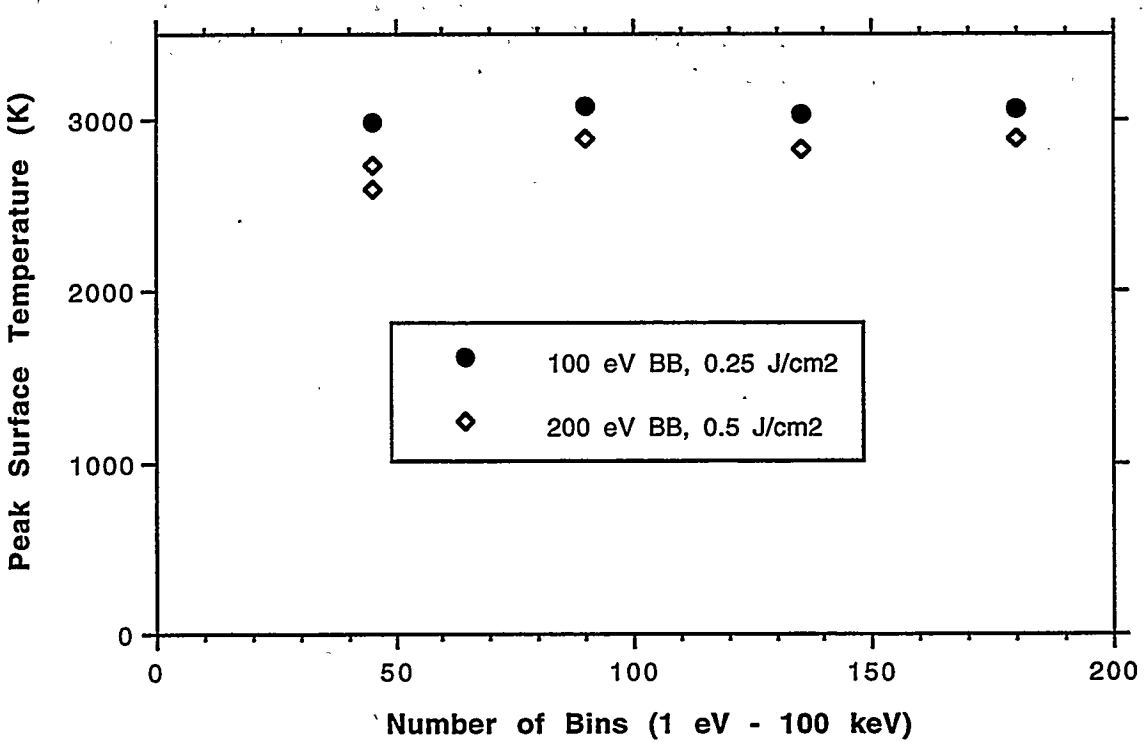

Figure 3-3: Photon group sensitivity study for fused silica using 1-ns pulses.

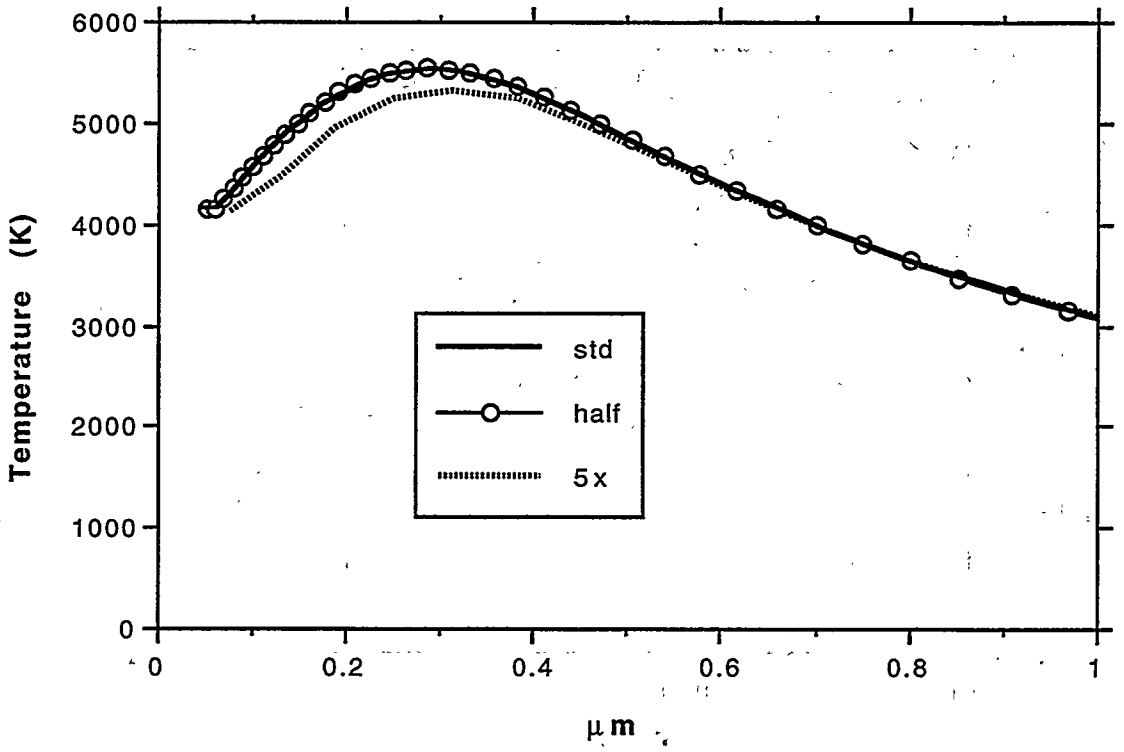

Figure 3-4: Grid size effect on temperature profiles in fused silica exposed to 250-eV blackbody x rays in a 1-ns pulse. The three cases are the standard grid (0.01 μm in first zone), half-size grid (0.005 μm), and five-times-larger grid (0.05 μm). All profiles are at time equals 10 ns.

4. Material Ablation Experiments

4.1 Introduction

Ablation experiments are the second step in the process of developing a validated material x-ray response model. One goal of these tests is to determine removal mechanisms for various materials. This guides the modeling efforts to predict removal under given conditions. For the tested materials, the modeling is then a direct means of extrapolating to their response in other ICF facilities. Also, with sufficient information on how the relative values of various material properties indicate one removal mechanism over another, reasonable predictions can be made for other materials not examined in these tests. The second goal of the experiments is to provide the quantitative data on ablation depths to benchmark the performance of the models.

4.2 Mechanisms for material removal

Several different removal mechanisms were identified during the course of experimentation. These are vaporization, thermal shock/spall, and liquid ejection. This section discusses the general features of each mechanism, while the following sections detail these phenomena in specific materials.

X-ray energy deposition in the fluence range of interest produces high surface temperatures, of order several thousand degrees. Vaporization from these hot solid or liquid surfaces into the chamber vacuum is expected for nearly any material. However, the amount of vapor removal may or may not be significant, depending on the particular thermal and chemical response of a material. This is because the rate of evaporation varies

exponentially with surface temperature, through the dependence on equilibrium vapor pressure.

Materials that ablate primarily through vaporization show several common features in the post-shot examinations. The exposed surfaces are smooth and flat, not significantly worse than the original finish. The steps measured by profilometry are sharp and well defined. The ablation depths increase linearly with the number of exposures, for multiply exposed sample regions.

Thermal shock/spall is the second material removal mechanism noted in the experiments. Damage starts when the melt layer generated after the x-ray exposure solidifies. This material will be in a stress-free state at an elevated temperature somewhat below the melt point. As it cools, the surface layer will be put under tension, because the underlying bulk material constrains any lateral motion. If the stresses exceed the tensile strength, brittle materials will develop thermal stress cracks on the surface. Subsequent x-ray exposures can remove damaged material in two ways. One cause is the shock and rarefaction waves generated by absorbing the x-ray pulse. The other mechanism is additional thermal stress on cooling the already damaged material.

Thermal stress cracks in the exposed surfaces are the obvious visual indications of materials susceptible to the thermal shock/spall process. The other clue is the presence of angular pits of a size consistent with the spall damage flakes.

The final removal mechanism is ejection of liquid from the exposed surface, easily seen in the aluminum exposures. For fluences above the damage threshold, a melt layer forms quickly during the x-ray pulse. The heating also causes thermal expansion, which accelerates the melted surface layer away from the bulk material. After the pulse ends, so does the rapid thermal expansion. The velocity of the surface layer then quickly drops to near zero as a result of tensile stresses from the bulk material. Two liquid ejection mechanisms are then possible. The deceleration of the liquid layer can cause *Rayleigh-Taylor instabilities* that make the surface wavy and eventually release material in the form of droplets. The short pulse duration may not allow sufficient time for instability growth in a single shot. Some "conditioning shots" may therefore be required to alter the surface geometry before material is removed. Kelly[1] noted a similar conditioning requirement for melt removal from metals exposed to laser pulses, although the mechanism is somewhat different. The second mechanism for melt layer removal is *sub-surface boiling*. This may be initiated by the passage of the rarefaction wave through hot liquid material just after the energy deposition pulse ends. This wave generates sufficient tensile stresses (negative pressures) to cause massive nucleation and growth of vapor bubbles. Hassanein and Konkashbaev[2] discuss melt-layer splashing due to both mechanisms in wall materials during tokamak disruptions.

Several observations are typical of materials subject to significant liquid removal. The surfaces tend to be wavy with well-rounded crests and valleys. Because of the lateral liquid motion, the surfaces are also very rough. Droplets are frequently observed, either resting on the surface or attached to a crest by a narrow neck of material. Near boundaries of regions with different

numbers of x-ray exposures, splash in the form of droplets or thin fibers is also commonly seen.

4.3 Nova X-ray Ablation Experiments

4.3.1 Experiment Description

4.3.1.1 Introduction

The Nova laser facility at LLNL is a unique resource for exploring material response to x rays. It is one of the most powerful laser facilities in the world. Over 30kJ of 0.35 μm laser light can be focused into hohlraums placed at the center of the target chamber. This energy is converted efficiently into x rays, providing a significant source for exposure testing. X-ray fluences, spectra, and pulse lengths are all in a range that is relevant to future ICF facilities. Models used to extrapolate material responses in other conditions will therefore have well-matched benchmark data. Finally, since the Nova laser has been operated for many years, the targets provide a well-characterized source of x rays. Experience with targets identical to those used in this campaign allows the spectra and energy output to be known reliably.

The material ablation studies on Nova were conducted over the course of 27 separate laser shots (see Table 4-1). On each of these shots, ten or eleven material samples were exposed to the x rays generated in the target hohlraum. Because many samples received multiple exposures, the total number of different pieces was 67. This section describes the methods and conventions used in performing the tests. Later sections will provide specific sample preparation details and present results for the different materials.

Table 4-1: Summary of Nova ablation experiments. Lengths are distances from target to the sample face.

Date	Target Name	Laser kJ	Pulse ns	BBT eV	Fluence J/cm2	Fluence J/cm2	Fluence J/cm2	Fluence J/cm2
					22 cm	**26 cm**	**31 cm**	**40 cm**
Nov 17 1995	RKK_HOHLSBS_24	25.14	2.2	195	3.24	2.32	1.63	0.98
	RKK_HOHLSBS_22	24.26	2.2	195	3.13	2.24	1.57	0.95
	RKK_HOHLSBS_16	25.36	2.2	195	3.27	2.34	1.65	0.99
			Avg	Fluence	3.21	2.30	1.62	0.97
					23 cm	**27 cm**	**32 cm**	**41 cm**
Dec 18 1995	TJO_ALBEDO_90	25.94	1.0	250	3.06	2.22	1.58	0.96
	TJO_ALBEDO_91	27.89	1.0	250	3.29	2.39	1.70	1.03
	TJO_ALBEDO_92	28.10	1.0	250	3.31	2.40	1.71	1.04
	TJO_ALBEDO_93	26.97	1.0	250	3.18	2.31	1.64	1.00
			Avg	Fluence	3.21	2.33	1.66	1.01
					21 cm	**25 cm**	**30 cm**	**39 cm**
Dec 19 1995	SGG_FBALL_29	25.49	2.2	200	3.60	2.54	1.77	1.05
	SGG_FBALL_30	24.94	2.2	200	3.53	2.49	1.73	1.02
	DHK_BLIMP_08	24.27	2.2	200	3.43	2.42	1.68	1.00
	DHK_BLIMP_09	26.06	2.2	200	3.69	2.60	1.81	1.07
	DHK_BLIMP_11	26.38	2.2	200	3.73	2.63	1.83	1.08
	DHK_BLIMP_10	23.97	2.2	200	3.39	2.39	1.66	0.98
			Avg	Fluence	3.56	2.51	1.75	1.03
					23 cm	**27 cm**	**32 cm**	**41 cm**
Jan 10 1996	TJO_ALBEDO_94	30.25	1.0	250	3.57	2.59	1.84	1.12
	TJO_ALBEDO_95	25.56	1.0	250	3.01	2.19	1.56	0.95
	TJO_ALBEDO_96	26.42	1.0	250	3.12	2.26	1.61	0.98
	TJO_ALBEDO_97	27.35	1.0	250	3.22	2.34	1.67	1.01
	TJO_ALBEDO_98	28.13	1.0	250	3.32	2.41	1.71	1.04
	TJO_ALBEDO_99	26.92	1.0	250	3.17	2.30	1.64	1.00
			Avg	Fluence	3.24	2.35	1.67	1.02
					22 cm	**26 cm**	**31 cm**	**40 cm**
Feb 22 & Feb 23 1996	SGG_FBALL_34	25.26	2.2	200	3.25	2.33	1.64	0.98
	SGG_FBALL_35	26.36	2.2	200	3.40	2.43	1.71	1.03
	DHK_BLIMP_12	25.66	2.2	200	3.31	2.37	1.67	1.00
	DHK_BLIMP_13	26.58	2.2	200	3.42	2.45	1.72	1.04
	DHK_HEP4RT_12	24.10	2.2	200	3.11	2.22	1.56	0.94
	DHK_HEP4RT_13	24.45	2.2	200	3.15	2.26	1.59	0.95
			Avg	Fluence	3.27	2.34	1.65	0.99
					22 cm	**26 cm**	**31 cm**	**40 cm**
Feb 23 1996	SGG_SNRT_20	11.92	1.0	210	1.54	1.10	0.77	0.46
	SGG_SNRT_21	11.94	1.0	210	1.54	1.10	0.77	0.47
			Avg	Fluence	1.54	1.10	0.77	0.47

X-ray exposure of five materials is reported in this chapter. Three were chosen as representative of candidate NIF first wall materials: boron carbide (along with boron), aluminum oxide, and silicon nitride. Fused silica was selected for these experiments as an optical material to be used in NIF. Finally, aluminum was tested because it is a typical structural material in the target chamber system (for supports and diagnostic components).

4.3.1.2 Sample preparation

Diagnosing of x-ray damage relies on examination of the exposed surfaces after the series of shots is completed. The surfaces must be sufficiently smooth to distinguish between exposed and unexposed (masked) areas and to quantify the changes. Since typical ablation steps are on the order of 0.1 μm (or smaller) for these test conditions, the initial surface finish must be somewhat better than this. Accordingly, samples were generally polished to a roughness of a few tens of nm. Because of some material porosity or particularly deep initial machining marks however, some pits were usuallypresent in the surfaces. Since these large features appear very different from the observed x-ray damage, they caused little problem in the experiments.

4.3.1.3 Sample mounting and masking

The nominal sample size used in this series of shots was 12.5 mm diameter and 5-6 mm thick. The sample fit in an aluminum cup and was held in place by an aluminum spacer ring and a stainless steel cap. A tight sliding fit was used for the cap to accommodate samples of various heights. The opening in the front face of the cap was smaller than the inside diameter

of the spacer ring, ensuring that x rays would hit the sample and not the holder body. The sample holder is shown in Figure 4-1.

All samples were introduced into the Nova chamber using a SIM (six inch manipulator) cart. The SIMs allow small experiments and diagnostics to be inserted and removed from the chamber between shots without the need for breaking vacuum on the entire Nova chamber. Carts ride on a pair of rails and are driven into and out of the chamber with a lead screw. In these experiments, the cart supported a 25 mm diameter rod that held four aluminum paddles, each of which could hold up to three individual sample holders. This arrangement is shown in Figure 4-2. The paddles were placed along the length of the central rod to provide various distances to the target, and so a range of x-ray fluences for the samples. The large number of mounting locations allowed the use of all eleven sample holders, usually for three different materials at three or four x-ray fluences on each Nova shot.

For both microscopy and profilometry, it is useful to have sharp steps between exposed and unexposed regions. Therefore thin (25 μm) tantalum masks were placed directly on the sample surface. These high-Z refractory masks would prevent any x-ray transmission while producing a minimum mass of ablated material. The primary mask had a donut shape, with a 5-6 mm central hole. This gave a clear border all around the exposed surface of the sample.

Secondary masks were also used during the series of experiments to multiply the usefulness of each sample. Tantalum semi-circles were used to cover half or three-quarters of the surface for selected shots. In a typical series

of four to six Nova shots, the samples were first exposed over the entire region inside the donut mask for a single shot. A semi-circle was then placed over the sample to protect half from further exposures. After an additional one or two shots, another semi-circle was added, protecting another quarter of the sample surface from more damage. The remaining quarter would then be exposed for the last two to four shots. This is shown in Figure 4-3. The result is a sample with areas that received from zero shots up to four or six shots, which proved beneficial in post-shot analyses.

4.3.1.4 Nova targets

All experiments in this series were conducted on a ride-along basis. These are Nova shots that would have run with SIM 5 (see below for description) either vacant or with a secondary diagnostic in place. Placing the material samples in this SIM location provided an excellent source of x rays, while not interfering with the main purpose of the Nova shot.

Hohlraums were chosen as the best x-ray sources for these material response experiments for several reasons. The x-ray radiation inside Nova hohlraums has been studied for many years, and so is well characterized. This is important for these shots where the x-ray conditions could not be measured. In addition, the emission from the laser entrance holes (LEH) of the hohlraums has a spectrum similar to what is expected on NIF. This makes these exposures more relevant to predictions of NIF material response.

All targets used in this experimental series were so-called Nova scale-1 size. The nominal dimensions are 2.8 mm long, 1.6 mm diameter with 1.2 mm diameter laser entrance holes. The gold wall thickness is 25-30 μm.

Nova targets often have copper shields attached that protect the field of view of some diagnostic, and/or separate metal foils to be used as x-ray backlighter sources. To the material samples, these items represent sources of metallic shrapnel that can interfere with the interpretation of x-ray exposure damage. Whenever possible, the shots used as ride-alongs had no shields or backlighters, or perhaps just small shields.

4.3.1.5 X-ray environment

As mentioned above, the ride-along shots, where material exposure was not the main purpose, could not be instrumented to measure the x-ray fluence on the samples. Numerical modeling was used to provide this information. The basis of the fluence calculation was a 1-D LASNEX numerical model of a scale-1 Nova hohlraum, which is the standard size target used for all shots. The same validated techniques discussed in Chapter 2 for the prediction of NIF x-ray fluences were applied to this case. X-ray losses from the LEHs were simulated in this 1-D model with a standard "leak source" in the code. The resulting conclusions for x-ray emission were that, of the laser energy in the hohlraum, 40% would be emitted out the LEH and 10% would come through or from the hohlraum wall. These fractions were then applied to 95% of the measured 3ω (0.35 μm) laser beam energy from the Nova shot (to allow for some scattering or back-reflection). The fluences at the sample surfaces was then determined using a 1/R-squared law with a Lambertian (cosine law) distribution for the LEH component and an isotropic distribution for the wall emission.

Given this distribution of x-ray energy in the Nova chamber, SIM 5 was the best choice for the exposure experiments. This tube points toward the

target at a 25° angle from the hohlraum axis, where the dominant LEH emission is over 90% of its peak value, based on its cosine distribution. This location is also out of the way of most on-axis shrapnel from shields and from the gold hohlraum material that expands mainly toward the waist.

4.3.1.6 Debris and shrapnel

Several sources of debris were present in these shots. The hohlraums themselves are totally vaporized, so at most the material samples would receive a rather light ion bombardment. Copper diagnostic shields mounted on the targets were the major source of metal on the samples, for shots where the shields were present. The copper tended to be in small droplets that stuck to the samples. Other sources were the target support structure and diagnostic snouts, generating mostly aluminum droplets. None of these debris and shrapnel sources was a serious problem in the experiments, because the surface area coverage of debris-affected areas tended to be small enough to work around.

4.3.1.7 Post-shot analysis

All observations and measurements from this series of experiments are based on post-shot analyses of the exposed samples. Optical microscopy, combined with SEM (scanning electron microscope) and AFM (atomic force microscope) images, provide the basis for conclusions on material removal mechanisms. Quantitative data on material removal depths was obtained by measuring surface height changes between regions exposed to different numbers of shots. A Tencor alpha-step 200 was the primary instrument used for this part of the analysis, supplemented in some cases by AFM data.

4.3.2 Fused Silica Response

4.3.2.1 Introduction

Four fused silica disks were exposed to x rays in a series of four ride-along Nova shots. Microscopy and profilometer scans performed after the shots determined material removal rates and indicate the removal mechanisms responsible. This section describes the experiment setup, presents the post-shot observations, and discusses the results in terms of likely removal mechanisms.

4.3.2.2 Experiment set-up

The previous section describes the sample holders, mounting fixtures, and test procedures used in the whole series of material response experiments. Therefore this section will be limited to specific conditions unique to the fused silica testing.

The fused silica samples were 12 mm diameter windows from Melles Griot Co. The material was optical quality synthetic fused silica. The 3 mm thick samples were flat and smooth to one wave He-Ne over 25 mm, so no additional polishing was required prior to testing. Areas of exposure with one, two, and four shots were produced using tantalum masks added after the first and second shots.

The targets were scale-1 Nova hohlraums with a small radiation burnthrough patch on one side. They had "standard drive shields" (1x2 cm) made of copper mounted on both ends of the hohlraum. There were no liners or windows (and so of course no gas fill). All ten Nova beams were pointed into the hohlraum with an energy of 2.7 kJ each in a 1 ns square

pulse. Previous spectral measurements with similar hohlraums under similar drive conditions showed an internal temperature of about 250 eV, so this was taken as the spectrum of radiation source for the samples. Table 4-2 summarizes the shots and conditions expected at each sample face.

Table 4-2: Summary of Nova shots used for fused silica exposure

Target Name	Nova Shot #	3w kJ	Pulse ns	BBT eV	23 cm J/cm2	27 cm J/cm2	32 cm J/cm2	41 cm J/cm2
TJO_ALBEDO_90	25121815	25.945	1.0 sqr	250	3.06	2.22	1.58	0.96
TJO_ALBEDO_91	25121819	27.892	1.0 sqr	250	3.29	2.39	1.70	1.03
TJO_ALBEDO_92	25121824	28.099	1.0 sqr	250	3.31	2.40	1.71	1.04
TJO_ALBEDO_93	25121828	26.969	1.0 sqr	250	3.18	2.31	1.64	1.00
			Avg	Fluence	3.21	2.33	1.66	1.01

4.3.2.3 Observations and measurements for fused silica

Optical microscopy was one important component of the post-shot material analysis. One obvious feature of the surfaces was that they were quite flat. Moving the lens up and down brought exposed regions (with the same number of shots) into focus simultaneously. For high x-ray fluence samples it was therefore easy to see distinct steps between surface regions with different number of exposures.

Examination under higher magnification showed no evidence of thermal stress cracking or shock damage to the surface. What was evident, however, was the presence of small bubbles in the surface on the higher-fluence samples. Figure 4-4 is a 155x view of the highest fluence sample that shows an increase in number and possibly size of the bubbles as the number of exposures increased. Figure 4-5 is a 750x view of the same sample in the region exposed four times. This shows the small pits scattered among the copper and aluminum droplets and the occasional shrapnel-induced crater.

Sample #2 (second highest fluence) has these same features, shown in the 155x view of Figure 4-6. A similar photo of sample #4 (lowest fluence) does not show the small bubbles developing. In fact, Figure 4-7 shows little to distinguish the regions of various exposures, apart from a few shrapnel craters in the area that saw four shots.

SEM scans were performed of the highest fluence sample to better examine the small surface bubbles. Figure 4-8 shows two examples of small clusters of bubbles in a region exposed to a single shot. Most of the features appear to have a central depression with a raised rim, leading us to believe that these are impact craters. The two larger craters in the top image are rather shallow, indicating a relatively slower impact velocity. Most of the other craters appear relatively deeper. In many of the pits, a bit of material is visible down inside, up against one side wall. These may be the impacting particles. Note that the largest crater shown here is only 1 μm in diameter, and there are many much smaller craters visible. This is consistent with the expected shrapnel size distribution, with large numbers of very small particles likely generated in the region of the target. Another feature seen in both images is cracks running through the string of impact craters, indicating penetration through the "melt" layer to the solid below.

SEM work also revealed some limited splashing from high exposure regions to masked adjacent regions. This material takes the form of very thin fibers (on the order of 0.1 μm diameter) that are several microns long. An example is shown in Figure 4-9. This process is likely of only secondary importance in material removal.

Profilometer measurements were made with a Tencor alpha-step 200. Scans of unexposed regions showed surface roughness of about 20 nm, ignoring occasional spikes from ablated material that deposited under the masks. At the lowest fluence this was essentially unchanged, although there was quite a bit more debris. Exposures at the next highest x-ray fluence showed some increase in roughness, but only to about 40-50 nm. Considering the 2.3 J/cm^2 fluence, the surface roughened to perhaps 100 nm, particularly in the four exposure region. Finally, the sample at the highest fluence had roughness of 20 - 40 nm after a single shot and about 150 nm after four exposures. The higher fluence samples also showed quite a bit more debris on the surface, because this sample was closest to the target and subtended the largest solid angle.

Because the surfaces were overall smooth and flat, the profilometry was able to clearly determine ablation step sizes, particularly in the higher fluence samples. The masking arrangement made it possible to measure steps between zero, one, two, and four exposure regions. This data showed a consistent removal for every shot, with no conditioning or other effects from the first exposures. The removal data are summarized in Table 4-3 and plotted in Figure 4-10. Also, representative profilometer scans are included as Figure 4-11.

An interesting and unexpected observation was that the aluminum disks located behind the fused silica were discolored. These darkened areas were in patterns matching the unmasked areas of the silica. Since the silica would stop essentially all x rays, the damage must be due to scattered laser light.

Table 4-3: Summary of ablation step size measurements for silica

Silica 1	**fluence =**	**3.21 J/cm^2**		**0.201**	**± 0.031**
	exposure 1	exposure 2	step	step/shot	
A	0	1	0.23	0.230	
	0	2	0.48	0.240	
	0	4	0.75	0.188	
B	0	1	0.20	0.200	
C	0	1	0.22	0.220	
	1	2	0.15	0.150	
D	0	4	0.72	0.180	
Silica 2	**fluence =**	**2.33 J/cm^2**		**0.082**	**± 0.013**
	exposure 1	exposure 2	step	step/shot	
A	0	1	0.090	0.090	
	1	2	0.070	0.070	
	2	4	0.190	0.095	
B	0	1	0.062	0.062	
	1	2	0.080	0.080	
	2	4	0.186	0.093	
Silica 3	**fluence =**	**1.66 J/cm^2**		**0.027**	**± 0.004**
	exposure 1	exposure 2	step	step/shot	
A	0	4	0.100	0.025	
B	0	1	0.033	0.033	
C	0	1	0.028	0.028	
E	0	1	0.022	0.022	
	1	2	0.027	0.027	
Silica 4	**fluence =**	**1.01 J/cm^2**		**0.005**	**± 0.001**
	exposure 1	exposure 2	step	step/shot	
B	0	4	0.0155	0.004	
C	0	4	0.0232	0.006	

4.3.2.4 Additional testing of fused silica

Two 5 cm diameter fused silica blanks were exposed to x rays and target debris on two Nova shots. This was done as a ridealong experiment on shots RKK_HOHLSBS_ 26&27 on January 23, 1996 using a fixture mounted in SIM 5. These shots used Nova scale 1 gas-filled hohlraum targets.

The samples received about 3.5 J/cm^2 x-ray fluence with a spectrum of 200 eV blackbody (not measured). An unknown amount of target debris (gold and copper) was also incident on the glass. The samples were mounted such that the normal to the sample surface was 45° from the direction to the target. The center of the samples was 22 cm from chamber center. Approximately one third of each sample's surface was shielded from direct x-ray exposure by a steel plate mounted 6 cm in front of the samples.

The silica samples were not specially polished. The substrates were Corning 7940 fused silica. One sample ("North") was coated with a triple thickness (240 nm) of silica sol gel AR coating, while the other sample ("South") was just the bare substrate material.

Interferometry was performed on these two samples, producing two significant results. First is that the removal depths are consistent with those measured in the highest-fluence half-inch sample. Second, the surfaces which had approximately 0.5 μm of material removed appeared to be about as flat as the original, unexposed parts of the samples. Confirmation of the uniform material removal helped in defining the phenomena likely responsible. Results are shown in Figure 4-12.

4.3.2.5 Discussion of removal mechanisms for fused silica

Vaporization appears to be the dominant mechanism of material removal for fused silica. This process is consistent with the uniform removal over a fairly large area (two inches), and the essentially flat surface left behind. Also the removal of the same amount every shot points to a purely one-

dimensional thermal phenomenon, in that no mechanical "pre-conditioning" of the surface is required to remove material.

The other two primary removal mechanisms noted in the Nova material response tests are thermal cracking/spall and liquid ejection. Thermal cracking was not evident in any of the fused silica optical microscopy, nor would any be expected for a material with such a low coefficient of thermal expansion. Liquid ejection tends to leave behind an uneven, wavy surface from the ejection of some droplets and retention of others. The exposed surfaces show no evidence of this, although the fine fibers seen in Figure 4-9 do indicate a small amount of liquid motion. Also, fused silica is amorphous and has no real melting point, but rather a decreasing viscosity with temperature. There is no sharp solid/liquid phase change with the potential for a volume increase that would drive any significant unstable liquid motion (splashing).

4.3.3 Silicon Nitride Response

4.3.3.1 Introduction

Three silicon nitride samples were exposed to x rays in a series of six ride-along Nova shots. Microscopy and profilometer scans performed after the shots determined material removal rates and indicate the removal mechanisms responsible. This section describes the experiment setup, presents the post-shot observations, and discusses the results in terms of likely removal mechanisms.

4.3.3.2 Experiment set-up

Section 4.3.1 describes the sample holders, mounting fixtures, and test procedures used in the whole series of material response experiments. Therefore this section will be limited to specific conditions unique to the silicon nitride testing.

The silicon nitride samples were hot pressed material by Ceradyne. Their material identification was Ceralloy 147, which had a density of 3.16 g/cc (99.4% of theoretical). This material is sintered with 1% MgO. The samples were polished before testing to better than 0.1 μm roughness. One sample was placed at each of the first, third, and fourth distances from the target. The tantalum masking arrangement gave full exposure on the first shot, half on the second, and one quarter on the third and fourth shots. For the fifth and sixth shots the masks were rotated one-eighth turn. This produced regions with six, four, three, two, one, and zero exposures on each sample.

Table 4-4: Summary of Nova shots used for silicon nitride exposure

Date	Target Name	3w kJ	Pulse ns	BBT eV	22 cm J/cm2	26 cm J/cm2	31 cm J/cm2	40 cm J/cm2
Feb 22 96	SGG_FBALL_34	25.256	2.2	200	3.25	–	1.64	0.98
&	SGG_FBALL_35	26.362	2.2	200	3.40	–	1.71	1.03
Feb 23 96	DHK_BLIMP_12	25.664	2.2	200	3.31	–	1.67	1.00
	DHK_BLIMP_13	26.577	2.2	200	3.42	–	1.72	1.04
	DHK_HEP4RT_12	24.098	2.2	200	3.11	–	1.56	0.94
	DHK_HEP4RT_13	24.449	2.2	200	3.15	–	1.59	0.95
			Avg	Fluence	3.27	–	1.65	0.99

The series of Nova shots covered six shots in all, and are listed in Table 4-4. Gas-filled, scale 1 hohlraums without shields were used in these experiments. Backlighters were used on the targets. Eight of Nova's beams were directed into the hohlraum at an energy of about 3.2 kJ each in a shaped

2.2 ns pulse (PS22). An internal temperature of about 200 eV can be inferred from previous spectral measurements on similar hohlraums.

4.3.3.3 Observations and measurements for silicon nitride

Optical microscopy was one important component of the post-shot material analysis. One obvious feature of the surfaces was that they were quite flat relative to the removal steps. Moving the lens up and down brought exposed regions (with the same number of shots) into focus simultaneously. For high x-ray fluence samples it was therefore easy to see distinct steps between surface regions with different number of exposures.

Examination under higher magnification showed no evidence of thermal stress cracking or shock damage. The surfaces also had none of the rounded features characteristic of a material that had been melted and rapidly cooled. As seen in Figure 4-13 for one shot at the highest fluence, the surface is composed of angular facets in the micron or submicron size range. These are presumably due to the original grain structure.

Microscopy also revealed some limited deposition of material on unexposed regions from adjacent exposed areas. The deposited material is in the form of particles up to about a micron in size. Figure 4-14 shows this phenomenon in the sample at the third highest fluence. The lowest fluence sample had essentially no redeposited material. On none of the samples could deposition be seen from high exposure regions to adjacent regions with fewer shots. This is likely because the deposited particles would blend in perfectly with the exposed surfaces' appearance.

A Tencor alpha-step 200 profilometer was used to measure surface topography and ablation step sizes after the x-ray exposures. Table 4-5 below summarizes roughness measured by the profilometer. These values are rather small compared to the removal depths, at least for the higher fluences with multiple shots. The resulting "clean" ablation steps meant that removal measurements could be made reliably. Figure 4-15 illustrates some typical profilometer scans. Note that removal was basically linear with number of exposures, with twice the ablation depth for twice as many shots. A summary of the removal depth results is given in Table 4-6, and these data are plotted as a function of x-ray fluence in Figure 4-16.

Table 4-5: Silicon nitride surface roughness measured by profilometer

Fluence	Roughness *
3.3 J/cm^2	0.4 μm
1.7 J/cm^2	0.3 μm
1.0 J/cm^2	0.2 μm

* = peak to valley, excluding isolated extreme values

4.3.3.4 Discussion of removal mechanisms for silicon nitride

Vaporization appears to be the dominant mechanism of material removal for silicon nitride. This process is consistent with the uniform removal and essentially flat surface left behind. Also the removal of the same amount every shot points to a purely one-dimensional thermal phenomenon, in that no mechanical "pre-conditioning" of the surface is required to remove material.

One interesting aspect of the vaporization is that the high equilibrium vapor pressure of silicon nitride is due almost totally to decomposition and

Table 4-6: Summary of ablation step size measurements for silicon nitride

Sil Nit 1	fluence = 3.27 J/cm2			0.414	± 0.066
	exp 1	exp2	step	step/shot	
A	0	1	0.42	0.420	
	0	4	1.39	0.348	
	0	6	2.29	0.382	
B	0	1	0.52	0.520	
	0	4	1.41	0.353	
	2	4	0.94	0.470	
C	0	1	0.35	0.350	
D	1	2	0.50	0.500	
	2	4	0.71	0.355	
	4	6	0.89	0.445	

Sil Nit 3	fluence = 1.65 J/cm2			0.191	± 0.042
	exp 1	exp2	step	step/shot	
A	0	4	0.740	0.185	
	4	6	0.420	0.210	
B	0	2	0.280	0.140	
	2	6	0.890	0.223	
C	0	2	0.260	0.130	
	2	6	0.830	0.208	
D	0	2	0.480	0.240	

Sil Nit 4	fluence = 1.0 J/cm2			0.105	± 0.006
	exp 1	exp2	step	step/shot	
A	2	6	0.395	0.099	
B	2	6	0.430	0.108	
C	0	4	0.400	0.100	
	2	4	0.210	0.105	
D	2	4	0.230	0.115	
E	1	3	0.210	0.105	

release of nitrogen gas. Composition curves provided by Wilemski[3] show other gaseous species comprise less than one part in ten thousand of the total vapor pressure. It seems likely, therefore, that the vaporization process produces not a stoichiometric vapor, but rather a mix of nitrogen gas and solid (or liquid) silicon particles. The silicon would be "blown off" the surface by the rush of underlying nitrogen gas during decomposition.

The other two primary removal mechanisms noted in the Nova material response tests are liquid ejection and thermal cracking/spall. Liquid ejection tends to leave behind an uneven, wavy surface from the ejection of some droplets and retention of others. The exposed surfaces show no evidence of this. Because silicon nitride has a low boiling point (~3500 K) and high melt temperature (somewhere above 3500 K), it is likely that a melt layer never forms on the surface. Thermal cracking was not evident in any of the silicon nitride optical microscopy. A typical cause of cracking is a melt layer that solidifies then is put under tensile loading as it cools. The lack of thermal cracking therefore supports the idea that no significant melt layer forms on the surface. Also, the crack-free surfaces are consistent with the fact that silicon nitride has a relatively high thermal shock resistance (roughly five times better than aluminum oxide). Since liquid ejection and thermal cracking/spall do not seem to play a role, silicon nitride vaporization is again supported as the dominant removal mechanism.

4.3.4 Response of Boron Carbide and Boron

4.3.4.1 Introduction

Twenty-eight samples of various forms of boron carbide and boron were exposed to x rays in four series of ride-along Nova shots. Table 4-7 summarizes the shots, x-ray fluences, and materials exposed. Microscopy and profilometer scans performed after the shots determined material response characteristics and indicated the mechanisms responsible. This section describes the experiment setup, presents the post-shot observations, and discusses the results in terms of likely removal mechanisms.

4.3.4.2 Sample Preparation

Section 4.3.1 describes the sample holders, mounting fixtures, and test procedures used in the whole series of material response experiments. Therefore this section is limited to specific conditions unique to these tests. The sources and preparation for each of the seven sample types are considered first. In the next part, the targets and laser conditions for each of the four Nova shot series are discussed.

Hot pressed boron carbide samples were obtained from Ceradyne Inc. The bulk material had a purity (measured by Rutherford backscattering[4]) of ≥ 99.9%. Samples were polished to better than 0.1 μm surface finish, except for isolated large pits. Because the locations of these pits were known and so would not interfere with the post-shot analyses, it was not necessary to prolong the polishing operation to remove them. The samples were exposed to three Nova shots on Nov. 17, 1995. One sample was placed at each of four distances from the target, with masking to expose first one-quarter, then one-half, then all of the surface on the three consecutive shots. A fifth sample was half exposed at the furthest location for two shots, then the mask was rotated and the sample moved to the second highest fluence location. This was an attempt to observe the effects of pre-exposure to target debris and low x-ray fluences before exposure to a higher fluence, simulating a possible NIF first wall scenario.

Additional hot pressed boron carbide samples were obtained from Reade Advanced Materials. The quoted purity was 99-99.5% for their Pressure Assisted Densification (PAD) material. Polishing brought the surfaces to better than 0.1 μm finish, except for some small remaining pits. As with the

Ceradyne material, one sample was placed at each of four distances from the targets. In the series of six Nova shots on Jan. 10, 1996, the masking was arranged to expose the full surface on the first shot, half on the next two shots, and one quarter on the remaining three shots.

Two samples of plasma sprayed boron carbide were obtained from Y-12 at Oak Ridge National Laboratory. The bulk material had a purity (measured by Rutherford backscattering[4]) of about 98.6%, with oxygen as the main impurity. The samples were polished at Y-12 to a 0.1 - 0.2 μm surface finish, with some larger pits still apparent. Two series of exposure tests were conducted on Nova, the first being three shots on Nov. 17, 1995 and the second being six shots on Jan. 10, 1996. One sample (labeled #20) was placed at the highest x-ray fluence location for all shots, with an arrangement of tantalum masks to give regions of from zero to nine shot exposures. The second sample was half exposed at the farthest location for two shots, then the mask was rotated and the sample moved to the second highest fluence location for the third shot of the first series. For the second series, the sample was placed at the third highest fluence location with a single 60% mask in place for all six shots.

Four samples each from two other sources of plasma sprayed boron carbide, Plasma Technology Inc. and Prometheus Technology Coatings Inc. (ProTeC), were also tested. The Plasma Tech material number was PTI 279. The bulk material had a purity (measured by Rutherford backscattering[5]) of 99.7%, with an atomic concentration of 83.7% boron, 16.0% carbon. The samples from ProTeC were produced by vacuum plasma spraying, and had a purity of 99.8%, again measured by Rutherford backscattering[4]. The atomic

concentration was 82.8% boron, 17.0% carbon. All samples were tested in an as-sprayed condition, with no polishing. One sample from each vendor was placed at each of four distances from the target for two shots on Feb. 23, 1996. All samples were fully exposed on the first shot and masked on half the surface for the second shot.

Six samples of boron were obtained from the Chemistry & Materials Science Department at LLNL. These were essentially fully dense chunks, labeled lot #7718 from an unknown supplier. Paperwork with the samples indicated a minimum purity of 99.9%. The boron pieces were potted in epoxy to facilitate handling of the irregularly shaped material. Samples were polished to better than 0.1 μm surface finish, except for isolated large pits that did not interfere with the post-shot measurements. Two samples were tested in Nova on Jan. 10, 1996 for a series of six shots. These were placed at the second and fourth highest fluence locations. The masking was arranged to expose the full surface on the first shot, half on the next two shots, and one quarter on the remaining three shots. An additional four samples were exposed in another series of six shots over Feb. 22 & 23, 1996. Here one sample was placed at each of the four distances from the target. The tantalum masking arrangement gave full exposure on the first shot, half on the second, and one quarter on the third and fourth shots. For the fifth and sixth shots the masks were rotated one-eighth turn to produce regions with six, four, three, two, one, and zero exposures on each sample. An exception is the lowest fluence sample, which was smaller than the others, permitting exposures of half for the first shot then one quarter for the remaining five shots.

One set of three plasma sprayed boron samples was also available for testing. These were supplied by General Atomics, and were produced from a powder with a stated purity of ≥99.9%. They felt that any impurities introduced in spraying would likely be less than a percent or two, which was acceptable for this testing. The samples were tested in an as-sprayed condition, with no polishing. One sample was placed at each of the first, third and fourth locations from the target for two shots on Feb. 23, 1996. Each sample was fully exposed on the first shot and masked on half its surface for the second shot.

4.3.4.3 Nova Shot Descriptions for boron carbide and boron exposures

The first series of Nova shots was conducted on Nov. 17, 1995, with a total of three shots. The targets were scale 1, 25-μm wall thickness Nova hohlraums with a patch on one side to study backscatter. There were no shields mounted on the hohlraums. These were gas filled targets, using propane on the first shot and methane on the remaining two shots. Nine of the ten Nova beams were pointed into the hohlraum with an energy of 2.7 kJ each in a 2.2-ns shaped pulse (PS22). Previous spectral measurements with similar hohlraums under similar drive conditions showed an internal temperature of about 195 eV, so this was taken as the spectrum of radiation source for the samples.

The next relevant series of Nova shots took place on Jan. 10, 1996, on six consecutive ride-along shots. The targets were scale 1, 25-μm wall Nova hohlraums with a small radiation burnthrough patch on one side. They had "standard drive shields" made of copper mounted on both ends of the hohlraum. There were no liners or windows (and so of course no gas fill).

All ten Nova beams entered the hohlraum with an energy of 2.7 kJ each in a 1-ns square pulse. An internal temperature of about 250 eV can be inferred from previous spectral measurements on similar hohlraums.

Table 4-7: Summary of Nova shots used for boron and boron carbide exposures

Date / Target Name	3w kJ	Pulse ns	BBT eV	Fluence J/cm2	Fluence J/cm2	Fluence J/cm2	Fluence J/cm2
Nov 17, 1995				**22 cm**	**26 cm**	**31 cm**	**40 cm**
RKK_HOHLSBS24	25.141	2.2	195	3.24	2.32	1.63	0.98
RKK_HOHLSBS22	24.264	2.2	195	3.13	2.24	1.57	0.95
RKK_HOHLSBS16	25.362	2.2	195	3.27	2.34	1.65	0.99
		Avg	Fluence	3.21	2.30	1.62	0.97
Materials:	boron carbide: hot pressed (Ceradyne), plasma sprayed (Y-12)						
Jan 10, 1996				**23 cm**	**27 cm**	**32 cm**	**41 cm**
TJO_ALBEDO_94	30.254	1.0	250	3.57	2.59	1.84	1.12
TJO_ALBEDO_95	25.559	1.0	250	3.01	2.19	1.56	0.95
TJO_ALBEDO_96	26.424	1.0	250	3.12	2.26	1.61	0.98
TJO_ALBEDO_97	27.348	1.0	250	3.22	2.34	1.67	1.01
TJO_ALBEDO_98	28.131	1.0	250	3.32	2.41	1.71	1.04
TJO_ALBEDO_99	26.919	1.0	250	3.17	2.30	1.64	1.00
		Avg	Fluence	3.24	2.35	1.67	1.02
Materials:	boron carbide: hot pressed (Reade), plasma-sprayed (Y-12) boron: solid chunks (LLNL C&MS)						
Feb 22&23, 96				**22 cm**	**26 cm**	**31 cm**	**40 cm**
SGG_FBALL_34	25.256	2.2	200	3.25	2.33	1.64	0.98
SGG_FBALL_35	26.362	2.2	200	3.40	2.43	1.71	1.03
DHK_BLIMP_12	25.664	2.2	200	3.31	2.37	1.67	1.00
DHK_BLIMP_13	26.577	2.2	200	3.42	2.45	1.72	1.04
DHK_HEP4RT_12	24.098	2.2	200	3.11	2.22	1.56	0.94
DHK_HEP4RT_13	24.449	2.2	200	3.15	2.26	1.59	0.95
		Avg	Fluence	3.27	2.34	1.65	0.99
Materials:	boron: solid chunks (LLNL C&MS)						
Feb 23, 1996				**22 cm**	**26 cm**	**31 cm**	**40 cm**
SGG_SNRT_20	11.923	1.0	210	1.54	1.10	0.77	0.46
SGG_SNRT_21	11.940	1.0	210	1.54	1.10	0.77	0.47
		Avg	Fluence	1.54	1.10	0.77	0.47
Materials:	boron carbide: plasma-sprayed (Plasma Tech & ProTeC) boron: plasma-sprayed (General Atomics)						

The third series of Nova shots occurred over Feb. 22 & 23, 1996, covering six shots in all. Gas-filled, scale-1 hohlraums without shields were used in

these experiments. Backlighters were used on the targets. Eight of Nova's beams were directed into the hohlraum at an energy of about 3.2 kJ each in a shaped 2.2-ns pulse (PS22). Previous work gives an estimated internal temperature of about 200 eV.

The fourth set of Nova experiments was performed on Feb. 23, 1996, with two shots. These used non-gas-filled targets with limited shields. Eight beams were used to drive the hohlraum, at 1.5 kJ each in a 1-ns square pulse. The peak internal hohlraum temperature was estimated to be 210 eV.

4.3.4.4 Observations and Measurements for boron carbide and boron

While there were differences in the x-ray response of the seven types of boron carbide and boron tested, they are grouped together in this section because the major conclusions about removal rates and mechanisms are similar. Profilometer scans show that these materials roughen somewhat on exposure to high x-ray fluences. However, even after multiple shots at the highest x-ray fluences, no net removal (steps) could be measured in the surfaces. Optical microscopy and SEM images showed isolated small pits in the surfaces. This indicates that most material removal was in the form of solid particles spalled off the surface. Finally, with the spectra and time scales of these experiments, the thresholds for x-ray damage were nominally at the lowest exposure level, about 1 J/cm^2.

The hot pressed boron carbide from Ceradyne provided the strongest evidence for thermal stress damage in the material. At the highest two fluences, a single exposure caused severe thermal stress cracking in a "dry lake bed" pattern. The surfaces roughened at this point due to curling of the

edges of the facets of the cracked surface. Figure 4-17 is an SEM image of this phenomenon on the highest fluence sample. Additional exposures to x-ray high fluences produce a rougher landscape with thermal stress cracks on the "floors" surrounded by rounded hills and ridges. The rounded structures appear to be locally melted edges of the facets that curled up after the first exposure. This behavior is seen in the lower half of the optical micrograph in Figure 4-18, in a region exposed to three high fluence shots. In the upper part of the picture, near the edge of the region masked to receive only a single shot, some rectangular shaped pits are evident, likely some thermally cracked particles removed by the thermal stresses. The third highest x-ray exposure of the Ceradyne material shows just faint cracks after the first exposure. After two more shots, there were many small rectangular pits in the surface, clear evidence for removal of the thermally cracked material. These features are shown in Figure 4-19. The lowest fluence shot showed essentially no evidence of damage either optically or with the profilometer, although AFM (atomic force microscope) measurements indicated that surface scratches from the diamond polishing were annealed.

Attempts at estimating mass removed were made using both profilometry and microscopy. At high fluence, profilometry scans of the Ceradyne boron carbide (Figure 4-20) showed the surface roughening from the initial <0.1 μm to 1-2 μm after a single shot and 3-5 μm after three shots. The roughening, which occurs primarily by curling of the crazes, is far larger than any material removal. The bottom of the roughness suggests some 0.5 μm pits are present, but any net removal is significantly less than the roughness and difficult to measure. As an alternative, material removal was estimated by combining AFM-measured depths of specific pits observed by optical microscopy with an

estimate of the fraction of the area covered by pits from optical micrographs. At the second lowest fluence, the average pit depth was 1/3 μm and the fraction of area removed was 10% or less, implying a cumulative average removal of about 0.03 μm for the three shots. At the highest fluence, the average pit depth is close to 1 μm and the pits cover perhaps half of the area, resulting in a cumulative average removal of up to 0.5 μm for the three shots. This value has a very large uncertainty because of the difficulty of determining the fractional area covered by pits.

Hot pressed boron carbide from the other supplier, Reade responded differently to the x-ray exposures, in that there was no thermal stress cracking evident. The surfaces were covered with small pits, which at the two highest fluences were surrounded by raised, rounded edges. This structure can be seen in Figure 4-21, which shows the highest fluence sample in the six shot / no shot region. Figure 4-22 shows typical profilometer scans across this same boundary. The surface roughness increased from the unexposed value of better than 0.1 μm to 0.5 - 1 μm in the multiply exposed region. There is no material removal step discernible, even after six shots. Photographs of the sample at the lowest fluence show some change in surface appearance in the exposed region. However, optical microscopy reveals no real pitting or other damage, and profilometry showed no change in surface roughness. This places the x-ray damage threshold at or just above 1 J/cm^2.

Although no surface steps were noted in the Reade profilometer scans, there was evidence of pitting in the surface. Therefore material removal was estimated on this basis, much as was done for the Ceradyne samples. In the highest fluence sample, the pits measured from 0.2 - 1 μm deep and covered

50% of the area after six shots. This corresponds to 0.2 - 0.3 μm removed in six shots, or 0.03 - 0.05 μm/shot.

The plasma sprayed boron carbide had a substantially different microstructure from the hot pressed material. The coating thickness is made up of "splats" of molten material that intertwine, harden, and adhere in a complex three-dimensional arrangement. The polishing process thins the surface splats, leaving some unsupported edges, and perhaps weakens the adhesion of some splats. Exposure to x rays of the polished samples from Y-12 therefore produced a third type of boron carbide response. In this case the x rays curled the edges of some of the thinner surface splats and removed some that were smaller or in some way weakly bonded to the other surface material. Figure 4-23 is an SEM image of the boundary between and unexposed and singly exposed region at the second highest fluence. Although pits are visible in the unexposed region due to the original coating porosity, the exposed area is clearly rougher. A 300x microscope photograph in Figure 4-24 shows regions with zero, two, six, and eight exposures to high x-ray fluences. It appears that repeated x-ray exposure etches away the plasma sprayed surface, leaving pits below ridges at near the original surface height. A profilometer scan in Figure 4-25 shows the increase in surface roughness from about 0.1 μm to 1 - 2 μm and the development of some pits in the 8-times exposed surface. However, no uniform ablation step is detectable, because there is still some polished surface remaining at the original level. At the lowest fluence, the Y-12 material showed just a faint change in the exposed surface region, along with a slight roughening. Therefore the damage threshold is probably just less than 1 J/cm^2.

As with the hot pressed boron carbide, a rough calculation of material removal was made for the Y-12 material from typical surface pit depth and areal coverage. After six shots at the highest x-ray fluence, 1 μm deep pits covering half the exposed surface was taken as a reasonable estimate. These figures give a material removal rate of about 0.08 μm/shot.

The solid boron material behaved quite a bit like the boron carbide samples. At the higher fluences, optical microscopy revealed thermal stress cracking of the surface. A sample exposed to the second highest fluence showed the same surface pattern of pits with raised, rounded edges as seen in the Reade boron carbide after 4 - 6 shots. Figure 4-26 shows such a region adjacent to areas exposed to one or two shots. The single shot region is broken into small sections by the thermal stresses, where the surface roughness comes from the curling of the edges of the sections. The doubly exposed area starts to have some of the rounded ridges of the 4 - 6 shot region. Profilometer scans, as in Figure 4-27, show the surface roughening without producing a measurable step in the surface level. At the lowest fluence, the surface started developing thermal stress cracks after just one shot, indicating a damage threshold somewhat lower than boron carbide.

Profilometer scans of the boron surface at the highest fluence do show rather deep pits develop after multiple exposures. These can again be used to quantify material removal rates. Using the estimate that 30% of the surface is covered with 2 μm deep pits after six shots, boron was removed at a rate of 0.1 μm/shot.

Figure 4-28 summarizes the results for boron carbide and boron. Removal depths at the lower fluences were estimated with the same procedure used at the highest fluence. Note that these results are presented as rough approximations principally to indicate trends and provide a relative comparison of boron carbide and boron with other potential first wall materials. For example, while the Reade material did seem to perform better than the other materials in this test, the differences are probably not significant.

The final series of two Nova shots on Feb. 23, 1996 was set up differently than the other experiments. The purpose of these shots was to compare the response of unpolished plasma sprayed samples from new vendors to x-ray exposure. The boron carbides from ProTeC and Plasma Tech and the boron from GA were included in this test. Figure 4-29 shows an SEM image of the highest fluence sample from ProTeC with areas of no, one, and two exposures. The image shows evidence of melting after exposure, visible as a loss of the finest scales of roughness in the original surface. The exposed surfaces seem to have these micron-sized bumps and ridges melted out. Some thermal stress cracking is also apparent under high magnification. The qualitative response was very similar in the other materials, except the GA boron sample was more prone to cracking.

The highest fluence sample of the GA boron was cleaned and weighed before the shots, then reweighed after the shots to measure material removal. The weight loss was 0.1 ± 0.1 mg, which corresponds to 1 ± 1 μm average removal. Obviously the exposed area was too small to provide a useful estimate of material removal. However, the exercise indicated that weight

loss measurements on a few square inches of first wall material would give useful results, and that method was adopted for later experiments.

4.3.4.5 Discussion of removal mechanisms for boron carbide and boron

Thermal stress / shock is the dominant removal mechanism for these materials, with the possible exception of the hot pressed boron carbide from Reade. The Ceradyne boron carbide and the boron show thermal stress cracking and all materials show surface roughening at the higher x-ray fluences. Continued exposures cause additional roughness and the appearance of angular pits in the surface. The pits seem to be locations where small sections of thermally shocked material has been flaked off or popped out by the additional thermal loading.

Observations of x-ray damage for these materials show evidence for melting of the surface in two ways. The rounded edges near pits of multiply exposed areas are a direct proof. Also, the most likely explanation for the thermal stress cracking is that the materials melt then "freeze in" a stress-relieved state at high temperatures, leading to surface tensile stresses on cooling. However, the melting does not appear to be the dominant material removal mechanism, because most surface pits have angular features indicative of solid removal. In addition, there is no evidence of "splashing" of the liquid near the boundaries of masked regions. At a minimum, the viscosity of the melt must be relatively high.

Vaporization does not appear to play a role in material removal at these fluences. This mechanism would manifest itself as an ablation step between

regions with different numbers of exposures. Since no such steps are visible, a rather low upper limit on the impact of vaporization can be established.

The major difficulty with this series of experiments was that the profilometer was unable to detect a characteristic removal depth for these materials, even at the highest x-ray fluences. Therefore the best that can be done with these data is estimate the removal rate based on typical pit depths and rough averages of surface coverage. These lead to something like less than 0.04-0.13 μm in six exposures at 3.2 J/cm^2. Use of some other technique will be needed to quantify the removal of small angular particles by thermal shock.

4.3.5 Aluminum Response

4.3.5.1 Introduction

Nine aluminum disks were exposed to x rays on Nova ride-along shots conducted between November 1995 and February 1996. Microscopy and profilometer scans performed after the shots determined material removal rates and indicate the removal mechanisms responsible. This section describes the experiment setup, presents the post-shot observations, and discusses the results in terms of likely removal mechanisms.

4.3.5.2 Experiment set-up

Section 4.3.1 describes the sample holders, mounting fixtures, and test procedures used in the whole series of material response experiments. Therefore this part will be limited to specific conditions unique to the aluminum testing.

The nine exposed samples were composed of one set of five, used in the three November 17, 1995 shots, and a set of four, used for six shots over February 22 & 23, 1996. The first set of samples was made from aluminum alloy 6061-T6 (>97.5% Al) cut to 0.5 inches diameter and 0.25 inches thick. These were polished to a surface finish of less than 0.1 μm roughness. The second set of aluminum samples was made from 1100 alloy (>99.0% Al), with one diamond-turned face with essentially the same level of surface roughness (<0.1μm).

Each sample in the first set was exposed to a single Nova shot with tantalum masking covering half of the surface. Three were performed in a position giving the third highest fluence, with one each at the second highest and the lowest fluences. The second set used one sample at each of the four distances from the target. These were all exposed to six shots, where tantalum masking produced areas of 0, 1, 2, 3, 4, & 6 exposures on each sample face.

The first series of Nova shots was conducted on Nov. 17, 1995, with a total of three shots. The targets were scale 1, 25-μm wall thickness Nova hohlraums with a patch on one side to study backscatter. There were no shields mounted on the hohlraums. These were gas filled targets, using propane on the first shot and methane on the remaining two shots. Nine of the ten Nova beams were pointed into the hohlraum with an energy of 2.7 kJ each in a 2.2 ns shaped pulse (PS22). Previous spectral measurements with similar hohlraums under similar drive conditions showed an internal temperature of about 195 eV, so this was taken as the spectrum of radiation source for the samples.

Table 4-8: Summary of Nova shots used for aluminum exposure

Date	Target Name	3w kJ	Pulse ns	BBT eV	22 cm J/cm2	26 cm J/cm2	31 cm J/cm2	40 cm J/cm2
Nov 17 95	RKK_HOHLSBS_24	25.141	2.2	195	3.24	2.32	1.63	0.98
	RKK_HOHLSBS_22	24.264	2.2	195	3.13	2.24	1.57	0.95
	RKK_HOHLSBS_16	25.362	2.2	195	3.27	2.34	1.65	0.99
			Avg	Fluence	3.21	2.30	1.62	0.97
Date	Target Name	3w kJ	Pulse ns	BBT eV	22 cm J/cm2	26 cm J/cm2	31 cm J/cm2	40 cm J/cm2
Feb 22 96	SGG_FBALL_34	25.256	2.2	200	3.25	2.33	1.64	0.98
&	SGG_FBALL_35	26.362	2.2	200	3.40	2.43	1.71	1.03
Feb 23 96	DHK_BLIMP_12	25.664	2.2	200	3.31	2.37	1.67	1.00
	DHK_BLIMP_13	26.577	2.2	200	3.42	2.45	1.72	1.04
	DHK_HEP4RT_12	24.098	2.2	200	3.11	2.22	1.56	0.94
	DHK_HEP4RT_13	24.449	2.2	200	3.15	2.26	1.59	0.95
			Avg	Fluence	3.27	2.34	1.65	0.99

The second series of Nova shots occurred over Feb. 22 & 23, 1996, covering six shots in all. Gas-filled, scale 1 hohlraums without shields were used in these experiments. Backlighters were used on the targets. Eight of Nova's beams were directed into the hohlraum at an energy of about 3.2 kJ each in a shaped 2.2 ns pulse (PS22). Previous work gives an estimated internal temperature of about 200 eV. Table 4-8 summarizes the shots and conditions expected at each sample face.

4.3.5.3 Observations and measurements for aluminum

Optical microscopy was one important component of the post-shot material analysis. The obvious feature of the exposed surfaces was that they were quite rough. The features seemed rounded, consistent with a frozen-in liquid surface that had been splashing around. All exposed surfaces appeared this way, though the surfaces with more exposures and at higher fluences were rougher. Another observation was that aluminum splashed from exposed areas, under the tantalum masks, onto unexposed regions. Figure 4-

30 shows a typical view. This splashing is strongly evident near all exposed areas of the highest two fluence samples of the second set. At the third highest fluence, the splashing is only visible adjacent to the region exposed to six shots. No splashing was visible on the lowest fluence sample.

Atomic Force Microscope (AFM) scans were performed on the low and high fluence samples from the first set. The higher fluence sample (2.3 J/cm^2) had a roughness of 5 μm (peak to valley), with a lateral scale of 10 - 20 μm between valleys, as seen in Figure 4-31. Distinct round droplets a few microns in diameter were scattered about the surface. Figure 4-32 shows the surface of the low fluence sample (1.0 J/cm^2). Here the general surface roughness appears to be about half to one micron in a wavy pattern. The craters visible in the image are evidently the result of impacts of small droplets of target debris. They measure 5 - 10 μm wide and about 2 μm deep. The aluminum surface was likely liquid or recently solidified at the time of the impacts, giving the pattern of splashed ejecta.

SEM images were obtained of these debris craters on the lowest fluence sample. The high magnification shot seen in Figure 4-33 illustrates the central depression with a raised, roughly circular rim. The crater floors have an elevated portion in the center, presumably either rebounding liquid aluminum or the piece of shrapnel that generated the crater.

One further serendipitous observation should be noted. A submicron-diameter fiber of the glue used to hold down the tantalum masks accidentally trailed on to the exposed area of the highest fluence sample in the second set. There the glue fiber received 3.3 J/cm^2 in a single shot. Figure 4-34 shows the

fiber as it passed from a masked to unmasked region of the sample surface. The exposed side shows the presence of a channel in the aluminum approximately ten times the width of the glue fiber. It appears that the rapid vaporization of the glue "blew" some of the liquid aluminum melt layer away from the fiber.

Table 4-9: Aluminum surface roughness measured by profilometer

Fluence	Single Shot	4-6 Shots
3.3 J/cm^2	2 μm	4-6 μm
2.4 J/cm^2	1.5 μm	4 μm
1.7 J/cm^2	1.2 μm	2.5-3 μm
1.0 J/cm^2	0.6 μm	1.5-2 μm

A Tencor alpha-step 200 profilometer was used to measure surface topography and ablation step sizes after the x-ray exposures of the aluminum samples. Table 4-9 summarizes roughness measured by the profilometer. The single-step roughness values are comparable to the removal depths, while the multiple shot removal depths are a factor of two or three higher. Obviously, removal measurements could only be made for regions exposed to four to six shots, where the roughness could be considered noise on top of the ablation step signal. A complication in computing removal per step arose because the profilometer measured only roughening, and no material removal, for regions exposed to one or two shots. Therefore the calculations for material removal per shot use the effective number of shots divided into the total ablation step. Figure 4-35 illustrates the roughening without a detectable step after two shots at the highest x-ray fluence. The 5-μm step visible after six shots in the second scan is therefore divided into four effective shots. These difficulties result in a large uncertainty in the removal depth measurements.

The removal depth results are given in Table 4-10, and are plotted as a function of x-ray fluence in Figure 4-36. No removal data is given for the lowest fluence because any removal (at most a few tenths of a micron per shot) was masked by the surface roughness.

Table 4-10: Summary of ablation step size measurements for aluminum. Step per shot calculations reflect surface roughening only after the first two shots (no detectable removal with profilometer). # effective shots are the number of shots past the initial two. Only effective shots are counted in step/shot because of this limitation in measuring removal.

A 1	**fluence =**	**3.3 J/cm2**			**1.18**	**± 0.196**
	exp 1	exp2	# eff shots	step	step/shot	
A	0	6	4	5.10	1.28	
B	0	4	2	2.44	1.22	
	0	6	4	5.28	1.32	
C	4	6	2	2.50	1.25	
	2	4	2	1.67	0.84	
		starting shots and depth	2	0.00		
A 2	**fluence =**	**2.4 J/cm2**			**0.95**	**± 0.151**
	exp 1	exp2	# eff shots	step	step/shot	
A	0	4	2	2.10	1.05	
	4	6	2	1.40	0.70	
B	0	4	2	2.14	1.07	
	4	6	2	1.81	0.91	
C	0	4	2	2.00	1.00	
		starting shots and depth	2	0.00		
A 3	**fluence =**	**1.7 J/cm2**			**0.61**	**± 0.210**
	exp 1	exp2	# eff shots	step	step/shot	
A	0	6	4	1.70	0.50	
B	0	6	4	1.60	0.48	
D	2	4	2	1.70	0.85	
		starting shots and depth	2	-0.30		

Metallographic cross-sections were made of the five samples in the first set and the highest fluence sample of the second set. Microscopy of these sections

was interesting because the melt depth was clearly distinguishable as a straight line, presumably parallel to the original surface. The surface of the solidified melt layer was very uneven, in some cases dropping down to the solid/melt interface, indicating complete removal of the melt. Most of the surface did have a substantial resolidified layer remaining, however. Figure 4-37 is a representative image from the optical microscopy. The micrographs were examined to determine the average thickness of this layer for each of the samples. There is a substantial variability in the results, due to the rough surfaces and the small sample statistics. The measurements are plotted in Figure 4-38 as a function of fluence. As a check on the consistency of the measurements and predictions, the remaining melt thickness is added to the material removal estimate at each fluence, and compared to the predicted total melt depth. This is shown in Figure 4-39. The curves generally agree, but there is clearly a good bit of scatter in the measurements.

4.3.5.4 Discussion of removal mechanisms for aluminum

Liquid ejection appears to be the dominant mechanism of material removal for aluminum. This process is consistent with the rough, wavy surface and uneven resolidified layer thickness. As mentioned, the micrographs and AFM scans also indicate the presence of small droplets on the surface. Further evidence is provided by the presence of splashed aluminum on the unexposed regions of the samples (except at the lowest fluence, where little or no ablation step could be measured). Aluminum has a large coefficient of thermal expansion, which could generate the forces and accelerations that would drive unstable liquid ejection. Comparisons with the model predictions of melt depth (Figure 4-39) show that approximately one third of the total melt layer is removed under these test conditions.

Vaporization was investigated as a possible contributor to the total removal depth. The ABLATOR model was applied to aluminum with the same x-ray loading used in these experiments. As discussed in chapter 3, the vaporization is assumed to occur from a flat, 1-D interface at a rate dependent on the surface temperature and saturation pressure at that temperature. Figure 4-40 shows that the vaporization from the surface is expected to be only about 10% of the total removal depth. Perhaps by including the added area of the rough surfaces seen in the experiments, this estimate might be increased to 30%. At this level, vaporization is a significant process to include in modeling, but it is not the dominant effect.

The other primary removal mechanism noted in other Nova material response tests was thermal cracking/spall. Thermal cracking was not evident in any of the aluminum optical microscopy, so this effect is likely not significant for aluminum. This is consistent with what would be expected for a ductile metal.

4.3.6 Aluminum Oxide Response

4.3.6.1 Introduction

Ten samples of various forms of aluminum oxide were exposed to x rays on Nova ride-along shots conducted on December 19, 1995. One other sample was tested on November 17, 1995. Microscopy and profilometer scans performed after the shots determined material removal rates and indicate the removal mechanisms responsible. This section describes the experiment setup, presents the post-shot observations, and discusses the results in terms of likely removal mechanisms.

4.3.6.2 Experiment set-up

Section 4.3.1 describes the sample holders, mounting fixtures, and test procedures used in the whole series of material response experiments. Therefore this section will be limited to specific conditions unique to the alumina testing.

The eleven exposed samples were composed of four sapphire (single crystal alumina) disks, four hot pressed alumina cubes, and three disks of alumina plasma sprayed on aluminum substrates. The sapphire samples were half-inch diameter windows from Edmund Scientific (stock #43-631). The 1 mm thick samples were optically flat to two waves He-Ne over 25 mm, so no additional polishing was required prior to testing. The hot pressed aluminum oxide samples were diamond polished to better than 0.1μm surface finish. All three of the sprayed alumina coating samples were fabricated at the Y-12 plant at ORNL. A conventional thermal spray process was used for two of these samples, while the third was produced with the HVOF (High Velocity Oxygen Fuel) process. The plasma sprayed samples were polished to about 0.3 μm roughness.

The x-ray exposures for ten of the eleven samples were conducted in a series of six consecutive Nova shots on December 19, 1995. One sample each of the sapphire and hot pressed alumina was placed at each of the four distances from the target. In addition, the HVOF material was placed at the highest fluence location and one of the thermal sprayed samples was located at the second highest fluence position. Each sample was masked to expose the full surface on the first shot, half on the next shot, and one quarter on the remaining four shots. The other thermal sprayed alumina sample was tested

on November 17, 1995, at the highest fluence location. It had tantalum masking arranged to expose first one-quarter, then one-half, then all the surface on the three consecutive shots.

The first series of Nova shots was conducted on November 17, 1995, with a total of three shots. The targets were scale 1, 25-μm wall thickness Nova hohlraums with a patch on one side to study backscatter. There were no shields mounted on the hohlraums. These were gas filled targets, using propane on the first shot and methane on the remaining two shots. Nine of the ten Nova beams were pointed into the hohlraum with an energy of 2.7 kJ each in a 2.2 ns shaped pulse (PS22). Previous spectral measurements with similar hohlraums under similar drive conditions showed an internal temperature of about 195 eV, so this was taken as the spectrum of radiation source for the samples.

Table 4-11: Summary of Nova shots used for aluminum oxide exposure

Date	Target Name	3ω kJ	Pulse ns	BBT eV	22 cm J/cm2	26 cm J/cm2	31 cm J/cm2	40 cm J/cm2
Nov 17 95	RKK_HOHLSBS_24	25.141	2.2	195	3.24	2.32	1.63	0.98
	RKK_HOHLSBS_22	24.264	2.2	195	3.13	2.24	1.57	0.95
	RKK_HOHLSBS_16	25.362	2.2	195	3.27	2.34	1.65	0.99
			Avg	Fluence	3.21	2.30	1.62	0.97
Date	Target Name	3ω kJ	Pulse ns	BBT eV	21 cm J/cm2	25 cm J/cm2	30 cm J/cm2	39 cm J/cm2
Dec 19 95	SGG_FBALL_29	25.488	2.2	200	3.60	2.54	1.77	1.05
	SGG_FBALL_30	24.938	2.2	200	3.53	2.49	1.73	1.02
	DHK_BLIMP_08	24.268	2.2	200	3.43	2.42	1.68	1.00
	DHK_BLIMP_09	26.056	2.2	200	3.69	2.60	1.81	1.07
	DHK_BLIMP_11	26.377	2.2	200	3.73	2.63	1.83	1.08
	DHK_BLIMP_10	23.966	2.2	200	3.39	2.39	1.66	0.98
			Avg	Fluence	3.56	2.51	1.75	1.03

The second series of Nova shots occurred on December 19, 1995, covering six consecutive shots. Gas-filled, scale 1 hohlraums without shields were

used in these experiments. Backlighters were used on the targets. Eight of Nova's beams were directed into the hohlraum at an energy of about 3.2 kJ each in a shaped 2.2 ns pulse (PS22). Previous work gives an estimated internal temperature of about 200 eV. Table 4-11 summarizes the shots and conditions expected at each sample face.

4.3.6.3 Observations and measurements for aluminum oxide

Optical microscopy was one important component of the post-shot material analysis. One observation was the development of surface (and possibly subsurface) bubbles from the x-ray exposures. This was noted in all the forms of alumina tested. Two other observations were noted in the sapphire and hot pressed materials, but not the sprayed samples. The first was thermal stress cracking over the exposed surfaces and the second was splashing at the edges of exposed regions onto unexposed or less exposed regions.

The development of bubbles at the surface is shown in the series of four micrographs included as Figure 4-41. The material sample in these images is sapphire exposed at the third highest fluence level (1.75 J/cm^2). The original surface in part a of the figure has a few small bubbles scattered about the surface. Part b shows that after a single shot, a large number of submicron bubbles appear, uniformly distributed over the surface. After the second shot of x rays, there tends to be somewhat fewer, though somewhat larger, bubbles at the surface, as seen in part c of the figure. The smaller bubbles seem to have coalesced at the thermal stress cracks. By the sixth exposure (part d), most all the small bubbles have vanished, leaving only some larger (1-2 μm) bubbles. These larger bubbles concentrated in the thermal stress cracks,

especially at intersections of cracks. Figure 4-42 illustrates similar behavior in the hot pressed alumina samples. The micrographs of parts a and c are from the sample exposed to the highest fluence, in regions of two and six exposures. Again the smaller, uniformly distributed bubbles from the early exposures are replaced by fewer, larger bubbles located primarily in the thermal stress cracks after more exposures.

Drawing on further optical microscopy, bubbles were found in samples at every fluence, even down to 1.0 J/cm^2. At the lowest fluence, bubbles were not seen in the sapphire after a single shot, but many were visible after two exposures. In the hot pressed material, there were just a few bubbles seen at the lowest fluence after six shots. As the fluence increased, so did the number of bubbles in the samples of either material.

Thermal stress cracking has already been shown in the images of Figures 4-41 and 4-42. All exposed areas of the sapphire and hot pressed alumina were covered by patterns of cracks, generally with spacings on the order of two to ten microns. Figure 4-42b shows angular pits in a hot-pressed alumina surface exposed to two shots. These are taken as evidence of the spall of solid, thermal shock damaged surface material. Few if any pits were seen in microscopy of the sapphire samples.

An interesting feature of the sapphire was that the cracks initially were all aligned in a regular orthogonal pattern. This is likely related to the anisotropic thermal expansion in this single crystal material. After a number of high fluence x-ray exposures, however, the cracking patterns became more random, indicating some degradation of the original crystal structure. This is

illustrated in Figure 4-43 for sapphire at the highest fluence, where regions of one and five exposures are visible. At the two lower fluences, the thermal stress cracks tended to stay aligned to the original crystal axes.

The other observation was that sapphire and hot pressed aluminum oxide splashed from regions of multiple shots to adjacent masked regions. A typical view is shown in Figure 4-44, at the edge of a singly exposed area of sapphire at the second highest fluence. The splashed material consists of submicron diameter fibers extending 5 - 10 μm into the unexposed surface. The amount of splashed material decreases with fluence, to the point where no splashing was visible on the lowest fluence sample.

Another surface feature was noted in the optical images of several of the sapphire and hot pressed alumina samples. Figure 4-45 shows the surface of the sapphire sample at the second highest fluence, in a two shot region. There are several circular ring-shaped objects visible, in the 5 - 10 μm diameter range. These do not appear to be related to either the thermal stress cracking or the smaller bubbles in the surface around them. These may be impact craters where surface melting has smoothed all features except the outer rims.

The rough surfaces of the plasma sprayed samples, and the fact that alumina is translucent, limited the detail that could be seen with optical microscopy. The most useful result was that side illumination at low magnification indicated a pitted surface. The SEM (Scanning Electron Microscope) was able to produce more detailed images, however. A series of micrographs was produced on the first sample tested, the thermal sprayed

alumina exposed to three shots. Figure 4-46 a-d shows the development of surface features after each exposure at the highest fluence. The unexposed surface is somewhat rough, with typical feature size of a few microns. The single shot area shows two interesting developments: spherical alumina droplets 5 - 10 μm diameter on the surface, sometimes connected with a similar diameter cylindrical neck; and surface bubbles a few microns in diameter. The two exposure area has some of the droplets and even more bubbles. In addition, pits are now visible, up to tens of microns in diameter. In the three shot region, there are more pits of various sizes, as many or more surface bubbles, and a few of the surface droplets.

A Tencor alpha-step 200 profilometer was used to measure surface topography and ablation step sizes after the x-ray exposures. Table 4-12 below summarizes roughness measured by the profilometer. These values are comparable to the removal depths, which meant that removal measurements be only made in regions exposed to four to six shots. A complication in computing removal per step arose because the profilometer measured only roughening, and no material removal, for regions exposed to one or perhaps two shots. Therefore the calculations for material removal per shot use the effective number of shots divided into the total ablation step. Figure 4-47a illustrates the roughening without a detectable step after one shot at the second highest x-ray fluence. Some pits are evident after two shots, but surface debris makes any net removal hardly detectable. The 1.2 μm step visible after six shots in the second scan (4-46b) is therefore divided into five effective shots. The difficulties with measuring the rough surfaces result in a large uncertainty in the removal depth measurements. The removal depth results are given in Table 4-13, and are plotted as a function of x-ray fluence in

Figure 4-48. No removal data is given for the lowest fluence sample of hot pressed alumina because any removal (likely less than 50 nm per shot) was masked by the surface roughness.

One further observation should be noted. The hot pressed alumina samples turned from their original white color to a yellowish-brown after x-ray exposure. The color change was stronger for higher fluences and more exposures.

Table 4-12: Surface roughness measured by profilometer in 4-6 exposure regions on aluminum oxide.

Material	Fluence	Roughness *
Sapphire	3.6 J/cm^2	0.6 μm
Sapphire	2.5 J/cm^2	0.4μm
Sapphire	1.75 J/cm^2	0.3 μm
Sapphire	1.0 J/cm^2	0.2 μm
Hot Pressed	3.6 J/cm^2	1 μm
Hot Pressed	2.5 J/cm^2	1 μm
Hot Pressed	1.75 J/cm^2	1 μm
Hot Pressed	1.0 J/cm^2	1 μm
Thermal Spray	2.5 J/cm^2	0.5 μm
HVOF	3.6 J/cm^2	1 μm

*** = estimated peak to valley, excluding largest spikes**

Table 4-13: Summary of ablation step size measurements for aluminum oxide. Step per shot calculations reflect surface roughening only after the first shot (no detectable removal with profilometer). # effective shots are the number of shots past the initial one. Only effective shots are counted in step/shot because of this limitation in measuring removal.

Sapphire 1	**fluence**	**3.6 J/cm2**			**0.22**	**± 0.020**
	exp 1	exp2	# eff	step	step/shot	
A	0	6	5	1.2	0.24	
B	1	6	5	1.0	0.20	
C	0	6	5	1.1	0.22	

Sapphire 2	**fluence**	**2.5**	**J/cm2**		**0.14**	**± 0.019**
	exp 1	exp2	# eff	step	step/shot	
A	0	4	3	0.5	0.17	
	0	6	5	0.7	0.14	
B	1	6	5	0.6	0.12	
C	2	6	4	0.6	0.15	
D	1	5	4	0.65	0.16	
E	0	5	4	0.5	0.13	

Sapphire 3	**fluence**	**1.75**	**J/cm2**		**0.10**	**± 0.017**
	exp 1	exp2	# eff	step	step/shot	
A	1	6	5	0.5	0.10	
B	0	6	5	0.4	0.08	
C	1	6	5	0.5	0.10	
D	0	6	5	0.6	0.12	
E	1	6	5	0.4	0.08	
F	2	6	4	0.5	0.13	
G	0	6	5	0.5	0.10	

Sapphire 4	**fluence**	**1.0**	**J/cm2**		**0.014**	**± 0.003**
	exp 1	exp2	# eff	step	step/shot	
A	1	6	5	0.06	0.01	
B	0	6	5	0.08	0.02	

Alumina 1	**fluence**	**3.6**	**J/cm2**		**0.23**	**± 0.046**
	exp 1	exp2	# eff	step	step/shot	
A	0	6	5	0.9	0.18	
B	0	6	5	1.4	0.28	
C	0	6	5	1.0	0.20	
D	2	6	4	1.0	0.25	

Alumina 2	**fluence**	**2.5**	**J/cm2**		**0.23**	**± 0.076**
	exp 1	exp2	# eff	step	step/shot	
A	0	6	5	1.2	0.24	
B	0	6	5	0.6	0.12	
C	0	6	5	1.0	0.20	
D	2	6	4	1.20	0.30	
E	2	6	4	1.2	0.30	

Alumina 3	**fluence**	**1.75**	**J/cm2**		**0.12**	**± 0.015**
	exp 1	exp2	# eff	step	step/shot	
A	0	6	5	0.7	0.14	
B	0	6	5	0.6	0.12	
C	1	6	5	0.6	0.12	
D	0	6	5	0.55	0.11	
E	0	6	5	0.5	0.10	

Plasma Spray	**fluence**	**2.5**	**J/cm2**		**0.21**	**± 0.014**
	exp 1	exp2	# eff	step	step/shot	
A	0	6	5	1.1	0.22	
B	0	6	5	1.0	0.20	

HVOF	**fluence**	**3.6**	**J/cm2**		**0.39**	**± 0.014**
	exp 1	exp2	# eff	step	step/shot	
A	0	6	5	2.0	0.40	
B	0	6	5	1.9	0.38	

4.3.6.4 Discussion of removal mechanisms for aluminum oxide

Vaporization was investigated as a possible contributor to the total removal depth. It is expected that the vaporization depth will be the lower limit for the measured removal for any material. The difference in the two depths is then the contribution of other removal mechanisms. The ABLATOR model was applied to aluminum oxide with the same x-ray loading used in these experiments. The vaporization is assumed to occur from a flat, 1-D interface at a rate dependent on the surface temperature and saturation pressure at that temperature, as discussed in Chapter 3. The vapor pressure curve used was developed by Wilemski[3] based on JANAF data. As shown in Figure 4-49, vaporization from the surface is expected to cause up to one third of the material removal at higher fluences. At lower fluences, the surface vaporization contribution is relatively much less.

The appearance of surface bubbles points to another removal mechanism, subsurface vaporization. Bubble nucleation and growth rates must be very high to have any significant effect on such short time scales. Thermal modeling shows peak temperatures of 4000 - 5000 K at the removal depths of the middle two x-ray fluences. Figure 4-50 shows the peak profile for the 1.75 J/cm^2 case, where the removal depth was 0.1 - 0.12 μm/shot. The transient analysis indicates that the 4000 K temperature at this depth will decay after only 10 ns. This will be discussed further in chapter 5.

Another primary removal mechanism noted in the NIF material response tests was thermal cracking/spall. Thermal cracking was evident in almost all of the aluminum oxide optical microscopy. Figure 4-42b showed where this damage led to removal of presumably solid chunks of material in the hot

pressed alumina. SEM and optical images also showed some pitting of the plasma sprayed material. The sapphire, however, did not show any pits from spall removal.

Liquid ejection is another possible mechanism of material removal for aluminum oxide. There is evidence both for and against the relative importance of this process. The SEM images of the thermal sprayed alumina in Figure 4-46 show droplets on the surface indicating a liquid removal process. The presence of splashed alumina on the unexposed regions of the samples (except at the lowest fluence) also shows some mobility of the liquid phase. On the other hand, liquid ejection would be expected to produce rounded, wavy surfaces, whereas the sapphire and hot pressed surfaces appeared angular and faceted. Also, comparisons with the model predictions of melt thickness, included in Figure 4-49, show that melt depth does not correlate well to removal depth.

In summary, aluminum oxide does not appear to have one single dominant damage mechanism. There is instead evidence for the contribution of several processes, that may change their relative effects depending on the particular form of alumina and x-ray exposure conditions.

References

1) Kelly, R., Rothenberg, J.E., "Laser Sputtering Part III. The mechanism of the sputtering of metal at low energy densities", Nucl. Inst. & Meth, B7/8, (1985), 755-763.

2) Hassanein A, Konkashbaev I., "Erosion of plasma-facing materials during a tokamak disruption", Atomic and Plasma-Material Interaction Data for Fusion, V5:193-224, Dec 1994.

3) Wilemski, G.,"Vaporization models for alumina, silicon carbide, and silicon nitride", LLNL internal memo, TAT 96-053.2, 7/24/96.

4) "RBS Analysis of Amorphous Targets", Report by Charles Evans & Associates to Ken Skulina, LLNL, dated 11/13/95.

5) "RBS Analysis of B_4C Samples", Report by Charles Evans & Associates to Ken Skulina, LLNL, dated 3/22/96.

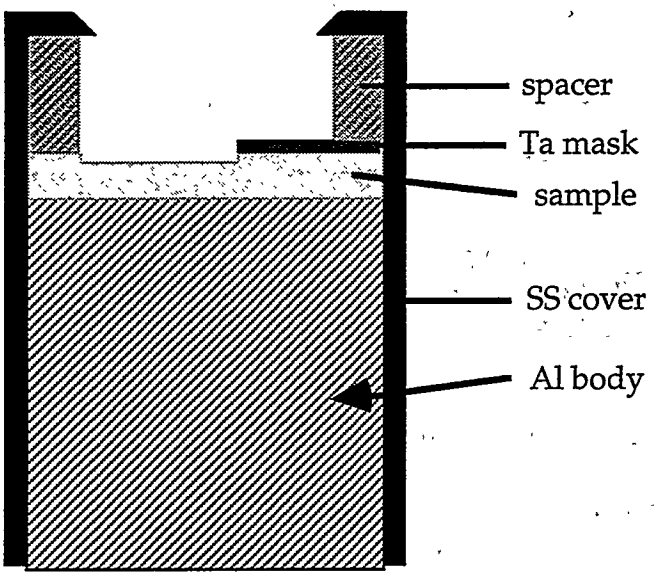

Figure 4-1: Cut-away view of sample holder

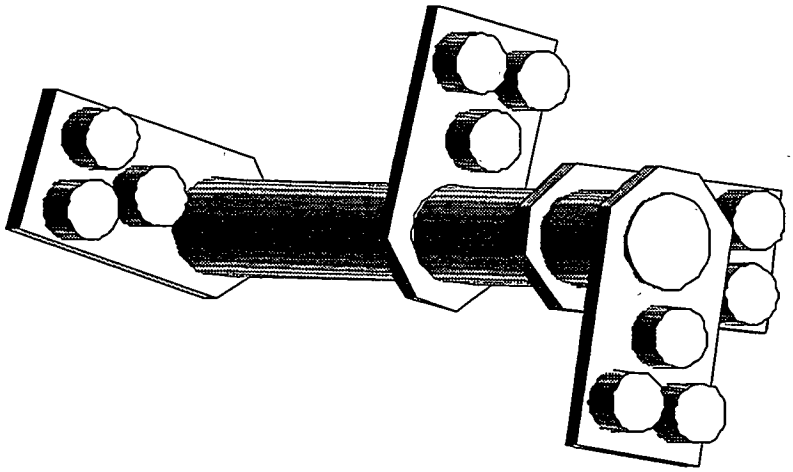

Figure 4-2: Arrangement of sample holders on central rod of SIM cart

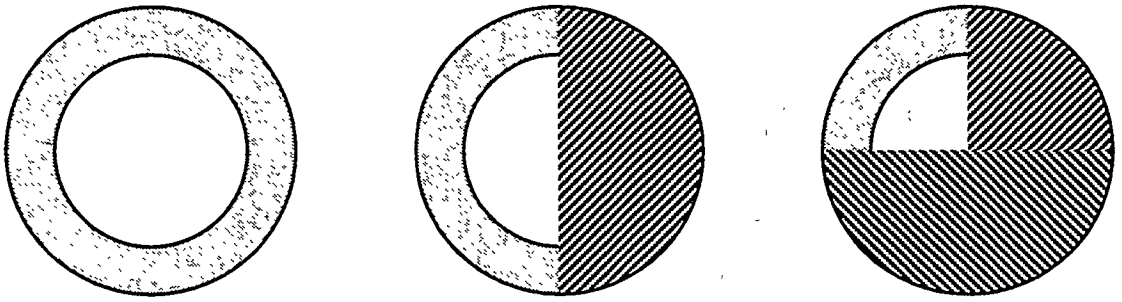

Figure 4-3: Masking for first shot, second shot, shots 3-n.

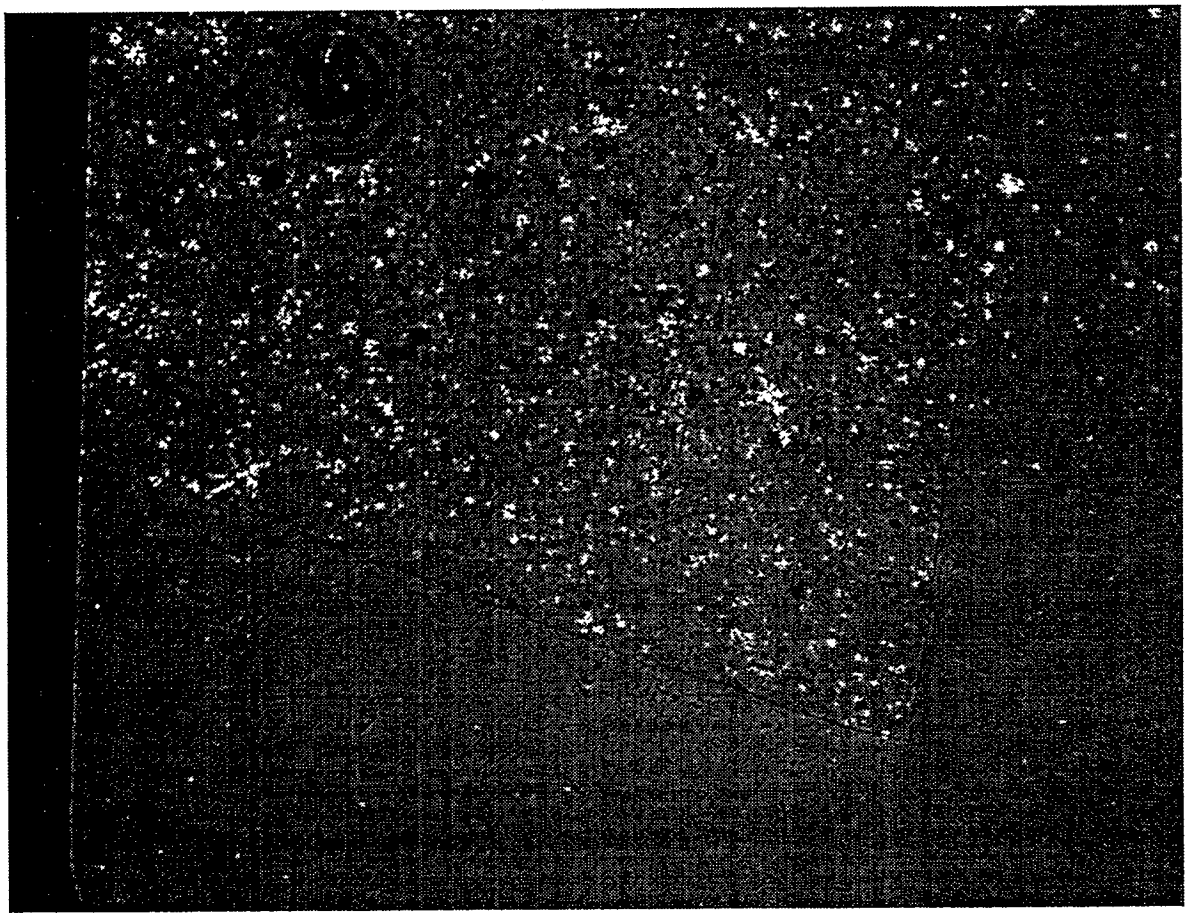

100 μm

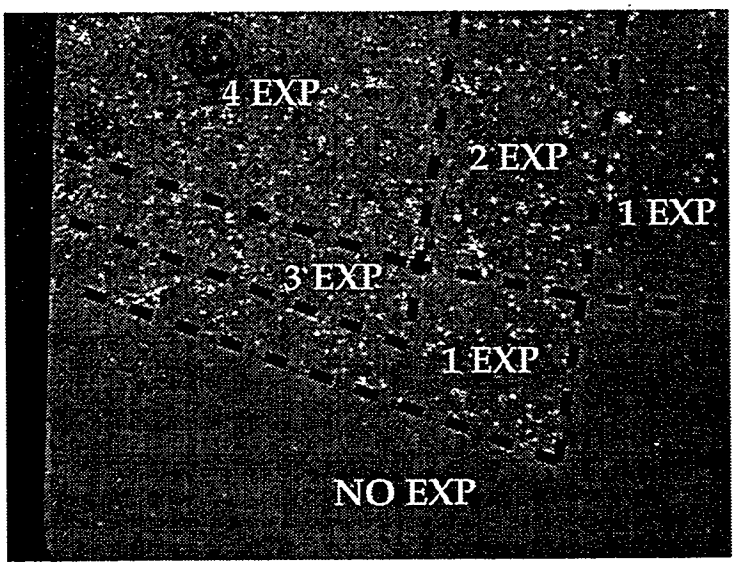

Figure 4-4: Optical image of silica at highest x-ray fluence. Bubbles, target debris, and shrapnel damage evident.

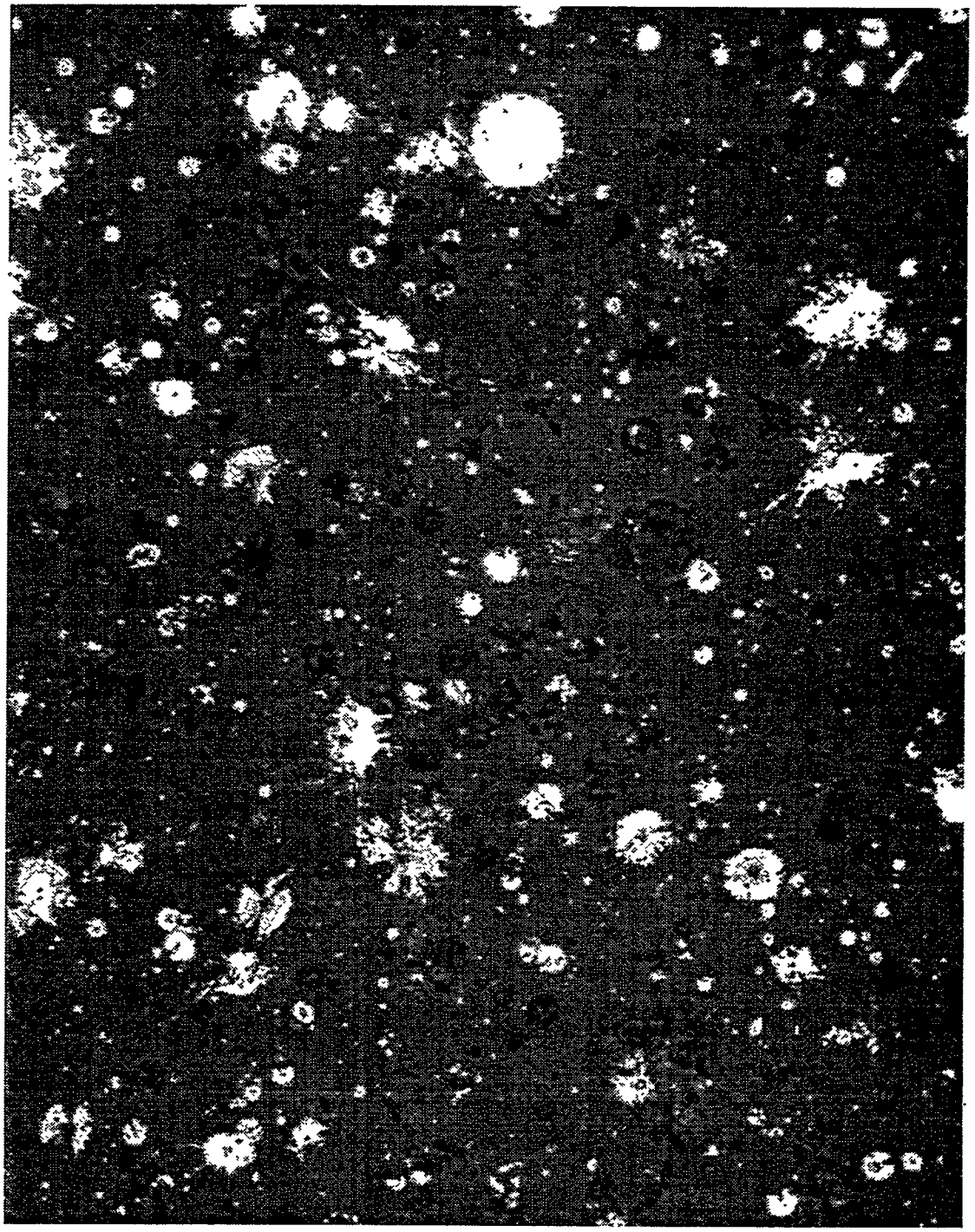

Figure 4-5: Optical image of fused silica at highest fluence in three shot region. Wide variety in sizes of metal droplets and damage pits.

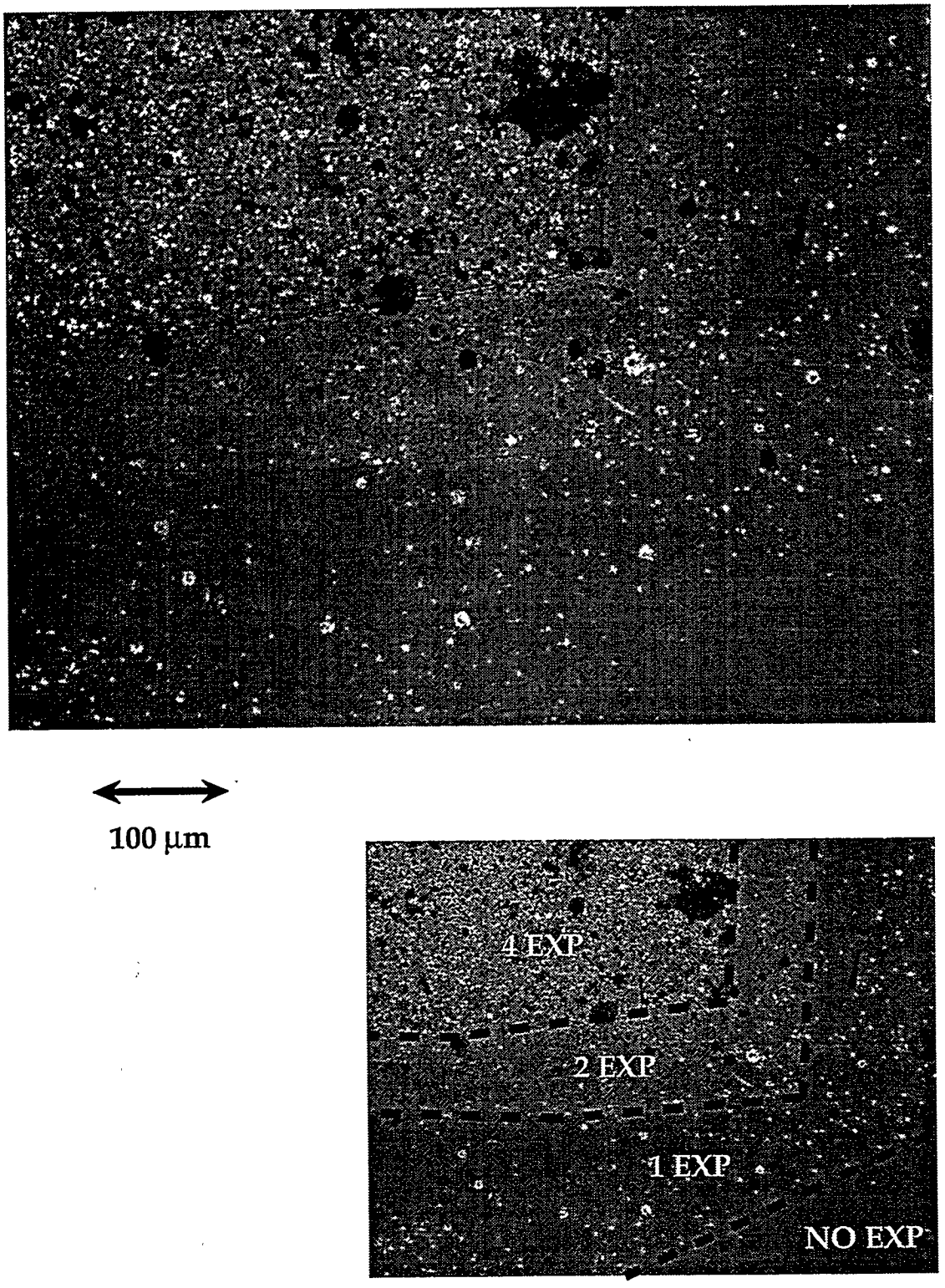

Figure 4-6: Optical image of silica at second highest fluence

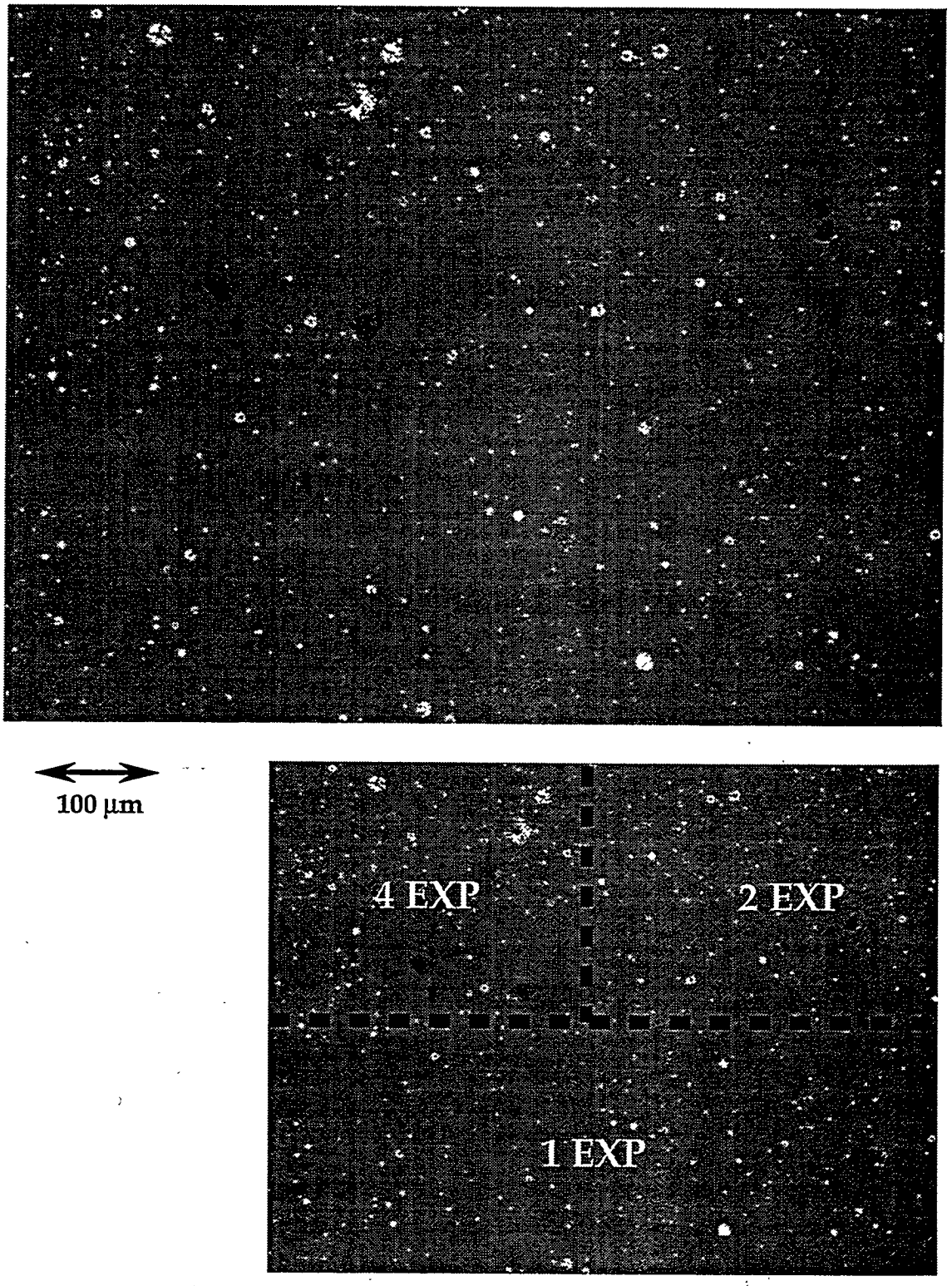

Figure 4-7: Fused silica at lowest x-ray fluence. Little x-ray damage, although some shrapnel craters appear.

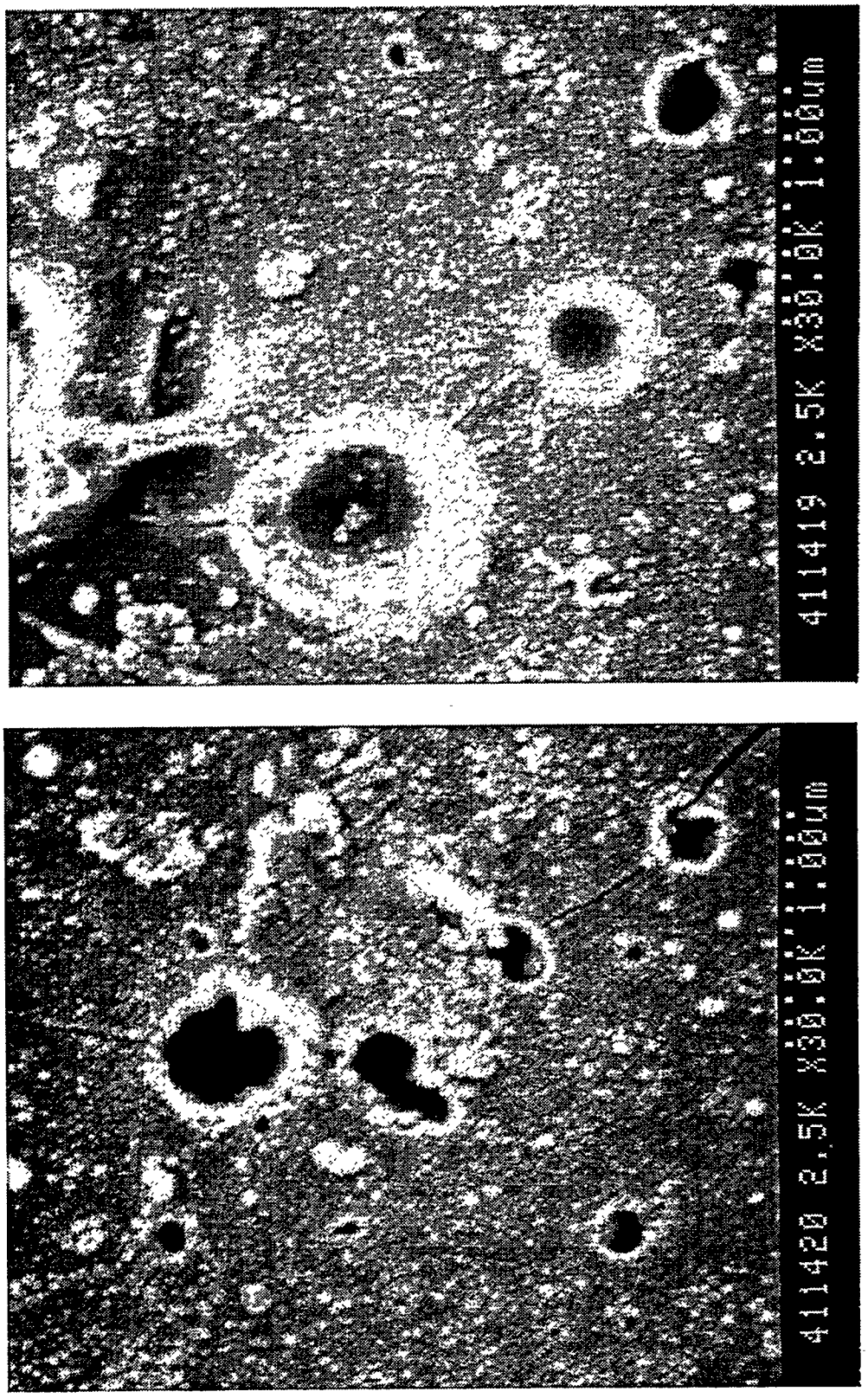

Figure 4-8: SEM images of small surface bubbles (craters) on highest fluence silica sample, in single exposure area. Note cracks connecting impact craters.

Figure 4-9: SEM image of highest fluence silica sample in regions of six shots (right) and one shot. Note thin silica fibers extending from six shot area, indicating some liquid splash.

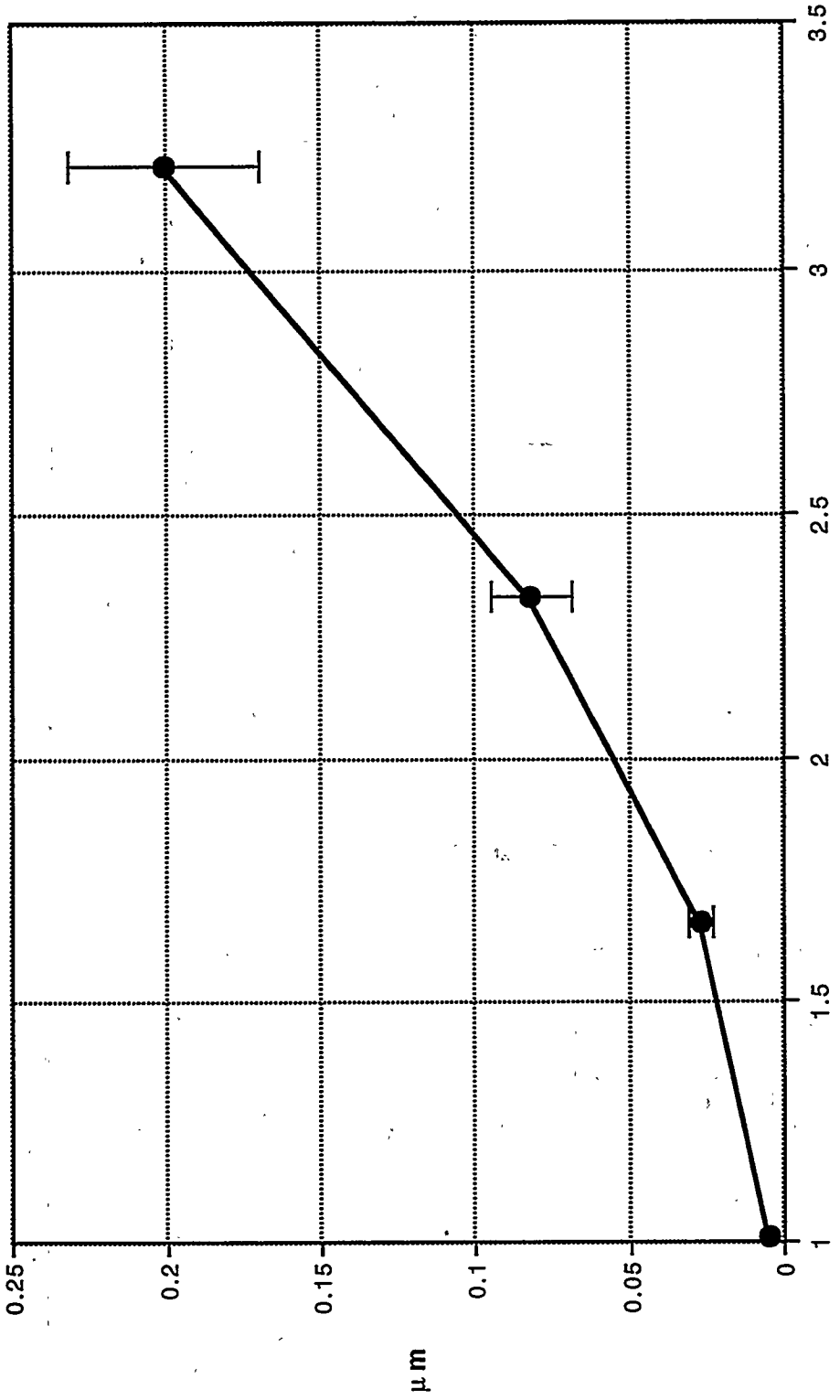

Figure 4-10: Measured fused silica removal depths for 250 eV blackbody x rays.

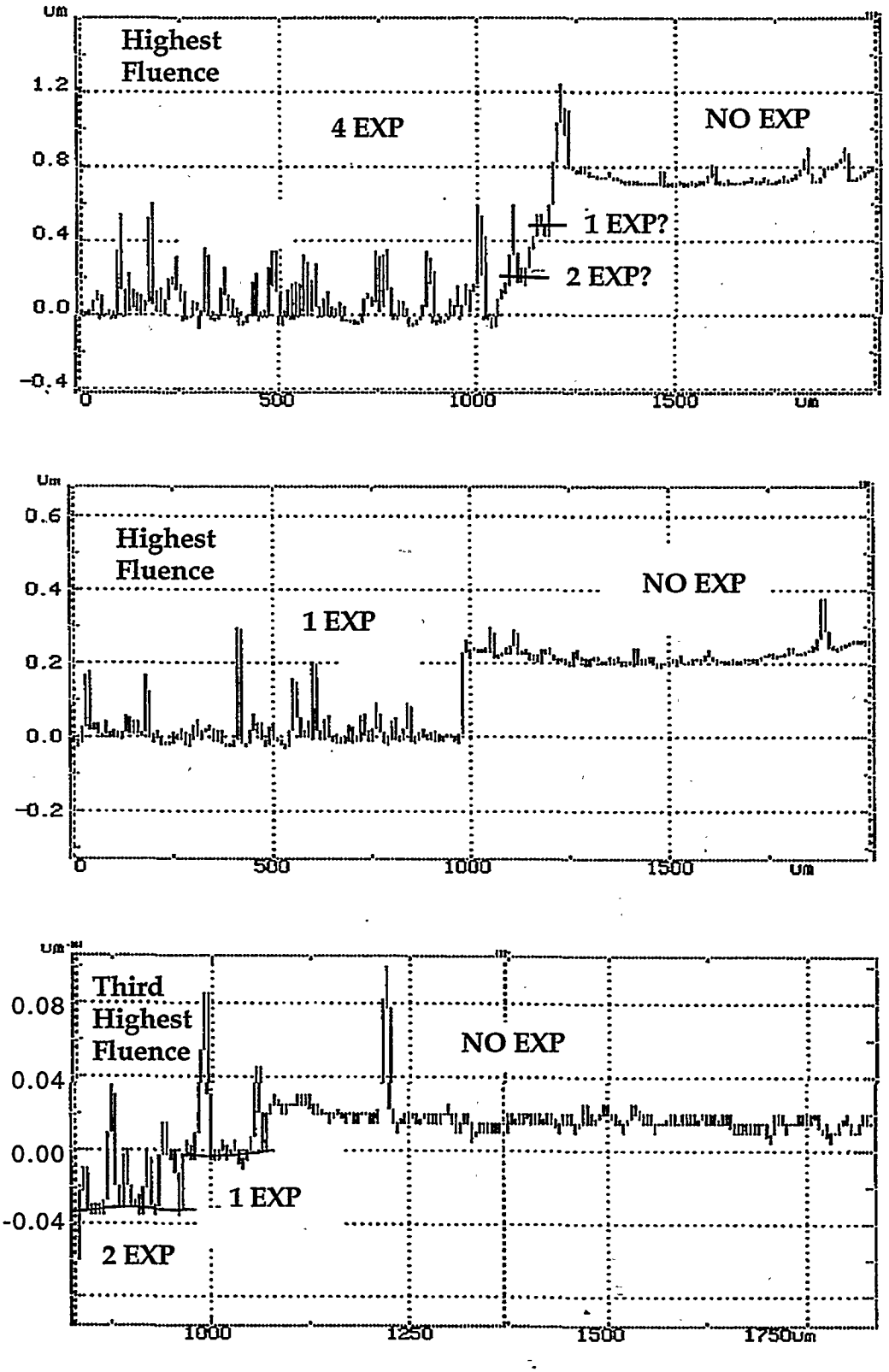

Figure 4-11: Typical silica profilometer scans

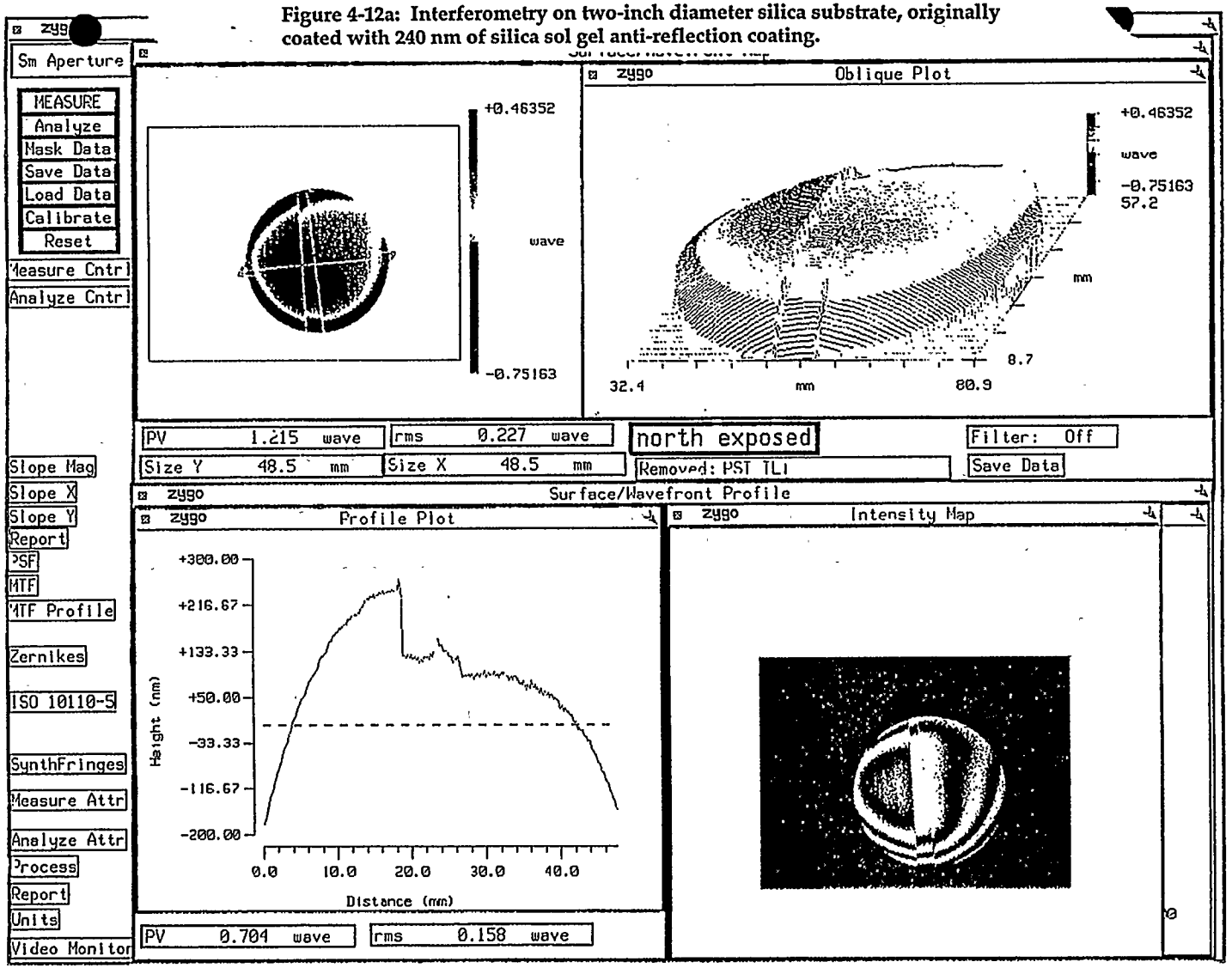

Figure 4-12a: Interferometry on two-inch diameter silica substrate, originally coated with 240 nm of silica sol gel anti-reflection coating.

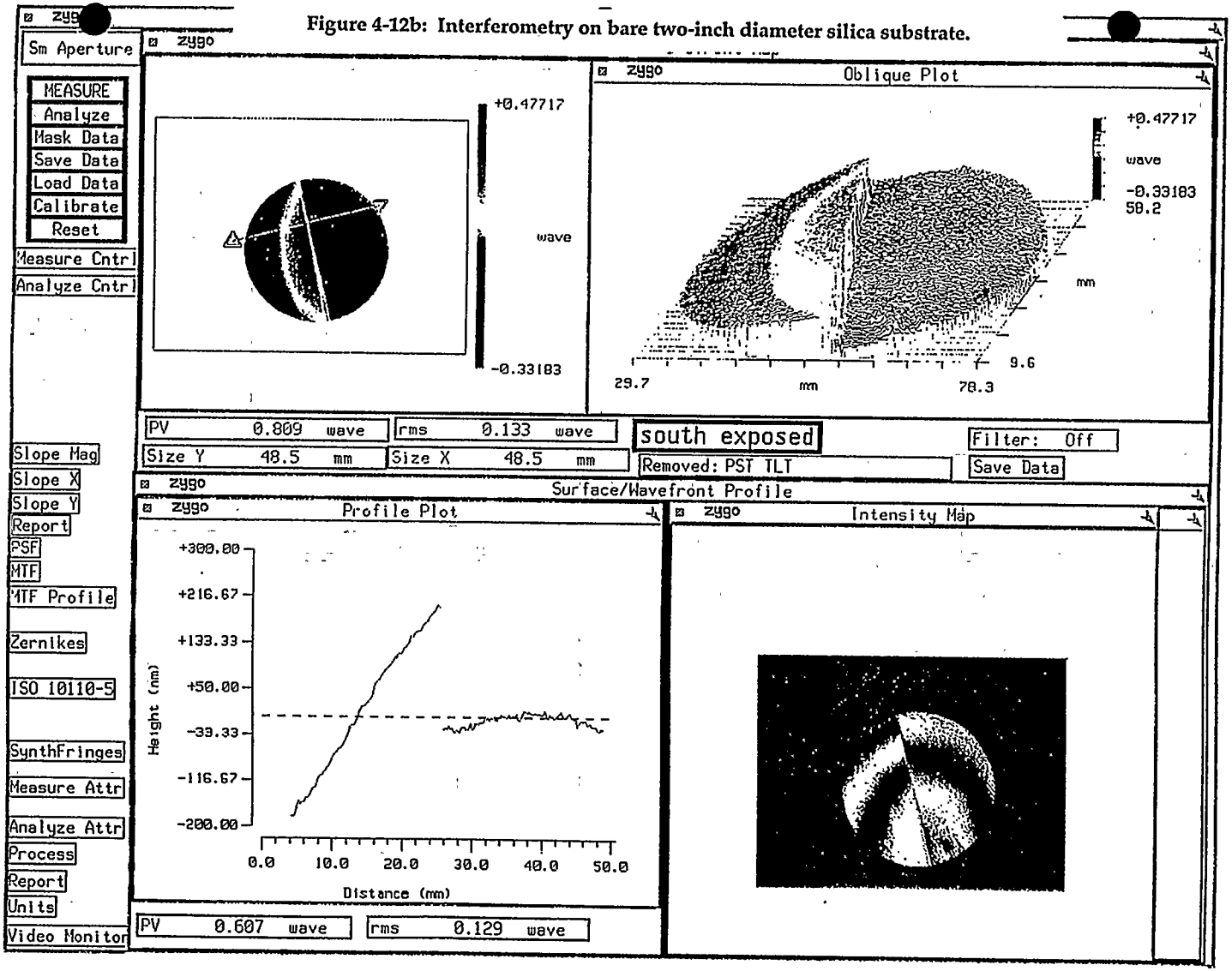

Figure 4-12b: Interferometry on bare two-inch diameter silica substrate.

Figure 4-13: Surface of silicon nitride after one shot at highest x-ray fluence. Surface appears to be composed of micron-sized angular facets. No evidence of thermal stress cracks.

Figure 4-14: Deposition of particulates on unexposed region of silicon nitride from area exposed to one shot at the third highest fluence.

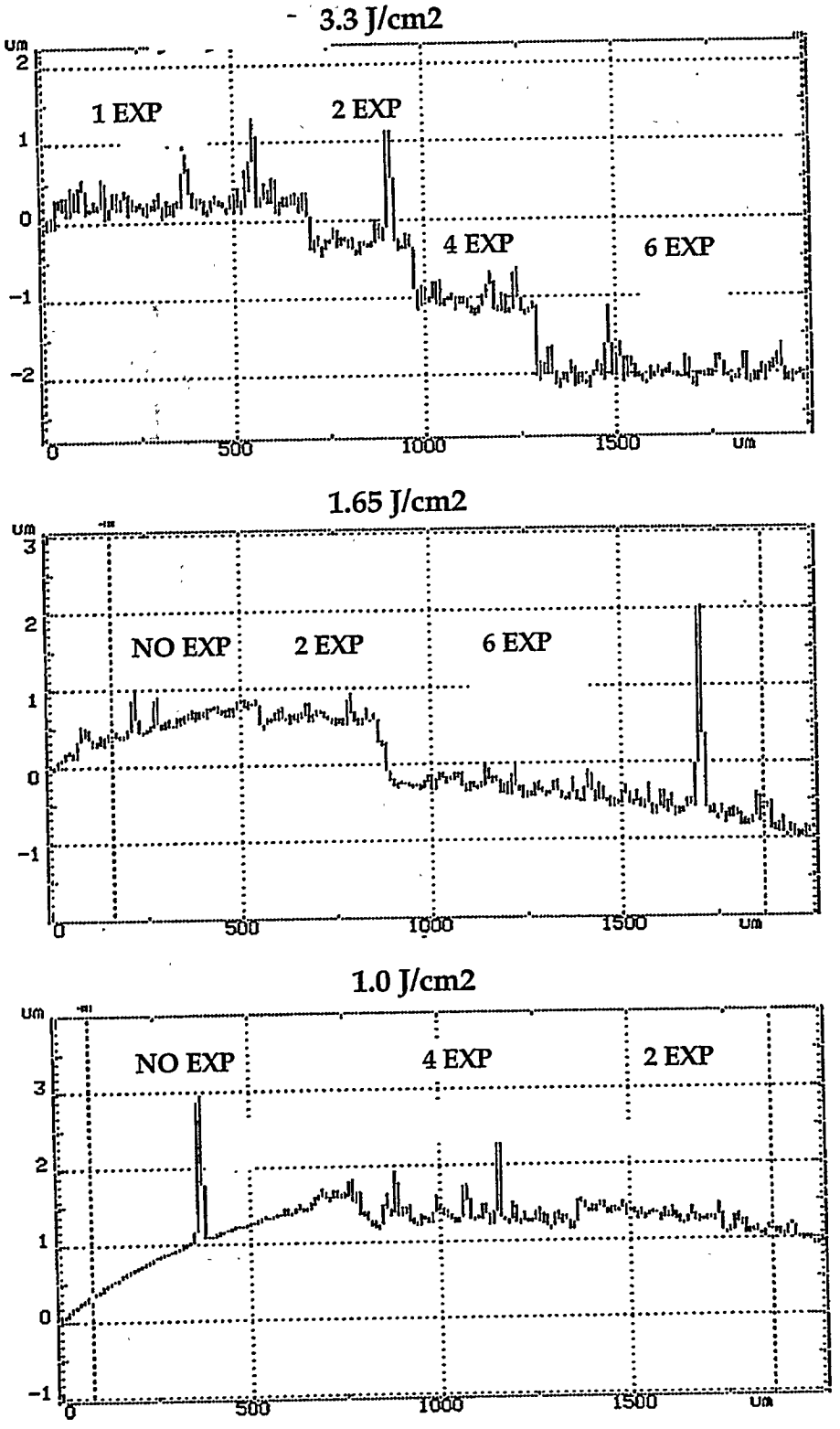

Figure 4-15: Typical profilometer scans for silicon nitride with easily mesured steps.

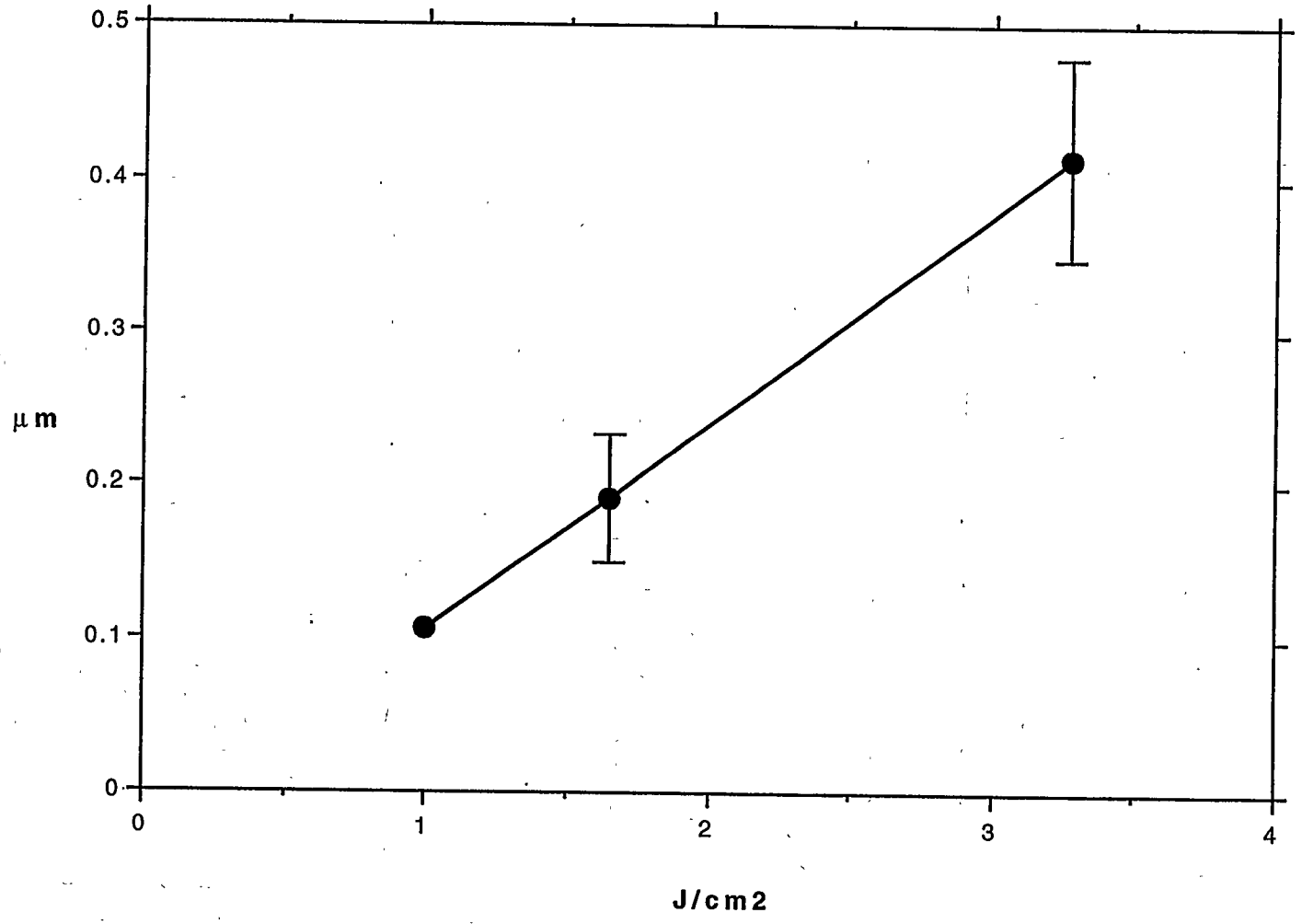

Figure 4-16: Measured removal depths for silicon nitride exposed to 200 eV BB x rays

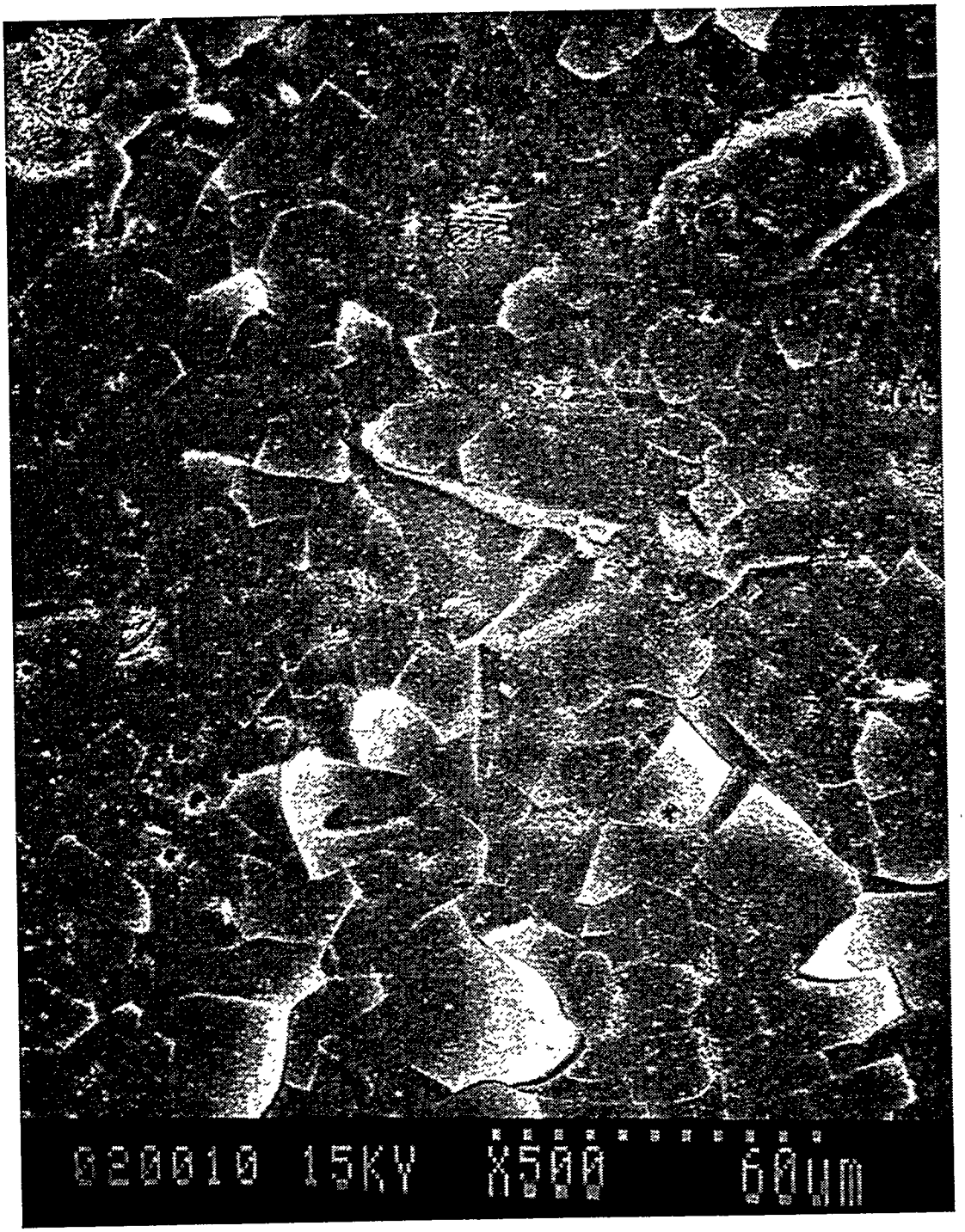

Figure 4-17: SEM image of thermal stress cracking in Ceradyne boron carbide at highest x-ray fluence. Lightest regions are raised above the mean level, showing curling of cracked surface sections.

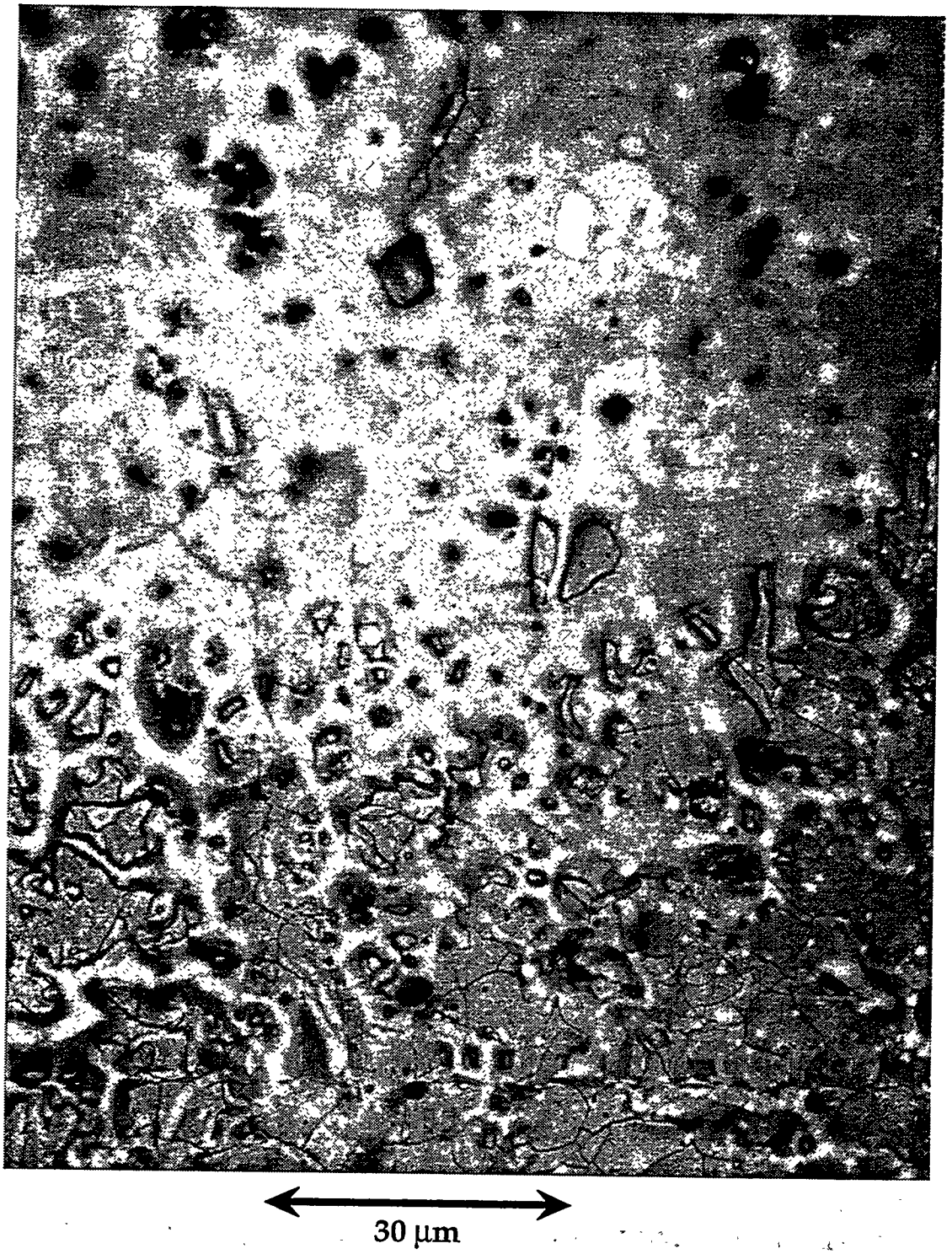

Figure 4-18: Optical image of Ceradyne boron carbide at highest fluence. Single shot (top) and triple shot (bottom) regions are shown. Angular pits can be seen, especially in the single shot region of this photograph.

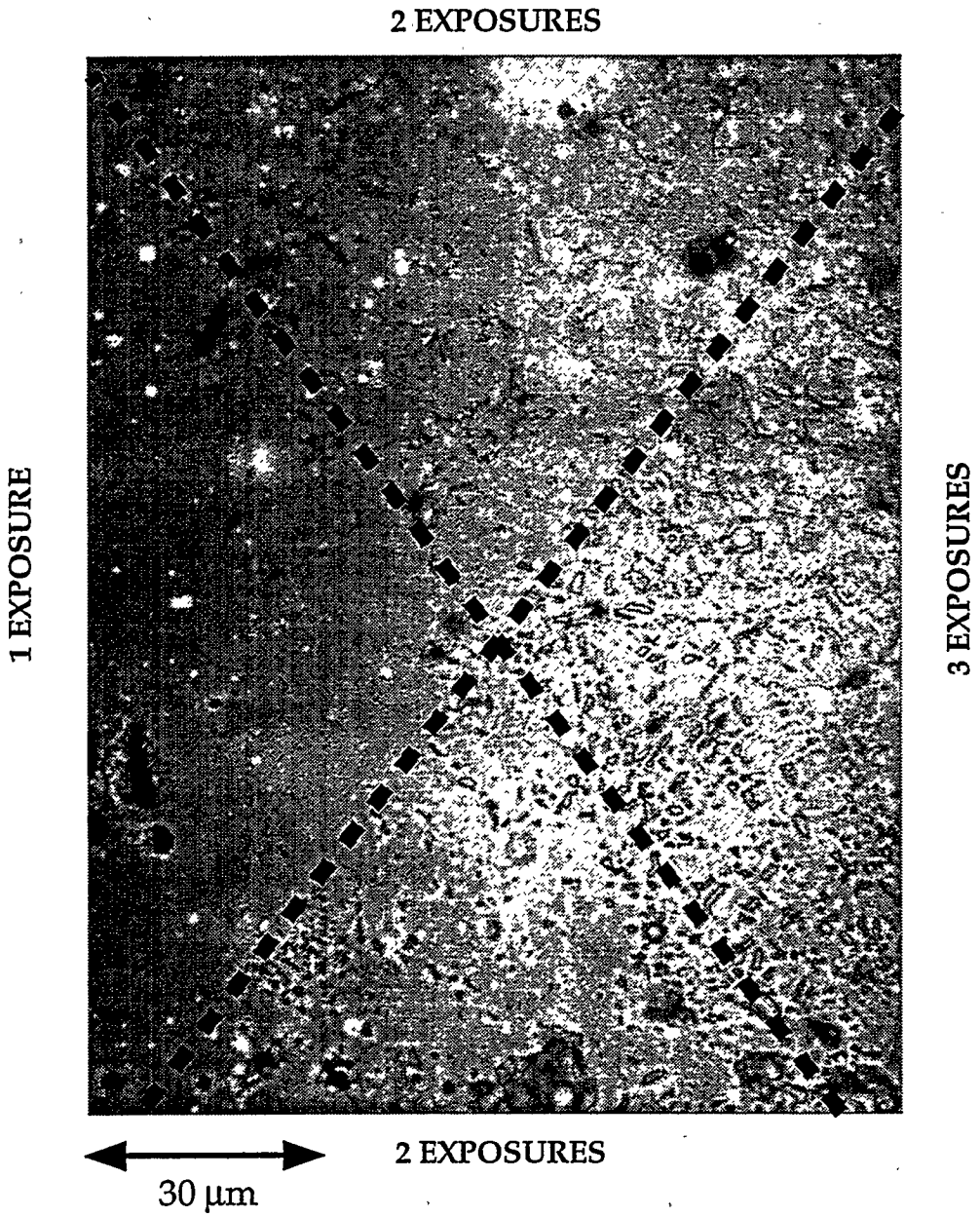

Figure 4-19: Ceradyne boron carbide at third-highest fluence showing regions with from one to three shots. Surface cracks are evident after 1-2 shots, while angular pits can be seen in the multiply exposed regions. This is evidence for spall of particulates as the dominant material removal process.

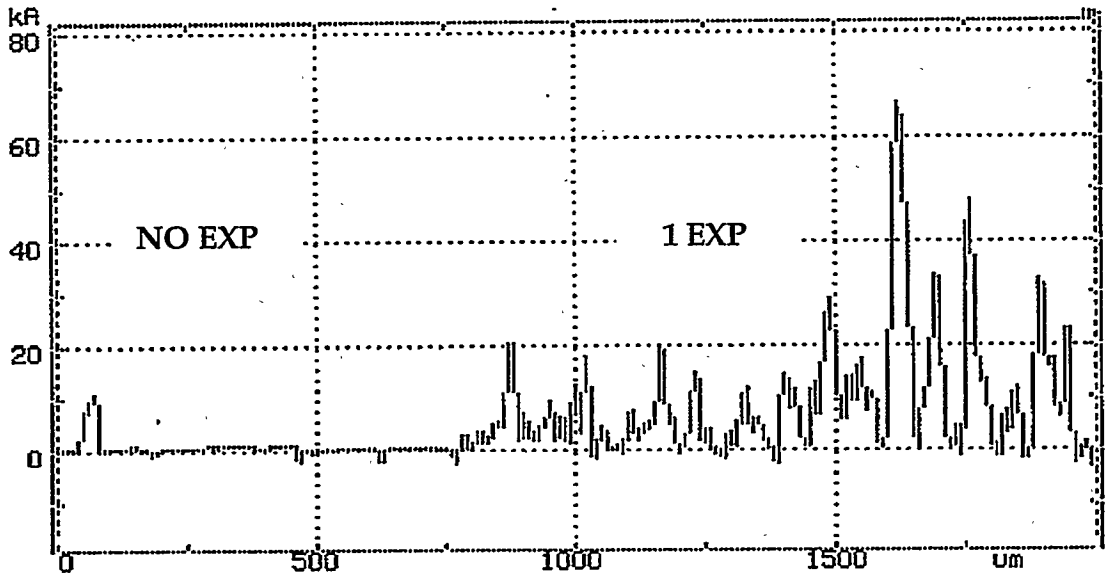

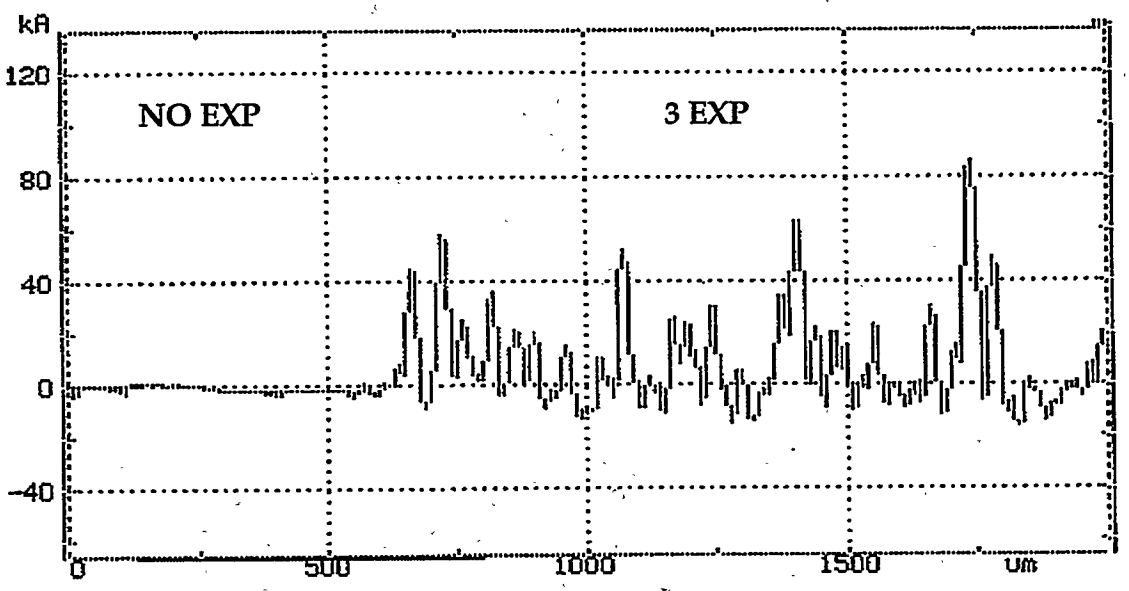

Figure 4-20: Profilometer scans of Ceradyne boron carbide at highest x-ray fluence showing roughening without measureable ablation steps.

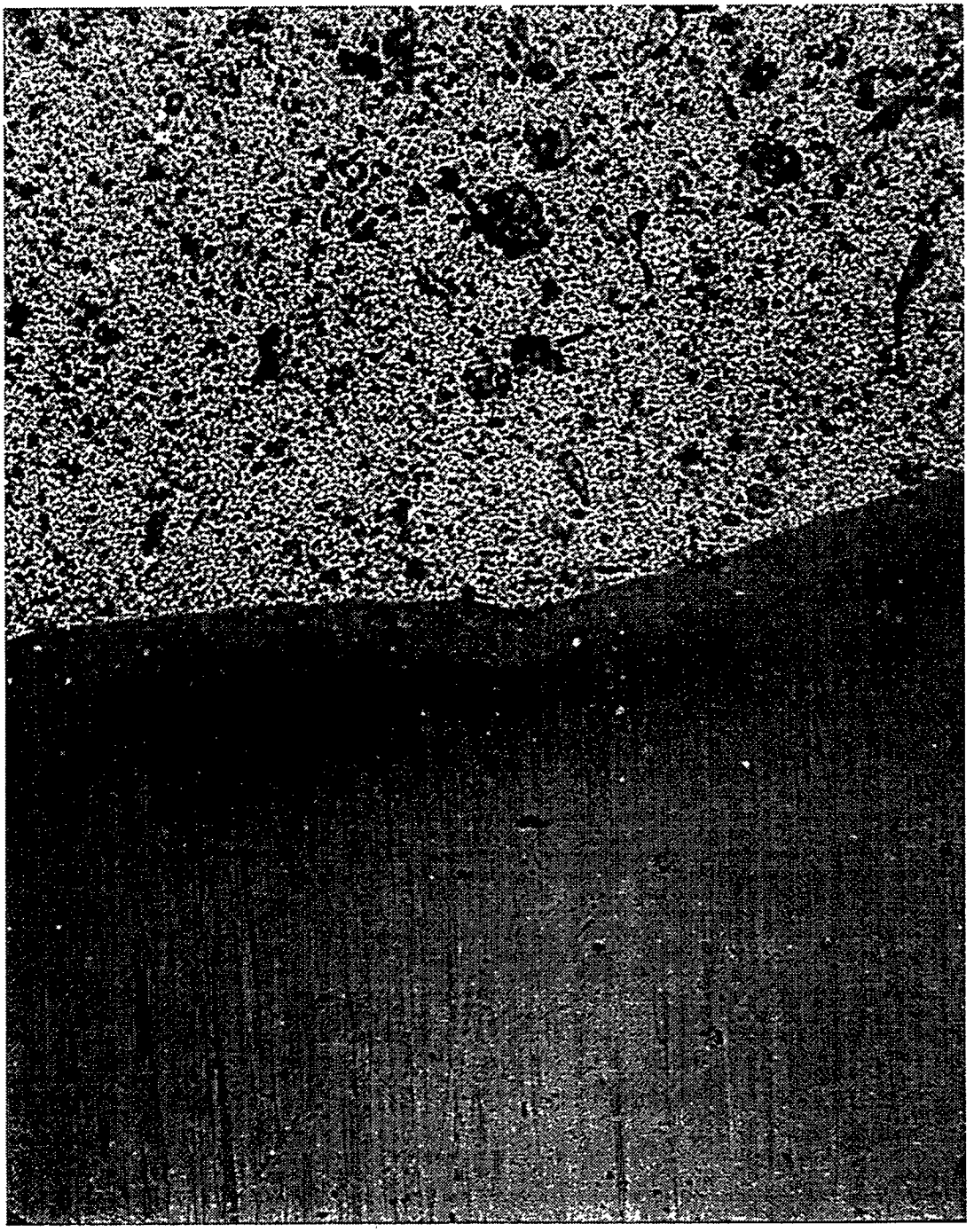

Figure 4-21: Reade boron carbide at highest fluence. Top had six exposures and bottom had none. Exposed surface is rough with many small pits, but no surface cracking.

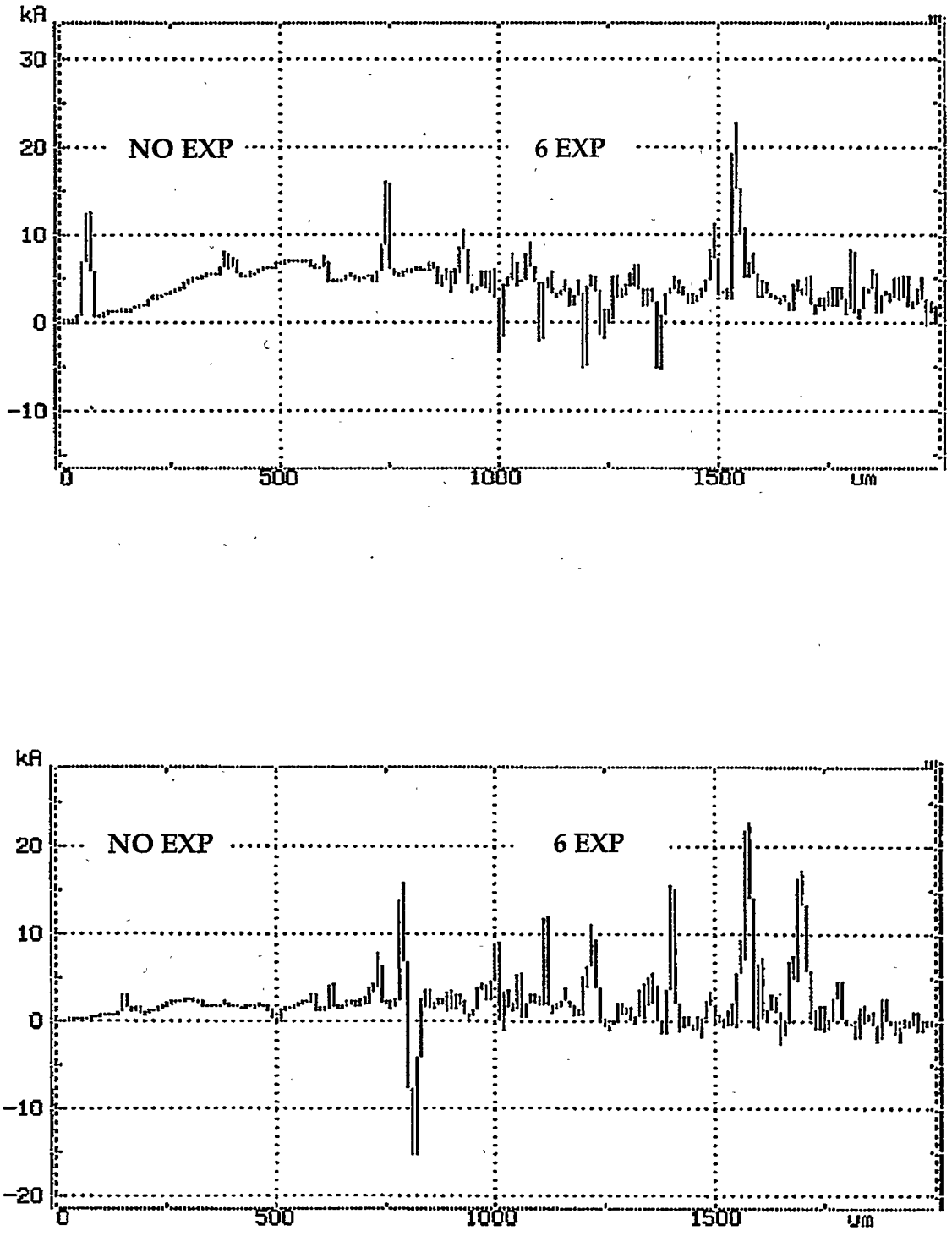

Figure 4-22: Profilometer scans of Reade boron carbide at highest x-ray fluence. No measureable ablation steps seen.

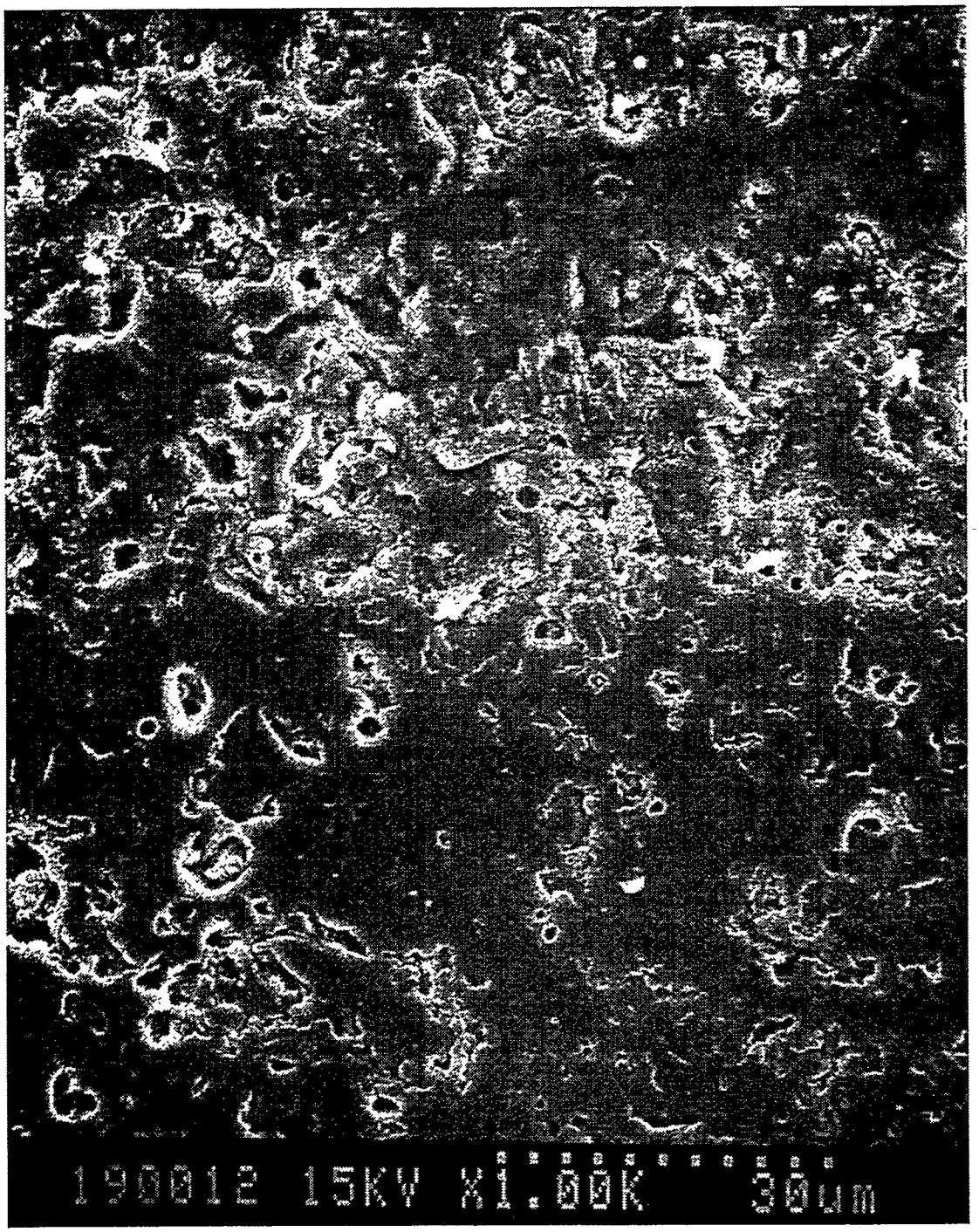

Figure 4-23: SEM image of plasma sprayed boron carbide from Y-12. Top half had single exposure to second highest fluence, while bottom was masked. Some of original polished surface was apparently flaked off by x-ray exposure.

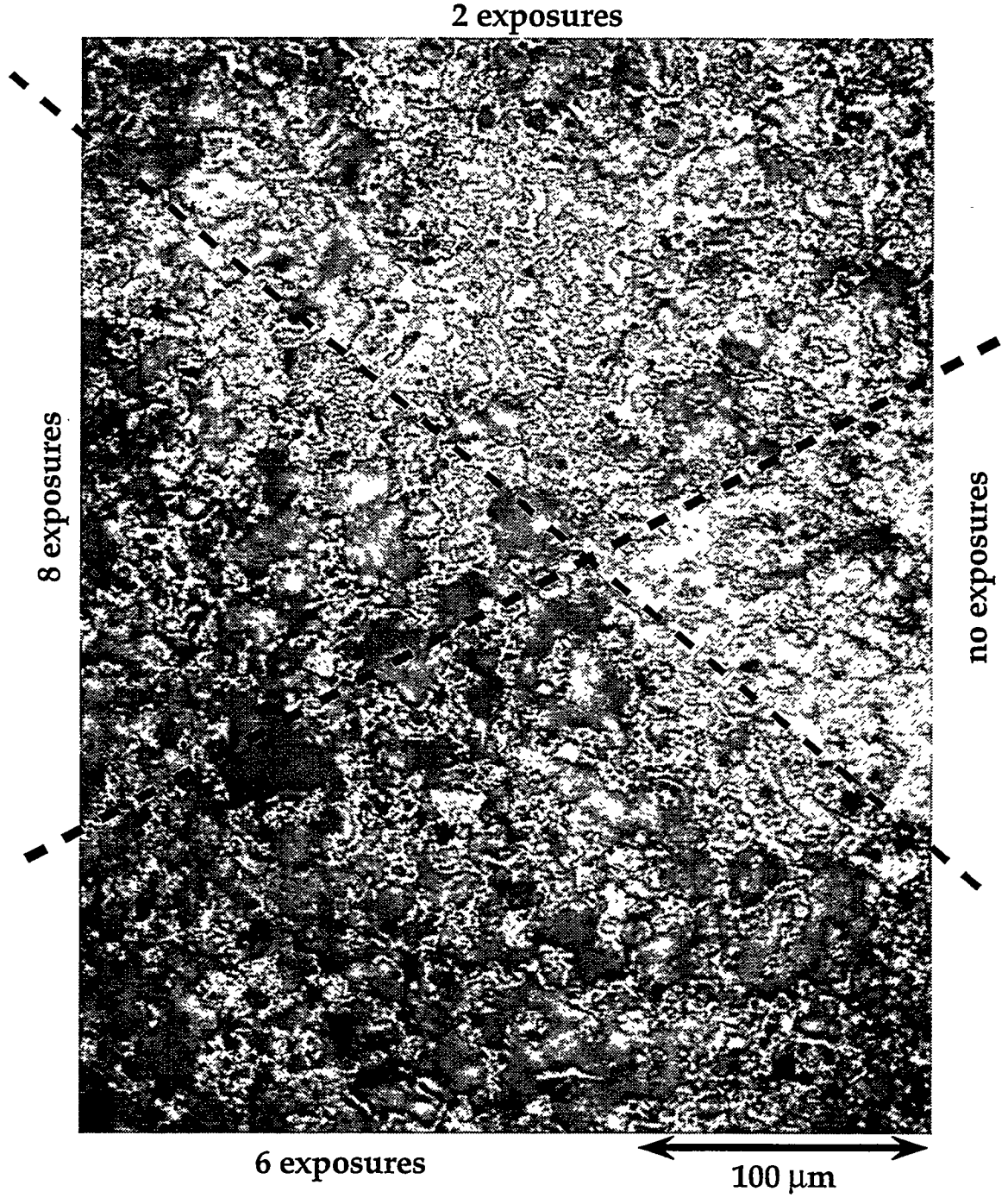

Figure 4-24: Plasma sprayed boron carbide (Y-12) from zero to eight exposures at highest fluence. Note removal of material below original surface in multiply-exposed regions.

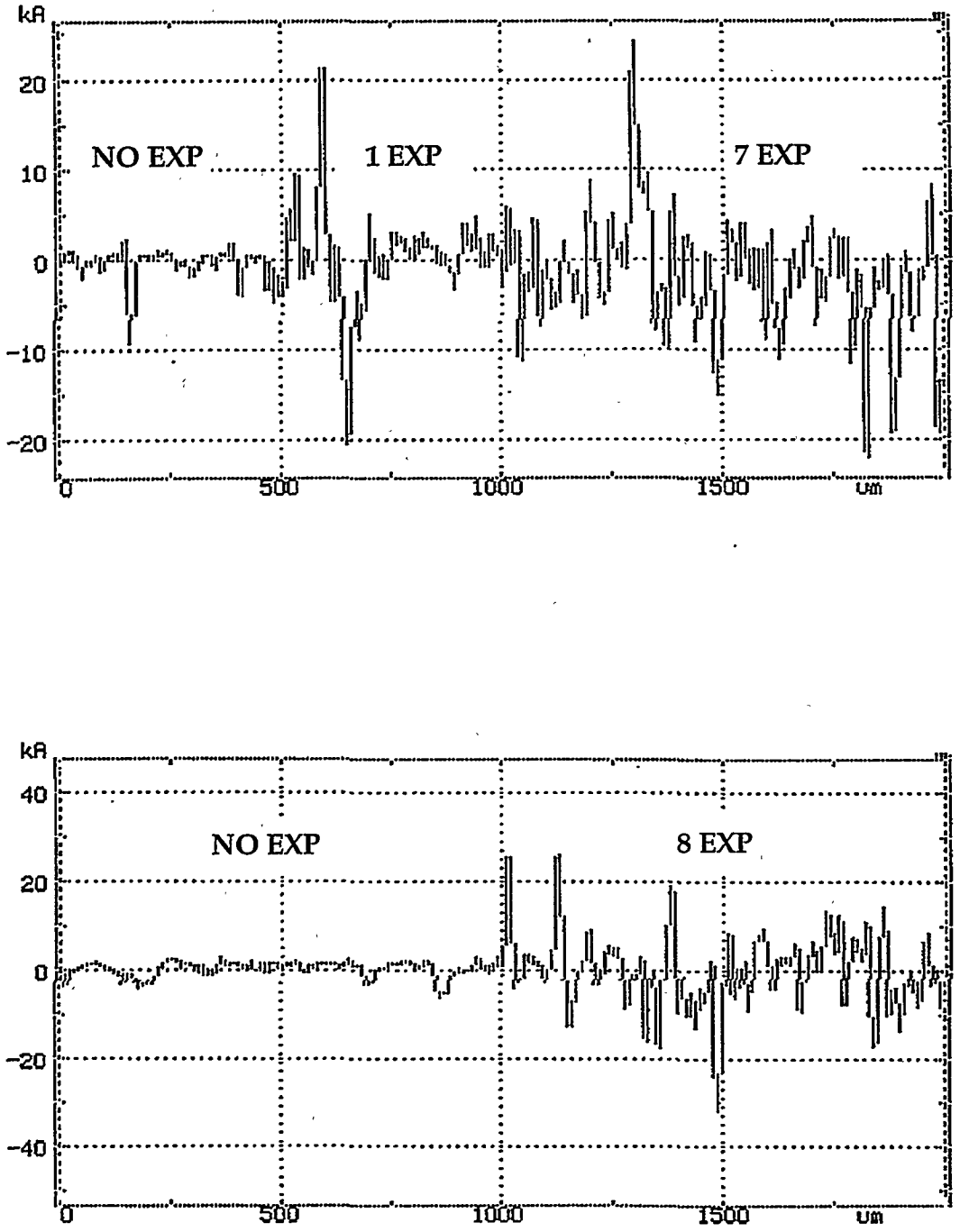

Figure 4-25: Profilometer scans of Y-12 boron carbide at highest x-ray fluence. Evidence of pits, but no uniform ablation steps.

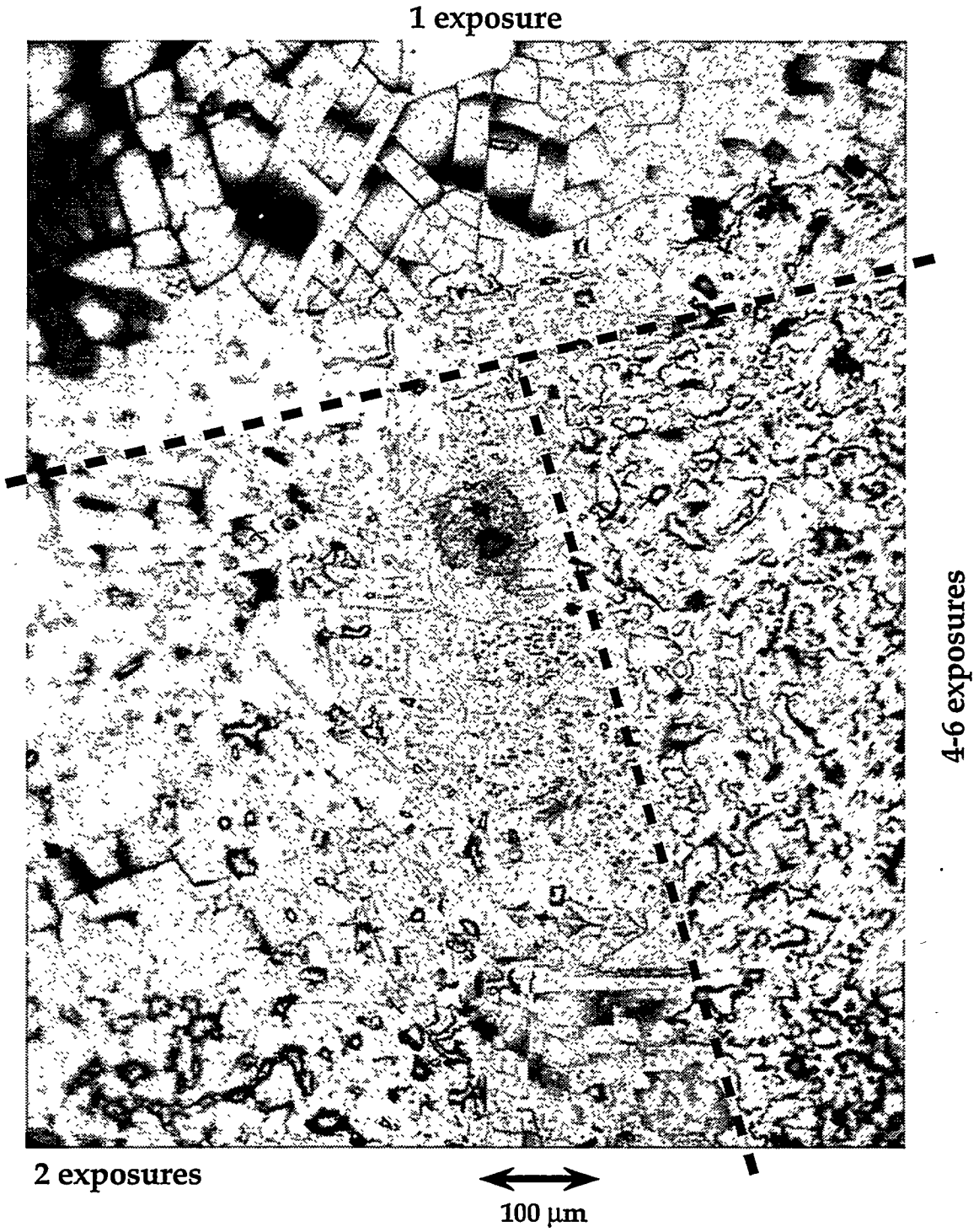

Figure 4-26: Boron exposed to the second highest fluence for 1, 2, & 6 shots. Initial large-area thermal stress cracks change to smaller, rougher areas after multiple shots.

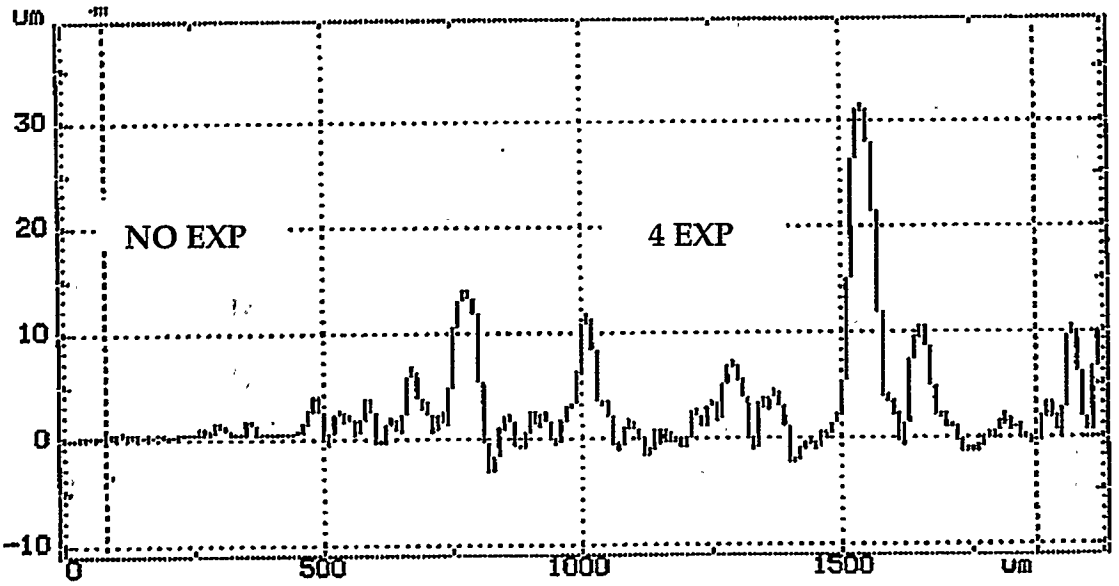

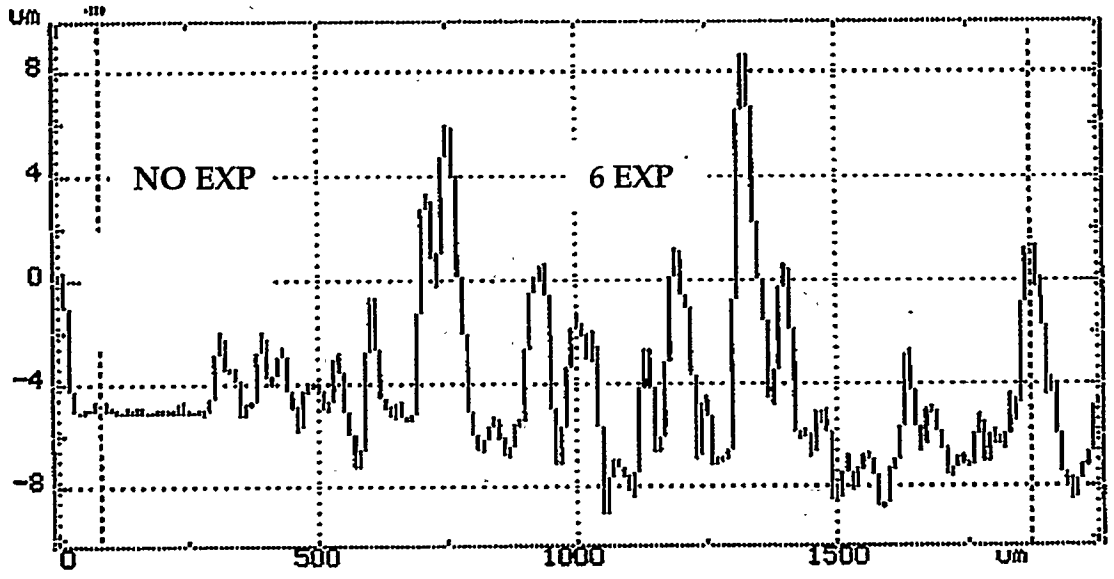

Figure 4-27: Profilometer scans of boron at highest x-ray fluence. Very rough surface with evidence of pits, but no uniform steps.

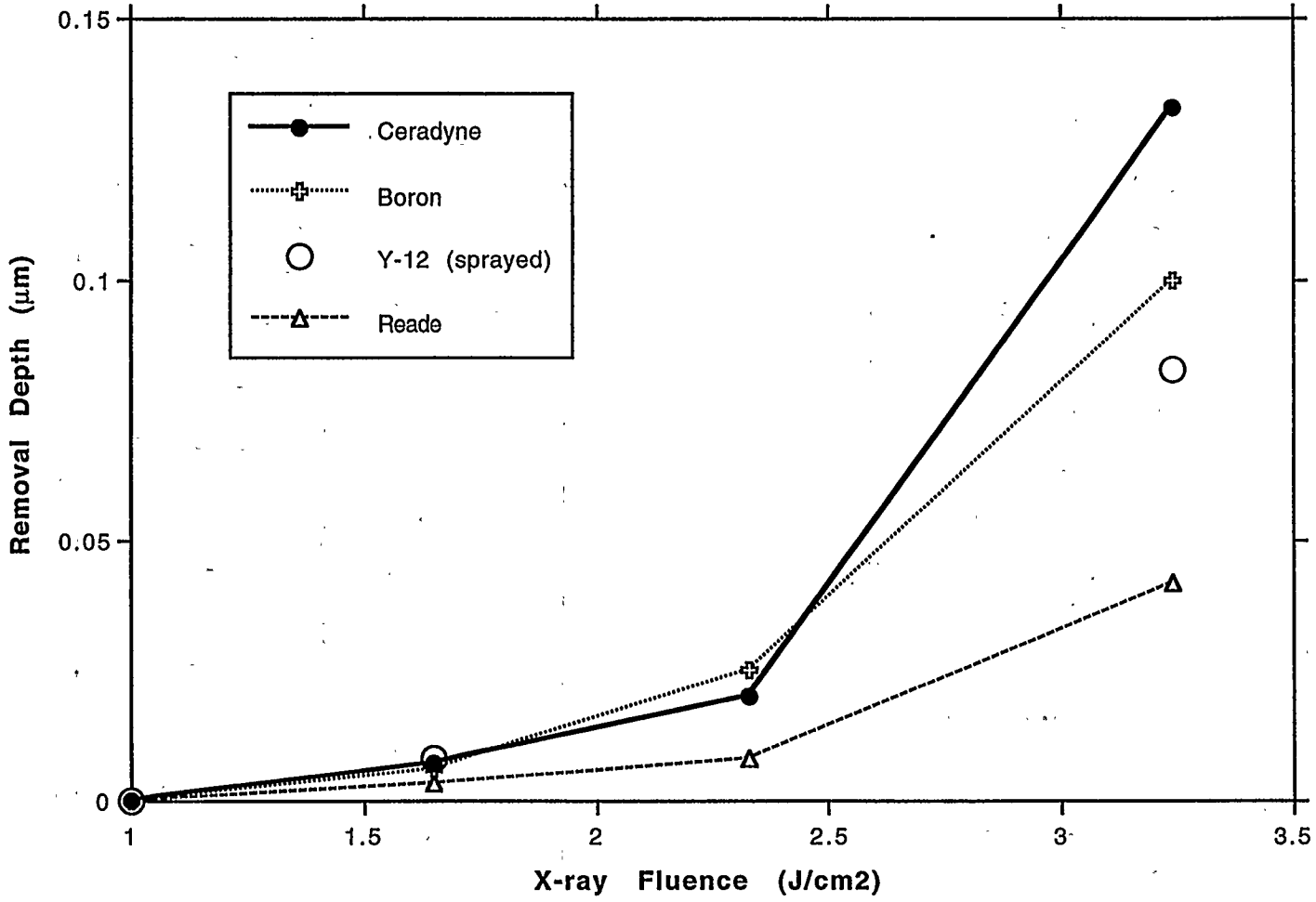

Figure 4-28: Approximate removal depths for boron carbide and boron for 200-250 eV blackbody x rays.

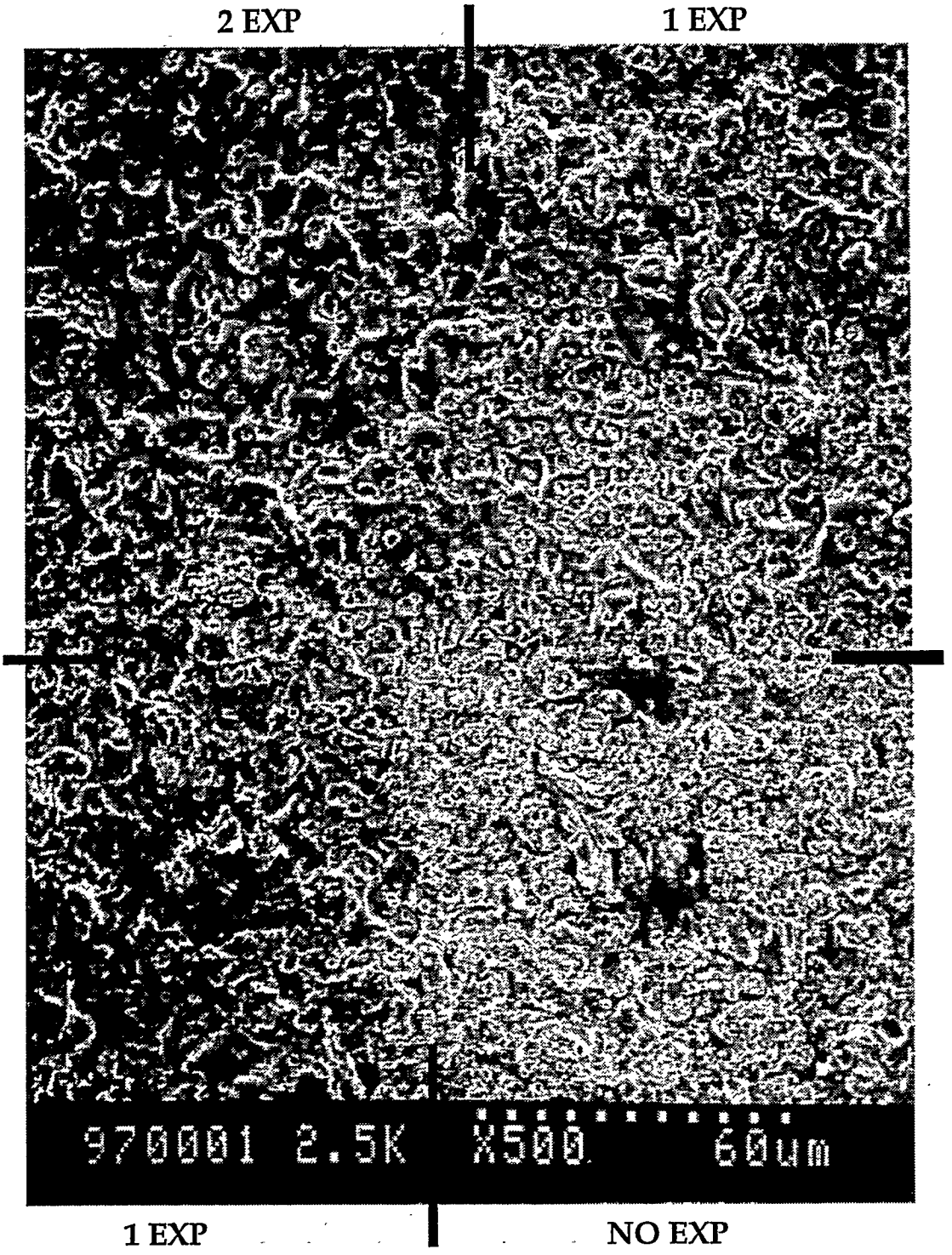

Figure 4-29: Plasma sprayed boron carbide from ProTeC, exposed to 1.5 J/cm2 x-ray fluence. The unexposed area is rough on scales of a few microns, while in exposed areas these features are melted out. Some thermal stress cracking is visible in exposed regions, particlularly under higher magnification.

Figure 4-30: Optical image of splash onto unexposed aluminum surface from single exposure region (top) at the highest x-ray fluence .

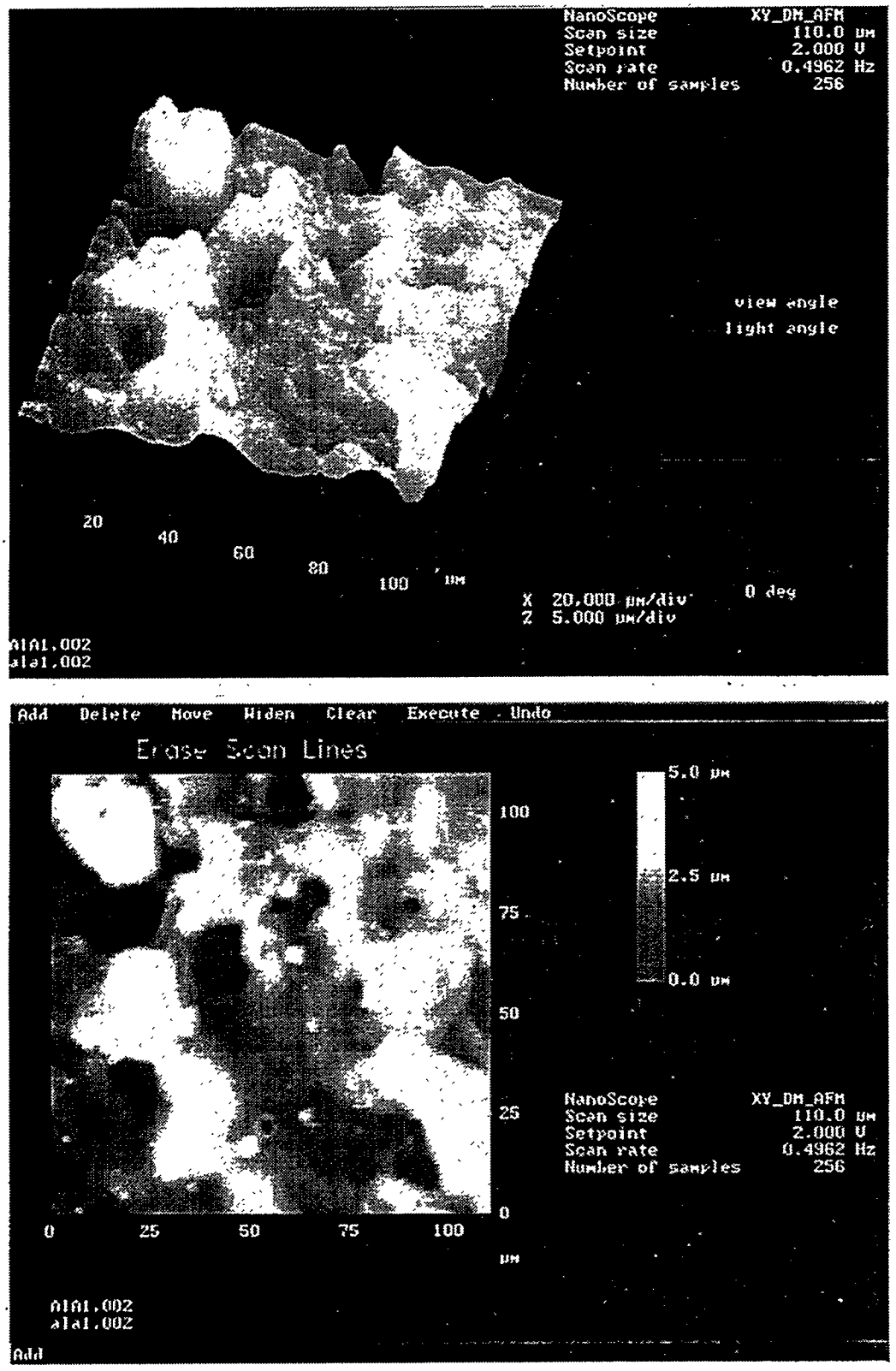

Figure 4-31: AFM image of single exposure of aluminum to 2.3 J/cm2. Note droplets visible in lower image.

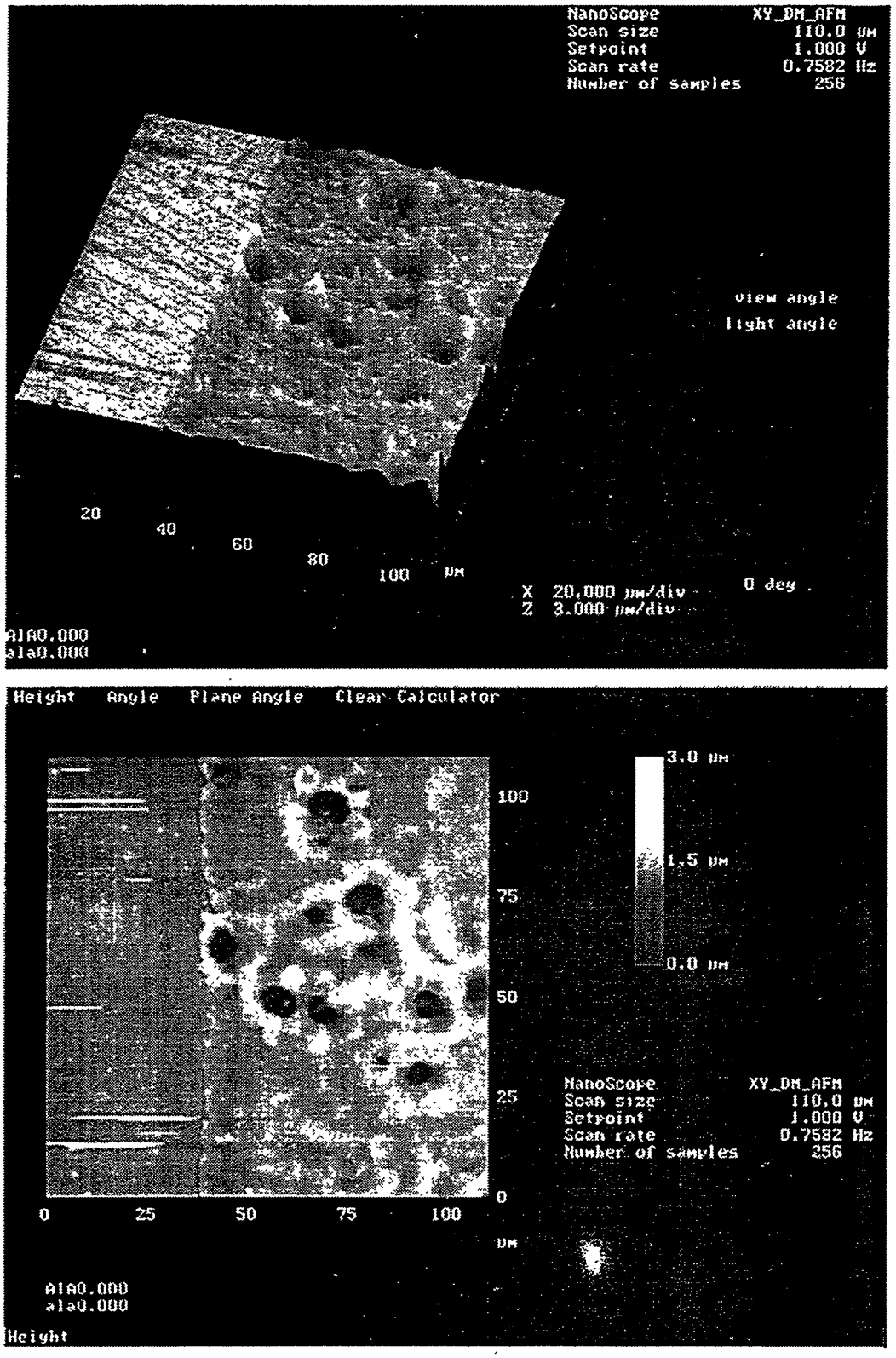

Figure 4-32: AFM image of presumed debris craters in aluminum single exposure region at lowest fluence (near 1.0 J/cm2).

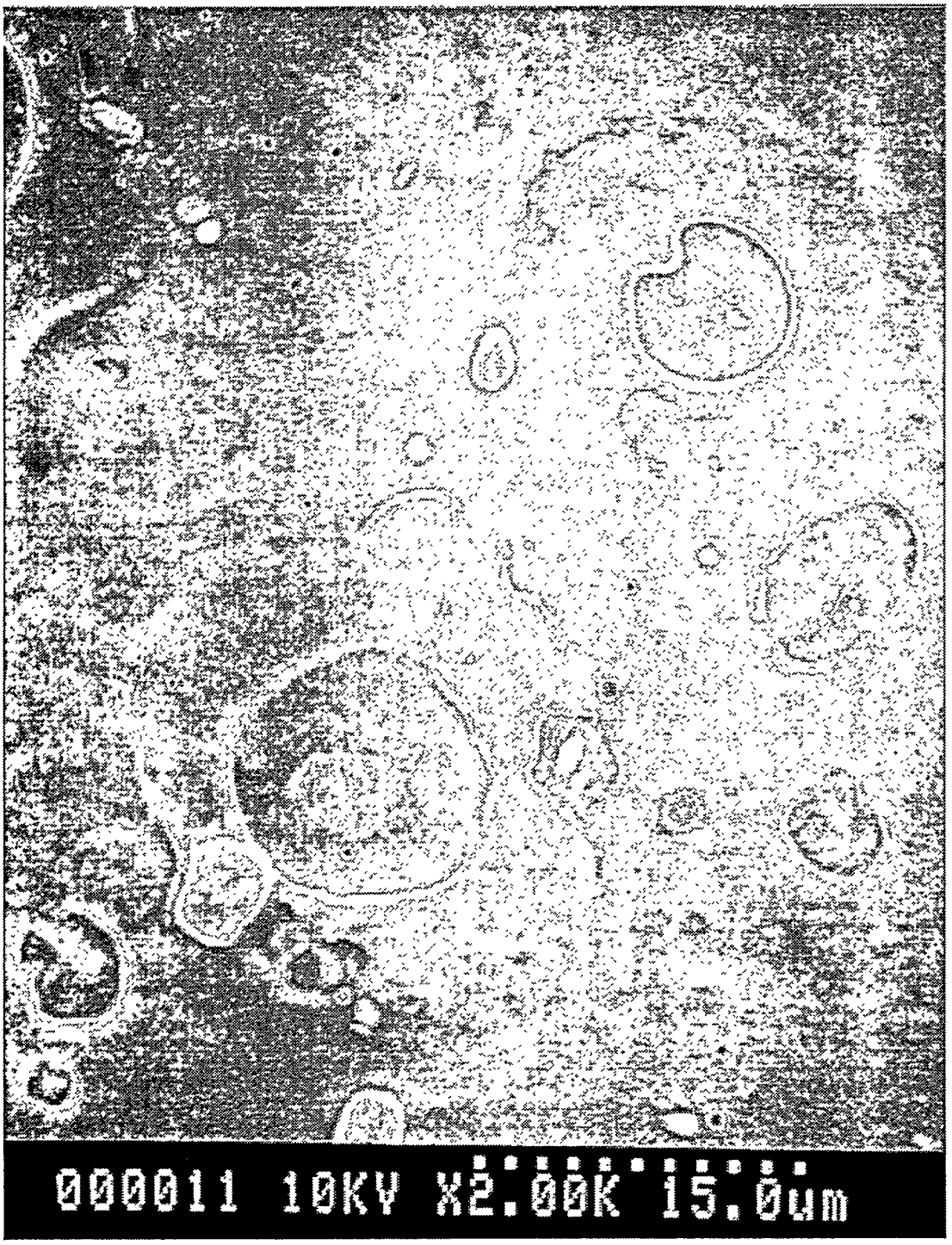

Figure 4-33: SEM image of debris crater from lowest fluence aluminum sample with single exposure.

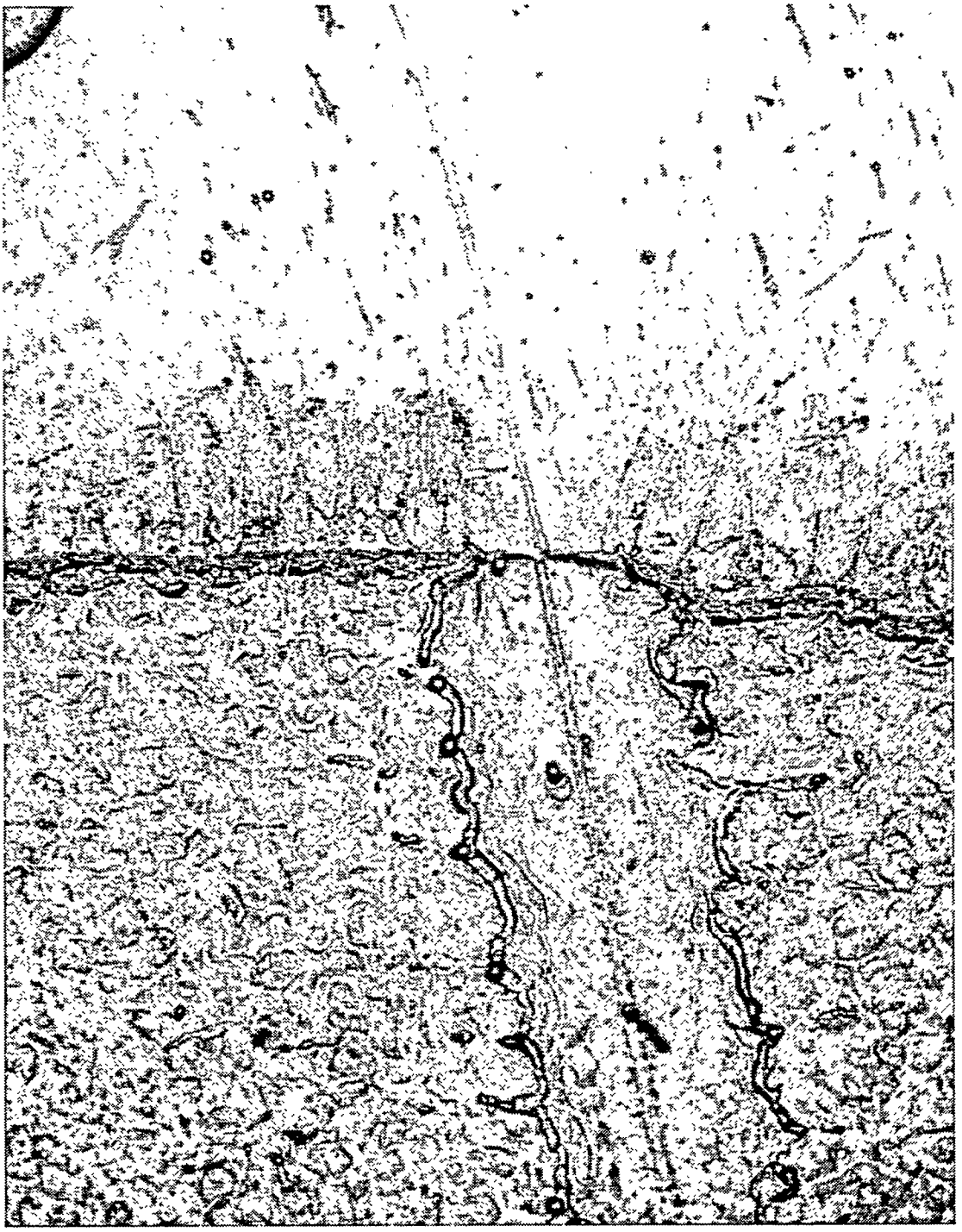

Figure 4-34: Fiber of glue across unexposed and single exposure regions at highest fluence. Note channel in aluminum melt layer cause by rapid vaporization of the glue. The channel is about 100 μm wide.

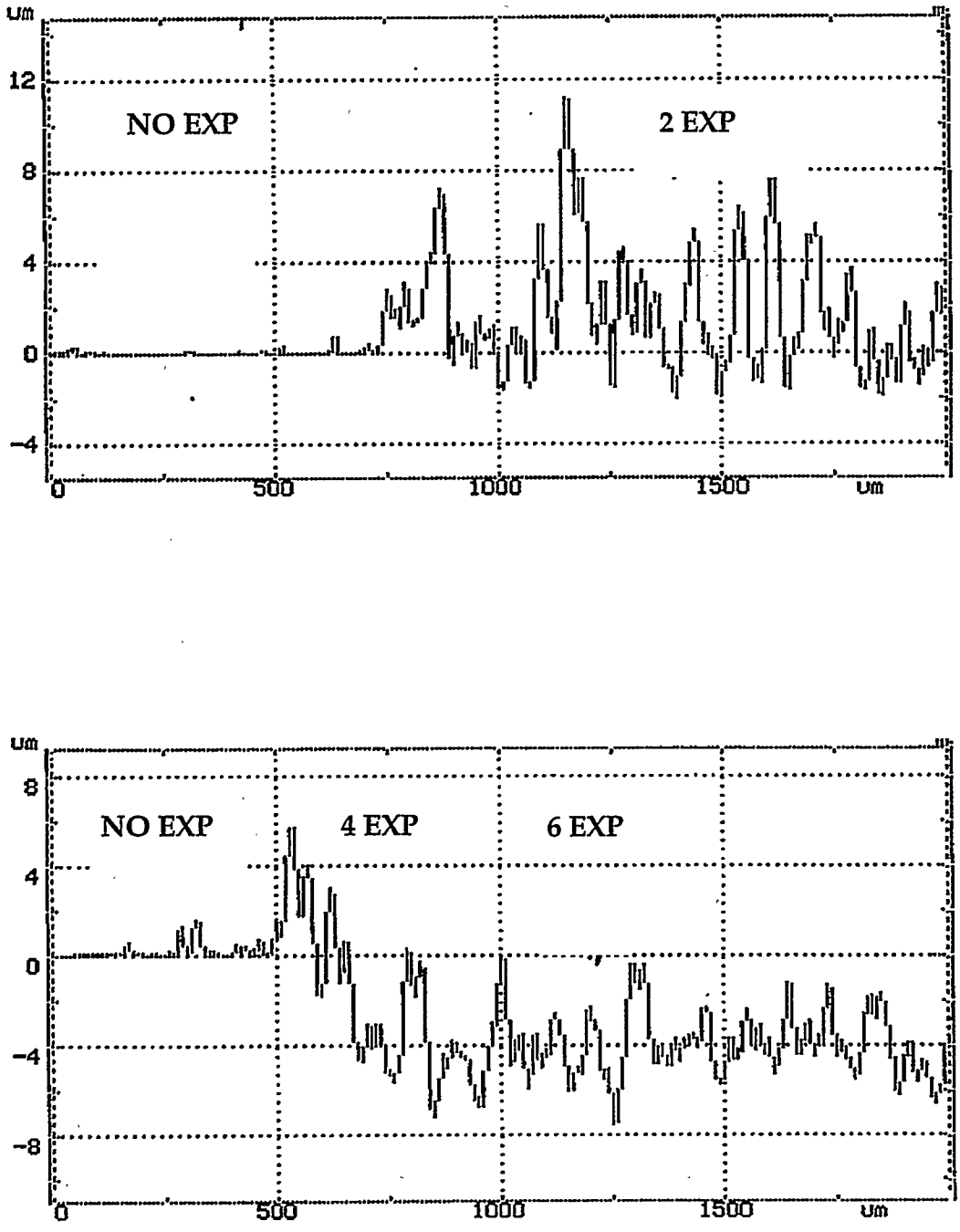

Figure 4-35: Profilometer scans of aluminum at highest fluence. Top scan shows roughening without ablation step after two shots. Bottom scan shows removal step after four and six shots.

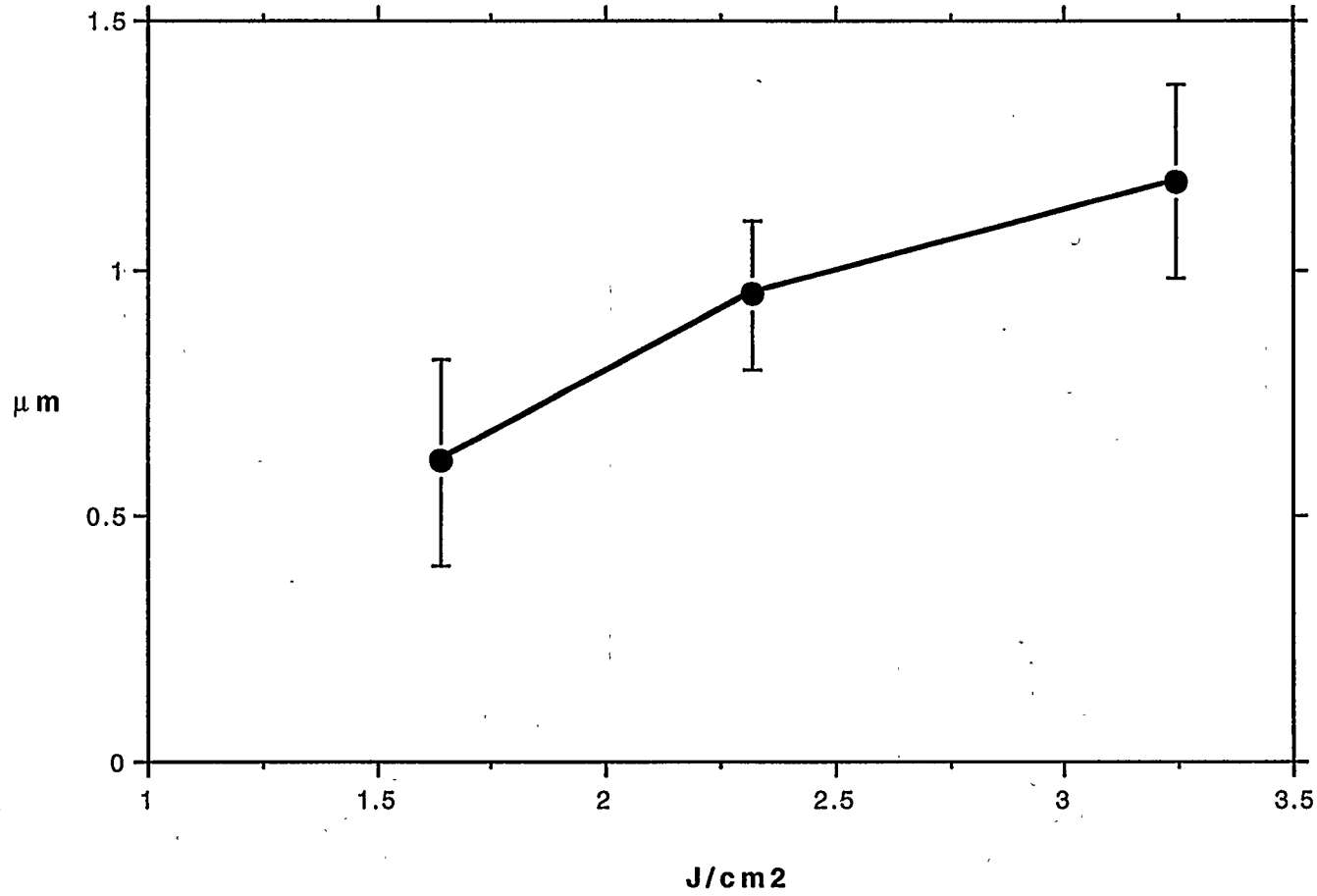

Figue 4-36: Measured removal depths in aluminum exposed to 200 eV blackbody x rays. No value is plotted at the lowest fluence (1.0 J/cm^2) because any removal depth was below the detection limit of about 0.1 μm/shot, given the 2 μm roughness seen on the profilometer scans.

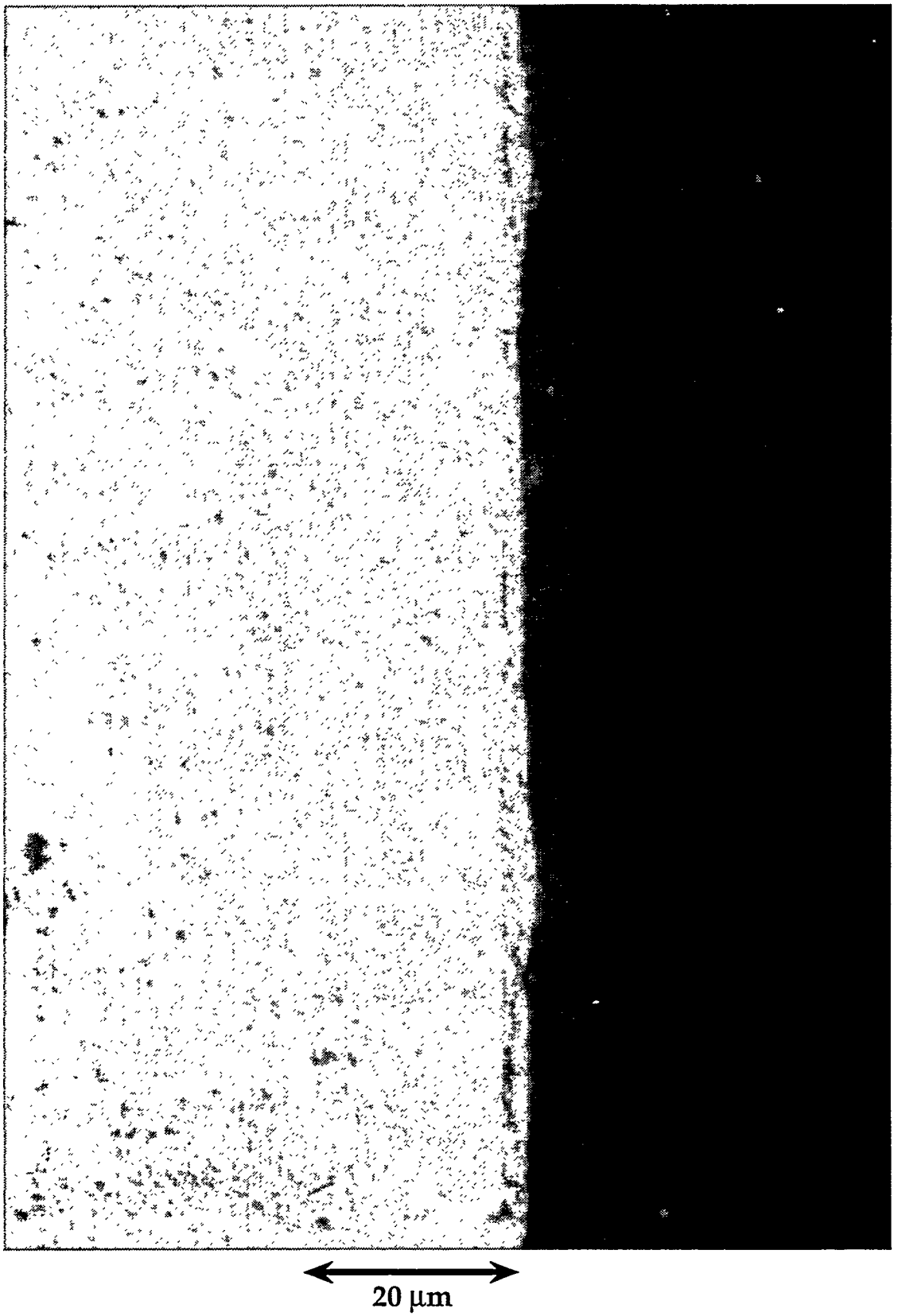

Figure 4-37: Resolidified aluminum melt layer after single shot at third highest fluence.

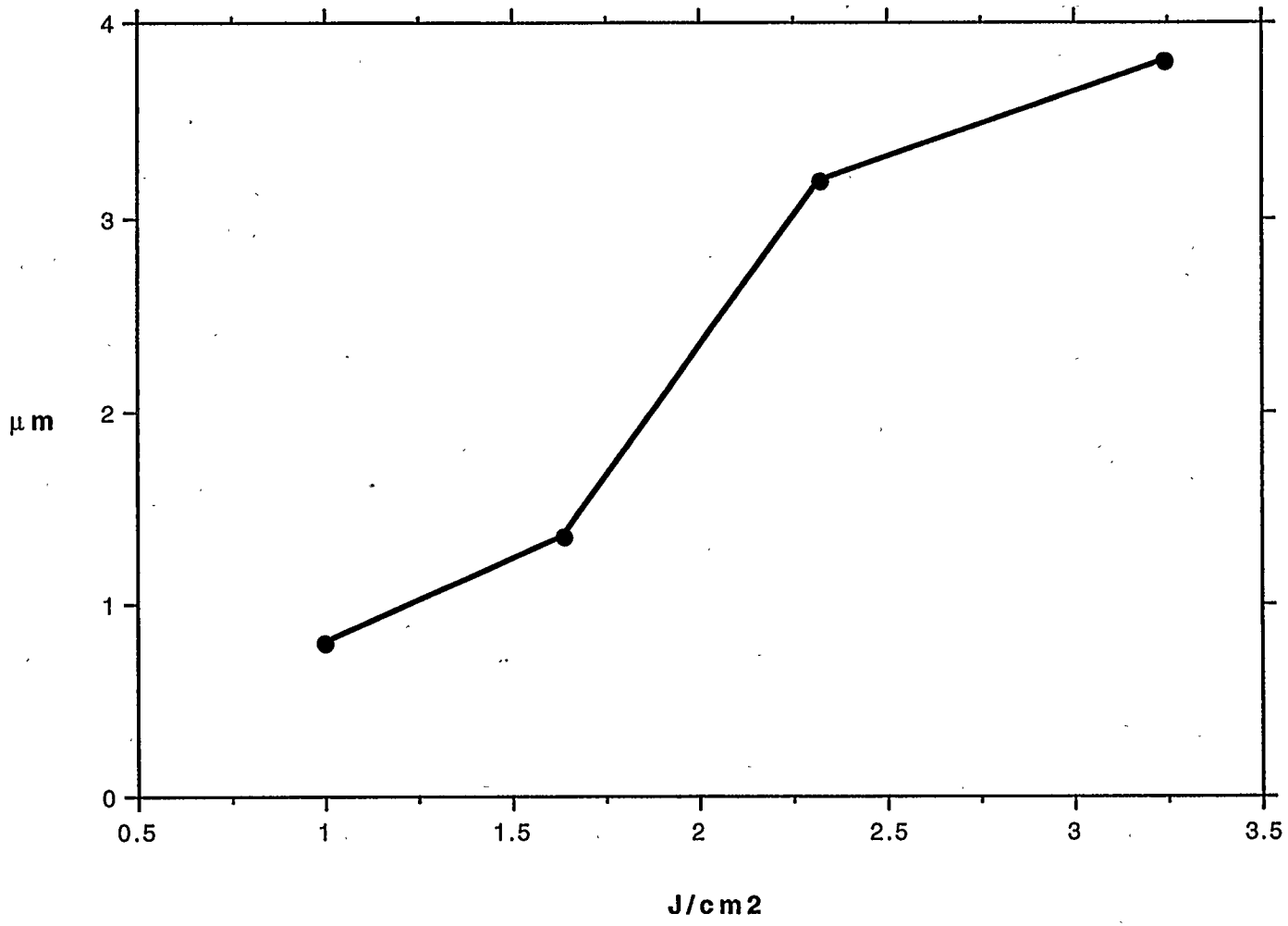

Figue 4-38: Thickness of resolidified aluminum melt layer after exposure to single shots of 200 eV blackbody x rays. Based on limited data from micrographs of metallographic sections.

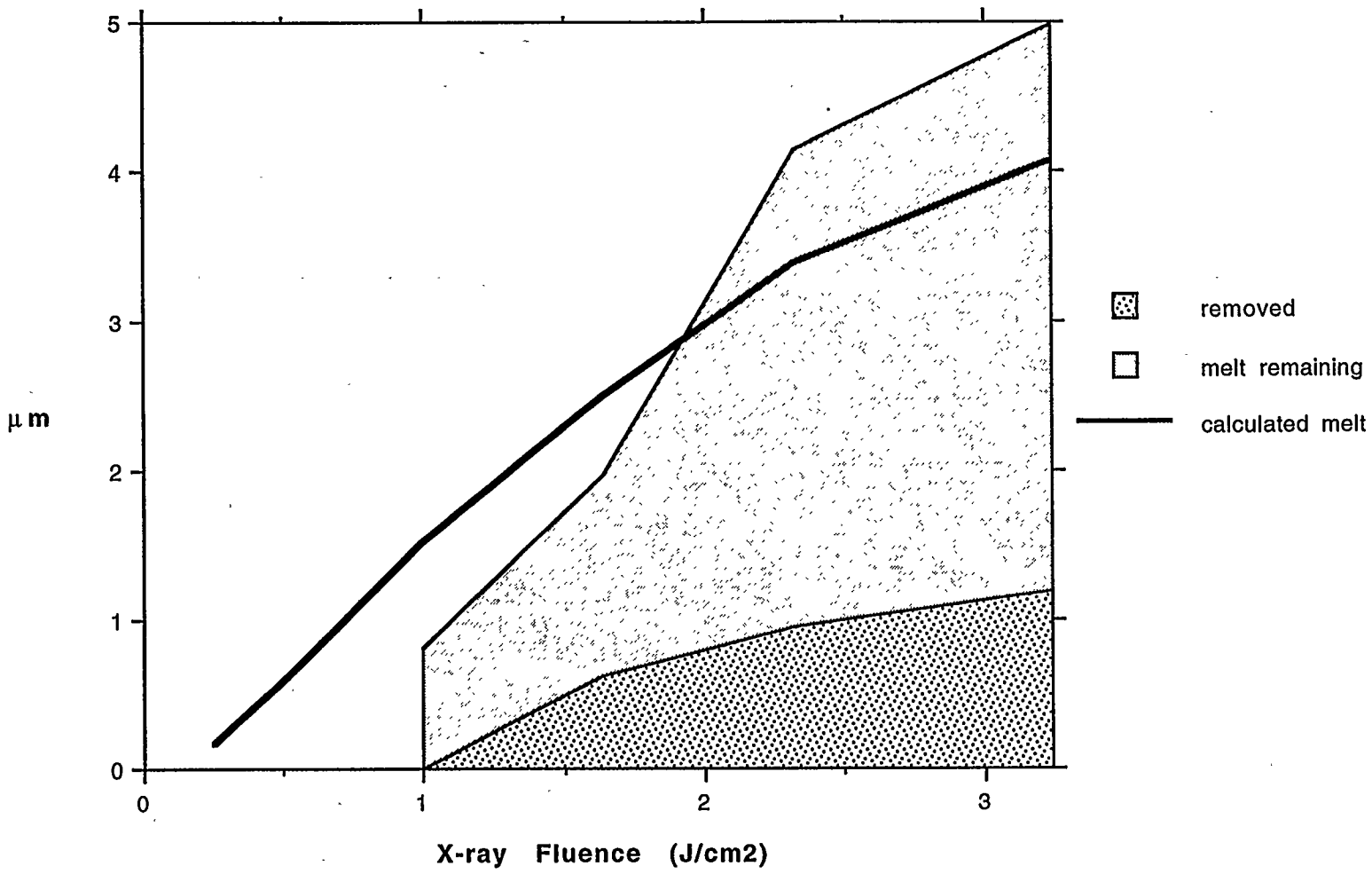

Figue 4-39: Sum of measured resolidified aluminum melt layer thicknesses and removal depths compared to predicted total melt depth. Agreement is reasonably good, considering the large scatter in the measured data.

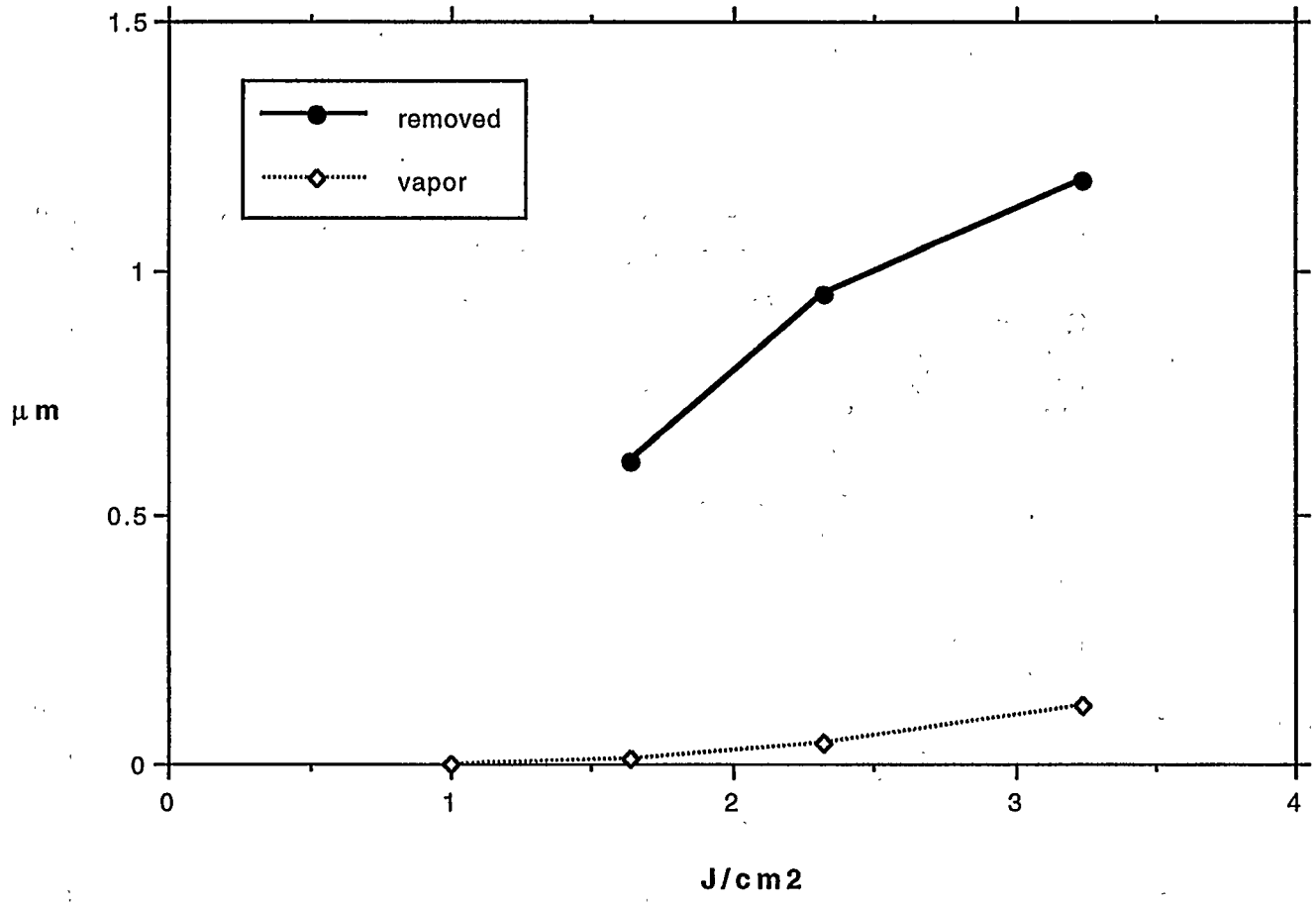

Figue 4-40: Measured aluminum removal depth compared to amount predicted for surface vaporization only. The increased vaporizing area due to the surface roughness might increase the vapor contribution to removal beyond the 1-D value shown here.

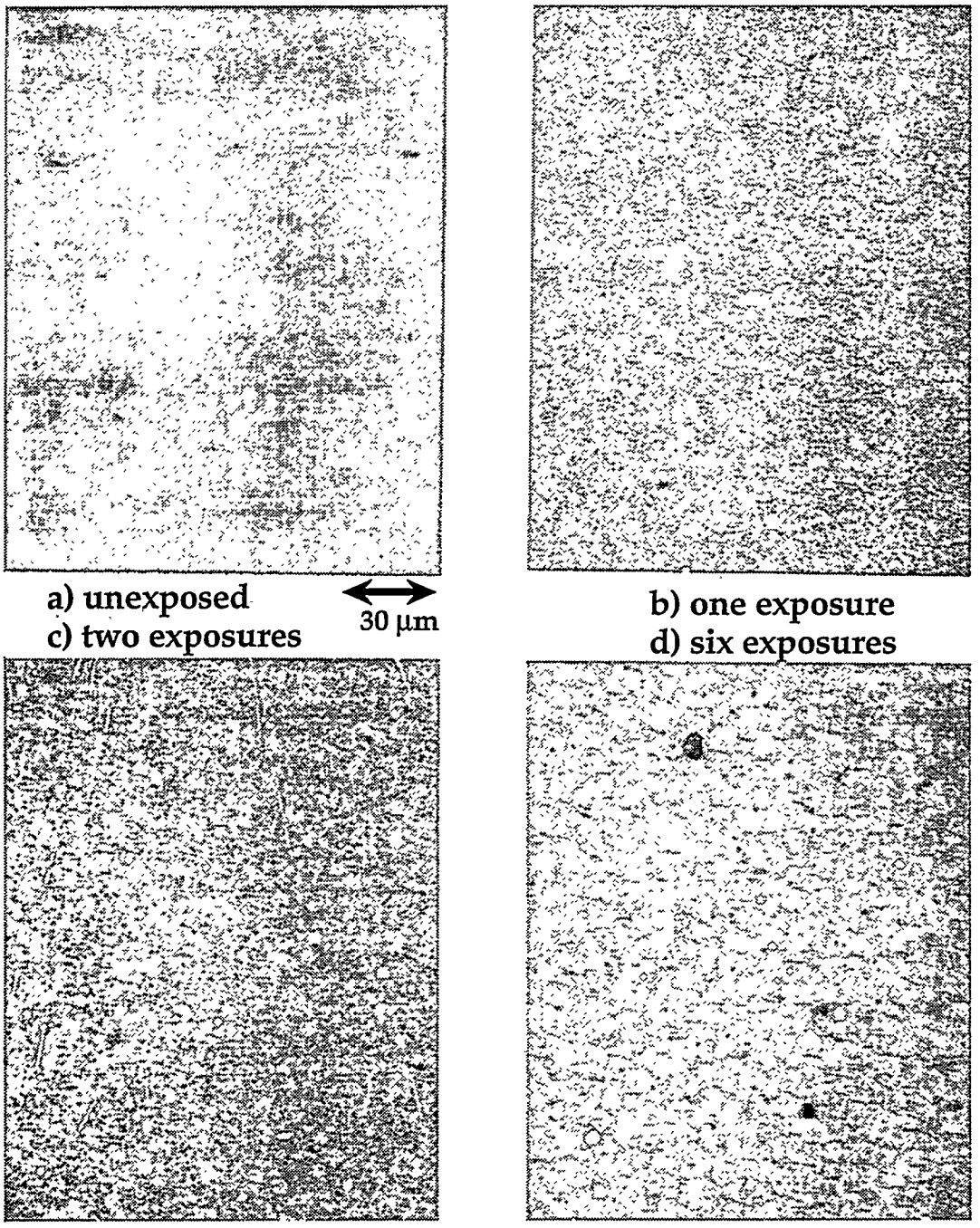

Figure 4-41: Sapphire at third highest fluence showing evolution of bubbles and cracks.

a) two exposure region

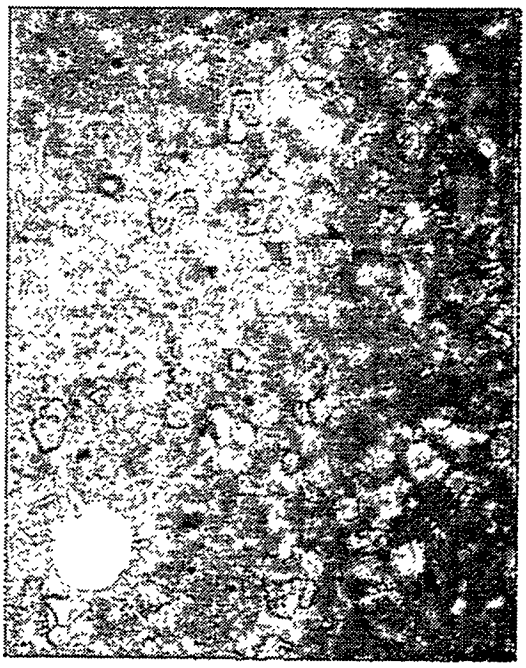

b) same as a), but with different focus to show spall removal

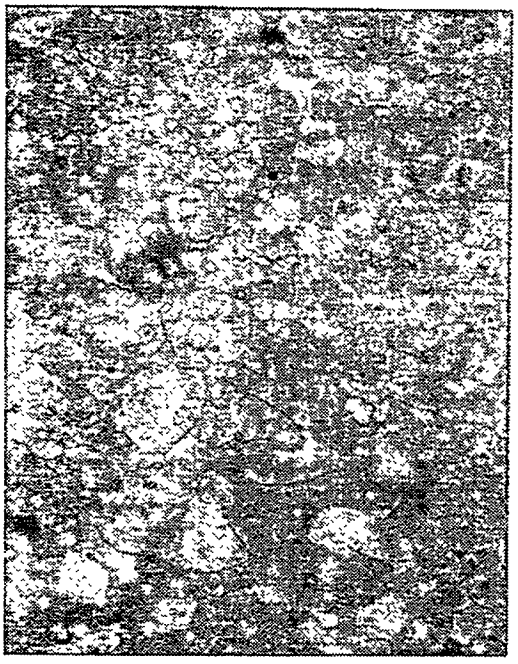

c) six exposure region

30 μm

Figure 4-42: Hot pressed alumina at highest fluence. Note small bubbles in a) growing to fewer larger bubbles in c). Evidence of spall of thermally shocked material is seen in b).

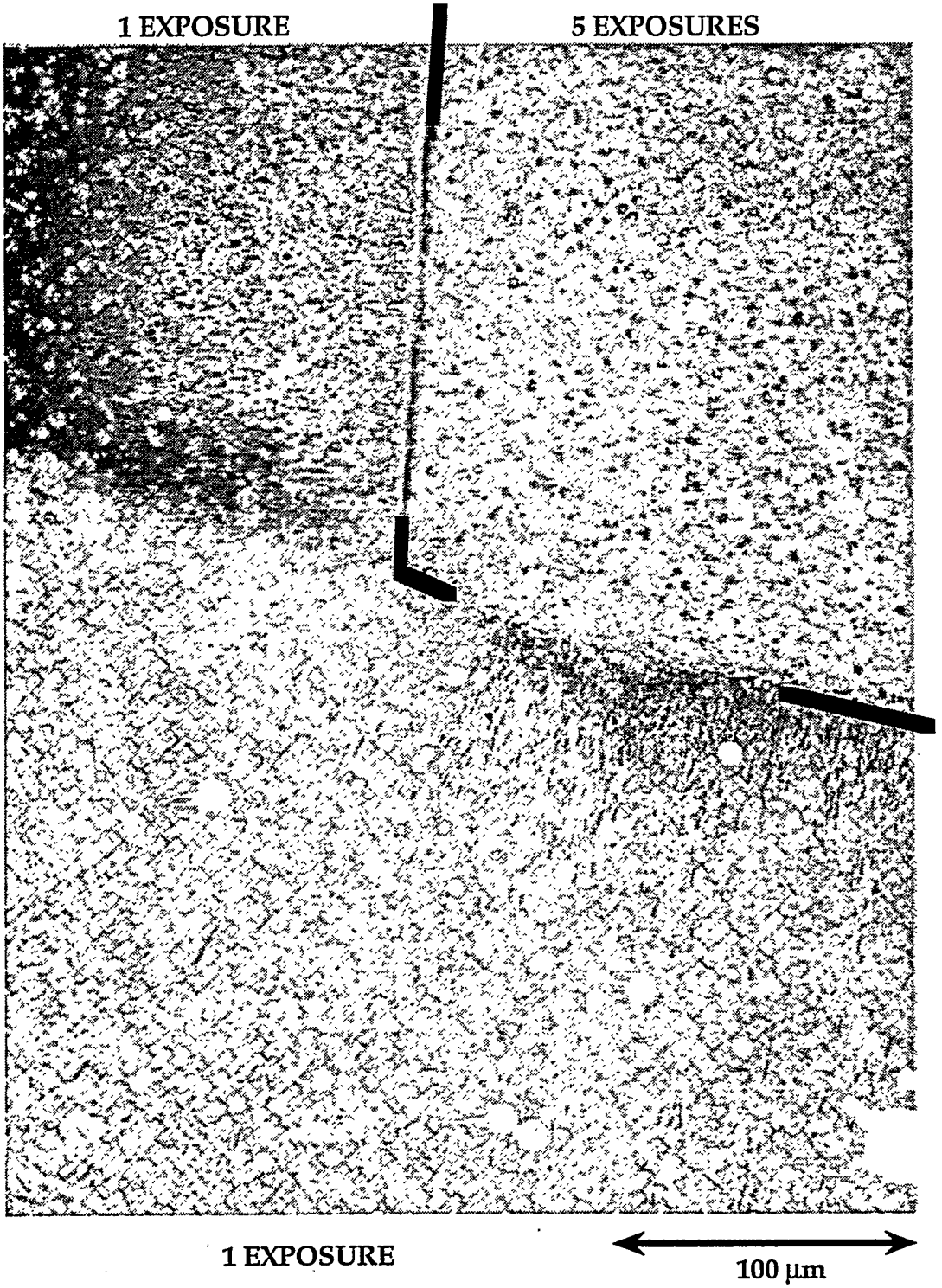

Figure 4-43: Sapphire at highest fluence showing thermal stress crack orientations. They are aligned with crystal after one shot and random after five exposures.

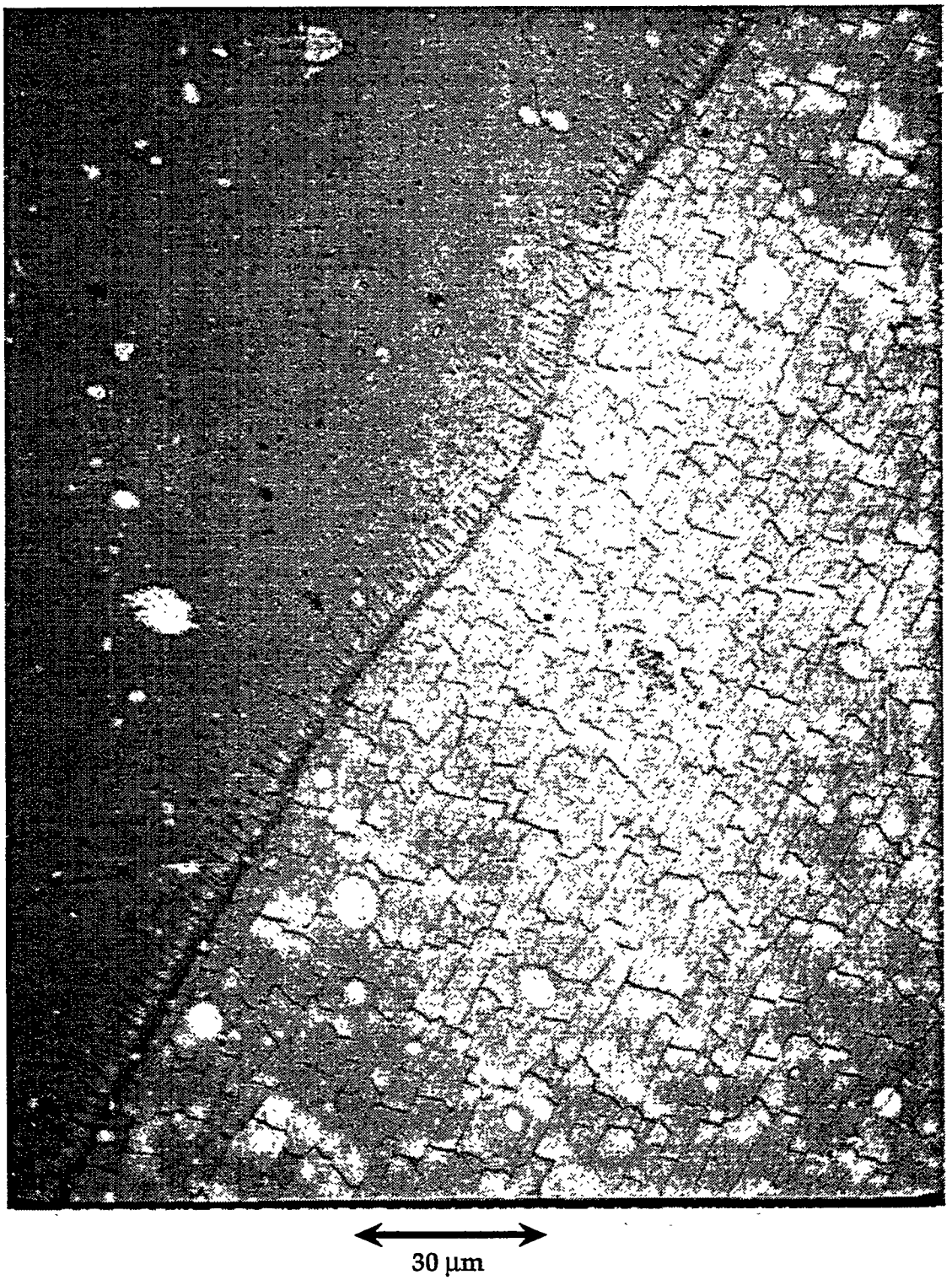

Figure 4-44: Splash on sapphire onto unexposed area from region of single exposure at second highest fluence.

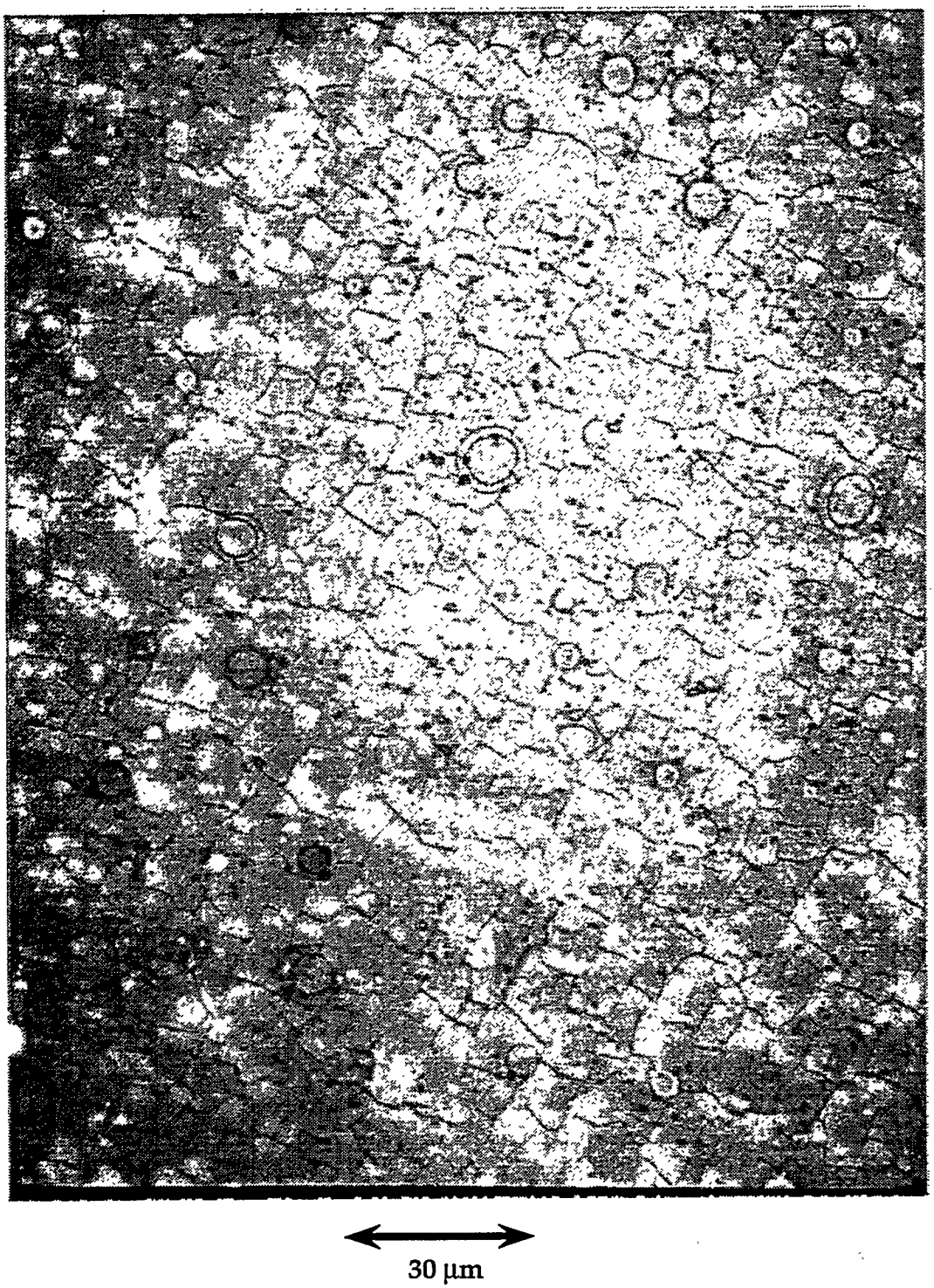

Figure 4-45: Possible impact craters on surface of sapphire. Region had two shots at second highest x-ray fluence.

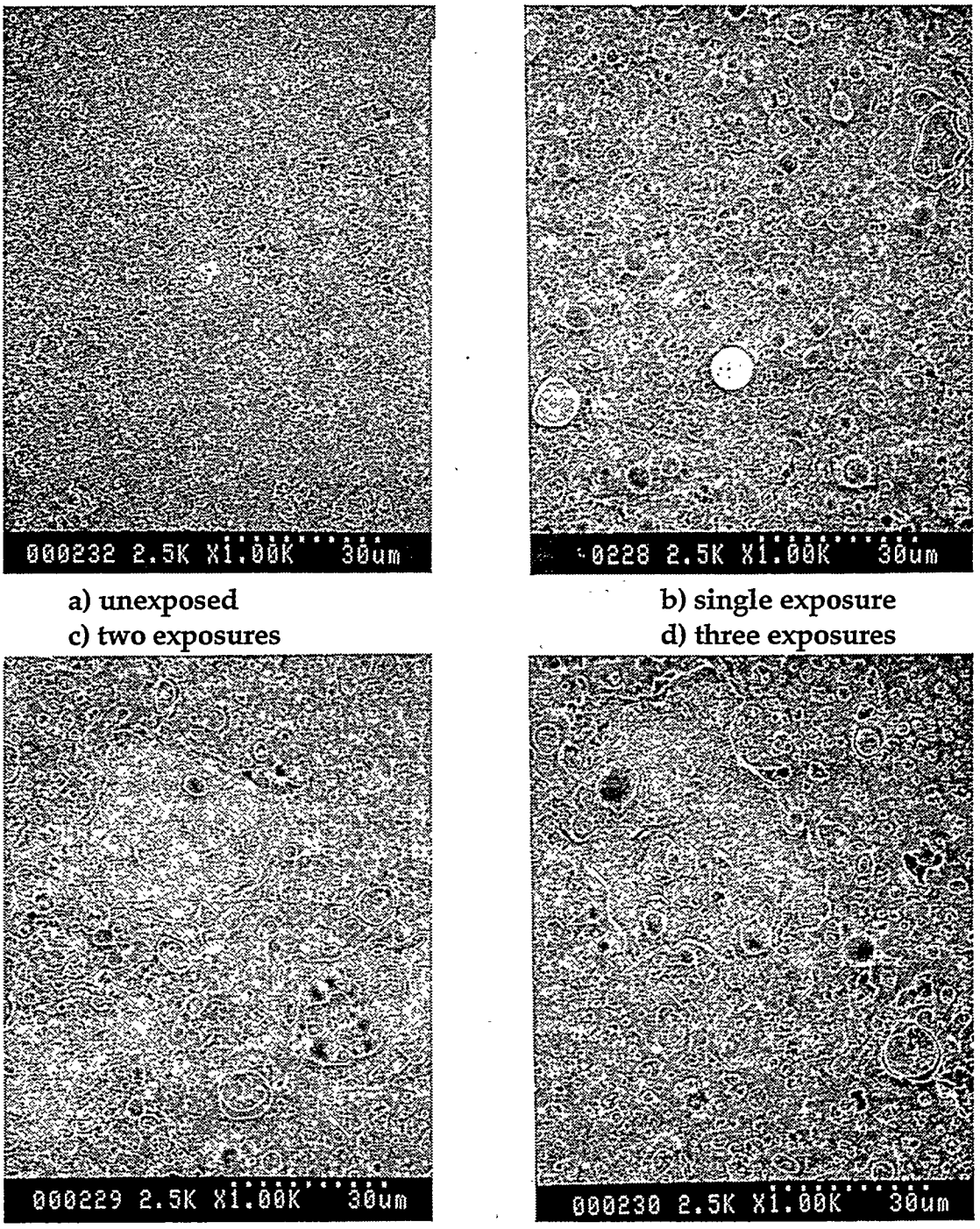

a) unexposed
b) single exposure
c) two exposures
d) three exposures

Figure 4-46: SEM images of first alumina thermal spray sample, exposed to 3.2 J/cm² x-ray fluence. Shows progression of damage for multiple shots.

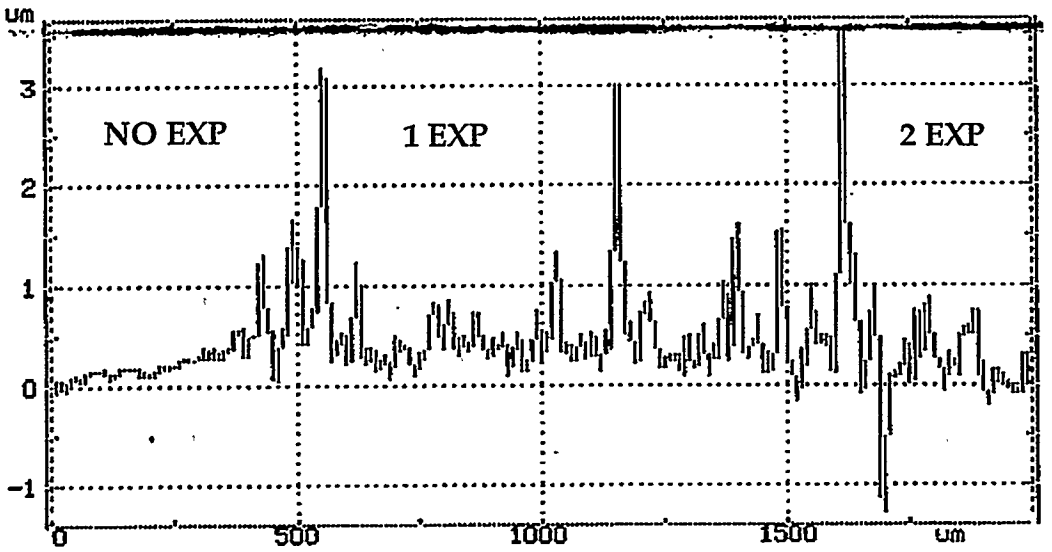

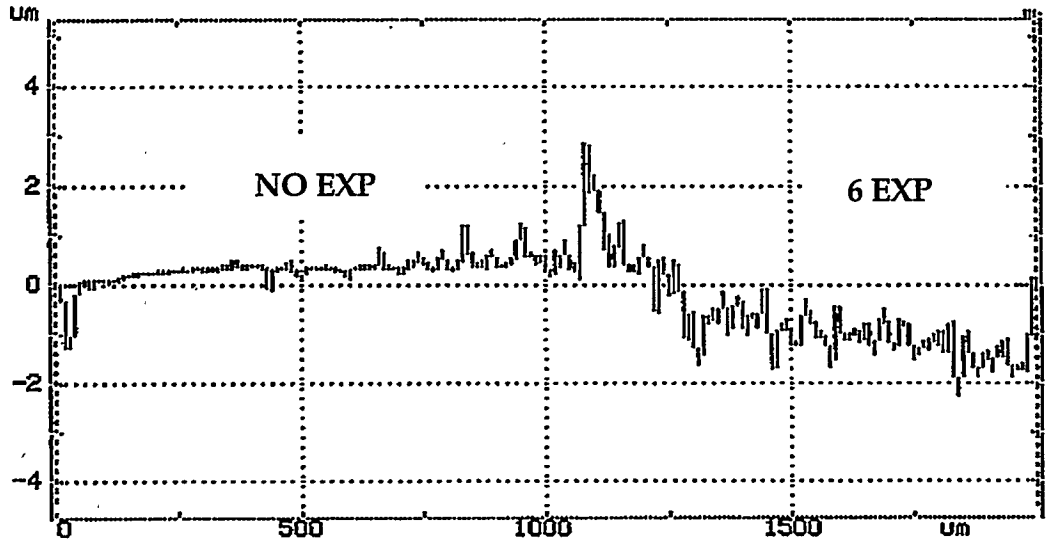

Figure 4-47a & b: Profilometer scans of hot pressed alumina at second highest x-ray fluence. Roughening without measurable removal is seen after one exposure.

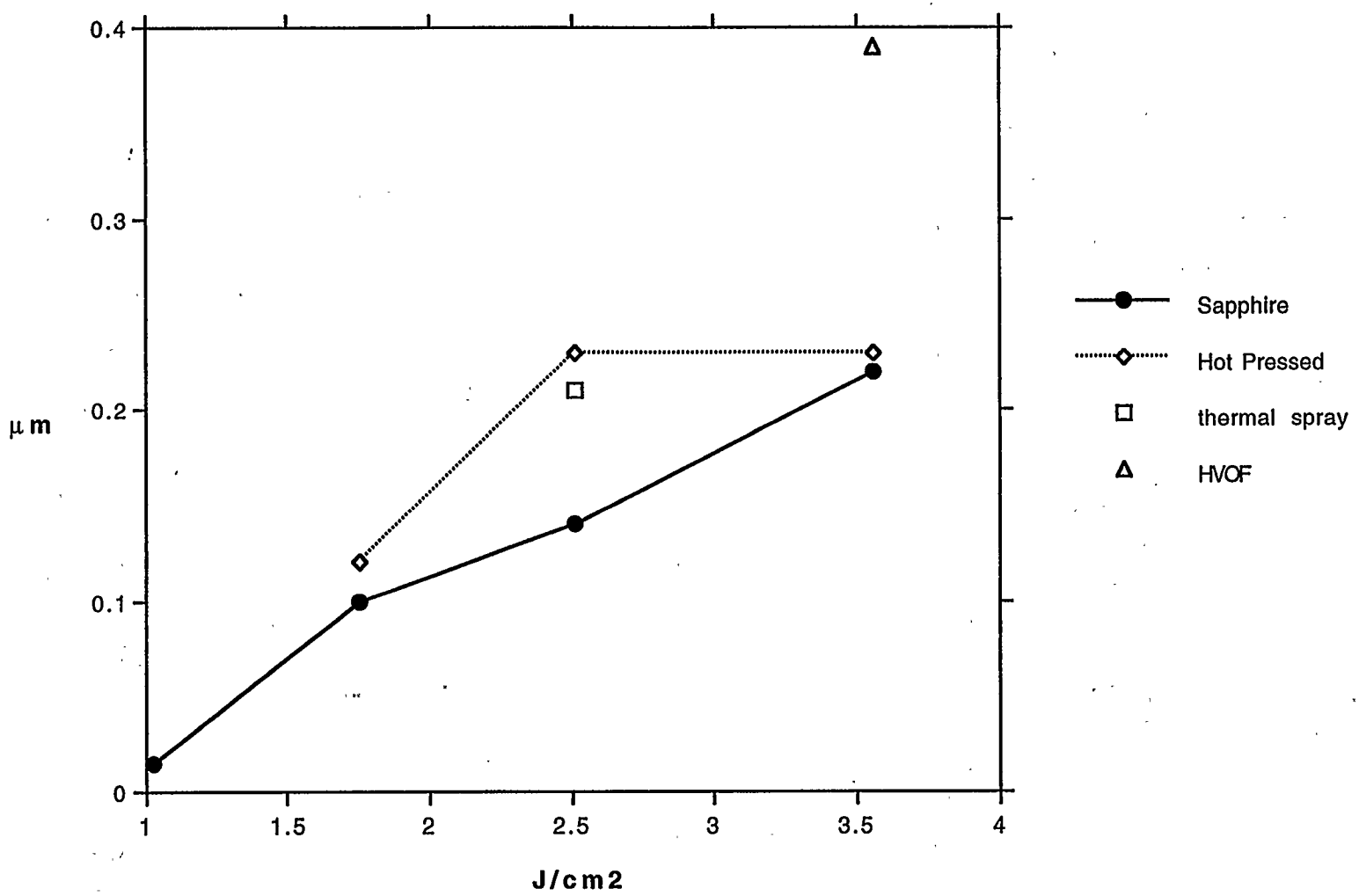

Figure 4-48: Measured removal depths per shot for alumina. X-ray source was 200 eV blackbody with a 2.2 ns pulse length.

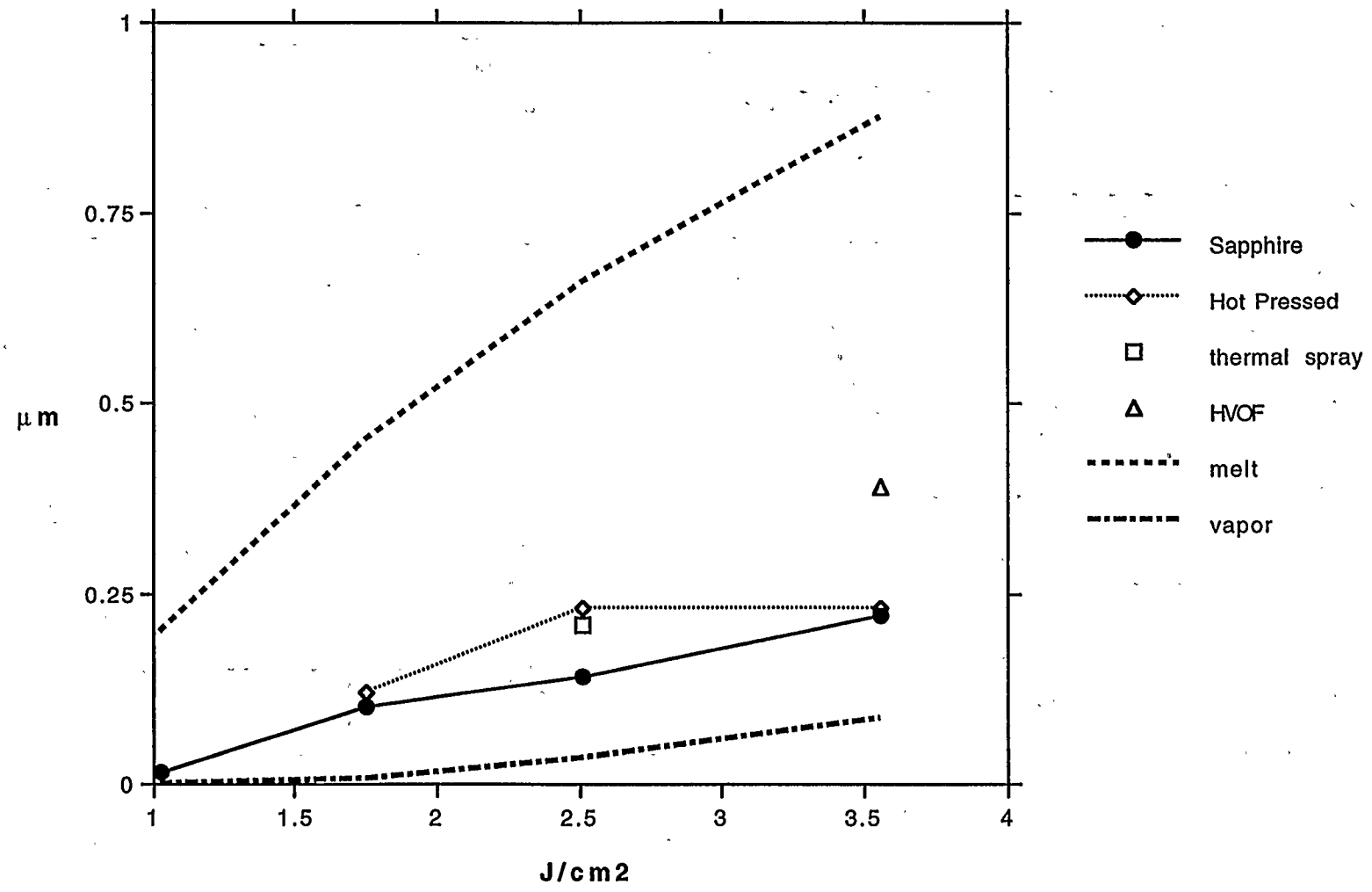

Figure 4-49: Measured removal depths for aluminum oxide compared to predicted surface vaporization and melt depths.

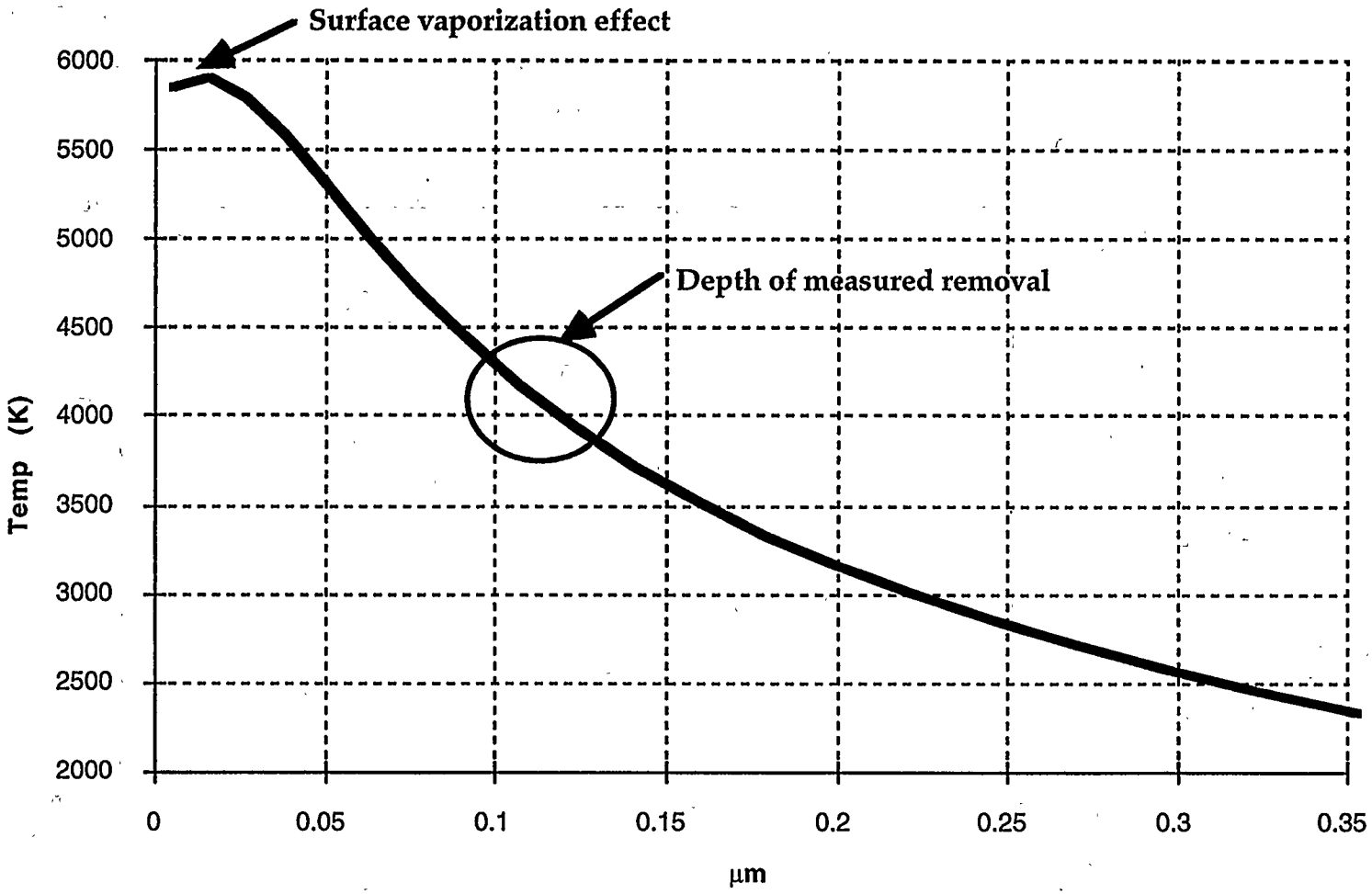

Figure 4-50: Peak temperature profile in alumina for 1.75 J/cm^2, 200 eV blackbody, 2.2 ns pulse. Measured material removal at these conditions was 0.1-0.12 μm, where peak temperature was about 4000 K. Surface vaporization causes slight temperature dip at front surface. Melt temperature is 2327 K.

5. Modeling of Experimental Results

5.1 Introduction

The experimental data from the previous chapter are very important as new information in material removal by x-rays, because only limited data is available for response under any conditions. The experiments gain additional value by serving to benchmark model predictions of material response to x rays of different fluences, spectra, and pulse lengths. One aspect of the modeling is to investigate the contributions of various removal mechanisms to the total ablation depth of a material. This is guided by the microscopy work of the previous chapter. Chapter 4 used the ABLATOR code to a limited extent in this way, particularly for estimating the contribution of surface vaporization. It is only through an understanding of the dominant ablation mechanisms that the models can extend the Nova data to other x-ray conditions. The second aspect of the modeling is to match, as well as possible, the total removal depths measured from the experiments. This benchmarking of the code gives confidence that predictions for other conditions will be accurate.

5.2 Fused Silica Modeling

5.2.1 Nova Experiments on Fused Silica

Four fused silica disks were exposed to x rays in a series of four ride-along Nova shots on December 18, 1995. X-ray fluences ranged from 1.0 to 3.2 J/cm^2, with a 250-eV peak blackbody spectrum in a short (1 ns) pulse. The samples were partially masked with tantalum foils to give areas with different numbers of shots on each sample. The experiment diagnostics were profilometer scans and optical microscopy performed after the shots. These indicated that exposed surfaces were relatively flat, with well-defined steps

between areas with different numbers of exposures. It seems clear that surface vaporization was the dominant process, rather than spallation of solid or liquid material. Profilometer scans were able to give accurate measurements of removal depths, even down to the lowest two fluences, because of the uniformity of removal. Figure 4-10 shows material removal depths on a per shot basis as a function of x-ray fluence. The error bars indicate the variations in the measured depths across various steps on the sample surfaces. For a more complete discussion of the experiments, see section 4.3.2.

5.2.2 Model Description - Fused Silica specifics

The fused silica response modeling relies on the use of many material properties to determine the energy deposition, heat transfer, hydrodynamics, and vaporization behavior. X-ray energy deposition uses cold cross sections for silicon and oxygen tabulated in Cullen et al[1]. These were combined on a weight-fraction basis for the fused silica material. For the typical x-ray spectra encountered in the Nova experiments, the deposition depth for 50% energy absorption was between half and three-quarters of a micron.

Thermal conductivity is an important parameter in the transient thermal response of a material. A quadratic fit was made to data from Touloukian[2] in the range from room temperature up to 1400 K, which is the top end of the data listed. Above this temperature, a constant thermal conductivity of about the 1200 K value was used. Figure 5-1 shows the variation of conductivity with temperature.

The model treats enthalpy in a zone as the primary thermal parameter, with temperature used as a secondary quantity. As mentioned in chapter 3,

this solves some problems associated with heat transfer in regions of a phase boundary. This scheme requires an empirical curve fit to produce a temperature when given an energy and the specific state of the material (solid, liquid, or vapor). The JANAF tables[3] provide the data needed in the solid/liquid region, while an empirical fit to vapor energies listed in a paper by Ree[4] covers the vapor region. As shown in Figure 5-2, the solid and liquid curves are essentially continuous, reflecting the fact that the amorphous fused silica has no real melt point, but rather monotonically decreases in viscosity. Another feature of the plot is the high values of vapor energy for a given temperature, reflecting the inclusion of the latent heat of vaporization.

The model uses a Grüneisen type equation of state in the treatment of the solid/liquid material. Specifically, the Steinberg model[5] for rapid transient loading is used, based on the Grüneisen pressure–energy relation combined with Hugoniot shock velocity–particle velocity relations. The relevant data for fused silica was obtained from Ree[4]. An ideal gas relation is assumed for the vapor. The complication is that fused silica does not vaporize as SiO_2 gas, but rather decomposes into a mixture of SiO, O_2, O, etc. The proportion of each component changes as a function of temperature and density. This has been modeled by Wilemski, as described in Reference 6. Fortunately, Wilemski found just a weak variation of composition with temperature and density, so the model uses constant values of thermodynamic gamma (1.3) and gas constant (210 J/kg K).

The vaporization model depends on a curve fit to a saturation pressure versus temperature relationship. Figure 5-3 shows the total equilibrium vapor pressure along with the partial pressure of each vapor component,

from the work by Wilemski. Applying the total pressure curve to the vaporization flux relation given in Chapter 3, equation (26) produces the curve plotted in Figure 5-4. This shows a very low vaporization rate below 4000 K, a moderate rate at 4500 K, and an additional order of magnitude increase at 5500 K.

Surface tension data is required to compute nucleation rates for the sub-surface boiling analysis. Kingery[7] provides information on the surface tension and its rate of change for temperatures between 1300 and 2100 K. At the critical point, estimated by Ree[4] to be about 11,600 K, the surface tension should drop to zero. A curve fit was made to match the value and slope at the lower temperatures and the critical point zero. Figure 5-5 shows the resulting relation as a function of temperature.

5.2.3 Modeling Results for Fused Silica

The numerical model was applied to conditions matching those of the Nova experiments. Specifically, a 1 ns square x-ray pulse with a constant 250 eV blackbody spectrum was deposited into fused silica. The temperature profiles and vaporization behaviors were monitored for the 200-ns run. Results of the total vaporization depth as a function of x-ray fluence are plotted in Figure 5-6, along with the Nova data. The fit is quite good, matching both the threshold fluence and the slope at higher fluences.

For a better description of the fused silica response, temperature profiles are presented in Figure 5-7 for one particular fluence (2.5 J/cm^2). Part a shows profiles taken every 0.1 ns during the 1.0 ns heating interval. Part b gives profiles from 1 ns to 10 ns in 0.5 ns intervals. The most interesting feature of

the plots is that energy loss from surface vaporization serves to limit the front surface temperature. Combined with the deposition-in-depth characteristic of x rays, this produces an interior region of perhaps 0.5 μm thick that is hotter than the front surface. This phenomenon will be discussed in more detail in the next section.

Another mechanism for ablation, noted in the aluminum and aluminum oxide results, is sub-surface vaporization. Here the bubble nucleation rate is computed in each zone at each time step. If conditions are such that a threshold rate is exceeded, the zone location is recorded. The maximum depth for several threshold rates is recorded through the code run. In addition, the total nucleation rates were integrated though time to give the total number of bubbles per cubic meter. Using the calculated value for critical bubble size of about 0.5 nm radius, a bubble density of $10^{26}/m^3$ gives a volume fraction of 5%. The maximum depth at which this threshold was reached was also determined. Figure 5-8 shows the results as a function of fluence, along with the measured removal data and the surface vaporization curve. As expected from observations and from the good fit of the surface vaporization, the sub-surface nucleation model is a poor fit to the silica removal data. Although the threshold for no damage is about right at 1 J/cm^2, the nucleation depth slope is roughly twice that of the measured removal data. The high nucleation rates are not caused by the rarefaction wave, but are due to purely thermal effects. Discussion of this phenomenon will be deferred until sections 5.5 and 5.6, where the distinctions between these two causes can be made clear.

The second goal of the response modeling mentioned in an earlier section was to determine the state of the ablated material. The model follows the hydrodynamics of the vapor with the same Lagrangian formulation used in the solid/liquid material. Therefore temperatures, densities, and so forth are tracked for the ablated zones. One check on performance of the gas dynamics of the hydrodynamics model is to plot velocity as a function of position at the end of the run. Again the 2.5 J/cm^2 case is used. Figure 5-9 shows that this is a straight line, consistent with the behavior of a nearly isentropic expansion of a compressed gas into a low density region.

5.2.4 Discussion of Fused Silica Results

It is instructive to compare the results of this new flux-limited surface vaporization model to predictions based on instantaneous-deposition energy profiles. As discussed in the modeling section, this approach vaporizes all material down to the depth that receives some cutoff energy density. Figure 5-10 is an energy profile (for the same x-ray fluence used in Figure 5-7) that illustrates this method. One possible cutoff energy is the total vaporization, or sublimation, energy, which is used in the TSUNAMI code.[8] Another choice, used in calculations performed by SRI[9], is the incipient vaporization energy, which is the energy of a liquid at some boiling temperature. This second method has the difficulty that more energy can end up in vapor enthalpy than the total energy deposited in the material. Figure 5-11 shows the predicted removal depths from these two cutoff energies as a function of x-ray fluence. Clearly neither approach produces a very good fit to the data. The incipient vaporization criterion significantly overpredicts removal because the latent heat is not accounted for in allowing the vapor to escape.

The other criterion, at the total vaporization energy, leaves a substantial amount of very hot material behind, so it underestimates removal depths.

An important result from the surface vaporization analysis is that it provides a mechanism for the vaporization of the hot material that initially has somewhat less than the energy needed to fully vaporize. Heat conduction can carry thermal energy toward the surface because the temperature there is lower than at a depth of a few tenths of a micron. This region near the surface can be thought of as having "excess" energy in that the material is hotter than the vaporizing surface. As this heat conducts to the surface, it continually provides the necessary vaporization energy at the surface. So the vaporization occurs not because the full cohesive energy is achieved in some bulk material, but rather just in the surface vapor flux. Over time, this process contributes to a significant increase in the total ablation depth compared to the instantaneous model. Of course, a significant amount of the "excess" energy is also conducted into the bulk material, reducing the energy available for vaporization.

The temperature profiles of Figure 5-7 show that surface vaporization has a strong effect on the temperature distribution near the surface. The "clamping" of the surface temperature at a relatively low value reflects what is essentially an energy balance. The competition is between the energy needed to vaporize at the rate set by the mass flux-temperature relation, and the rate at which energy is conducted to the surface from the adjacent higher temperature interior region. When the temperatures and thermal gradients are highest, the vaporization is most rapid. Later in time the vaporization rate necessarily decreases because of the reduction in conduction heat flux to

the surface. The changing thermal balance with time can be seen in both Figure 5-12, which extracts the surface temperature from the Figure 5-7 profiles, and Figure 5-13, where the total removal depth is plotted. As expected from the surface temperature gradients, the vaporization rate is greatest right at the end of the x-ray pulse and shows a gradual decay afterwards. What is noteworthy is that while the energy was deposited in just 1 ns, the vaporization continues for on the order of 200 times longer.

5.2.5 Conclusions for Fused Silica Modeling

The surface vaporization model agrees very well with the experimental data, both in the threshold fluence and removal depths at higher fluences. This provides further evidence, beyond exposed surface morphology, for vaporization as the dominant removal mechanism in fused silica. In addition, the model's excellent performance validates its use for predicting the response of fused silica in ICF target chambers.

5.2.6 Sensitivity Study of Fused Silica X-ray Response

This section describes a short sensitivity study on the response of fused silica designed to address the scaling of the response with pulse length and x-ray source spectrum. The parameter studies presented here deal with the response of fused silica to a single blackbody spectrum of x rays in a square pulse. The fluence level for all runs was 2.5 J/cm^2, which caused somewhat less than 0.1 μm of ablation in the original Nova test. All calculated material removal is due to vaporization from the surface, which previously was determined to be the dominant ablation mechanism for fused silica.

Sensitivity to X-ray Spectrum (Tr)

A series of runs was made with the ABLATOR code for response to blackbody (BB) spectra from 100 to 400 eV. The input pulse length was 1 ns in all cases. As shown in Figure 5-14, the resulting vaporization depths depend very strongly on the x-ray spectrum. The amount of ablated material due to a 100-eV BB is more than three times higher than the same energy input as a 300-eV BB.

To understand why the removal depth is sensitive to the x-ray spectrum, first consider the effect of a colder source. Because photoelectric cross-sections tend to be significantly higher at the lower photon energies, the absorption depths correspondingly decrease. With a given amount of energy deposited in a shallower depth, the material exposed to the colder spectrum reaches higher temperatures. An example of this is shown in Figure 5-15 as the peak temperature profiles due to 100-eV and 300-eV blackbody sources. From earlier discussions, the maximum vaporization rate increases exponentially with surface temperature. The colder spectrum generates a higher surface temperature as well as higher near-surface temperatures to sustain the vaporization by heat conduction to the surface. Thus the silica ablation depths are significantly greater for the colder x-ray spectra.

Sensitivity to X-ray Pulse Length

Several cases were run with a 220-eV blackbody spectrum for pulse lengths from 1 to 100 ns. Figure 5-16 is a plot of the vaporization depths from this study. In contrast to the spectral results, the response seems to be relatively insensitive to pulse length. Increasing the pulse by a factor of 100 (1 - 100 ns) only decreases the ablation depth by about 25%.

That the ablation decreases with longer pulses is expected because more time is available to conduct heat from the hot surface layer to the cooler bulk material. However, the temperature gradients (and so heat flow rates) decrease rapidly with distance into the material. So while the peak temperature changes rapidly, diffusion of heat away from the front half micron or so requires considerably more time. This statement is especially true for fused silica, which has a fairly low thermal conductivity. The slow change in temperature at 0.8-μm depth evident in the plot in Figure 5-17 shows that the bulk material does not "pull down" the near surface temperatures on the 100-ns time scale. So whether the x rays are deposited in 1 or 100 ns, the energy in the surface layer that contributes to vaporization is relatively unchanged. The end result is a small sensitivity to pulse length.

5.3 Silicon Nitride Modeling

5.3.1 Nova Experiments on Silicon Nitride

Three silicon nitride samples were exposed to x rays in a series of six ride-along Nova shots on February 22 & 23, 1996. X-ray fluences ranged from 1.0 to 3.3 J/cm^2, with a 200-eV blackbody spectrum in a short (2.2 ns) pulse. The samples were partially masked with tantalum foils to give areas with different numbers of shots on each sample. The experiment diagnostics were profilometer scans and optical microscopy performed after the shots. These indicated that exposed surfaces were relatively flat, with well-defined steps between areas with different numbers of exposures. It seems clear that surface vaporization was the dominant process, rather than spallation of solid or liquid material. This is consistent with the relatively low decomposition temperature of silicon nitride. Above 2150 K (at one atmosphere pressure), the material decomposes into nitrogen gas and silicon.

Profilometer scans were able to give accurate measurements of removal depths, even down to the lowest two fluences, because of the uniformity of removal. Figure 4-16 shows material removal depths on a per shot basis as a function of x-ray fluence. The error bars indicate the variations in the measured depths across various steps on the sample surfaces. For a more complete discussion of the experiments, see section 4.3.3.

5.3.2 Model Description – Silicon Nitride Specifics

This section details the material property data used in modeling silicon nitride. X-ray energy deposition uses cold cross sections for silicon and nitrogen tabulated in Cullen et al.[1] These were combined on a weight-fraction basis for the silicon nitride. For the typical x-ray spectra encountered in the Nova experiments, the deposition depth for 50% energy absorption was between half and three-quarters of a micron.

Thermal conductivity was modeled with a fourth-order polynomial fit to data from Touloukian[10] in the range from room temperature up to 2000 K, which is the highest temperature listed. Above this temperature, a constant thermal conductivity of about the 2000 K value was used. Figure 5-18 shows the variation of conductivity with temperature.

The model requires an empirical curve fit to return a temperature when given an energy and the specific state of the material (solid or vapor). No mention is made in the literature about a liquid phase of silicon nitride, because the material decomposes at a relatively low temperature (2150 K in air). The JANAF tables[3] provide the energy and temperature data needed in the solid region.

The energy/temperature relationship for the vapor requires special treatment because the decomposition process is unlike a stoichiometric vaporization. For example, in fused silica the equilibrium vapor is composed of a mixture of SiO, O_2, O, and other species, with the proportion of each component changing as a function of temperature and density[4]. The equilibrium vapor pressure of silicon nitride, however, is due almost totally to nitrogen gas. In an equilibrium situation, the surface layer would be enriched in silicon as the material decomposed at high temperatures. But as discussed by Tovstonog[11], at sufficient ablation rates the silicon is not left behind, but rather is "blown" off the surface by the large underlying pressure of nitrogen gas. The ABLATOR model incorporates the assumption that the ablated material consists of nitrogen gas mixed stoichiometrically with silicon droplets. The energy of the "vapor" is the sum of these two components. The resulting temperature versus energy curves are shown in Figure 5-19.

The vaporization model depends on a curve fit to a saturation pressure versus temperature relationship. Figure 5-20 shows the total equilibrium vapor pressure along with the partial pressure of each vapor component, from the work by Wilemski[12]. As mentioned above, his composition data show nitrogen as the dominant species, with other gaseous species comprising less than one part in ten thousand of the total vapor pressure.

Applying the vapor pressure curve of Figure 5-20 to the vaporization flux relation (Chapter 3, equation 26) produces the curve plotted in Figure 5-21. This shows a very low vaporization rate below 2000 K and a very high rate (>0.1 μm/ns) above 3200 K. Note that a rate of 1 μm/ns is equivalent to 1 km/sec.

The model uses a Grüneisen type equation of state in the treatment of the solid material. Specifically, the Steinberg model[5] for rapid transient loading is used, based on the Grüneisen pressure–energy relation combined with Hugoniot shock velocity–particle velocity relations. The relevant data for silicon nitride was obtained from the ASM Handbook[13]. An ideal gas relation is used for the vapor, which is assumed to be composed of only the nitrogen gas. The silicon mass is carried along with the nitrogen, but it gives no contribution to the pressure in the "vapor" zones.

5.3.3 Modeling Results for Silicon Nitride

The numerical model was applied to conditions matching those of the Nova experiments. Specifically, a 2.2-ns square x-ray pulse with a constant 200-eV blackbody spectrum was deposited into silicon nitride. The temperature profiles and vaporization behaviors were monitored for the 100-ns run. Results of the total vaporization depth as a function of x-ray fluence are plotted in Figure 5-22, along with the Nova data. The fit is quite good, matching both the threshold fluence and the slope at higher fluences.

For a better description of the silicon nitride response, temperature profiles are presented in Figure 5-23 for one particular fluence (1.65 J/cm^2). Part a shows profiles taken every 0.2 ns during the 2.2 ns heating interval. Part b gives profiles at the peak and from 2.5 ns to 10 ns in 0.5 ns intervals. The most interesting feature of the plots is that energy loss from surface vaporization serves to limit the front surface temperature. Combined with the deposition-in-depth characteristic of x rays, this produces an interior region of perhaps 0.3 μm thick that is hotter than the front surface. This phenomenon will be discussed in more detail in the next section.

5.3.4 Discussion of Silicon Nitride Results

The temperature profiles of Figure 5-23 show that surface vaporization strongly effects the temperature distribution near the surface. The "clamping" of the surface temperature at a relatively low value reflects what is essentially an energy balance. This is the same phenomenon seen in fused silica. The changing thermal balance with time can be seen in both Figure 5-24, which extracts the surface temperature from the Figure 5-21 profiles, and Figure 5-25, where the total removal depth is plotted. As expected from the surface temperature gradients, the vaporization rate is greatest right at the end of the x-ray pulse and shows a gradual decay afterwards. Note that while the energy was deposited in just 2.2 ns, the vaporization continues for on the order of 5 - 10 times longer.

The new flux-limited surface vaporization model results compare very favorably to predictions based on instantaneous-deposition energy profiles, as shown in Figure 5-26. This second approach vaporizes all material down to the depth that receives some cutoff energy density. This is the same type of comparison made for fused silica in section 5.2.4.

Another form of material removal considered was sub-surface vaporization, which is believed to be an important mechanism for some other materials (aluminum, for example). In this process, the pressure release from the front surface propagates through the hot interior material as a tensile wave, causing explosive bubble nucleation and growth. The instantaneous vapor generation below the surface then "blows off" the material above this depth. ABLATOR analyses modeled silicon nitride response to Nova x-ray exposure conditions. Pressure profiles after the end of

the x-ray pulse show that while the pressures drop, they always remain positive. The plot of vaporization depth as a function of time (Figure 5-25) shows that at this time, about 2.5 ns, there is strong vaporization from the surface. This coincides with high surface pressures, which overwhelm or negate the rarefaction wave. Without a tensile wave to drive rapid bubble nucleation and growth, sub-surface boiling is very unlikely. Another reason to discount the possibility of sub-surface boiling is that the material likely remains as a solid up to its decomposition temperature. This makes the mechanism of internal bubble nucleation, due to purely thermal conditions, much harder to imagine.

5.3.5 Conclusions for Silicon Nitride Modeling

The surface vaporization model agrees very well with the experimental data, both in the threshold fluence and removal depths at higher fluences. This provides further evidence, beyond exposed surface morphology, for vaporization as the dominant removal mechanism in silicon nitride. In addition, the model's excellent performance validates its use for predicting the response of vaporizing materials in ICF target chambers.

5.4 Boron Carbide and Boron Modeling

5.4.1 Nova experiments on Boron Carbide and Boron

Twenty-eight samples of various forms of boron carbide and boron were exposed to x rays in four series of ride-along Nova shots between November 17, 1995 and February 23, 1996. X-ray fluences ranged from 1.0 to 3.3 J/cm^2, with a 200 - 250 eV blackbody spectrum in a short (1 - 2.2 ns) pulse. The samples were partially masked with tantalum foils to give areas with different numbers of shots on each sample. The experiment diagnostics were

profilometer scans and various forms of microscopy of the exposed surfaces performed after the shots. The observations show that these materials roughen somewhat on exposure to high x-ray fluences. However, even after multiple shots at the highest x-ray fluences, no net removal (steps) could be measured in the surfaces. Optical microscopy and SEM (scanning electron microscope) showed isolated small pits in the surfaces. This indicates that most material removal was in the form of solid particles spalled off the surface. Removal rates were estimated based on typical pit depths and average fractions of surface coverage. Figure 4-28 shows material removal depths on a per shot basis as a function of x-ray fluence. For a complete discussion of the experiments, see section 4.3.4.

5.4.2 Model Description -- Boron Carbide and Boron Specifics

This section details the material property data used in modeling boron carbide and boron. X-ray energy deposition uses cold cross sections for boron and carbon tabulated in Cullen et al.[1] These were combined on a weight-fraction basis for the boron carbide. For the typical x-ray spectra encountered in the Nova experiments, the deposition depth for 50% energy absorption was between one-half and one micron.

Thermal conductivity was modeled with polynomial fits to data from Touloukian[2] in the range from room temperature up the highest temperatures listed (1000 K for B_4C and 1400 K for boron). Above these temperatures, the curve fits extrapolated the data to give essentially a constant thermal conductivity of about the end point value. Figure 5-27 shows the variation of conductivities with temperature for the two materials.

The model requires an empirical curve fit to return a temperature when given an energy and the specific state of the material (solid, liquid, or vapor). The JANAF tables[3] provide the energy and temperature data needed in the solid and liquid regions for both materials and for boron vapor. Figures 5-28 and 5-29 show these relations for boron carbide and boron, respectively.

The energy/temperature relationship for the boron carbide vapor requires special treatment because the composition of chemical species in the vapor varies depending on pressure, temperature, and the degree to which thermodynamic equilibrium is attained. Above 3000K, B_4C is unstable with respect to liquid boron and solid/liquid carbon, but it is unclear whether there is sufficient time for rearrangement of the condensed phases in the short vaporization pulses. Also in the vapor phase, numerous species can exist (dimers, trimers, etc.), but the time scale for growth of these components may be too long to be relevant to the ablation process. Wilemski[14] has worked out the thermodynamics of various scenarios to produce specific energy relations in the vapor. The B_4C vapor curve in Figure 5-28 shows the case used in the ABLATOR model, which assumes only B and C vapor above B_4C.

The vaporization model depends on a curve fit to a saturation pressure versus temperature relationship. Figure 5-30 shows the total equilibrium vapor pressures for boron and B_4C, from JANAF and the work by Wilemski, respectively. Applying these curves to the vaporization flux relation produces the curves plotted in Figure 5-31. The plot shows very low vaporization rates below about 5000 K and a high rate (0.01 - 0.1 μm/ns) above 7000 K.

The model uses a Grüneisen type equation of state in the treatment of the solid material. Specifically, the Steinberg model[15] for rapid transient loading is used, based on the Grüneisen pressure – energy relation combined with Hugoniot shock velocity – particle velocity relations. The relevant data for boron carbide were obtained from a report by Steinberg[15] and from the ASM Handbook[13]. Boron's mechanical properties were assumed to be similar. Ideal gas relations were used for the vapor phases, which in B_4C was assumed to be composed of only B and C gases.

Thermal stress appears to play the major role in the x-ray ablation of boron carbide and boron. The techniques of section 3.7.4 are used to evaluate this damage mechanism using peak temperature profiles and the thermo-mechanical properties given in Table 5-1. Applying these bulk material properties to a process that will occur on the micron scale, and so inside a single grain of material, may lead to some error. More accurate material constants would be required if a full crack nucleation and growth model were to be implemented. However, for the rough arguments presented here, the errors are not likely to be significant.

Table 5-1: Room temperature boron carbide material properties for thermal stress calculations

α – coeff of thermal expansion	6×10^{-6} / °C
E – Young's modulus	445 GPa
ν – Poisson's ratio	.19
σ-compressive	12 GPa

Data Sources: ASM Engineered Materials Handbook (13) and Steinberg (15)

5.4.3 Modeling Results for Boron Carbide and Boron

The numerical model was applied to conditions matching those of the Nova experiments. Specifically, a 1-ns square x-ray pulse with a 250-eV blackbody spectrum was deposited into boron carbide. The temperature profiles and vaporization behaviors were monitored for the 100-ns runs. Results of the total vaporization depths as a function of x-ray fluence are plotted in Figure 5-32, along with the Nova data. As anticipated from the microscopy and profilometry, vaporization played just a small role in the removal of material at the test x-ray fluences. The analysis points to two causes for limited vaporization: low atomic number (Z) elements and low vapor pressure. Opacities of low-Z materials are relatively small for the x-ray photon energies in these tests, giving a greater average deposition depth. Spreading the energy in depth lowers the surface temperature, which as Figure 5-31 shows, dramatically reduces the vaporization rate. Figures 5-30 and 5-31 also indicate that relatively high temperatures must be attained to vaporize these low vapor pressure materials.

The peak temperature profiles (at the end of x-ray deposition) are presented in Figure 5-33 for four 250-eV blackbody x-ray fluences (3.25 – 1.0 J/cm^2) into boron carbide. The curves for the lower three fluences show the flat profile at the surface characteristic of an insulated face. In the highest-fluence case, there is a peak just inside the surface, because energy loss from surface vaporization serves to limit the front surface temperature. From this curve and the vaporization rate information from Figure 5-31, it can be seen that the boron carbide only reaches the intermediate vaporization regime. After a short time (~1.5 ns), the surface temperature drops by 1000 degrees, lowering the evaporation rate by an order of magnitude. Thus the

vaporization effectively shuts off very quickly and little material is lost. Figure 5-33 also shows the solid/liquid transition region at the 2743 K melt temperature for the three higher fluences. The 1.0 J/cm^2 surface temperature falls just below the melt point.

The temperature profiles of Figure 5-33 provide the basis for thermal stress calculations according to the method of section 3.7.4. Applying equation (33) of that section to these temperatures results in the thermal stress profiles shown in Figure 5-34. The flat region at the front of the three higher fluence cases corresponds to the melted or partially melted material. The drop-off to zero stress occurs in the region of softened solid. The peak stress for each case is at or near 8 GPa, which exceeds the tensile strength (155 MPa) by a factor of about 50. Therefore the assumed depth of the thermal stress cracks in the boron carbide will be near the point where the thermal stress reaches zero.

Ablation of boron carbide and boron occurs by formation of isolated pits in the surface. The removal depths were calculated based on pit depth and an estimate of their areal coverage. Pit depth is expected to correlate to the depth of thermal stress cracking, because down to this level the brittle material is fairly heavily fractured and so susceptible to further crack propagation. Figure 5-35 plots pit depths as a function of x-ray fluence for the various forms of boron carbide and boron. Since these depths generally exceed the predicted melt depths (also shown in the figure), the softening phenomenon in the heated solid is likely important. Figure 5-35 also shows predicted thermal crack depths (from Figure 5-34), which generally agree with the measurements, although there is significant scatter in the data.

Another step is required in the ablation process after the thermal stress damage, specifically a mechanism for removal of some of the damaged sections. One possible cause is the continued stress of thermal cycling from subsequent x-ray exposures. Probably a better explanation is the passage of the shock and rarefaction waves from additional x-ray shots. High tensile stresses are developed in this process, though only for a short period of time. The rapid passage of these waves gives insufficient time for the nucleation and growth of voids, even though the tensile strength is exceeded. There may, however, be adequate time to extend some of the thermal stress cracks far enough to give spall of thermally damaged "flakes".

The development and propagation of the shock and rarefaction waves are shown in Figure 5-36. The specific case is boron carbide with 2.3 J/cm^2 of 250-eV blackbody x rays in a 1-ns square pulse. Shocks (positive pressure pulses) develop during heating and propagate into the bulk. As soon as the x-ray energy shuts off, the thermal expansion of the surface layers stops and a strong tensile wave is launched into the material. Part a of the figure shows spatial profiles at time intervals of 0.1 ns. Part b extracts the peak tensile stress information at various depths. The stress falls from zero at the free surface, where there is no tensile stress possible, to a maximum tensile value at about 1.5 - 3 μm. Spall is most likely to occur at the maximum crack depth, in this case 0.6 μm, because this is the most highly stressed region with a fracture nucleation site already existing.

Another way to view the tensile stress information is with temporal profiles at selected points. Figure 5-37 gives the pressure history in boron carbide at the predicted maximum thermal crack depth for each of the four

fluences (1.0, 1.65, 2.3, and 3.25 J/cm^2). As discussed above, the tensile stresses from the rarefaction wave do exceed the tensile strength at all but the lowest fluence, but only for 0.5 ns or less. Note that all these locations are within solid material, so the tensile strength is applicable.

5.4.4 Discussion of Boron Carbide and Boron Results

The thermal stress analysis provides a means of predicting the depth of the damage pits in the boron carbide and boron. This is particularly important since these depths exceed the melt depths by a significant amount. The assumption of softening of hot solid material is what extends the high thermal stress beyond the melt depth. One problem is that this method predicts thermal stress cracking at 1.0 J/cm^2, where none is found in the boron carbide. At this fluence, the material does not melt, so the predicted damage is based on the approximate stress relief model in the code.

The shock history plot in Figure 5-37 for the lowest fluence agrees with the experimental observation of no material removal in boron carbide. At the three highest fluences, the curves show that it is plausible that the tensile wave removes solid flakes of damaged material. This removal is observed to be at isolated spots on the surface, indicating that the process might best be analyzed by statistical methods. Such methods have been developed for brittle crack growth[16], but their implementation is beyond the scope of this study.

5.4.5 Conclusions for Boron Carbide and Boron Modeling

The surface vaporization model provides a lower bound for material removal at a given fluence. For boron carbide and boron, the amount

vaporized at typical first wall x-ray fluences will be minimal. Material removal in the form of flakes of thermally shocked material is the dominant process. The ABLATOR model predicts the depths of the pits to within the experimental scatter, and shows that the strength of the tensile wave is sufficient to cause tensile failure in at least some of the damaged material.

5.5 Aluminum Modeling

5.5.1 Nova experiments

Nine aluminum disks were exposed to x rays in two series of ride-along Nova shots between November 17, 1995 and February 23, 1996. X-ray fluences ranged from 1.0 to 3.3 J/cm^2, with a 200-eV blackbody spectrum in a short (2.2 ns) pulse. The samples were partially masked with tantalum foils to give areas with different numbers of shots on each sample. The experiment diagnostics were profilometer scans and various forms of microscopy of the exposed surfaces performed after the shots. In addition, some of the samples were sectioned to permit examination of the full damage layer thickness. The observations show that these materials roughen significantly (several microns) on exposure to high x-ray fluences. The roughness required multiple x-ray exposures on a surface before profilometry could measure the removal depths above the roughness "noise". Optical microscopy and SEM (scanning electron microscope) showed wavy surfaces with substantial evidence for liquid motion. This indicates that most material removal was in the form of liquid spalled off the surface. Figure 4-46 shows material removal depths on a per shot basis as a function of x-ray fluence. For a complete discussion of the experiments, see section 4.3.5.

5.5.2 Model Description – Aluminum Specifics

This section details the material property data used in modeling aluminum. X-ray energy deposition uses cold cross sections tabulated in Cullen et al.[1] For the typical x-ray spectra encountered in the Nova experiments, the deposition depth for 50% energy absorption was about three-quarters of a micron.

Thermal conductivity is an important parameter in the transient thermal response of a material. Aluminum's high conductivity causes rapid heat loss from the surface into the bulk material. Polynomial fits were made to data from Touloukian[2] in the range from room temperature up to the melt temperature (966 K) in solid and in the liquid above this temperature. Figure 5-38 shows the variation of conductivities with temperature for the two phases. These data are for pure aluminum, which was used for most the Nova samples. Alloy 6061-T6 (>97.5% Al) was used for the initial, single-shot samples that were eventually sectioned for melt thickness examination.

The model requires an empirical curve fit to return a temperature when given an energy and the specific state of the material (solid, liquid, or vapor). The JANAF tables[3] provide the energy and temperature data needed in the solid, liquid, and vapor regions at the reference pressure of 1 bar. The solid and liquid data are essentially independent of pressure, as is the vapor with the assumption of ideal gas behavior. Figure 5-39 shows these relations for the three phases of aluminum based on enthalpy. Enthalpy and internal energy are essentially the same for the condensed phases. For the vapor, conversion is accomplished using $h=u+pV$.

The model uses a Grüneisen type equation of state in the treatment of the solid and liquid material. Specifically, the Steinberg model[5] for rapid transient loading is used, based on the Grüneisen pressure–energy relation combined with Hugoniot shock velocity–particle velocity relations. Ideal gas relations were used for the vapor phase.

The vaporization model depends on a curve fit to a saturation pressure versus temperature relationship. Figure 5-40 shows the total equilibrium vapor pressure for aluminum, from Dushman.[17] Applying this curve to the vaporization flux relation produces the curve plotted in Figure 5-41. The plot shows a low vaporization rate below about 4000 K and a high rate (0.01 - 0.1 μm/ns) above 5500 K. Note that a rate of 1 μm/ns is equivalent to 1 km/sec.

Another form of vaporization is considered for aluminum, specifically sub-surface boiling. The motivation for considering this material removal mechanism is the observation of very rough surfaces with evidence of droplet ejection on many of the x-ray exposure samples. The relations for nucleation rate (section 3.7.3) require surface tension as the only new material parameter beyond those already introduced. Data provided in Murr[18] gives the surface tension and its rate of change with temperature at the melt point. At the other end of the liquid range, the surface tension must fall to zero at the critical point, estimated to be 5726 K in the SESAME tables[19] for aluminum. The slope at the critical point is taken from the Eötvös relation (discussed in Murr)

$$\sigma = k(T_c - T)V^{-2/3} \qquad (1)$$

where T_c is the critical temperature, V is the molar volume, and k is a constant with a value of 2.1 ergs/°C for most liquids. A cubic spline curve fit was used between the two known endpoints and slopes to provide data at intermediate temperatures. Figure 5-42 shows the resulting surface tension as a function of temperature.

5.5.3 Modeling Results for Aluminum

Figure 5-43 presents the Nova removal depths, with the addition of the measured thickness of resolidified aluminum and the predicted melt depth. At the higher fluences, it can be seen that about one quarter to one third of the melt layer is removed under these conditions. The goal of the analysis that follows is to determine a mechanism that predicts such a partial removal process.

The numerical model was applied to conditions matching those of the Nova experiments. Specifically, a 2.2-ns square x-ray pulse with a 200-eV blackbody spectrum was deposited into aluminum. The temperature profiles and vaporization behaviors were monitored for the 100-ns runs. Results of the total vaporization depths as a function of x-ray fluence are plotted in Figure 5-44, along with the Nova data. As anticipated from the microscopy and profilometry, vaporization played just a small role in the removal of material at the test x-ray fluences.

Figures 5-45 through 5-48 present temperature profiles for four 200-eV blackbody x-ray fluences (3.25 – 1.0 J/cm^2) into aluminum, from the peak at 2.2 ns out to 5.0 ns. In the two highest-fluence cases, there is a peak just inside the surface, because energy loss from surface vaporization serves to

limit the front surface temperature. After a short time (~2.5 ns), heat conduction into the bulk material drops surface temperatures by more than 2000 degrees, lowering evaporation rates by at least an order of magnitude. Thus the vaporization effectively shuts off very quickly and little material is lost. It is the high thermal conductivity of the aluminum that minimizes evaporative material removal.

The two higher-fluence temperature plots also show several zones at the very front that become significantly hotter than the liquid surface material. Absorption of x rays after vaporization heats these zones, which have no means to remove the energy quickly, increasing their temperatures rapidly. Energy deposition in ablated vapor is termed vapor shielding, because some of the incoming energy is prevented from reaching the ablation front. This phenomenon is particularly important in laser ablation and in plasma ablation (as from a disruption event in a magnetic fusion machine) where the shielding effect can be very significant. In this x-ray exposure situation, however, there is generally not enough material vaporized before the end of the x-ray pulse to appreciably change the energy deposition profile. Therefore the code's treatment of these hot vapor zones as maintaining cold x-ray opacities and having no radiation transport will not introduce significant errors, at least in the fluence range of interest, a few J/cm^2.

The temperature profiles for the lower two fluences (Figures 5-47 and 5-48) show the flat profile at the surface characteristic of an insulated face, as these fluences do not produce significant vaporization. The plots also show the solid/liquid transition regions at the 933 K melt temperature.

The development and propagation of the rarefaction waves are shown in Figures 5-49 to 5-52. Shocks (positive pressure pulses) develop during heating and propagate into the bulk. As soon as the x-ray energy shuts off, the thermal expansion of the surface layers stops and a strong tensile wave is launched into the material. These figures show spatial profiles at time intervals of 0.1 ns to 0.5 ns beginning at the end of the x-ray pulse. The peak negative pressures are on the order of 1 GPa, but these last only a few tenths of a nanosecond at any one location.

Equation (29) of section 3.7.3 was applied to each zone to determine the local bubble nucleation rate. Figure 5-53 presents a typical result of nucleation rate ($m^{-3}s^{-1}$) as a function of depth for the 1.65 J/cm^2 case. The various curves represent spatial profiles of log(J) at intervals of 0.1 ns between 2 and 3 ns. At times near the peak of the rarefaction wave, J reaches near its maximum value for this situation, about 10^{40} $m^{-3}s^{-1}$. The region where these high J values are found, near 0.5 μm in this case, has both a relatively high temperature (and so a high P_{sat}) and large negative pressures. These two terms appear as $(\eta P_{sat} - P)^2$ in the denominator of an exponential, which drives the exponential to its maximum value of one, giving the peak nucleation rate.

With such very high nucleation rates, the short duration of the tensile pulse will still be sufficient to generate significant amounts of vaporized material. As is typical in nucleation analysis, some threshold value must be selected as the cutoff for defining a "sufficient" rate. The procedure adopted here is to record the maximum depth over all time steps for various levels of the nucleation rate ranging from 10^{25} to 10^{40}. Comparison of these

maximum depths with the measured material removal as a function of x-ray fluence will guide the choice of this cutoff nucleation rate. Figure 5-54 presents these results. From these curves, a "critical" nucleation rate of 10^{30} appears to provide the best fit to the data. Note that no sub-surface boiling is predicted at 1.0 J/cm^2 since the maximum predicted J-values fall many orders of magnitude short of any of these potential nucleation thresholds.

Another way to set a threshold for sub-surface vaporization is to examine the volume fraction of vapor bubbles. As discussed in section 3.7.3, this analysis involves integrating the nucleation rate with time (in each zone) to obtain the number of bubbles per unit volume. The critical bubble size must also be calculated, which works out to be about 1-nm radius in regions of high nucleation rate. A simple calculation reveals that an integral of 10^{26} bubbles/m^3 will give a vapor volume fraction of 40%. This curve is also plotted on Figure 5-54. Note that reducing this arbitrary threshold by an order of magnitude has almost no effect on the location of the curve.

5.5.4 Discussion of Aluminum Results

The nucleation rate threshold curves shown in Figure 5-54 have generally the same slope and threshold fluence as what was observed experimentally. This provides some confidence that the sub-surface boiling model has the proper physics in it. Also encouraging is the relative insensitivity of the J-threshold curves over 15 orders of magnitude. This means that predictions of material removal using this technique will not be significantly changed by the exact value of the threshold chosen. Finally, the nucleation rate providing the best fit, 10^{30} m^{-3}s^{-1}, is a very high rate, consistent with the original assumption that even a short time under these conditions will create large

amounts of vapor. This is further reinforced by the reasonably good fit to the data seen with the integral-J (bubbles per unit volume) curve.

5.5.5 Conclusions on Aluminum Modeling

The experimental observation that liquid ejection is the dominant removal mechanism for aluminum is well explained with the ABLATOR model. One aspect of this conclusion is that evaporation is predicted to have a negligible contribution to the ablation depth. The other result of the modeling effort is that sub-surface boiling (vapor explosion) can be predicted with simple homogeneous nucleation theory. An appropriate choice of threshold nucleation rate provides a very good fit to the experimental removal data, which suggests that the important mechanisms are understood.

5.6 Aluminum Oxide Modeling

5.6.1 Nova experiments on Alumina

Nine aluminum oxide disks were exposed to x rays in two series of ride-along Nova shots on November 17, 1995 and December 19, 1995. X-ray fluences ranged from 1.0 to 3.5 J/cm^2, with a 200-eV blackbody spectrum in a short (2.2 ns) pulse. The samples were partially masked with tantalum foils to give areas with different numbers of shots on each sample. The experiment diagnostics were profilometer scans and various forms of microscopy of the exposed surfaces performed after the shots. The observations show that alumina roughens significantly (0.5 - 1 μm) on exposure to high x-ray fluences. Optical microscopy and SEM (scanning electron microscopy) showed evidence of liquid motion (splashing), thermal stress cracking, and bubbles under the surface. These indicate that most

material removal was in the form of liquid and/or solid spalled off the surface by some combination of sub-surface boiling and thermal shock/spall. Figure 4-37 shows material removal depths on a per shot basis as a function of x-ray fluence. For a complete discussion of the experiments, see section 4.3.6.

5.6.2 Model Description – Aluminum Oxide Specifics

This section details the material property data used in modeling aluminum oxide. X-ray energy deposition uses cold cross sections for aluminum and oxygen tabulated in Cullen et al.[1] and combined according to weight fraction. For the typical x-ray spectra encountered in the Nova experiments, the deposition depth for 50% energy absorption was about one third of a micron.

Thermal conductivity is an important parameter in the transient thermal response of a material. Aluminum oxide's conductivity drops by a factor of four between room temperature and 1000 K. Polynomial fits were made to data from Touloukian[2] in the range from room temperature up to the end of available data at 2000 K. From this temperature to the melt point (2327 K) in solid and in the liquid above this temperature, a constant conductivity was used. Figure 5-55 shows the variation of conductivities with temperature.

The model requires an empirical curve fit to return a temperature when given an energy and the specific state of the material (solid, liquid, or vapor). The JANAF tables[3] provide the energy and temperature data needed in the solid and liquid, while an empirical fit to vapor energies listed in a paper by Kovitya[20] covers the vapor region. Figure 5-56 shows these relations for the three phases of aluminum oxide based on enthalpy. Enthalpy and internal

energy are essentially the same for the condensed phases. For the vapor, conversion is accomplished using h=u+pV. One notable feature of the plot is the high value of vapor energy for a given temperature, reflecting the inclusion of the latent heat of vaporization.

The model uses a Grüneisen type equation of state in the treatment of the solid and liquid material. Specifically, the Steinberg model[5] for rapid transient loading is used, based on the Grüneisen pressure–energy relation combined with Hugoniot shock velocity–particle velocity relations. Data for these relations was obtained from Marsh[21] and Lynch et al.[22] Ideal gas relations were used for the vapor phase. The complication is that aluminum oxide does not vaporize as Al_2O_3 gas, but rather decomposes into a mixture of O_2, AlO, Al, and other vapor species. The proportion of each component changes as a function of temperature and density. This has been modeled by Wilemski, as described in Reference 12. Fortunately, Wilemski found just a weak variation of composition with temperature and density, so the model uses constant values of thermodynamic gamma (1.55) and gas constant (267.5 J/kgK).

The vaporization model depends on a curve fit to a saturation pressure versus temperature relationship. Figure 5-57 shows the total equilibrium vapor pressure for alumina, from Wilemski.[12] Applying this curve to the vaporization flux relation produces the curve plotted in Figure 5-58. The plot shows a low vaporization rate below about 5000 K and a high rate (0.01 - 0.1 μm/ns) above 6000 K. Note that a rate of 1 μm/ns is equivalent to 1 km/sec.

Another form of vaporization is considered for aluminum oxide, specifically sub-surface boiling. The motivation for considering this material removal mechanism is the observation of rough surfaces with evidence of liquid splashing on many of the x-ray exposure samples. The relations for nucleation rate (section 3.7.3) require surface tension as the only new material parameter beyond those already introduced. Data provided in Shpil'rain[23] gives the surface tension for aluminum oxide and its rate of change with temperature near the melt point. At the other end of the liquid range, the surface tension must fall to zero at the critical point, estimated to be 16,000 K in the SESAME tables[19] for aluminum oxide. An exponential fit to the data near the melt point provides the desired functional relation. Figure 5-59 shows the resulting surface tension as a function of temperature.

Thermal stress appears to play the major role in the x-ray ablation of aluminum oxide. The techniques of section 3.7.4 are used to evaluate this damage mechanism using peak temperature profiles and the thermo-mechanical properties given in Table 5-2. As was the case with modeling boron carbide, applying these bulk material properties to a process that will occur on the micron scale may lead to some error. However, for the rough arguments presented here, the errors are not likely to be significant.

Table 5-2: Room temperature aluminum oxide material properties for thermal stress calculations

α – coeff of thermal expansion	11.7×10^{-6} / °C
E – Young's modulus	350 GPa
ν – Poisson's ratio	.30
σ-compressive	2.1 GPa

Data Source: Lynch (reference 22)

5.6.3 Modeling Results for Aluminum Oxide

Surface Vaporization

The numerical model was applied to conditions matching those of the Nova experiments. Specifically, a 2.2-ns square x-ray pulse with a 200-eV blackbody spectrum was deposited into aluminum oxide. The temperature profiles and vaporization behaviors were monitored for the 100-ns runs. Results of the total vaporization depths as a function of x-ray fluence are plotted in Figure 5-60, along with the Nova data. As anticipated from the microscopy and profilometry, surface vaporization is not the dominant material removal mechanism for alumina. This process accounted for perhaps one third of the ablation depth at the higher fluences, falling to almost no contribution at the lower fluences.

Figure 5-61 presents the peak temperature profiles (at the end of x-ray deposition) for four 200-eV blackbody x-ray fluences (3.56 – 1.0 J/cm^2) into aluminum oxide. The curves for the lower two fluences show the flat profile at the surface characteristic of an insulated face. In the two highest-fluence cases, there is a peak just inside the surface, because energy loss from surface vaporization serves to limit the front surface temperature. From these curves and the vaporization rate information from Figure 5-58, it can be seen that the alumina reaches the high vaporization rate regime. After a short time (a few nanoseconds), however, the surface temperatures (and so evaporation rates) drop due to conduction losses to the bulk and the energy lost to the vapor. Figure 5-61 also shows the solid/liquid transition region at the 2743 K melt temperature for all four x-ray fluences.

Sub-Surface Boiling

The method of section 3.7.3 was applied to each zone to determine the local bubble nucleation rate. Figure 5-62 presents a typical result of nucleation rate as a function of depth for the 2.5 J/cm^2 case. The various curves represent spatial profiles of log(J) at intervals between 1 and 2.4 ns. At times near the peak of the rarefaction wave, high values of J (above 10^{25} m^{-3}s^{-1}) reach their maximum penetration depth into the material. The region where these high J values are found, between 0.1 and 0.15 μm in this case, has both a relatively high temperature (and so a high P_{sat}) and large negative pressures. These two terms appear as $(\eta P_{sat} - P)^2$ in the denominator of an exponential, which drives the exponential to its maximum value of one, giving the peak nucleation rate.

There is a significant difference in the behavior of the nucleation rate for aluminum oxide as compared to aluminum. This can be seen in the plot of Figure 5-63, which shows time histories of J at various depths in the alumina for the 2.5 J/cm^2 case. At depths below 0.10 μm, the nucleation rate rises to very high levels before the rarefaction wave arrives (at 2.2 - 2.3 ns), and persists at these levels long after the passage of the wave. Figure 5-64 shows the nucleation rate profiles for this case at 3, 4, and 5 ns. This plot indicates that the alumina to a depth of about 0.09 μm is at a the very high nucleation rate for several nanoseconds. These high rates are caused by high internal temperatures, that correlate to high saturation vapor pressures and low surface tensions. High nucleation rates due solely to high temperatures and not the influence of the tensile wave will be referred to as "thermal" nucleation rates.

The maximum penetration depths for both the "tensile" and the "thermal" nucleation rate peaks were calculated over a range of x-ray fluences. Several cutoff rates, from 10^{20} to 10^{35} were considered for the "tensile" depths, while the "thermal" depths were estimated for a cutoff of about 10^{25}. In addition, the total nucleation rates were integrated though time to give the total number of bubbles per cubic meter. Using the calculated value for critical bubble size of about 1-nm radius, a bubble density of 10^{26} /m^3 gives a volume fraction of 40%. The maximum depth at which this threshold was reached was then determined. Figure 5-65 gives the results of these ABLATOR calculations along with the experimental removal data for comparison. All the nucleation rate / depth curves have a substantially higher damage threshold than experimentally observed (1.75 - 2.0 J/cm^2 compared to 1.0 J/cm^2). The high threshold is due to the need for substantial saturation vapor pressures to obtain large nucleation rates, which requires rather high temperatures. The slopes of the set of "tensile" curves and the integral curve seem to be too high when compared to the removal data, although the results for one alumina form (High Velocity Oxygen Fuel plasma spray material) are well matched. The slope of the "thermal" curve seems to follow the trend in the data somewhat better. Some thoughts on these behaviors will be given in the Discussion section. Note that the nucleation rate / depth calculations also contained the surface vaporization phenomenon, so these depths are totals and should not be added to the vaporization depths.

Thermal Stress/Spall

The temperature profiles of Figure 5-61 provide the basis for thermal stress calculations according to the method of the previous section. Applying

equation (33) of section 3.7.4 to these temperatures results in the thermal stress profiles shown in Figure 5-66. The flat region at the front surface corresponds to melted or partially melted material. The drop-off to zero stress occurs in the region of softened solid. The peak stress for each case is at or near 11 GPa, which exceeds the tensile strength by a factor of about 40. Therefore the assumed depth of the thermal stress cracks in the aluminum oxide will be near the point where the thermal stress reaches zero.

After the thermal stress damage occurs, the passage of shock and rarefaction waves from additional x-ray shots can cause removal of some of the damaged sections. Figure 5-67 gives the normal stress history in aluminum oxide at the predicted maximum thermal crack depth for each of the four fluences (1.0, 1.75, 2.5, and 3.56 J/cm^2). As discussed above, the tensile stresses from the rarefaction wave do exceed the tensile strength at all x-ray fluences, but only for 0.2 ns or less. Note that all these locations are within solid material at about 650 K, so the tensile strength at this temperature is used.

5.6.4 Discussion of Aluminum Oxide Results

Sub-surface boiling with the "tensile" model is based on the assumption that the hot, relatively quiescent liquid is traversed by a strong tensile wave that initiates massive bubble nucleation and growth as is propagates. The presence of high "thermal" nucleation rates (and so bubble growth) occurring before the tensile wave arrives will substantially change the pressure environment in the liquid, invalidating the simple "tensile wave" treatment. Because temperatures in the liquid are not strongly affected by the local pressure variations, the thermally caused bubble nucleation process will

likely still occur. This is especially true considering the relatively long times predicted for the liquid to be in a high nucleation rate condition. Therefore these calculations indicate that at least some sub-surface boiling is likely for alumina. It is apparent, however, that a substantially improved model of bubble growth and associated liquid expulsion would be required to make quantitative removal estimates.

One problem with the sub-surface boiling model is that the threshold for damage is quite a bit higher than seen in the Nova experiments. In addition to missing the material removal behavior, the consistent observations of surface or sub-surface bubbles, even at the lowest fluences, are not accounted for. One possible explanation is heterogeneous nucleation, which has a lower threshold than does homogeneous nucleation. For example, the lowest fluence sapphire sample shows no bubbles after a single shot, but many after two shots. Small particles of target debris or thermal stress cracks may provide sites for initiation of bubble nucleation.

The thermal shock/spall phenomenon is the best candidate for causing alumina removal at the lower x-ray fluences. This mechanism has a lower threshold for damage (melt energy) than the mechanisms based on vaporization. In addition, virtually all the alumina samples showed thermal stress cracking, even after just a single shot. Also, studies with exposure of aluminum oxide to 0.53-μm laser irradiation at 5 J/cm^2 have shown "thermal-stress-induced exfoliation" to be the dominant removal mechanism.[24] The shock history curves in Figure 5-67 show that it is plausible that the tensile wave removes solid flakes of thermal-stress damaged material. This removal is observed to be at isolated spots on the

surface, indicating that the process might best be analyzed by statistical methods. Such methods have been developed for brittle crack growth[16], but their implementation is beyond the scope of this study.

5.6.5 Conclusions for Aluminum Oxide Modeling

Aluminum oxide has a very complex response to x rays, in that material removal cannot be attributed to a single-mechanism. At the higher fluences, ablation appears to be primarily due to vaporization, both from the surface and from sub-surface boiling. At lower fluences where not enough energy is present to drive vaporization, thermal stress cracking and subsequent surface roughening and spall of damaged flakes likely account for the bulk of the observed removal depth. The ABLATOR model provides a basis for these conclusions, and can be used to predict the higher fluence material response with some measure of accuracy. The code lacks the sophisticated brittle material damage models needed to quantify removal in the low-fluence cases.

References

1) Cullen, D E;Chen, M H;Hubbell, J H;Perkins, S T;Plechaty, E F;Rathkopf, J A;Scofield, J H., "Tables and graphs of photon-interaction cross sections from 10 eV to 100 GeV derived from the LLNL evaluated photon data library (EPDL)", LLNL, UCRL-50400-V6-Rev-4, 1989.

2) Touloukian, YS., Thermophysical Properties Of High Temperature Solid Materials, Collier-Macmillan, 1967.

3) Stull, DR., Prophet, H., JANAF Thermochemical Tables, USGPO, Washington, D C, 1975.

4) Ree, F H., "Equation Of State Of The Silicon Dioxide System", LLNL, UCRL-52153, 1976.

5) Steinberg, D J., "Equation of state and strength properties of selected materials", LLNL, UCRL-MA-106439, 1991.

6) Wilemski, G., "Silica vapor pressure and energy calculations", TAT 96-008.2, March 22, 1996.

7) Kingery, WD, "Surface Tension of Some Liquid Oxides and Their Temperature Coefficients", J. Am Cer Soc V42 N1, 6-10, (1959).

8) Chen, XM., "A Study of Thermal Hydraulic and Kinetic Phenomena in HYLIFE-II – An Inertial Confinement Fusion Reactor", PhD dissertation, UC Berkeley, Jan 1993.

9) Tokheim, RE., Seaman, L., Curran, DR., "Threats from Radiation Effects in the Proposed Nova Upgrade", SRI Intl Final Report for LLNL, Sept, 1992.

10) Touloukian, Y. S.;HO, C. Y., Thermophysical Properties Of Selected Aerospace Materials, TEPIAC/CINDAS, West Lafayette, 1977.

11) Tovstonog, V.A., "Experimental Investigation of Thermal Decomposition of Silicon Nitride", High Temperature, 1993 May-Jun, V31 N3:535-542.

12) Wilemski, G., "Vaporization models for alumina, silicon carbide, and silicon nitride", LLNL Technical memo, TAT 96-053.2, July, 1996.

13) Schneider, S.J.Jr, Editor, ASM Engineered Materials Handbook, Volume 4: Ceramics and Glasses, ASM International, Metals Park, OH, 1989.

14) Wilemski, G., "Vaporization models for boron carbide, boron, and carbon", LLNL Technical Memo, TAT 96-057.2, Aug 1996.

15) Steinberg, D J., "Equations of state for the ceramics BeO and B_4C", LLNL, UCID-16946, Nov 1975.

16) Curren DR, Seaman L, Shockey DA, "Dynamic Failure of Solids," Physics Reports, A Review Section of Physics Letters, Vol. 147, Nos. 5 & 6, pp. 253-388, March 1987.

17) Dushman S, Scientific Foundations of Vacuum Technique, 2nd Ed, John Wiley & Sons, New York, 1962.

18) Murr LE, Interfacial Phenomena in Metals and Alloys, Addison-Wesley, Reading, Mass., 1975.

19) Holian, KS, T-4 Handbook Of Material Properties Data Bases, Los Alamos National Laboratory, LA-10160-MS, 1984.

20) Kovitya P, "Thermodynamic and Transport Properties of Ablated Vapors of PTFE, Alumina, Perspex, and PVC in the Temperature Range 5000-30,000K", IEEE Trans Plasma Science, Vol PS-12, N1, March 1984.

21) Marsh SP, LASL Shock Hugoniot Data, University of California Press, Berkeley, 1980.

22) Lynch JF, Ruderer CG, Duckworth WH, Engineering Properties of Selected Ceramic Materials, Amer Ceramic Soc, Columbus OH, 1966.

23) Shpil'rain EE, Yakimovich KA, Tsitsarkin AF, "Surface Tension of Alumina up to 2750°C and the Wetting Angle Near the Melting Point", High Temperature, vol.11, (no.5):894-900, Sept.-Oct. 1973.

24) Rothenberg JE, Kelly R, "Laser Sputtering, Part II: the Mechanism of the Sputtering of Al_2O_3", Nucl Inst & Meth, B1, pp 291-300, 1984.

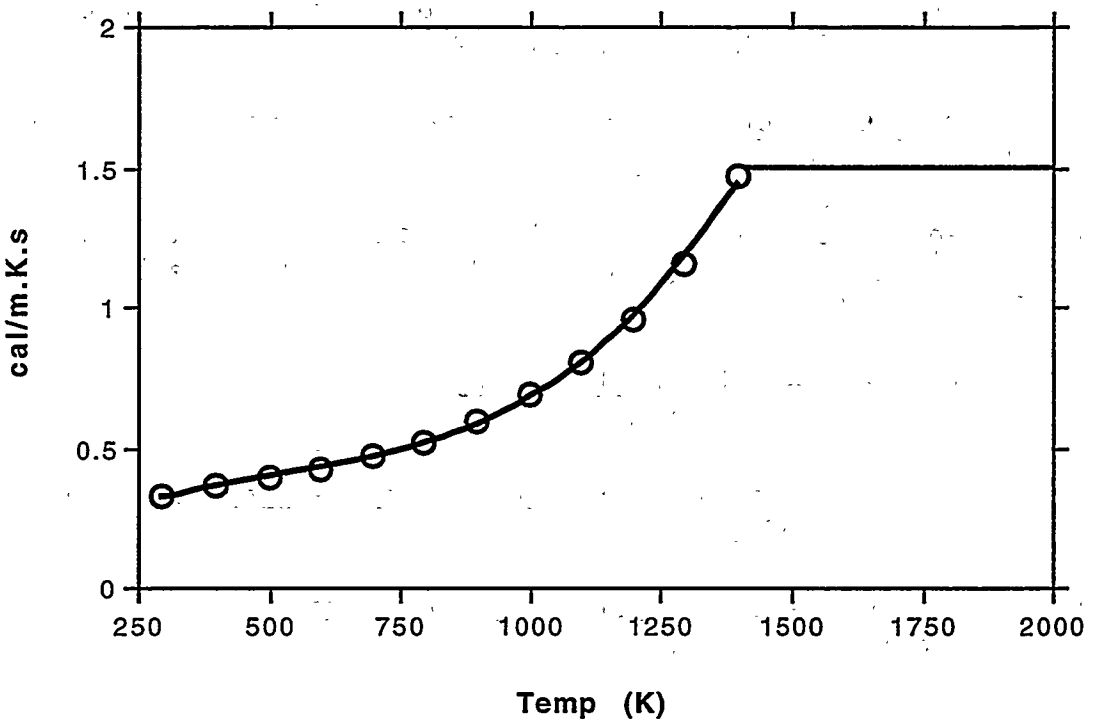

Figure 5-1: Thermal conductivity relation used for fused silica. A fit to data from Touloukian is used below 1400 K, with a constant value used at higher temperatures where no data was available.

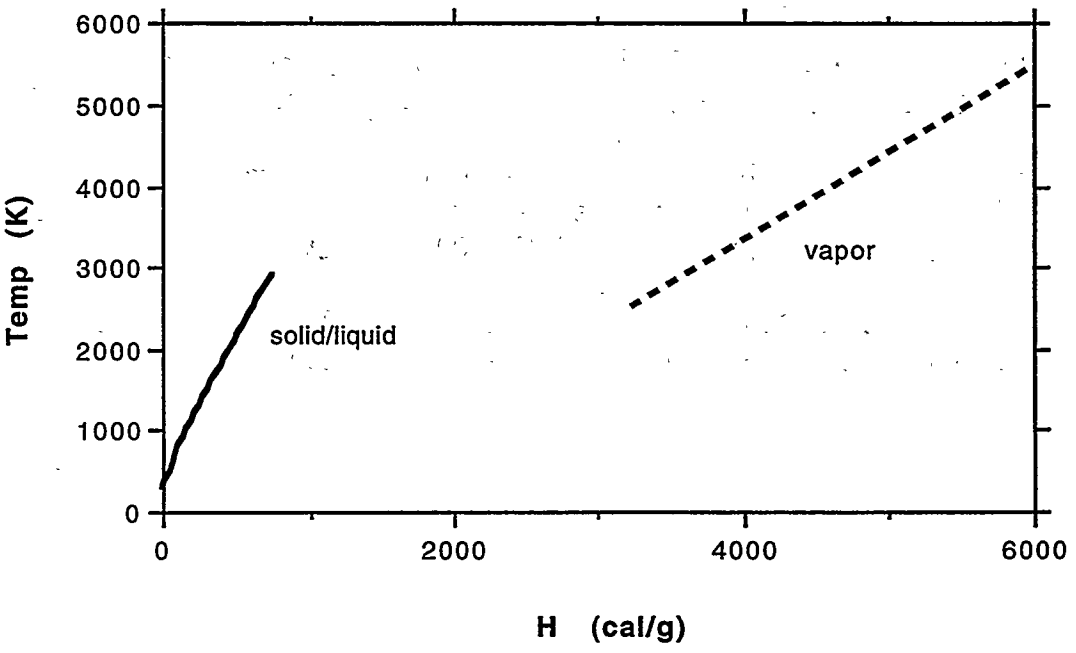

Figure 5-2: Correlation of fused silica temperature to specific enthalpy.

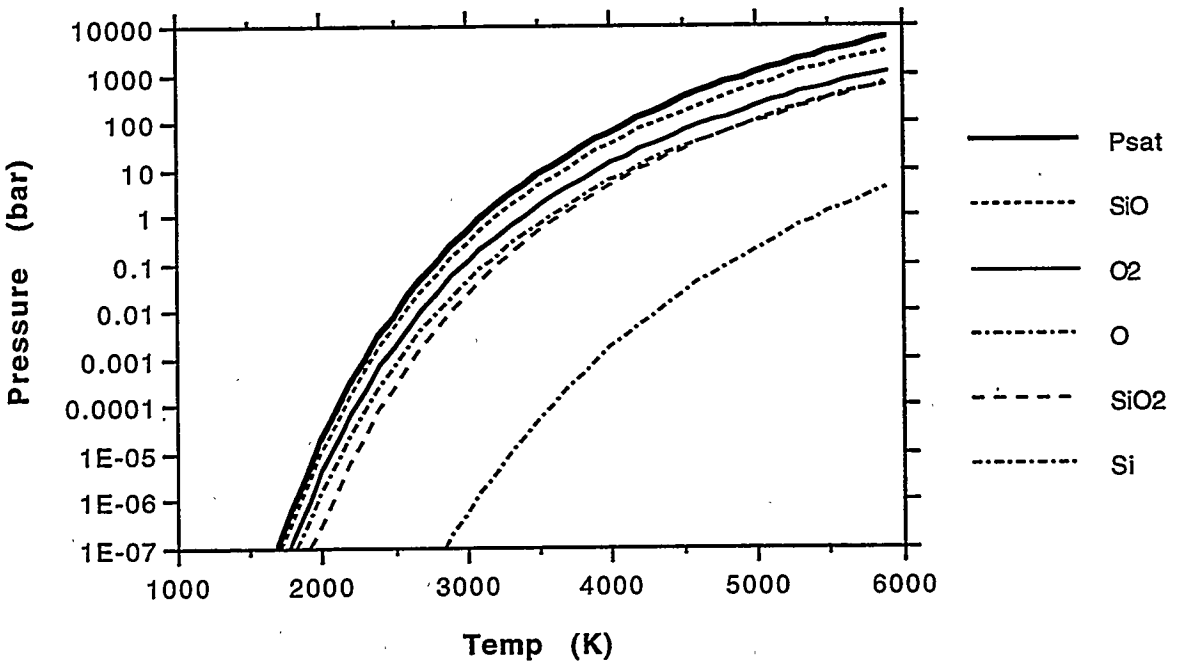

Figure 5-3: Fused silica vapor pressure as a function of temperature. Total value along with each constituent are shown for ideal gas. From Wilemski.

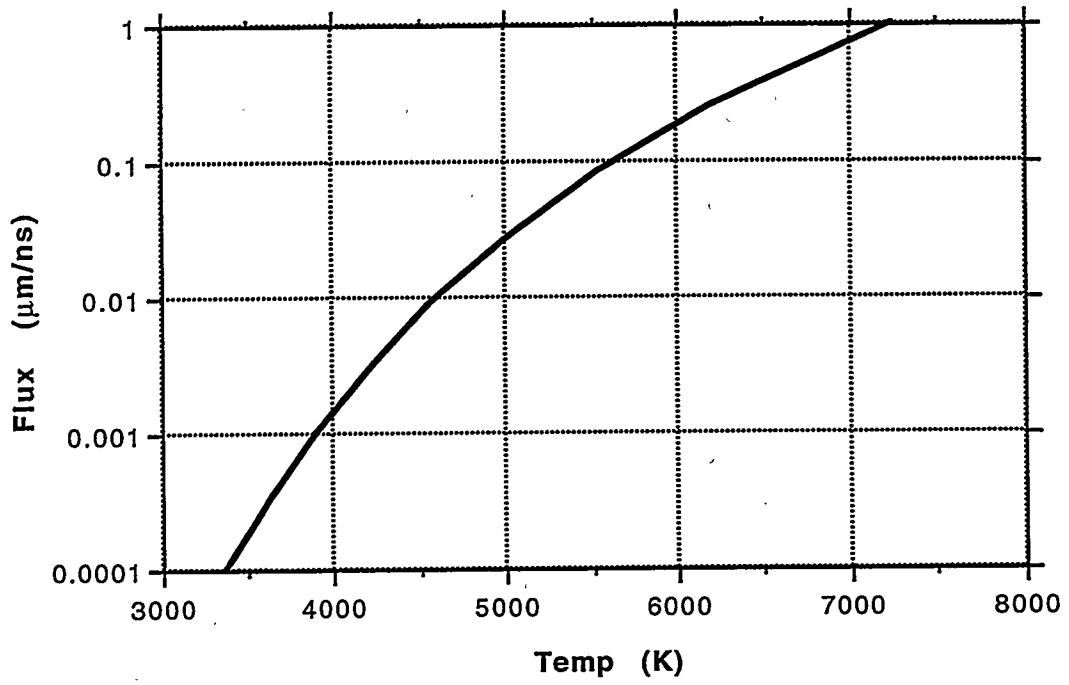

Figure 5-4: Evaporation flux for fused silica based on equilibrium rate with no recondensation.

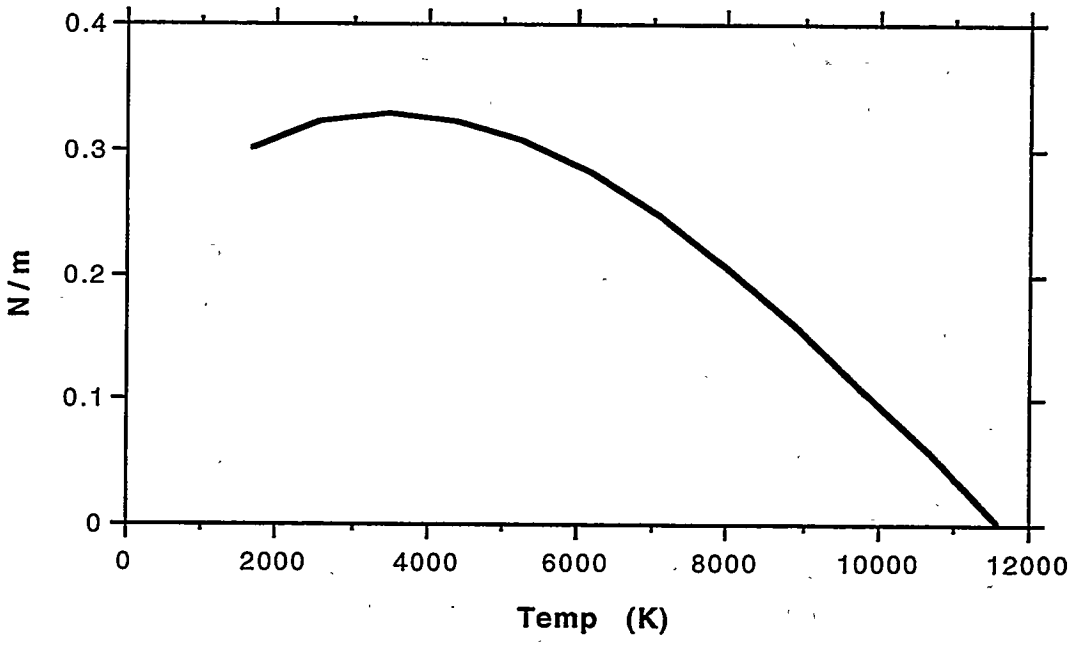

Figure 5-5: Fused silica surface tension from fit to data near 2000 K and zero value at critical point.

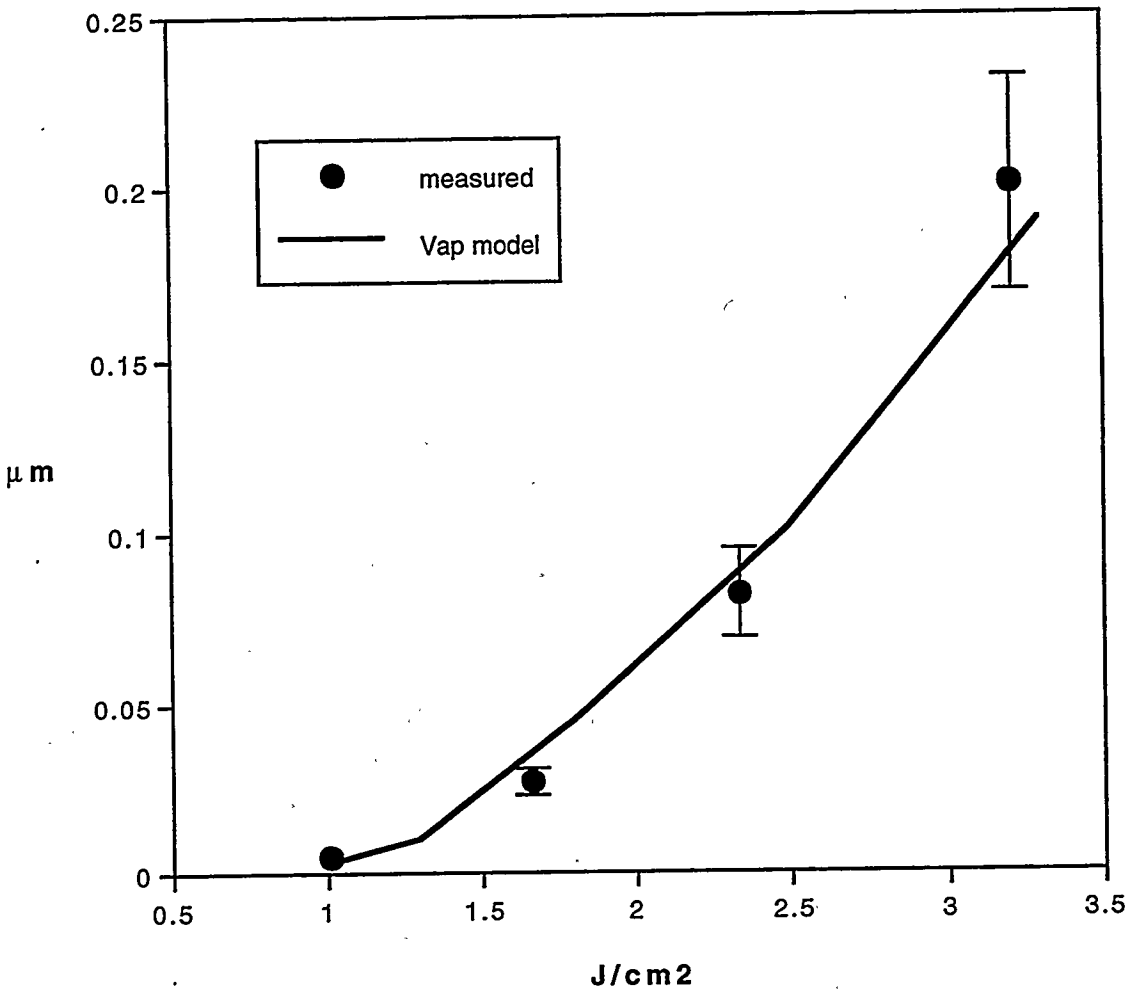

Figure 5-6: Vaporization model prediction of fused silica removal depth as a function of x-ray fluence. 250 eV x-ray spectrum in a 1 ns pulse.

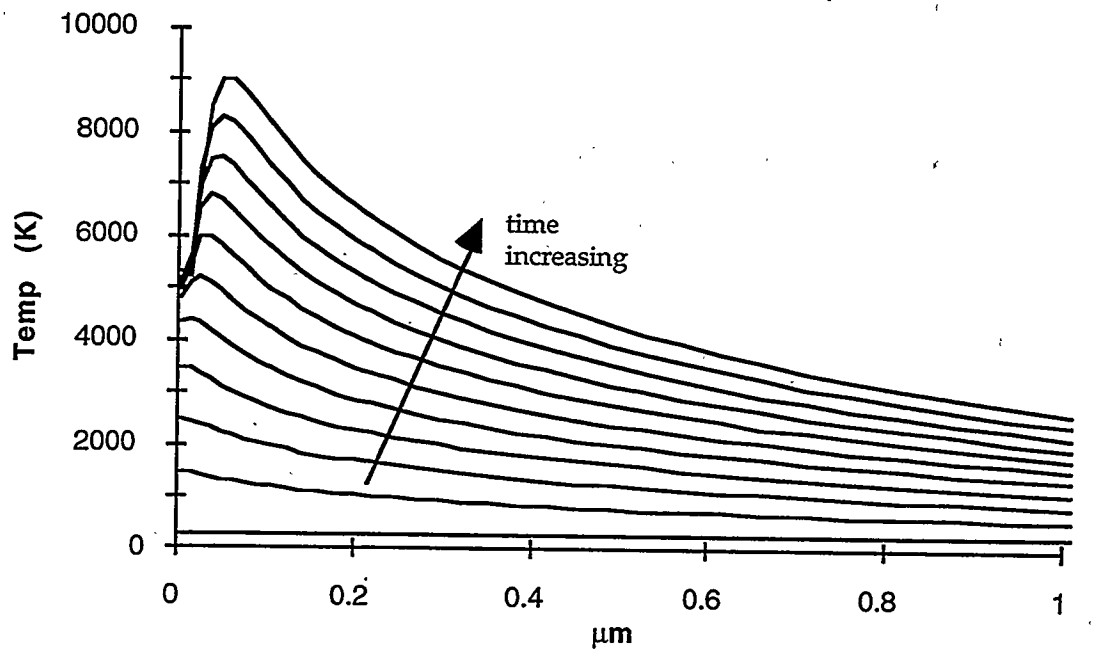

Figure 5-7a: Temperature profiles in fused silica every 0.1 ns during heating with 1-ns square pulse at 2.5 J/cm^2 of 220-eV blackbody x rays. Front surface temperature limited by vaporization flux energy balance.

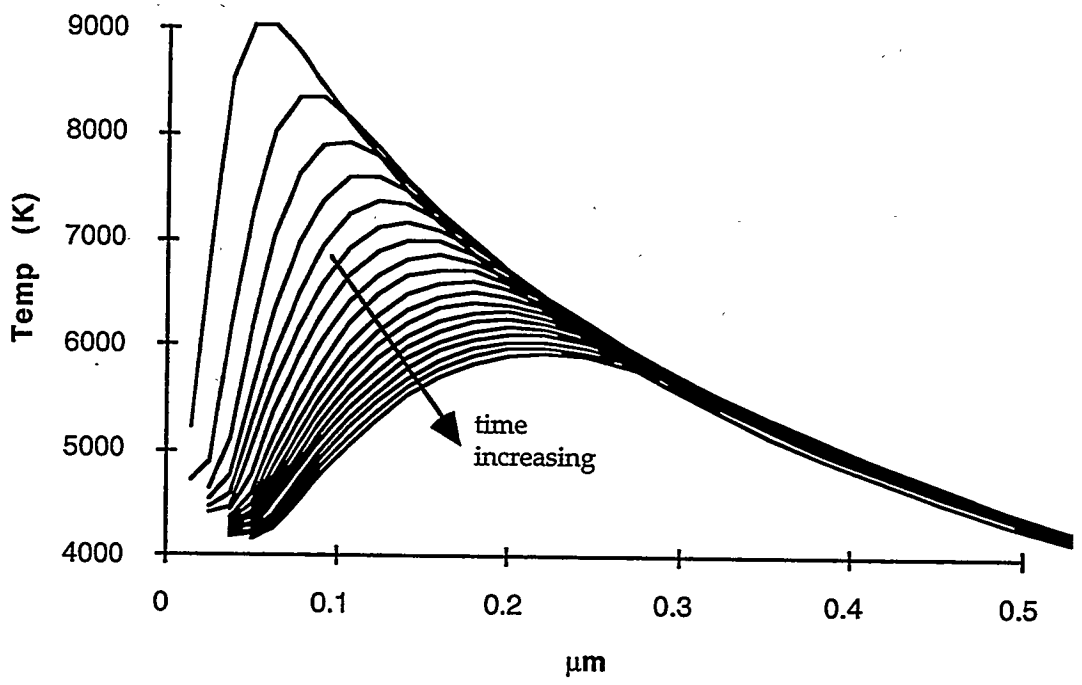

Figure 5-7b: Temperature profiles in fused silica every 0.5 ns (1 - 10 ns) during cooling after 1-ns square pulse at 2.5 J/cm^2.

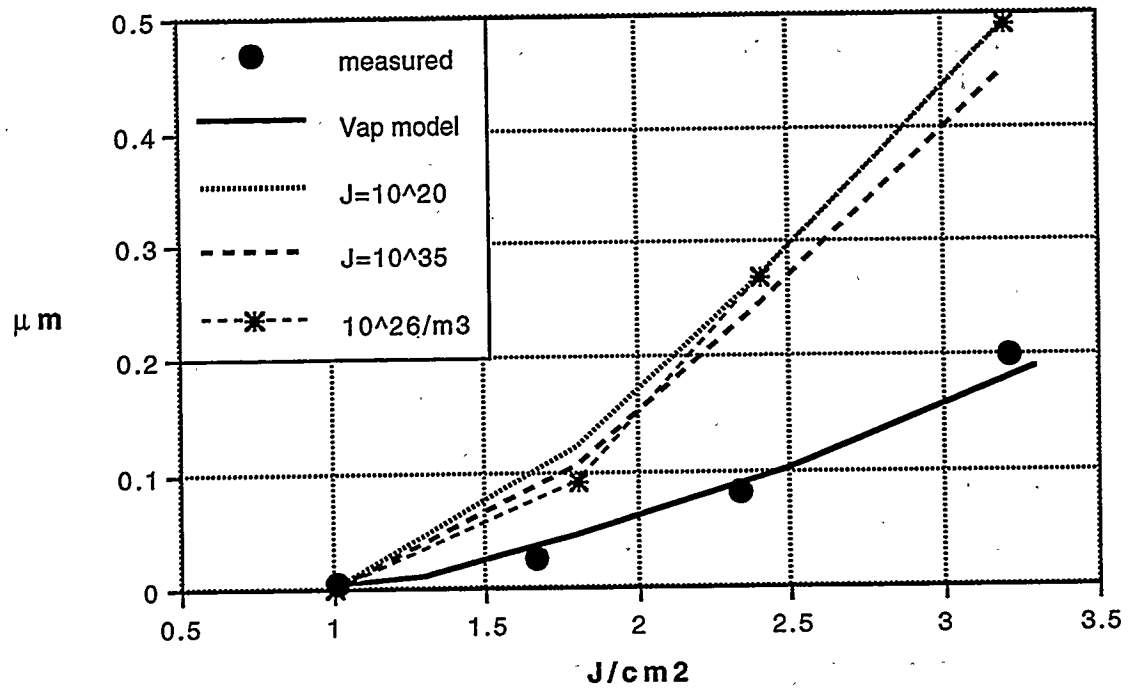

Figure 5-8: Depths of peak bubble nucleation rates in fused silica for 220-eV blackbody x rays in a 1-ns pulse. These rates are due to thermal effects, not the passage of a tensile wave. J is given in units of $m^{-3}s^{-1}$. Last curve is depth the integral of J with time reaches 10^{26} bubbles/m^3 (5% by volume).

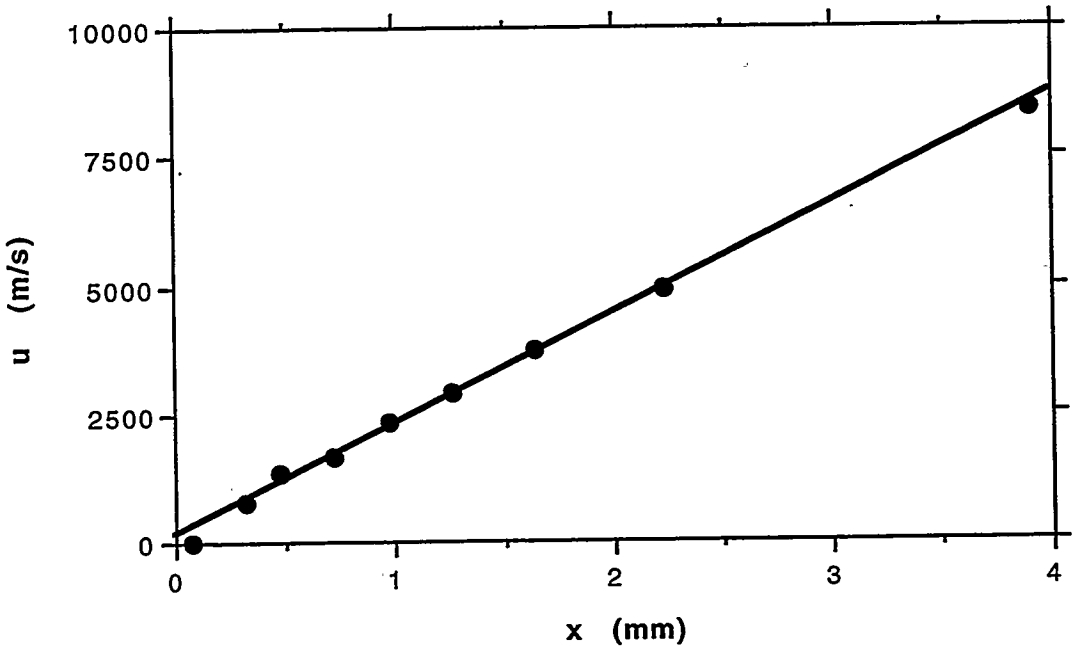

Figure 5-9: Silica vapor velocity as a function of position at the end of the 2.5 J/cm^2 run (500 ns). Curve fit shows expected linear relation for an isentropic expansion. x is distance from the original surface.

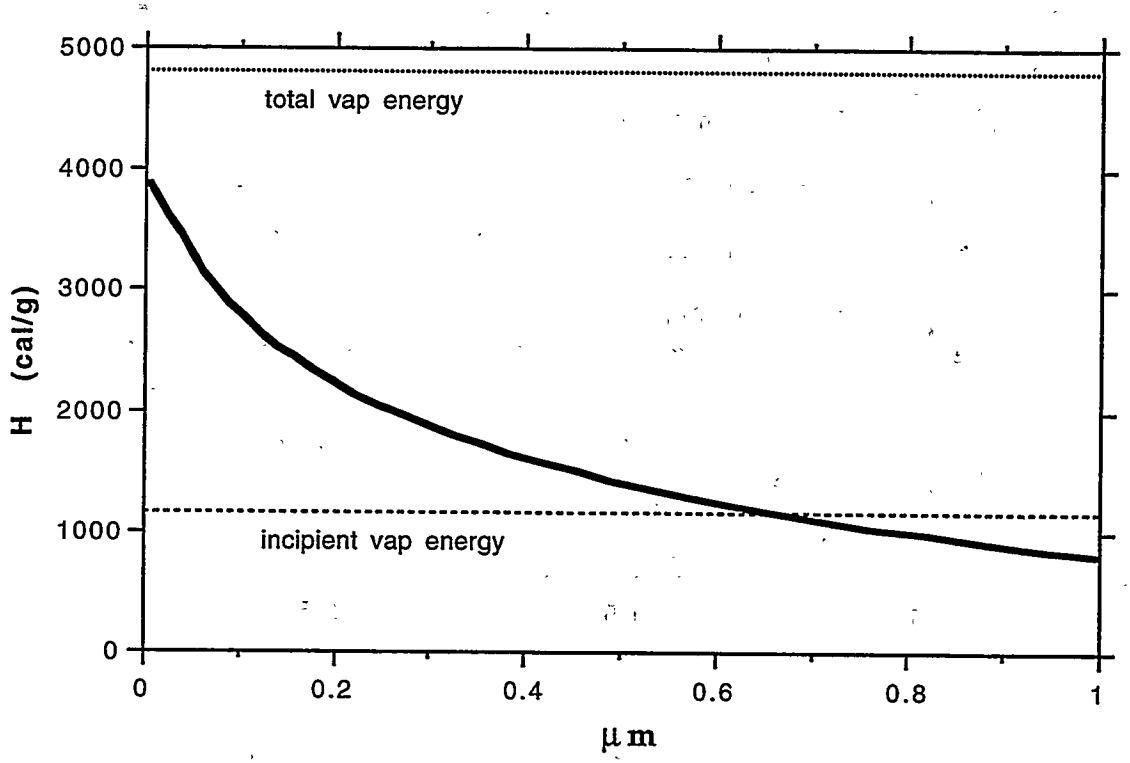

Figure 5-10: Energy profile in silica for instantaneous deposition of 2.5 J/cm2 of 220-eV blackbody x rays. No removal is predicted based on total vaporization energy criterion, and about 0.6-0.7 μm based on incipient vaporization.

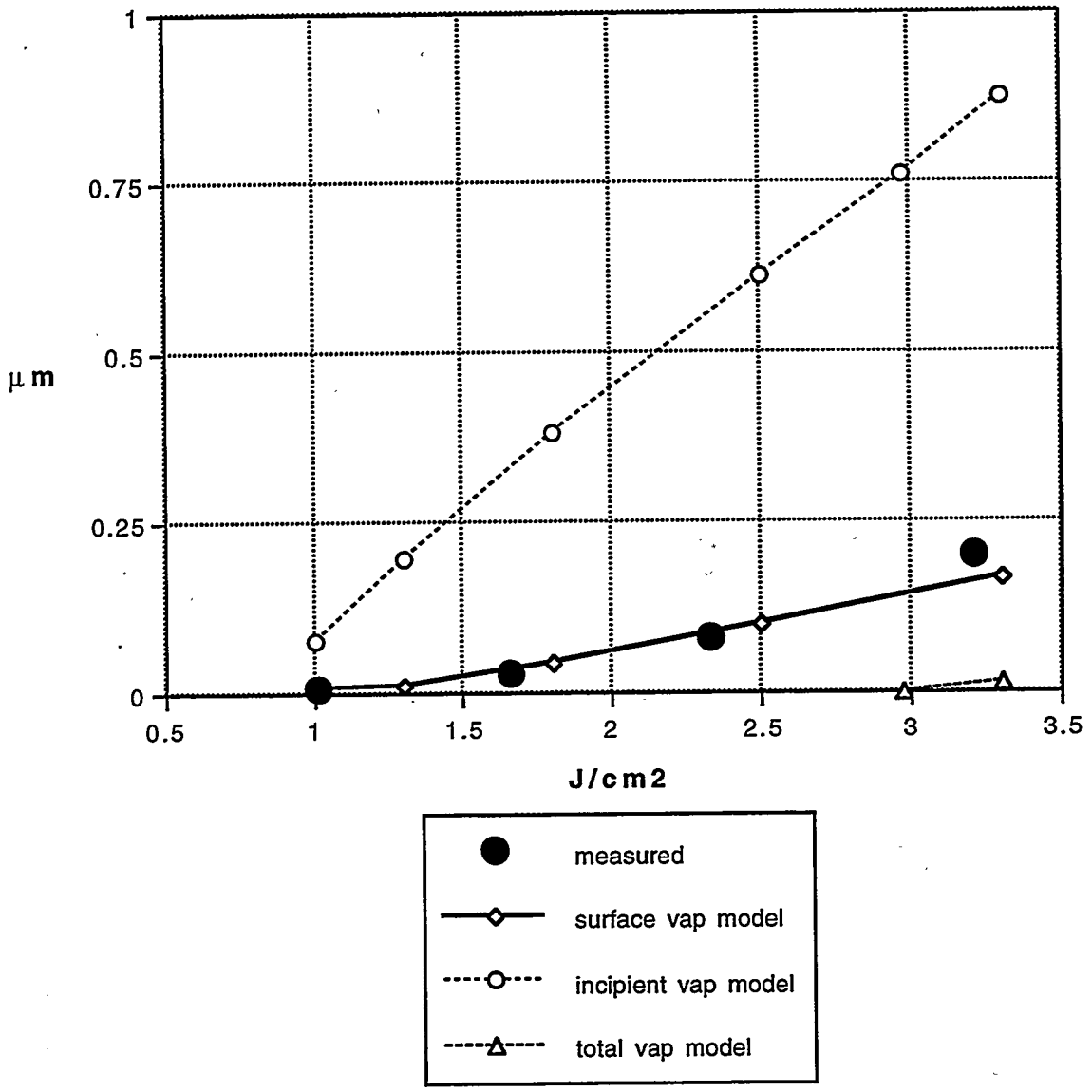

Figure 5-11: Measured silica removal along with predictions based on instantaneous deposition method and on the surface vaporization model. "total vap" is removal to the point where the material has the complete vaporization energy, including latent heat. "incipient vap" is removal to the depth where the material is hot enough to vaporize, but lacks the vaporization energy (hot solid/liquid).

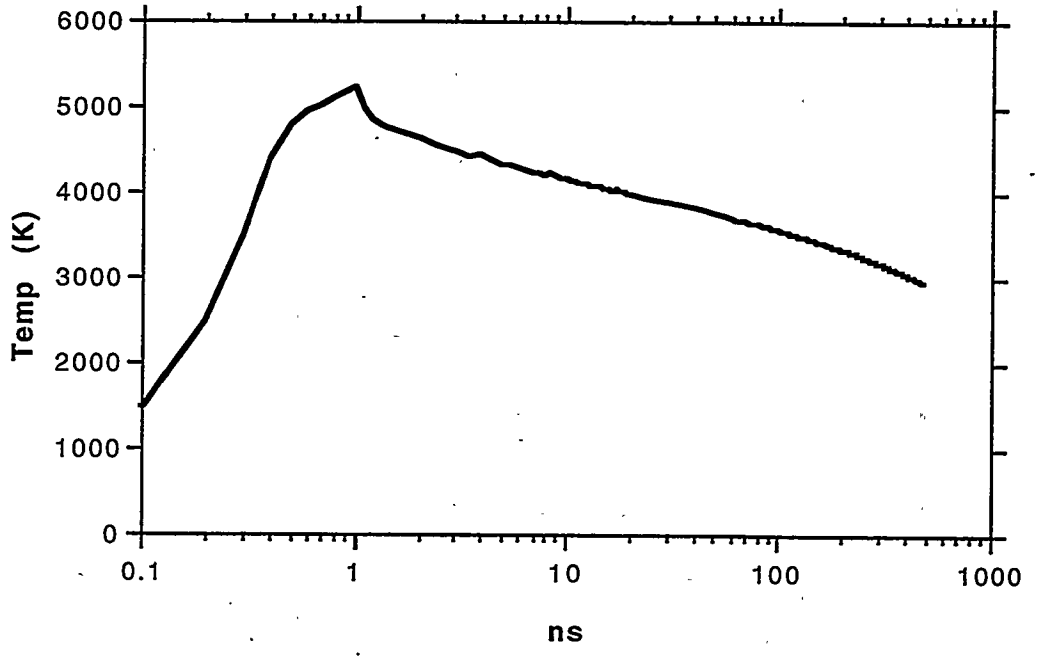

Figure 5-12: Fused silica surface temperature as a function of time for 2.5 J/cm^2 fluence, 250-eV BB, 1-ns pulse.

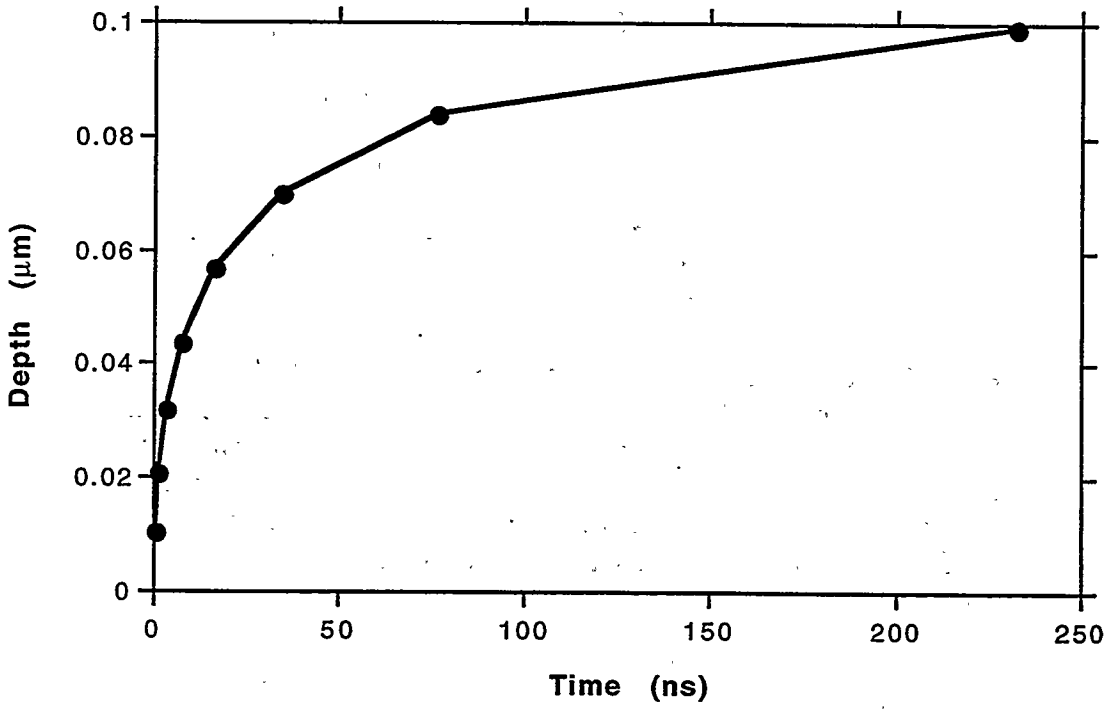

Figure 5-13: Vaporized depth in fused silica as a function of time for the 2.5 J/cm^2 case. (250-eV blackbody spectrum, 1-ns square pulse). From ABLATOR model.

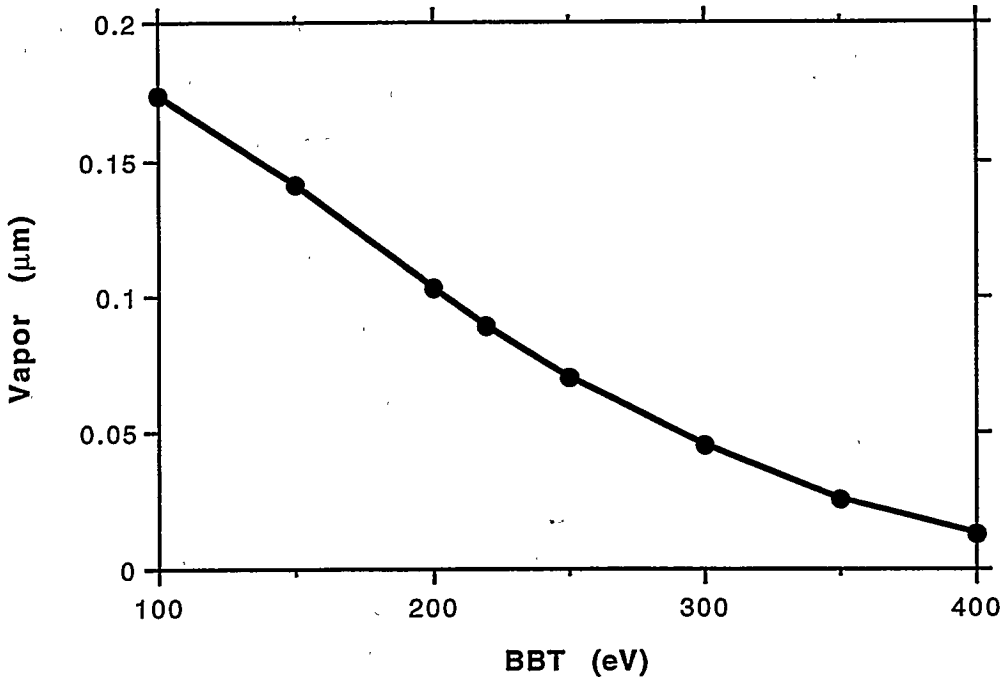

Figure 5-14: Spectral sensitivity of vaporized depth for fused silica exposed to 2.5 J/cm^2 x-ray fluence in a 1-ns pulse at 220-eV blackbody spectrum.

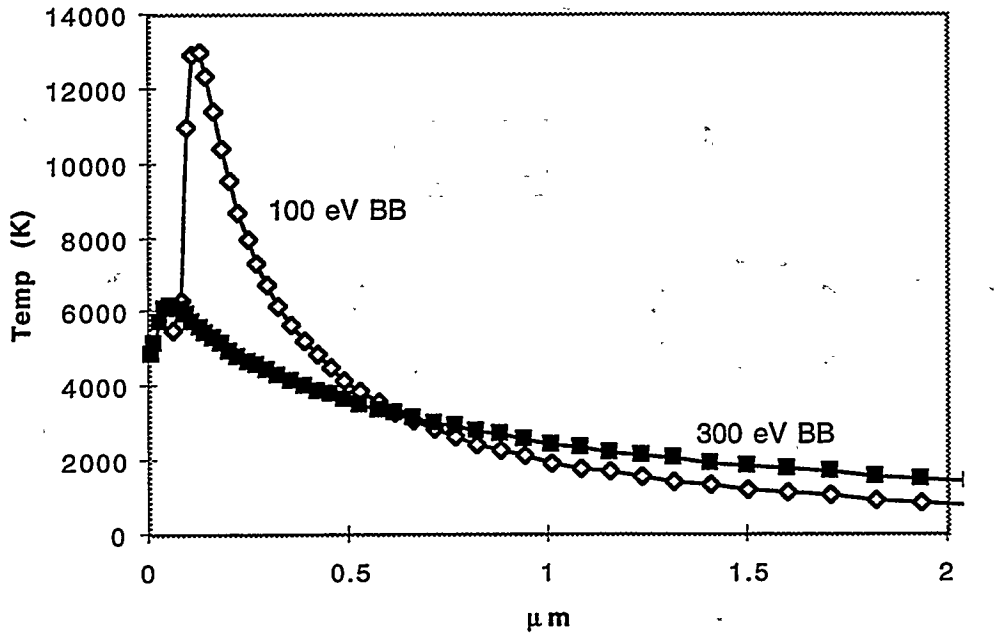

Figure 5-15: Peak temperature profiles in fused silica for 2.5 J/cm^2 x-ray fluence in a 1-ns pulse. Vaporization is enhanced by higher surface and subsurface temperatures with the colder x-ray spectrum.

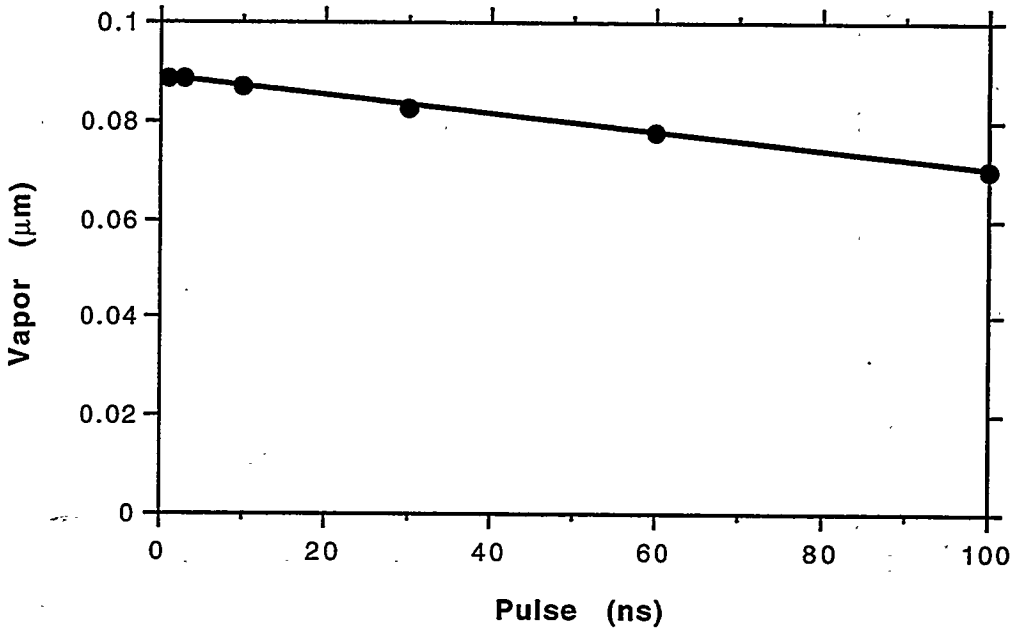

Figure 5-16: Pulse length sensitivity of vaporized depth for fused silica exposed to 2.5 J/cm^2 x-ray fluence at 220-eV BB.

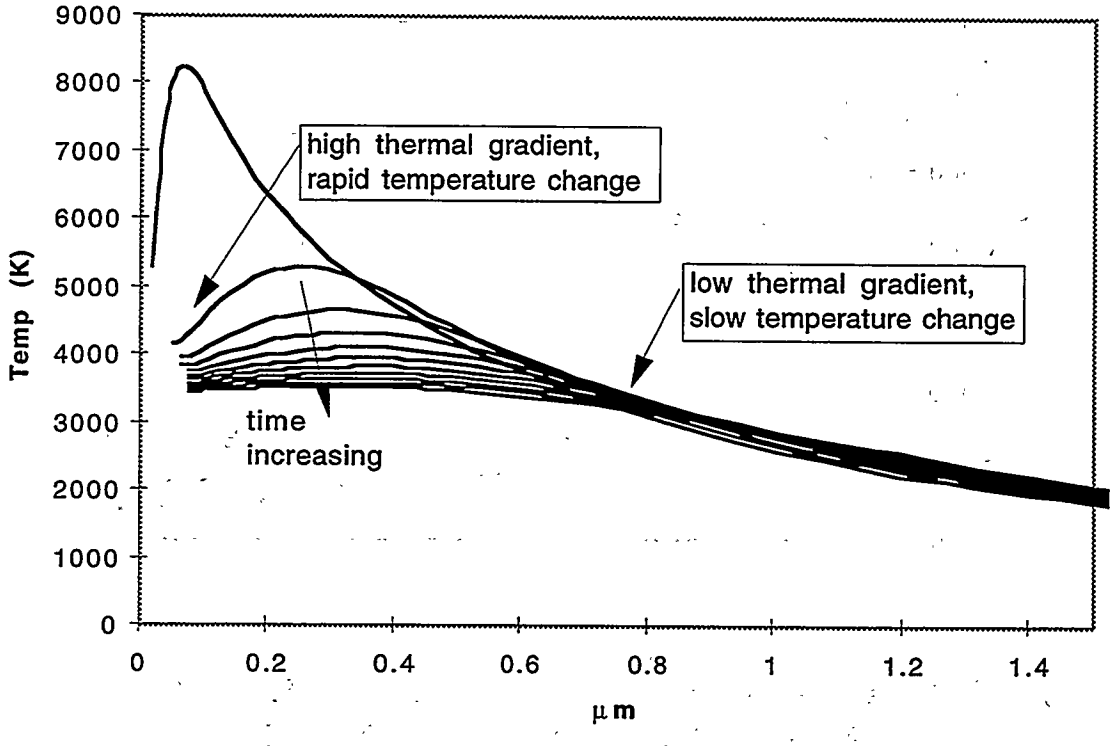

Figure 5-17: Temperature profiles in silica after 2.5 J/cm2 of 220-eV BB x rays in a 1-ns pulse. Curves are at the peak (1 ns), then at 10ns, 20ns, out to 100 ns.

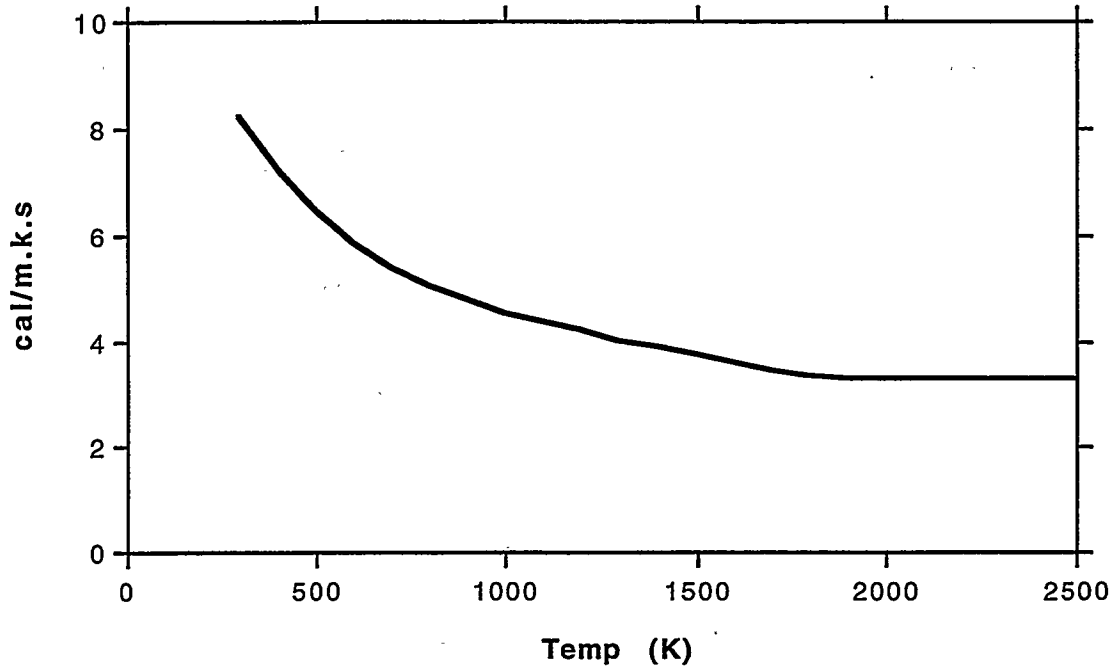

Figure 5-18: Thermal conductivity relation used for silicon nitride. A fit to data from Touloukian[8] is used below 2000 K, with a constant value used at higher temperatures where no data was available.

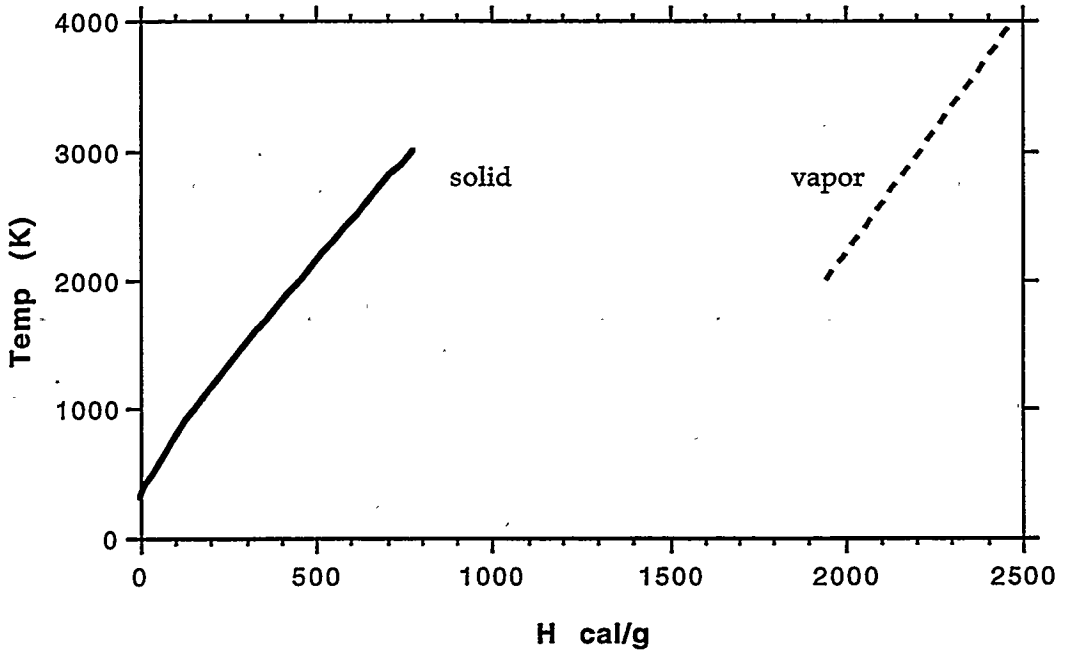

Figure 5-19: Correlation of silicon nitride temperature to specific enthalpy. The "vapor" energy is the sum of nitrogen gas and silicon liquid stoichiometrically evolved from the surface.

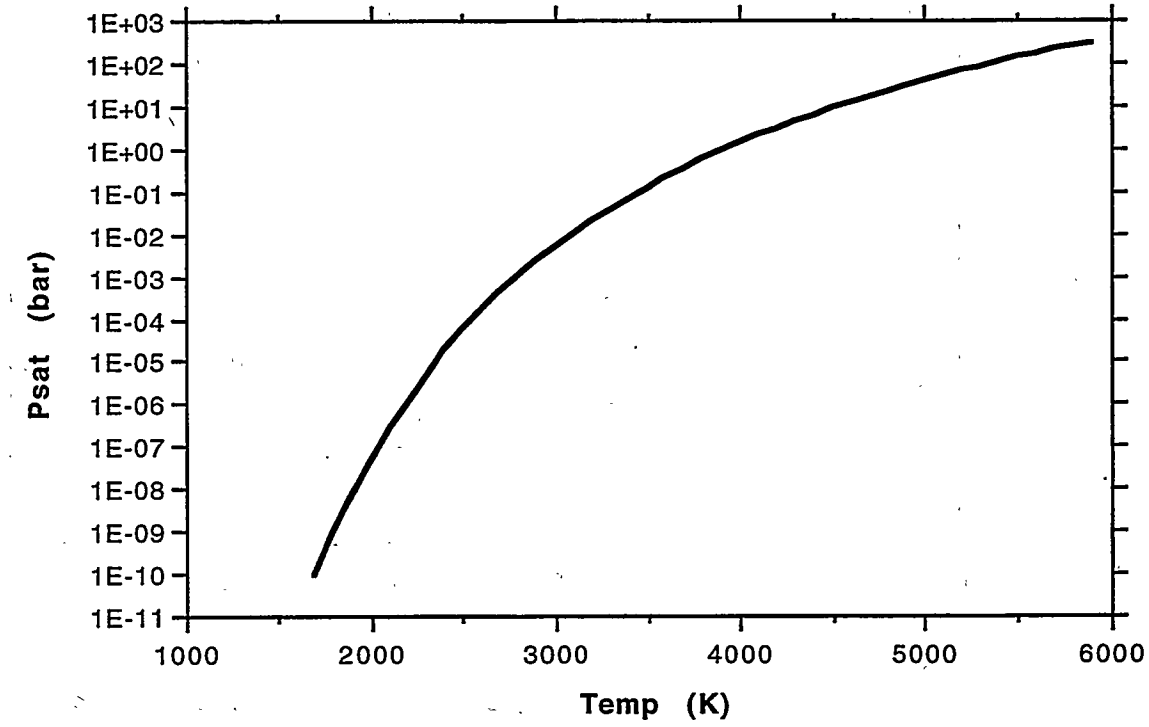

Figure 5-20: Silicon nitride vapor pressure as a function of temperature. Composed almost entirely of nitrogen gas. From Wilemski.

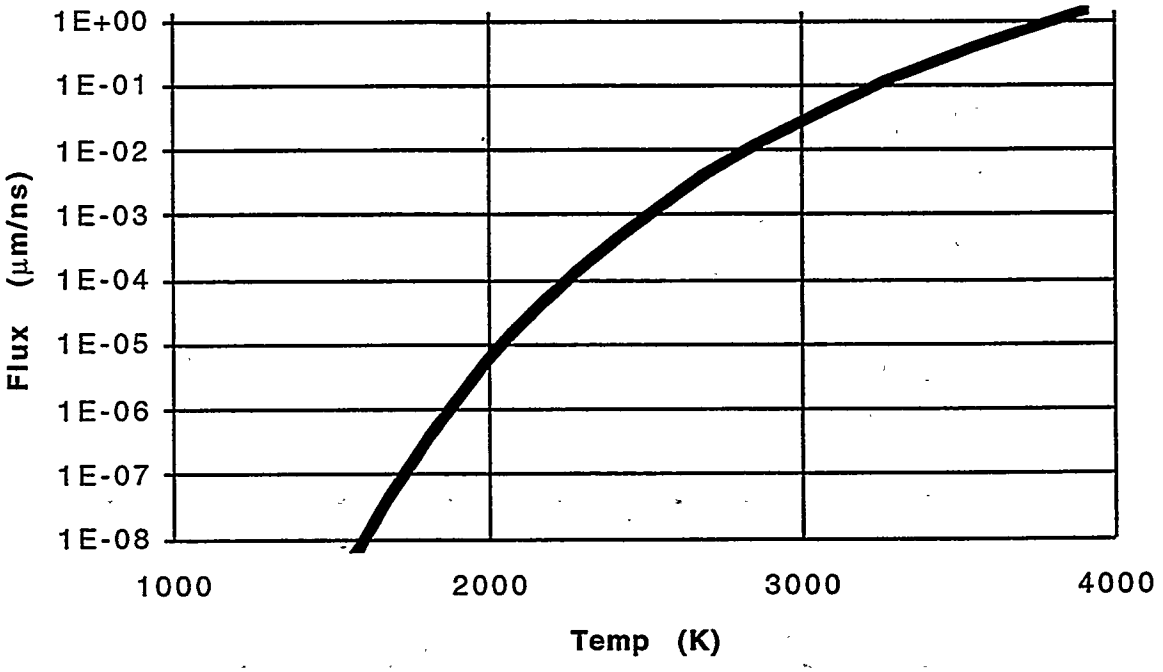

Figure 5-21: Evaporation flux for silicon nitride based on equilibrium rate with no recondensation.

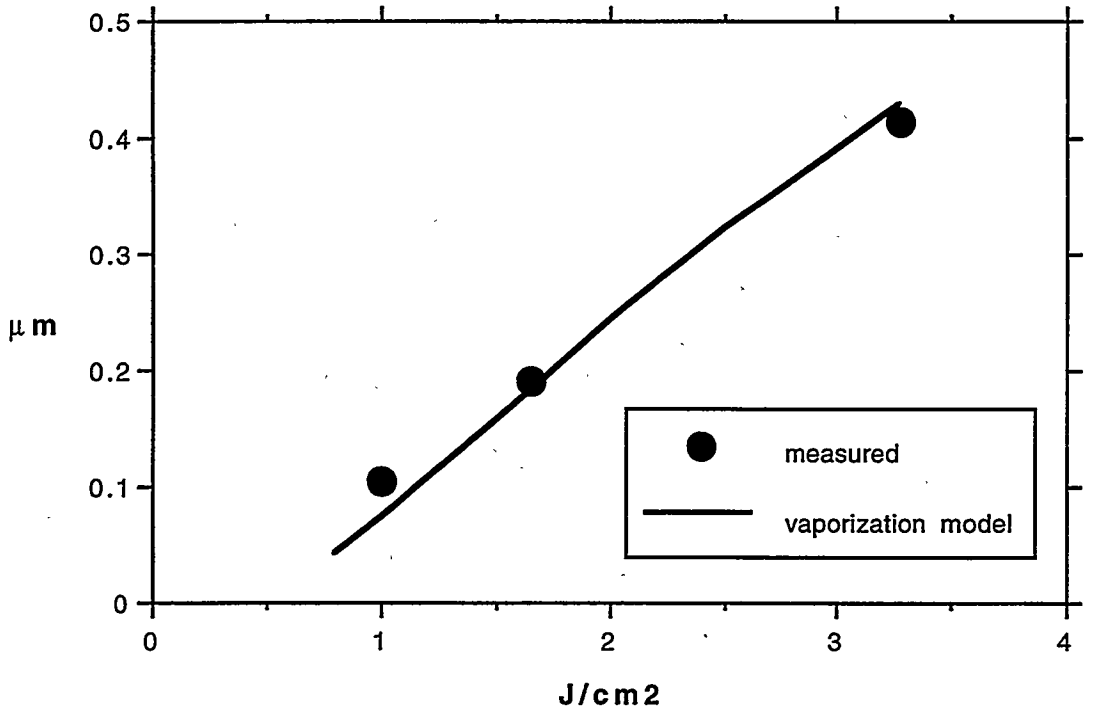

Figure 5-22: Vaporization model prediction of silicon nitride removal depth as a function of x-ray fluence. 200-eV BB x-ray spectrum in a 2.2-ns pulse.

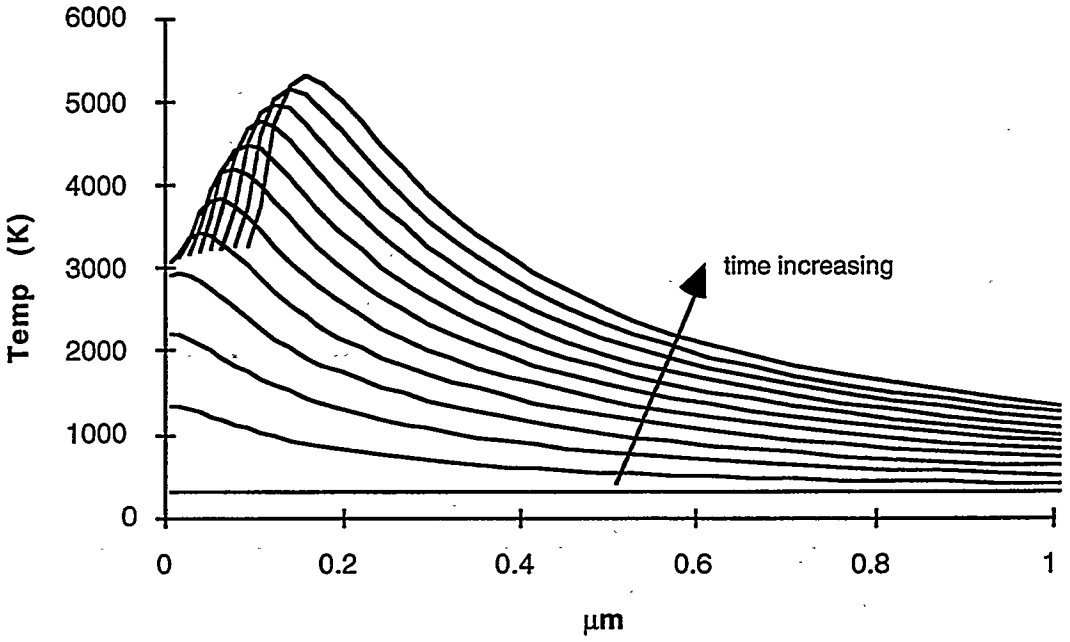

Figure 5-23a: Temperature profiles in silicon nitride every 0.2 ns during heating with 2.2-ns square pulse at 1.65 J/cm^2 and 200-eV BB.

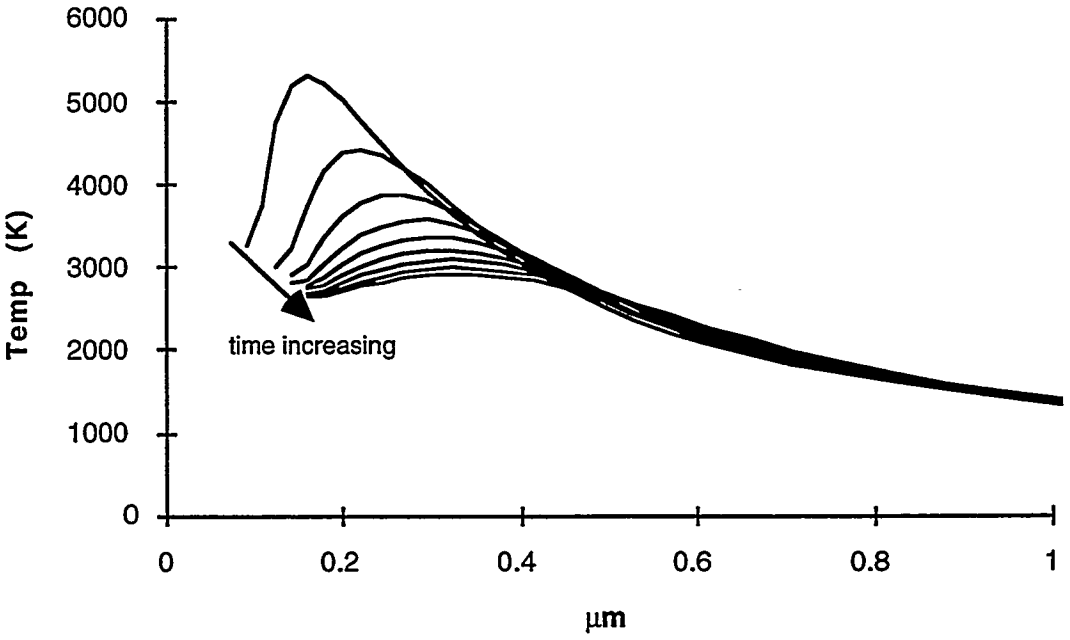

Figure 5-23b: Temperature profiles in silicon nitride at peak (2.2 ns) and every 0.5 ns (2.5 - 10 ns) during cooling after 2.2-ns square pulse at 1.65 J/cm^2 with a 200-eV blackbody spectrum.

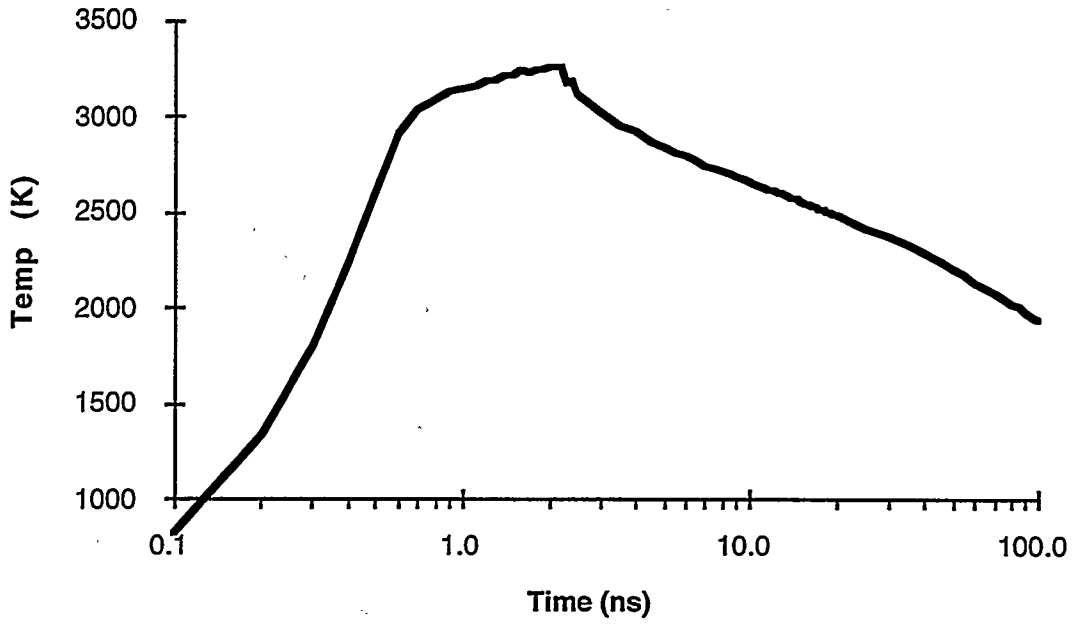

Figure 5-24: Silicon nitride surface temperature as a function of time for 1.65 J/cm^2 fluence in a 2.2-ns pulse with a 200-eV blackbody spectrum.

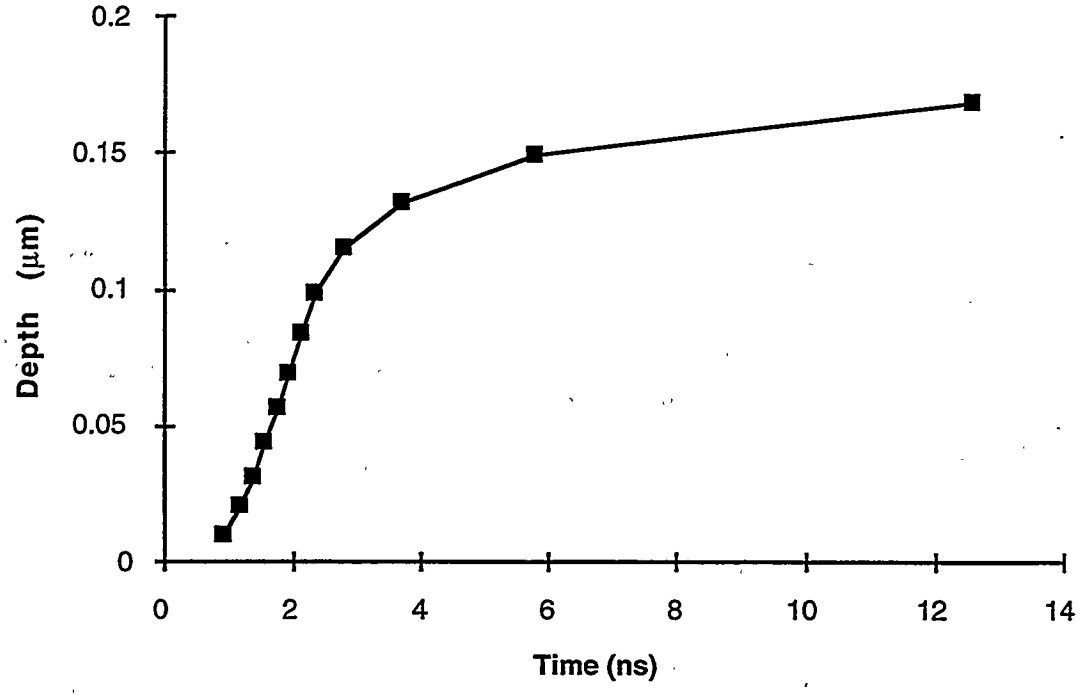

Figure 5-25: Vaporized depth in silicon nitride as a function of time for 1.65 J/cm^2 case.

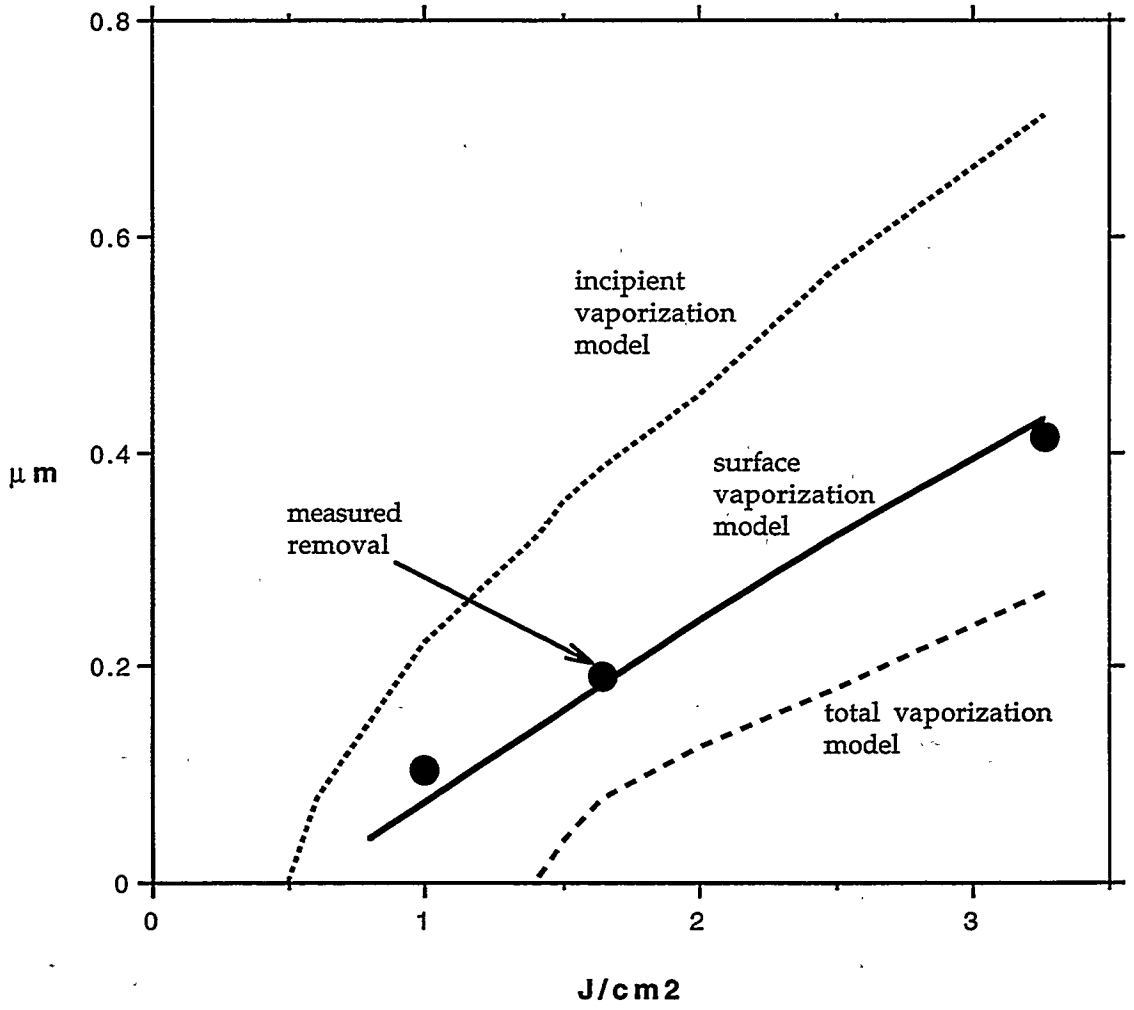

Figure 5-26: Measured silicon nitride removal along with predictions based on the surface vaporization model and on the instantaneous deposition method. "total vaporization" is removal to the point where the material has the complete vaporization energy, including latent heat. "incipient vaporization" is removal to the depth where the material is hot enough to vaporize, but lacks the vaporization energy (hot solid).

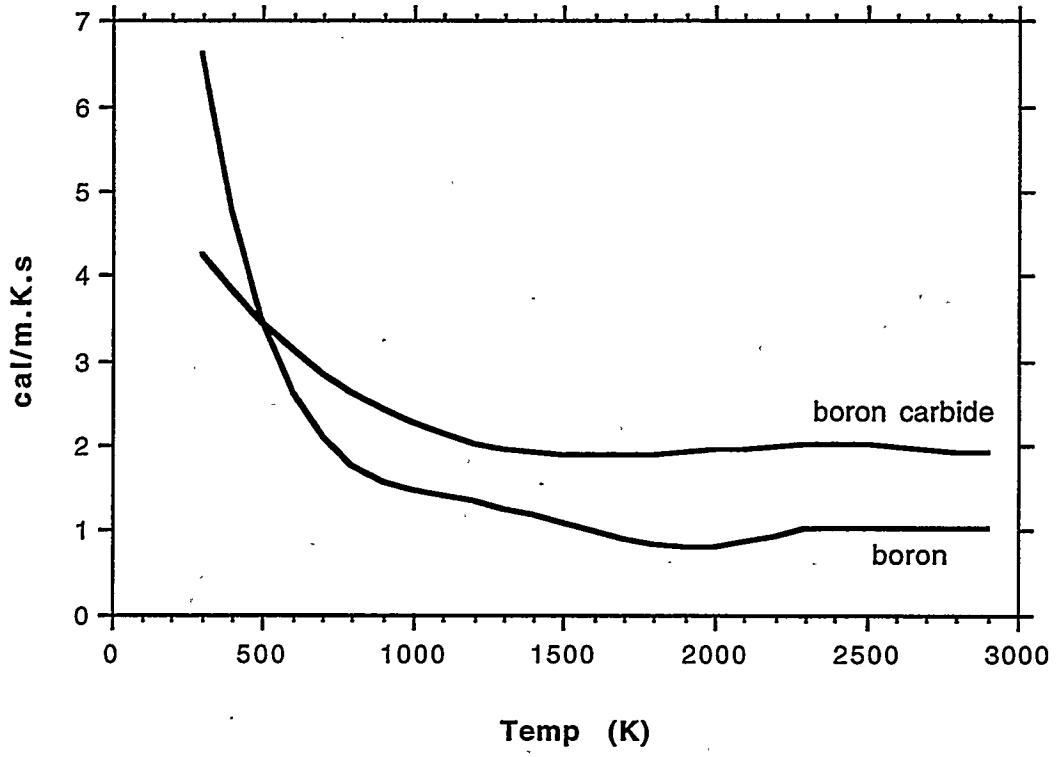

Figure 5-27: Thermal conductivity relations used for boron carbide and boron.

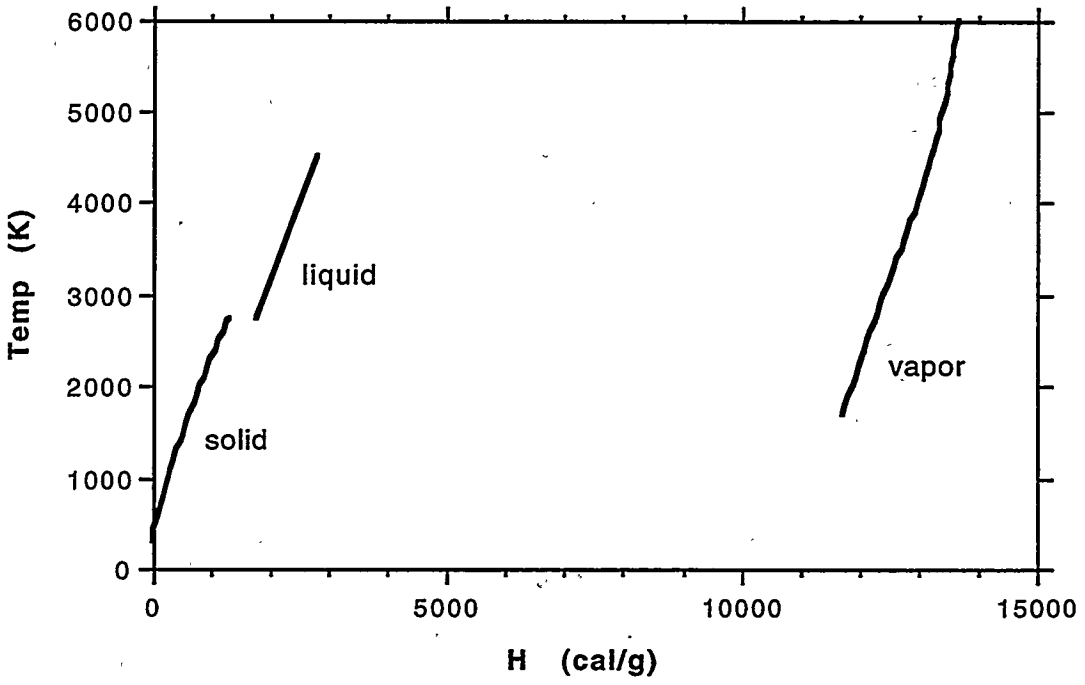

Figure 5-28: Correlation of boron carbide temperature to specific enthalpy.

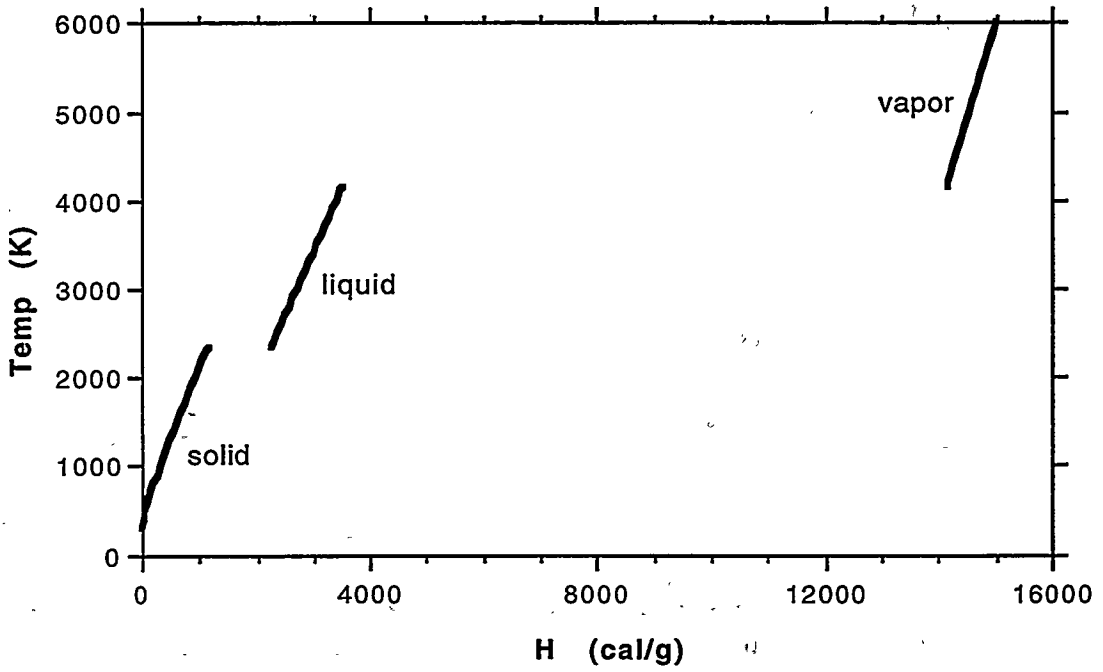

Figure 5-29: Correlation of boron temperature to specific enthalpy.

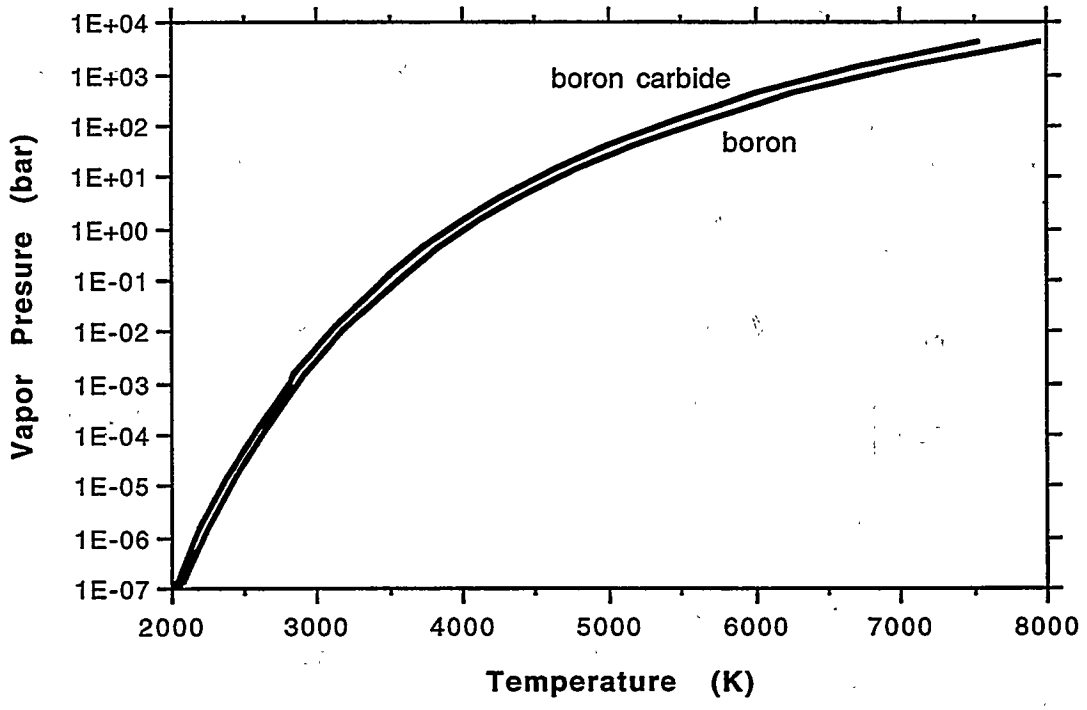

Figure 5-30: Equilibrium vapor pressures as a function of temperature.

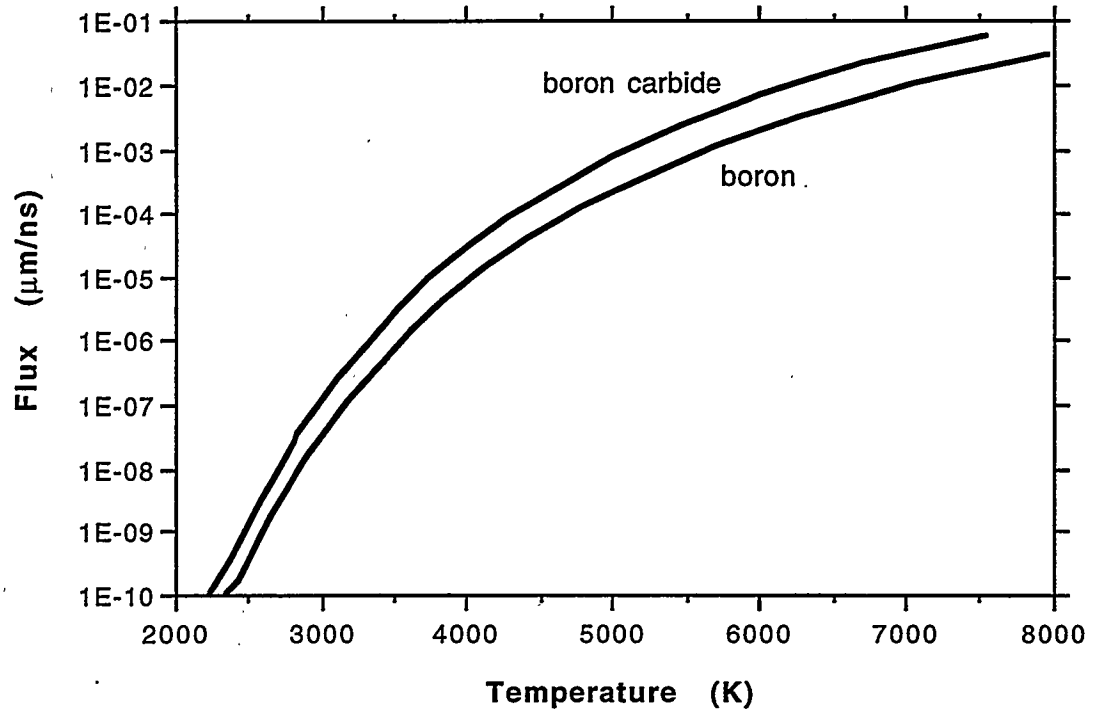

Figure 5-31: Evaporation flux based on equilibrium rate with no recondensation.

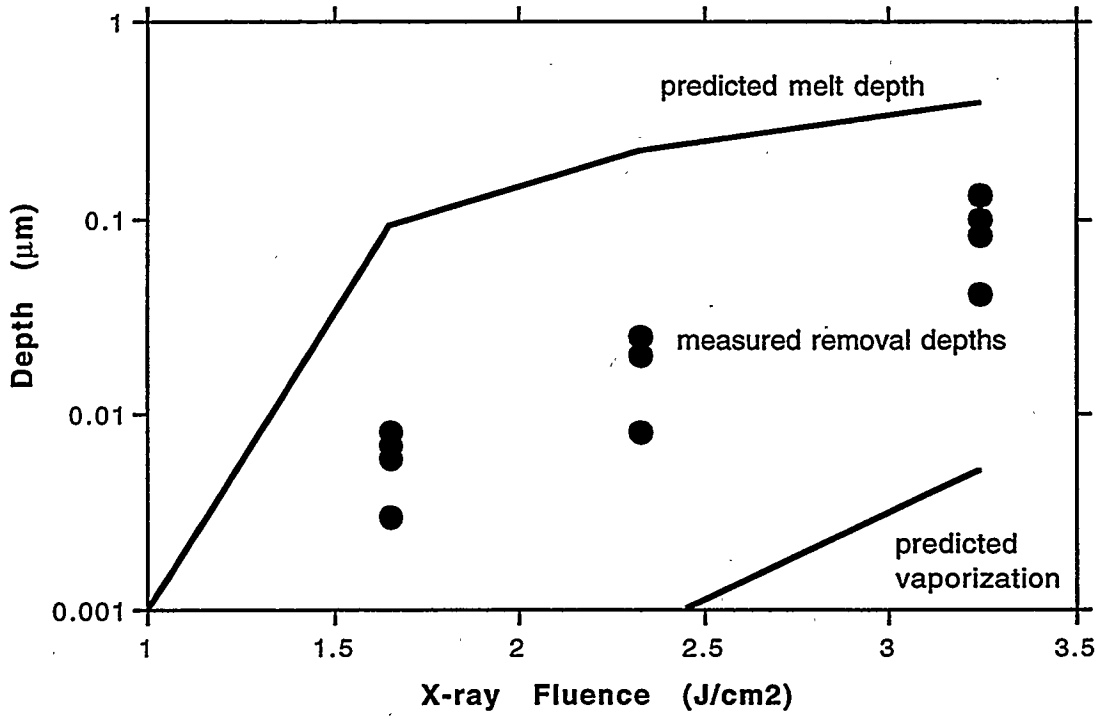

Figure 5-32: Comparison of model predictions of boron carbide vaporization removal depth and melt depth to measured removal data as a function of x-ray fluence. 250-eV BB x-ray spectrum in a 1-ns pulse.

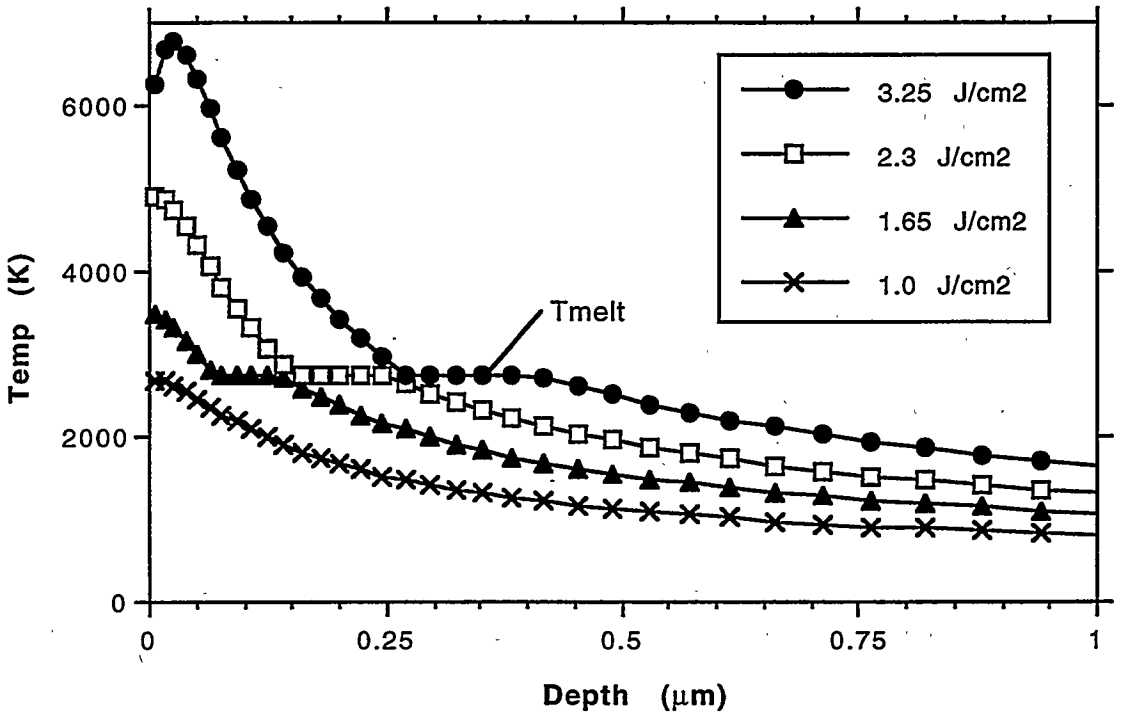

Figure 5-33: Peak temperature profiles in boron carbide for x-ray deposition with a 250-eV blackbody spectrum in a 1-ns square pulse.

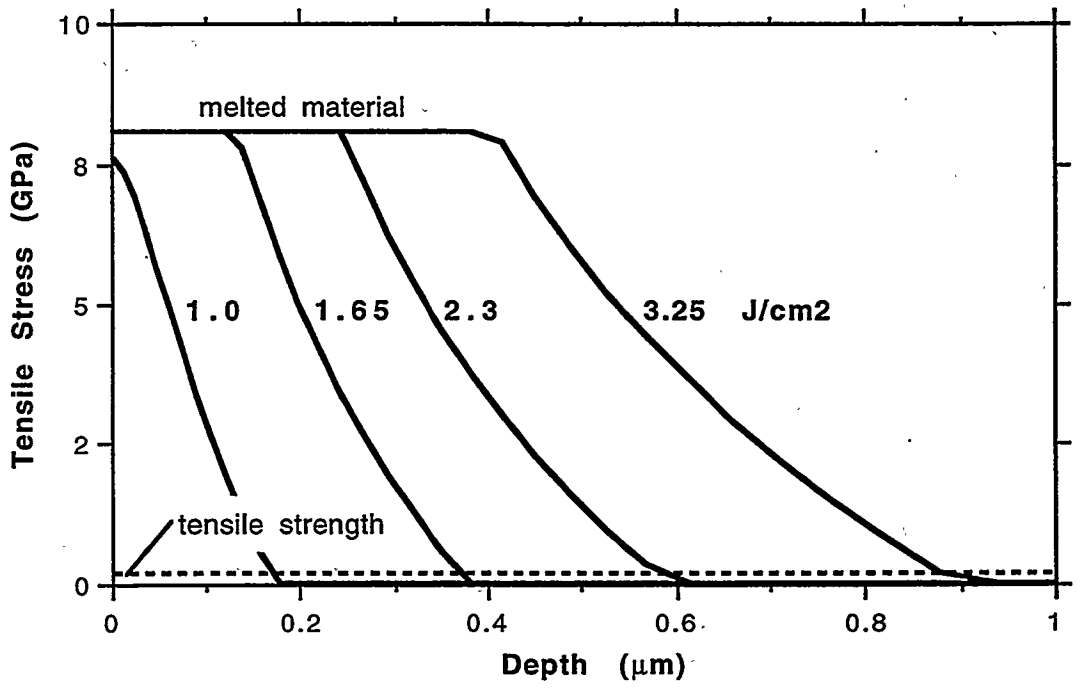

Figure 5-34: Thermal stress profiles in boron carbide based on peak temperature profiles of Figure 5-33 and a linear softening model.

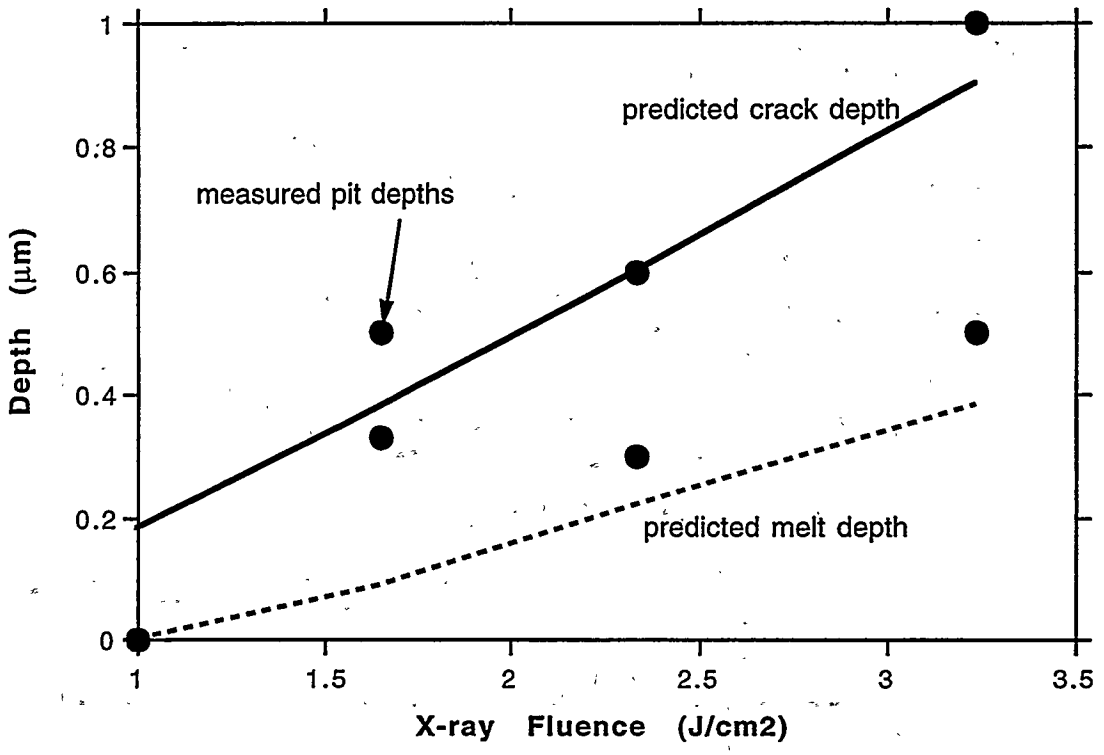

Figure 5-35: Average pit depths in boron carbide surfaces compared to predicted thermal stress crack depths, predicted melt depths, and measured removal depths as a function of x-ray fluence.

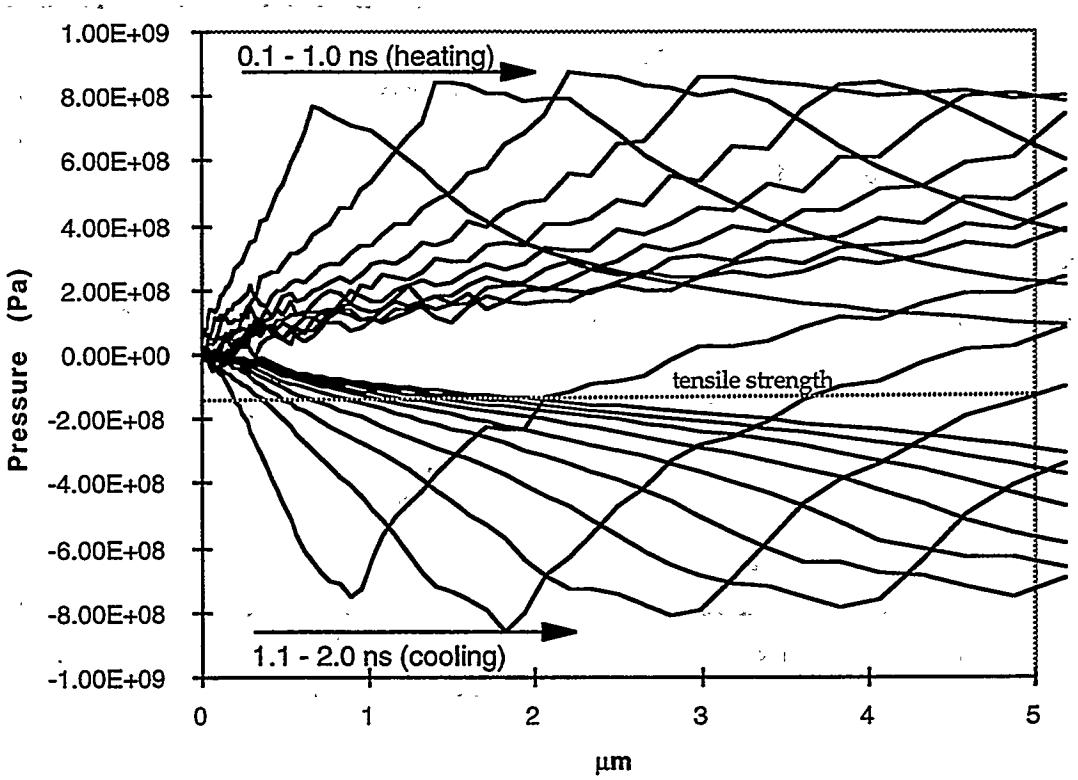

Figure 5-36a: Development and propagation of shock and rarefaction waves in boron carbide exposed to 2.3 J/cm^2 of 250-eV blackbody x rays in 1-ns pulse.

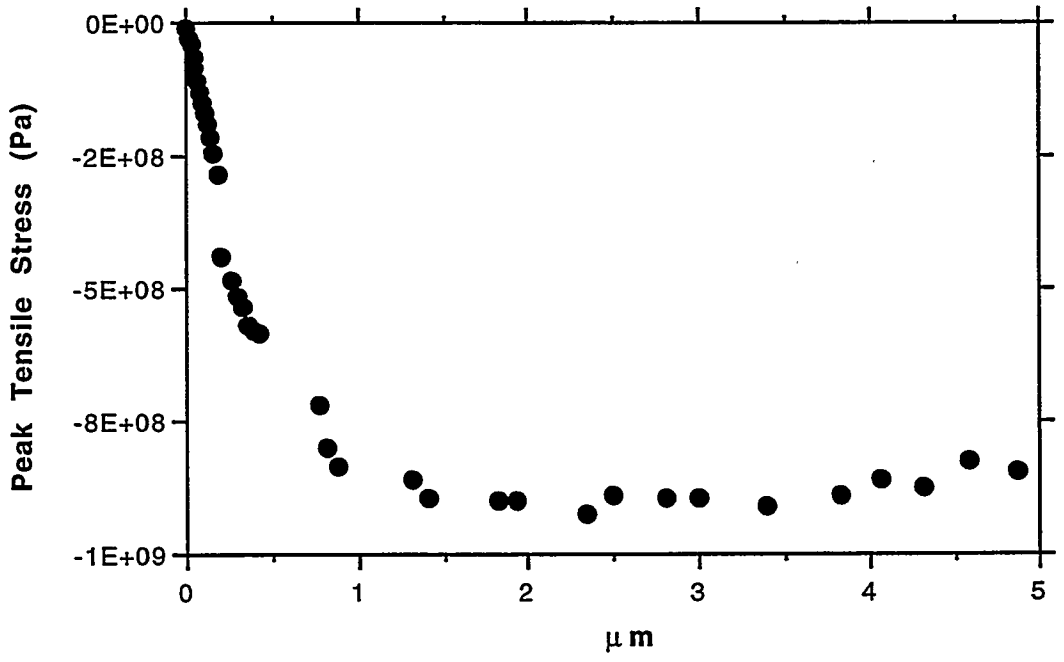

Figure 5-36b: Peak tensile stress in boron carbide as a function of depth. Same x-ray conditions as part (a).

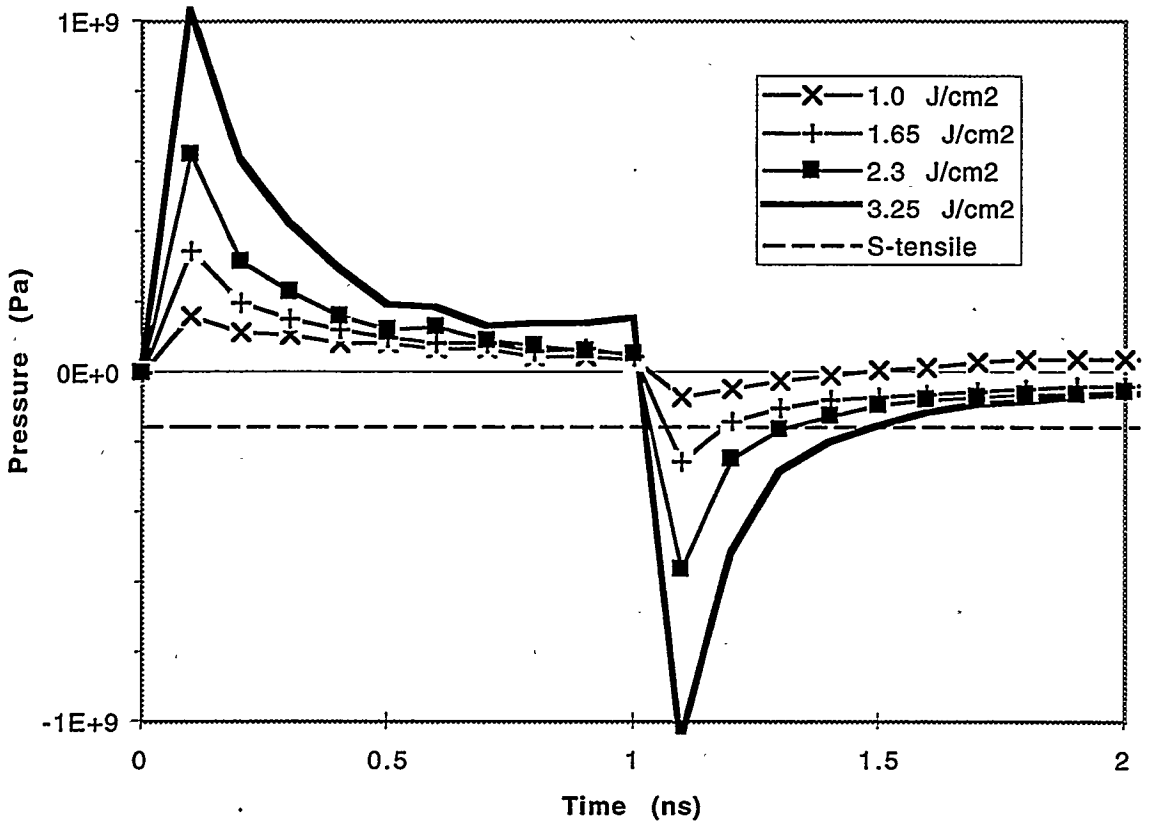

Figure 5-37: Pressure history in boron carbide at depth of maximum thermal stress crack for four x-ray fluences of 250-eV blackbody spectrum in 1-ns pulse. Depths from analysis plotted in Figure 5-33. Tensile stress is exceeded briefly at the higher fluences.

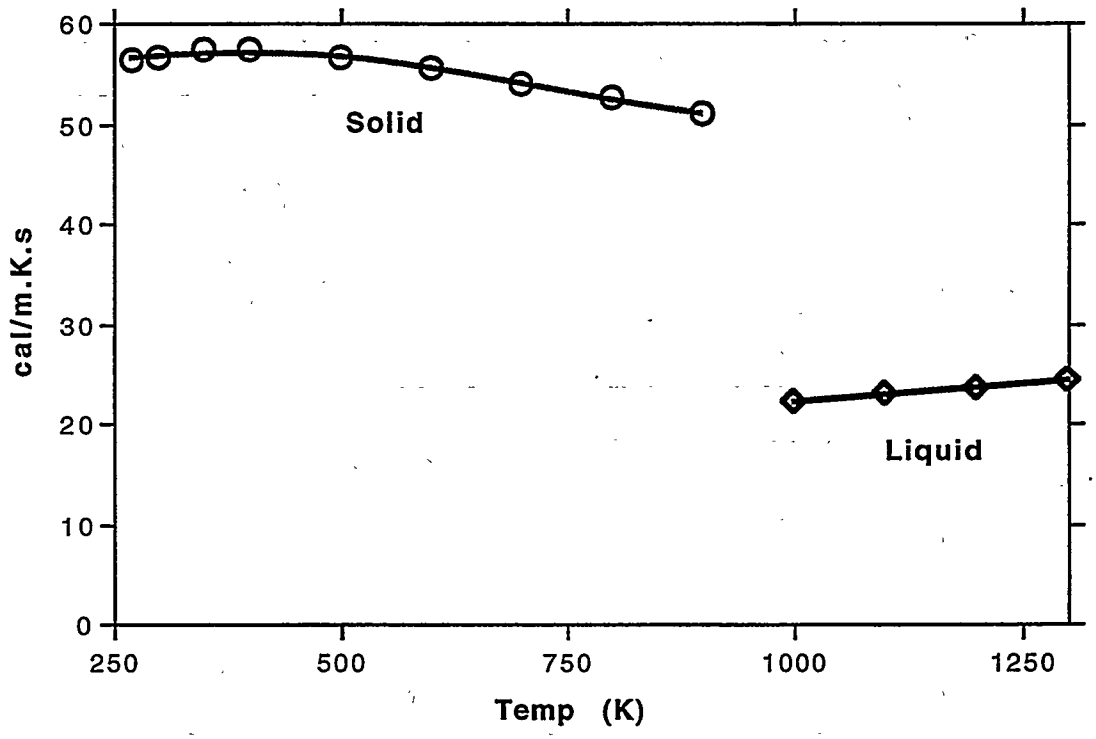

Figure 5-38: Thermal conductivity relations used for aluminum.

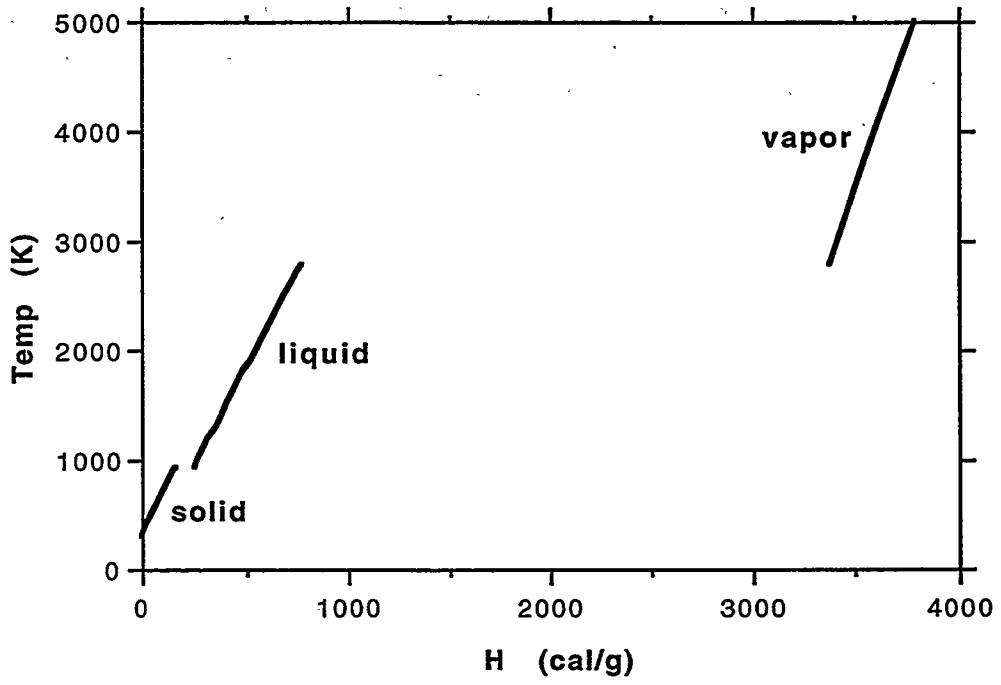

Figure 5-39: Correlation of aluminum temperature to specific enthalpy.

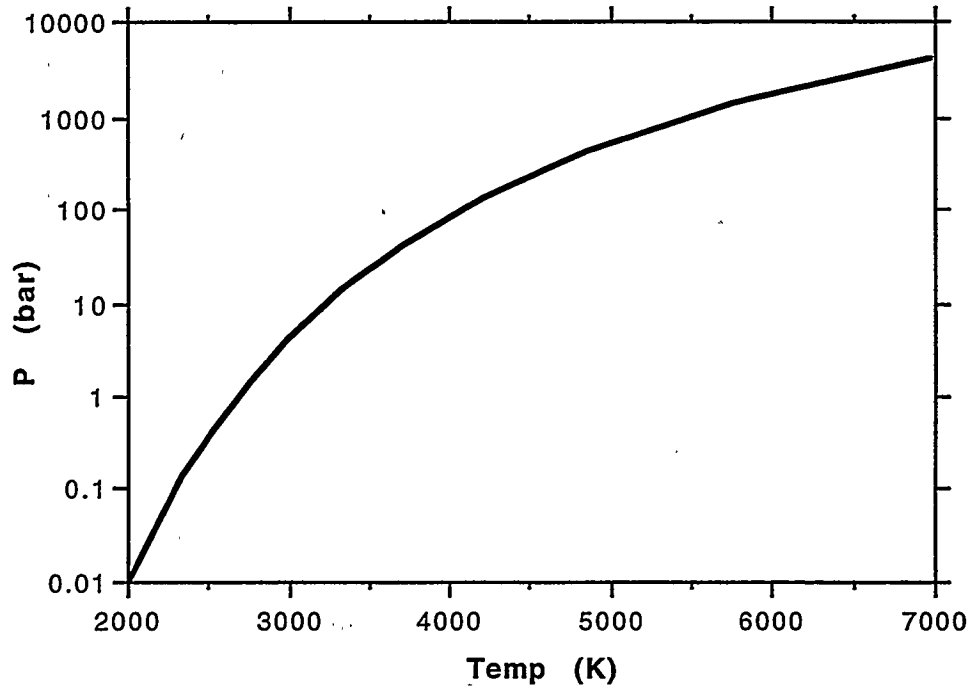

Figure 5-40: Equilibrium aluminum vapor pressure as a function of temperature.

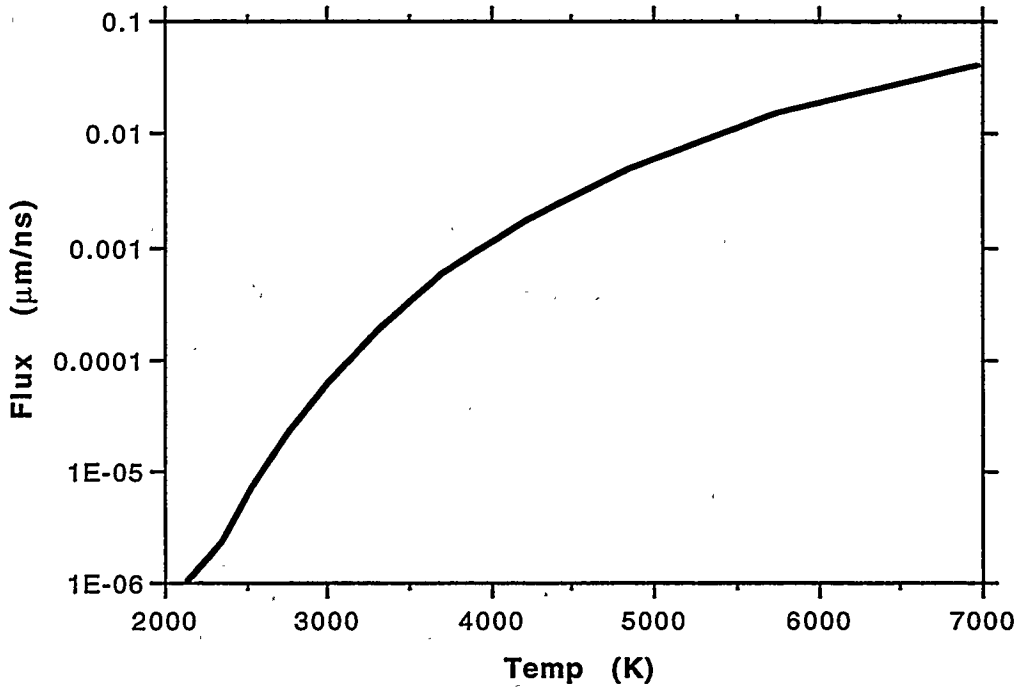

Figure 5-41: Aluminum evaporation flux based on equilibrium rate with no recondensation.

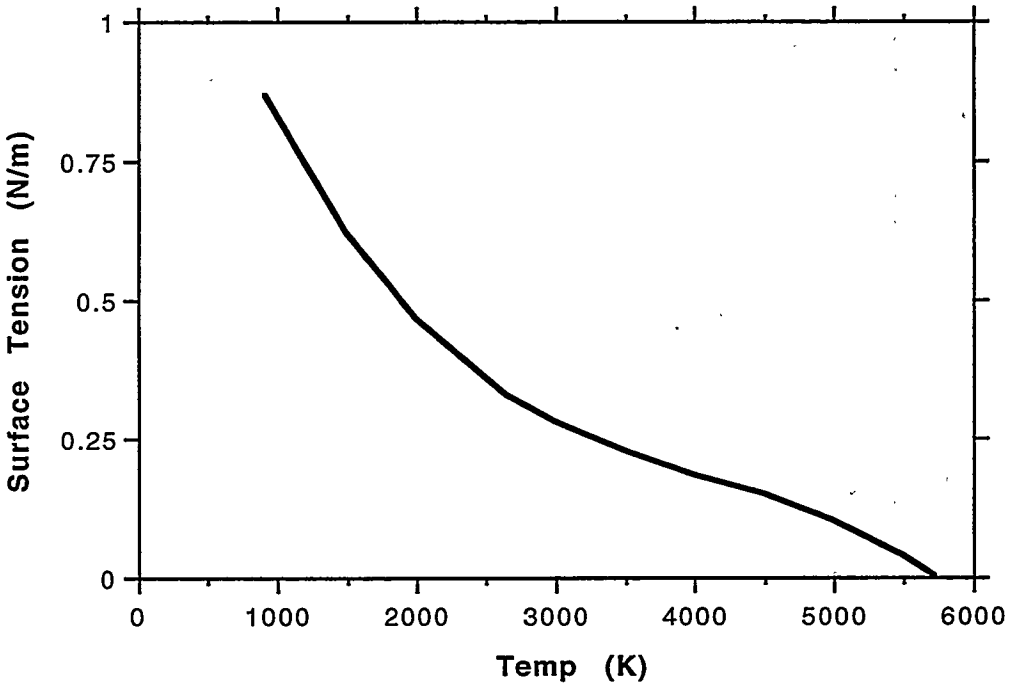

Figure 5-42: Aluminum surface tension between the melt and critical points.

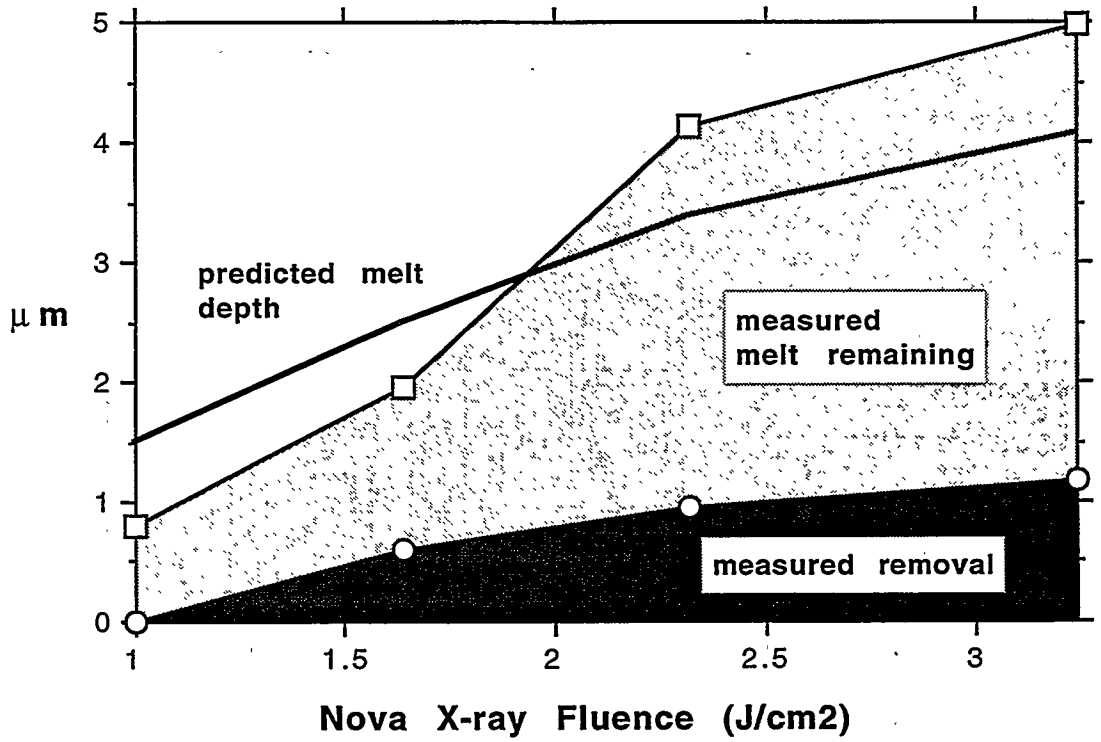

Figure 5-43: Response of aluminum to x-ray deposition with a 200-eV blackbody spectrum in a 2.2-ns square pulse. Note that about one quarter of the melt layer is removed at higher fluences.

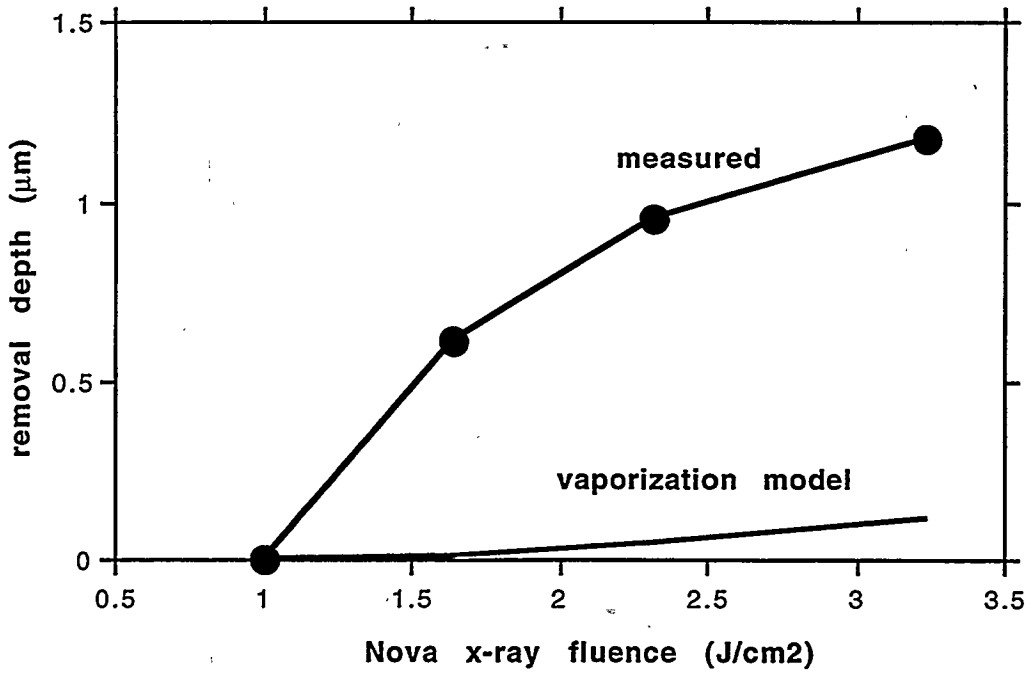

Figure 5-44: Comparison of predicted vaporization depth to measured aluminum x-ray response. 200-eV blackbody spectrum in a 2.2-ns square pulse.

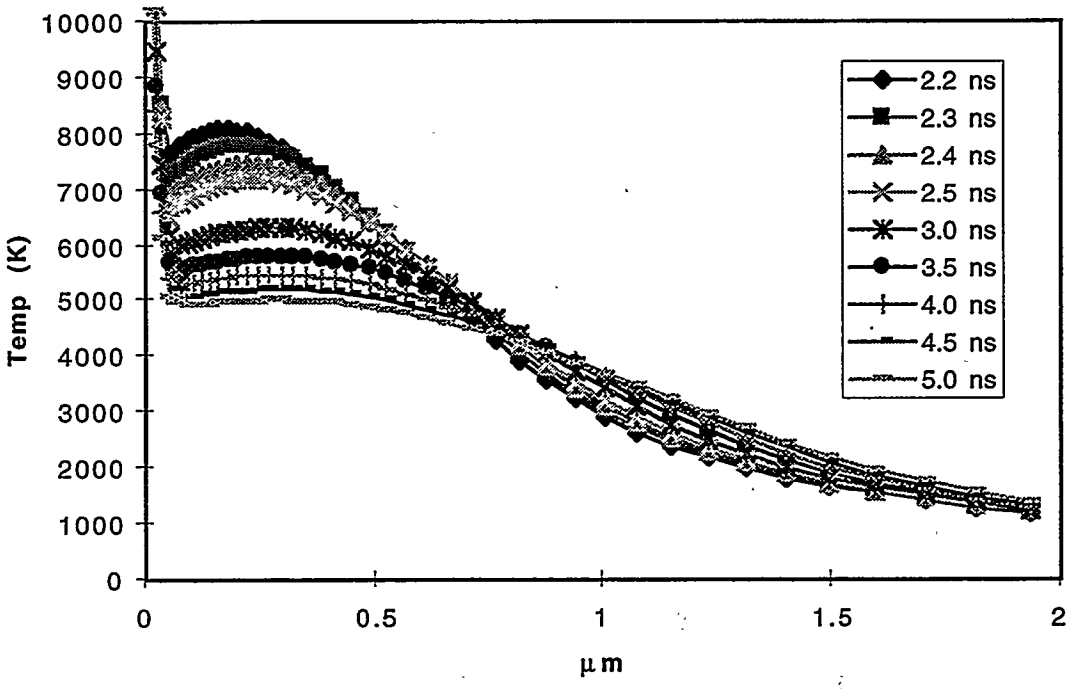

Figure 5-45: Temperature profiles in aluminum after 2.2-ns pulse of 200-eV blackbody x rays at 3.25 J/cm^2. From peak at 2.2 ns to 5 ns.

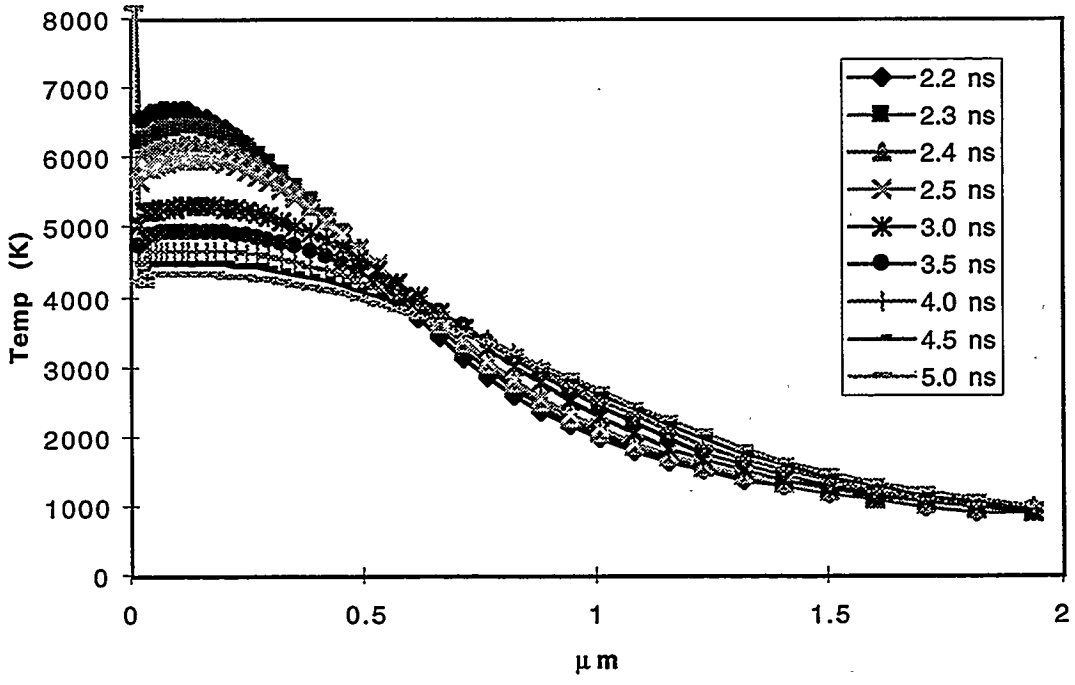

Figure 5-46: Temperature profiles in aluminum after 2.2-ns pulse of 200-eV blackbody x rays at 2.3J/cm^2. From peak at 2.2 ns to 5 ns.

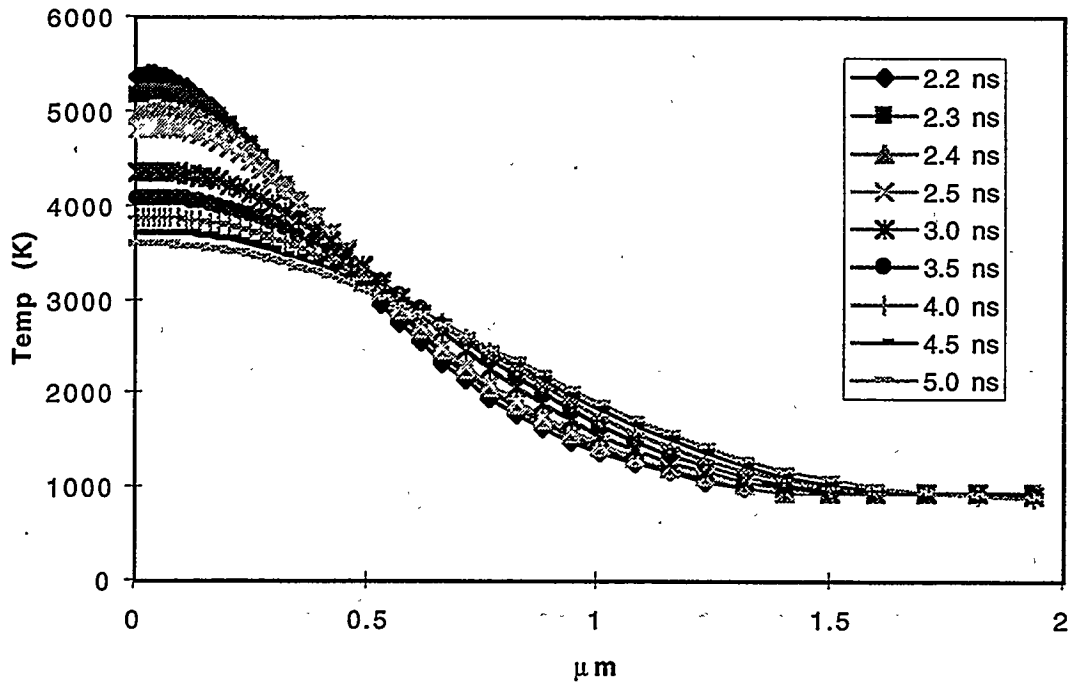

Figure 5-47: Temperature profiles in aluminum after 2.2-ns pulse of 200-eV blackbody x rays at 1.65 J/cm^2. From peak at 2.2 ns to 5 ns.

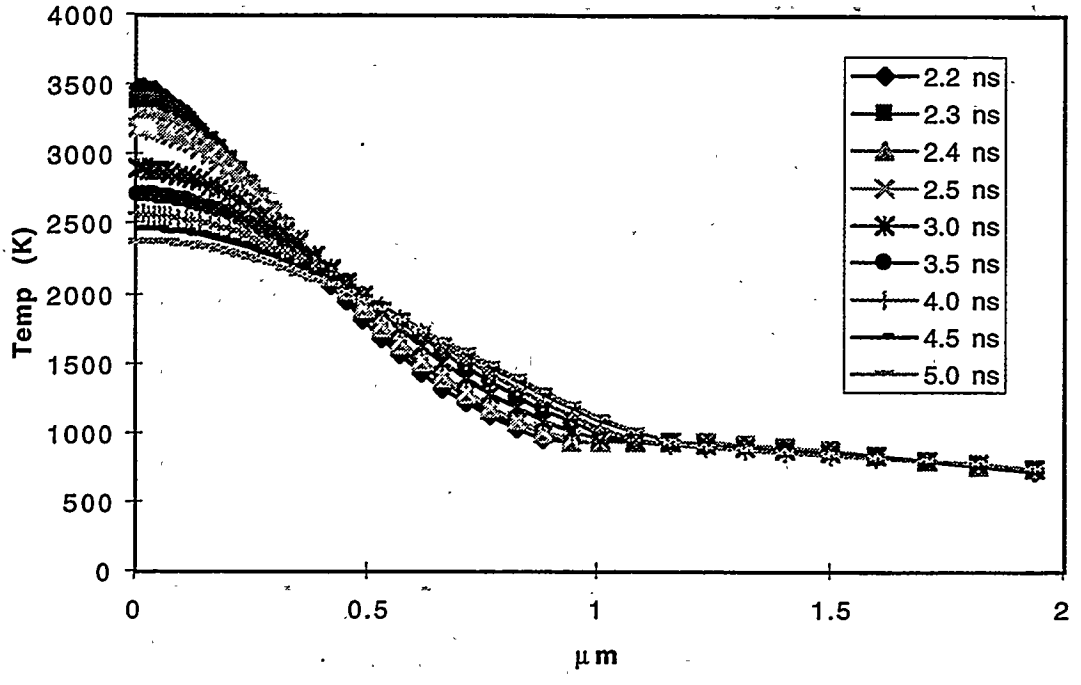

Figure 5-48: Temperature profiles in aluminum after 2.2-ns pulse of 200-eV blackbody x rays at 1.0J/cm^2. From peak at 2.2 ns to 5 ns.

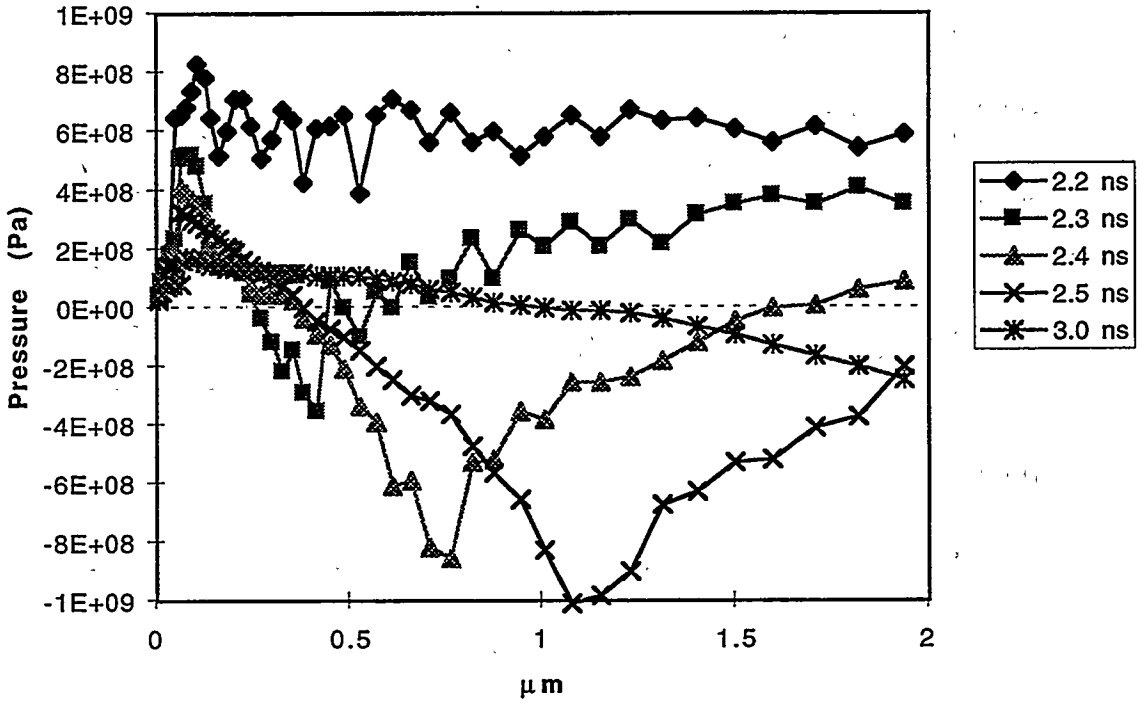

Figure 5-49: Pressure profiles in aluminum after 2.2-ns pulse of 200-eV blackbody x rays at 3.25 J/cm^2. Pressure is positive in compression.

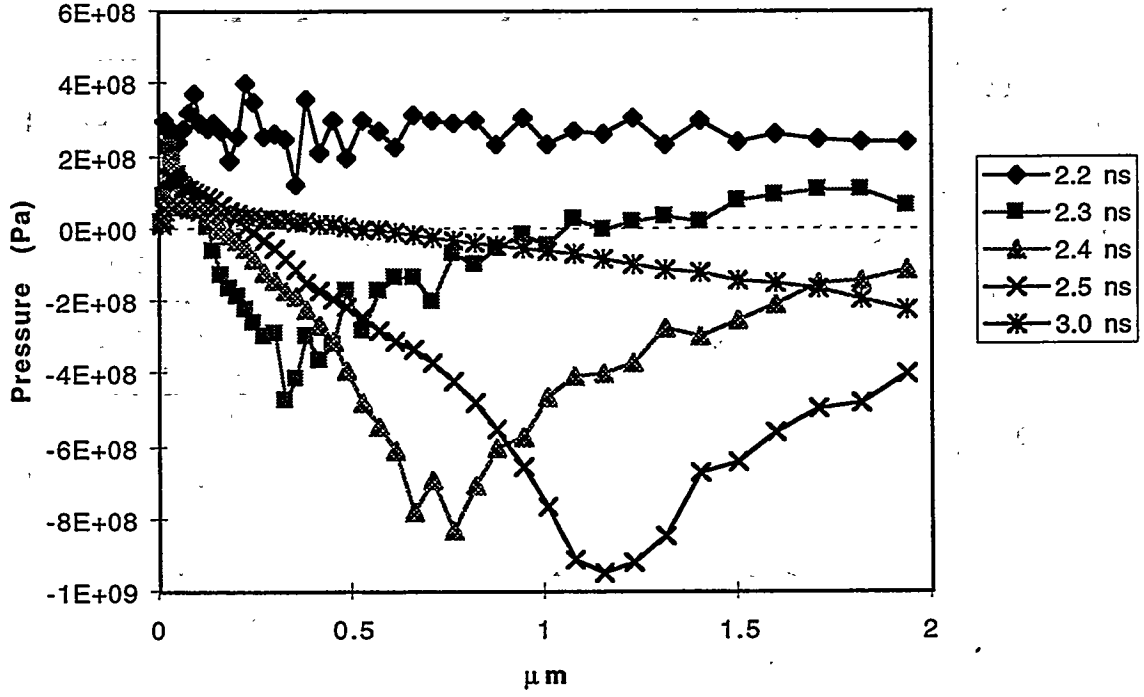

Figure 5-50: Pressure profiles in aluminum after 2.2-ns pulse of 200-eV blackbody x rays at 2.3 J/cm^2.

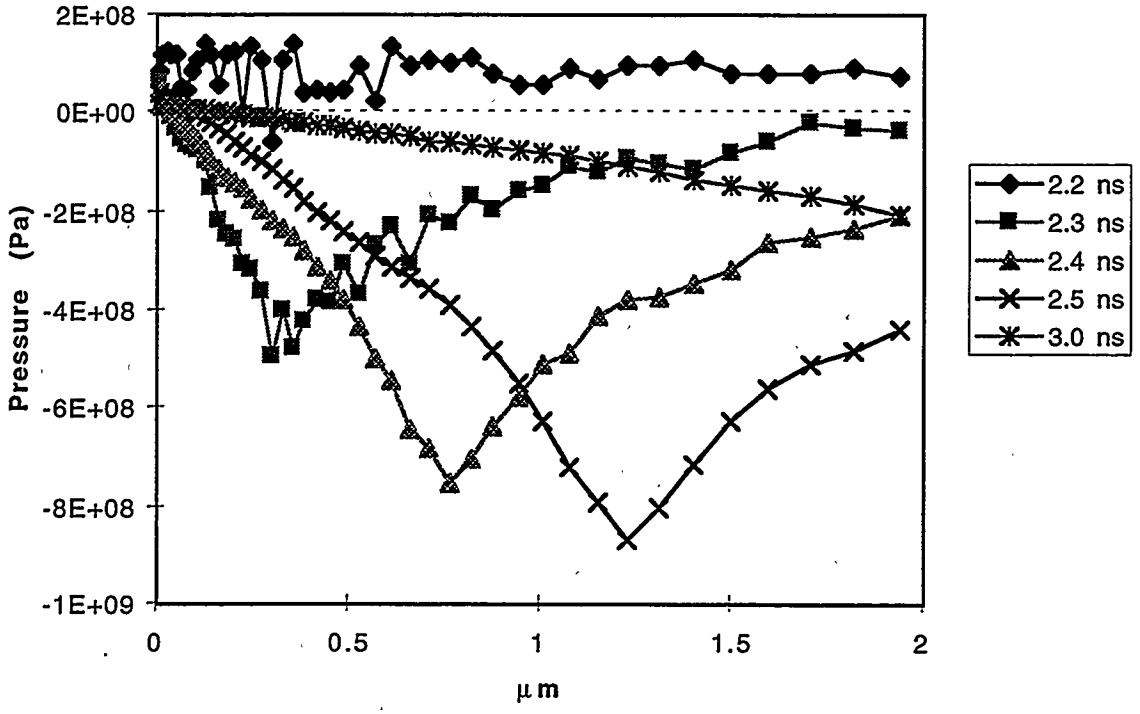

Figure 5-51: Pressure profiles in aluminum after 2.2-ns pulse of 200-eV blackbody x rays at 1.65 J/cm^2. Pressure is positive in compression.

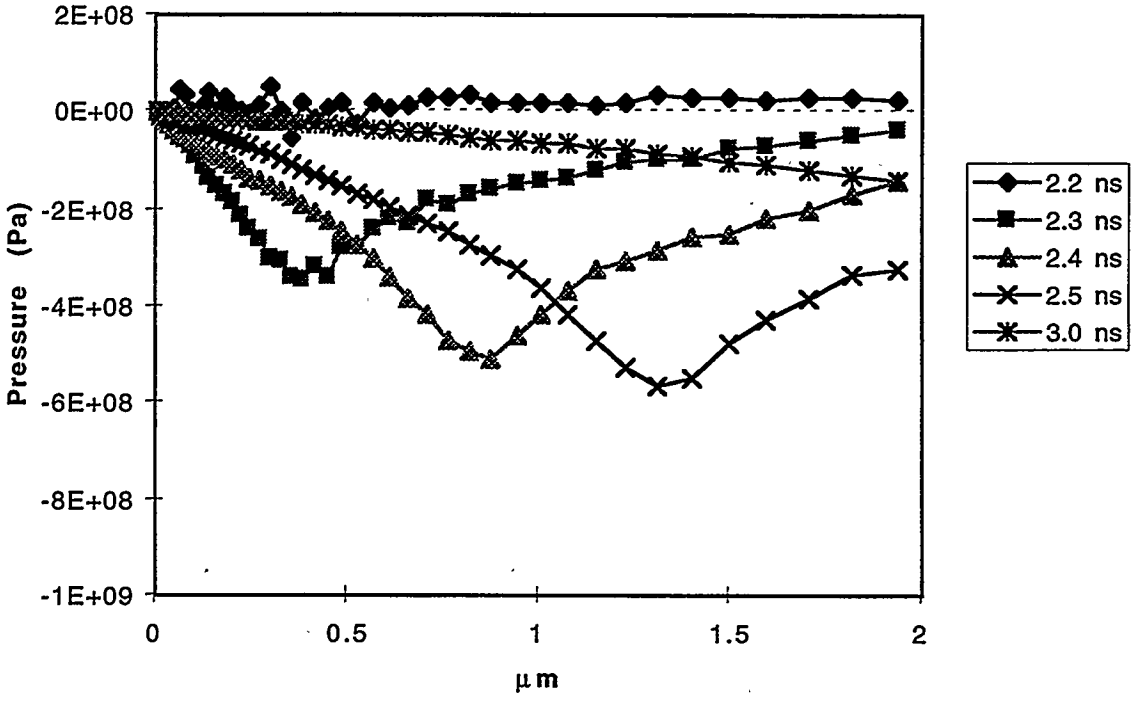

Figure 5-52: Pressure profiles in aluminum after 2.2-ns pulse of 200-eV blackbody x rays at 1.0 J/cm^2.

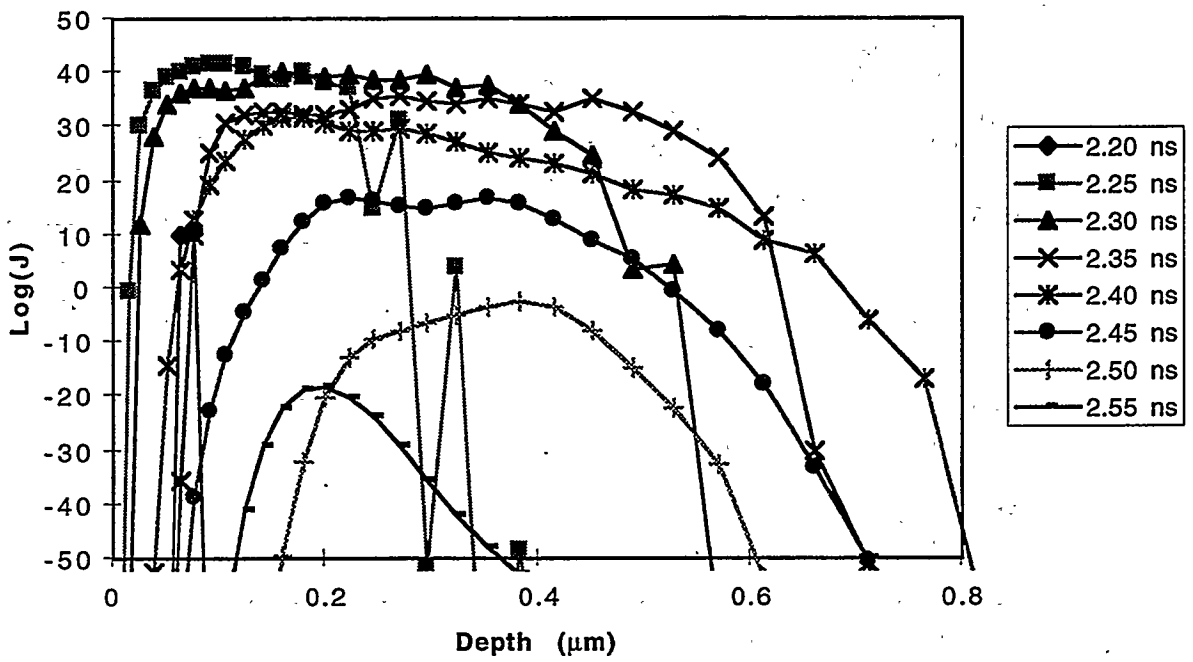

Figure 5-53: Nucleation rate ($m^{-3}s^{-1}$) during passage of rarefaction wave for aluminum exposed to 1.65 J/cm2 of 200-eV BB x rays in a 2.2-ns pulse.

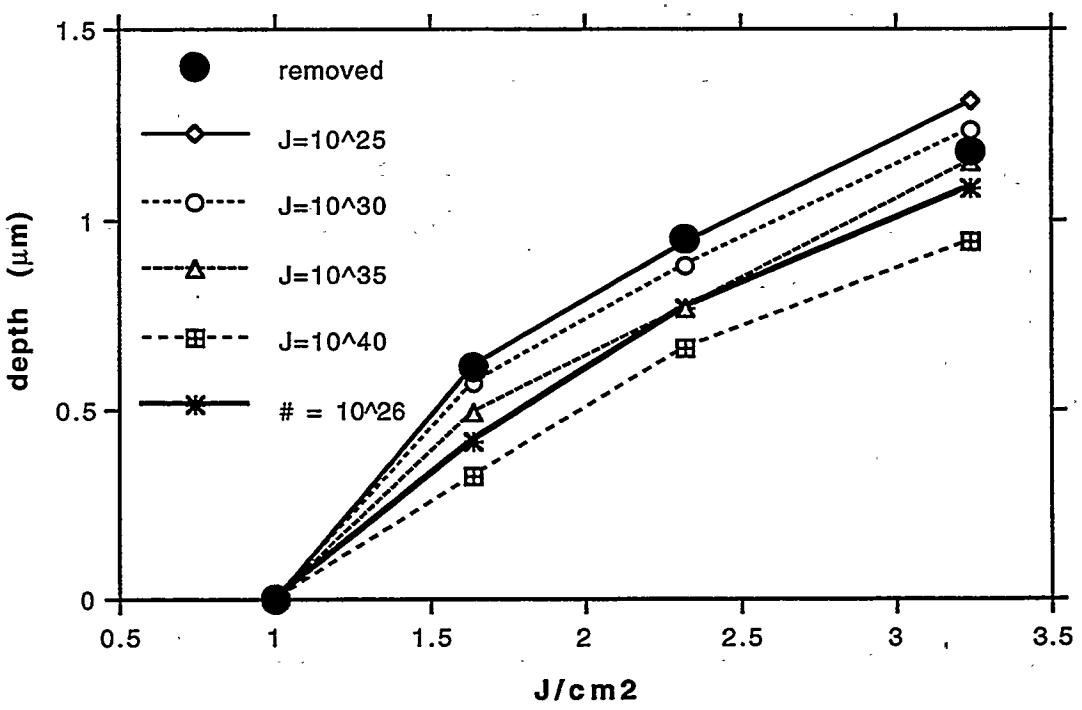

Figure 5-54: Comparison of maximum nucleation rate depth profiles to measured aluminum removal depths. A curve for integrated number of bubbles is also shown. Units for J are $1/m^3s$ and for integral $1/m^3$. X-ray source is a 200-eV blackbody in a 2.2-ns pulse.

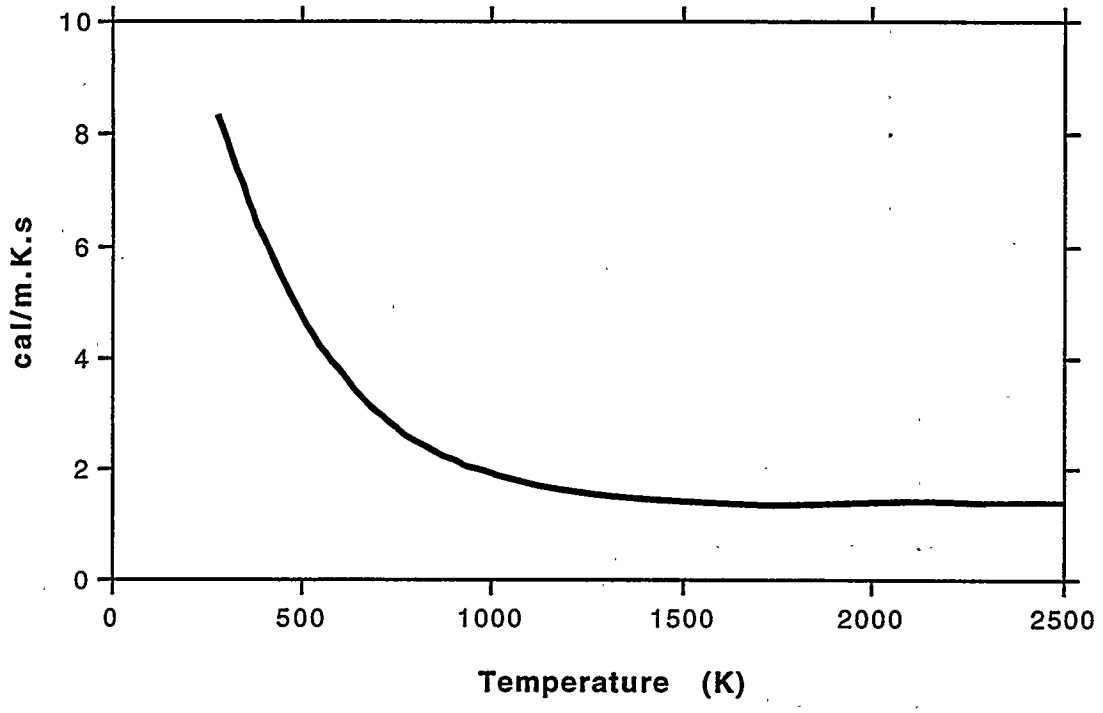

Figure 5-55: Thermal conductivity relation used for aluminum oxide.

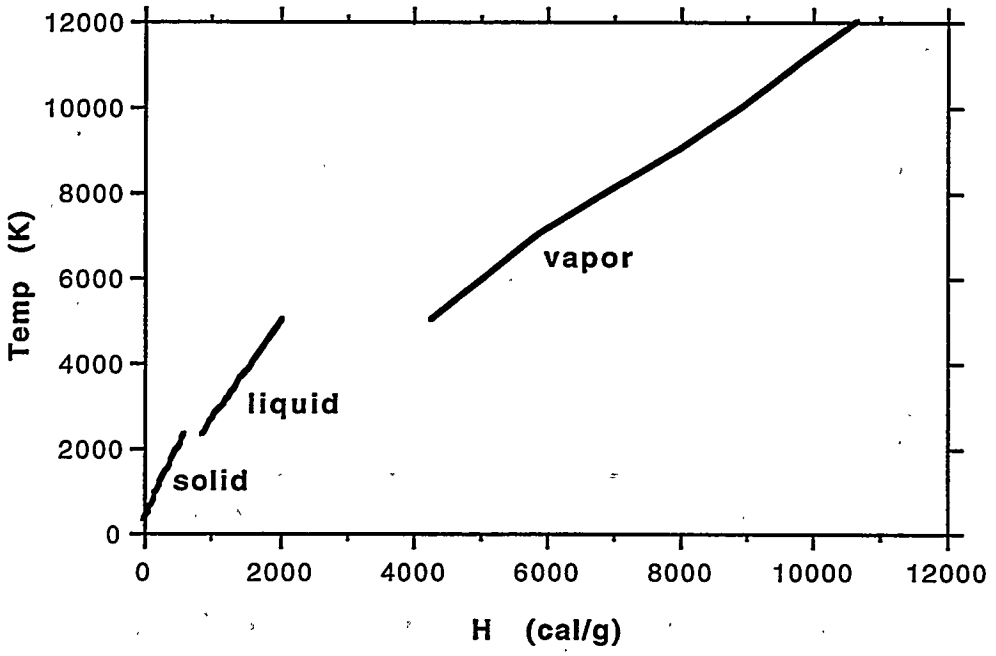

Figure 5-56: Correlation of alumina temperature to specific enthalpy.

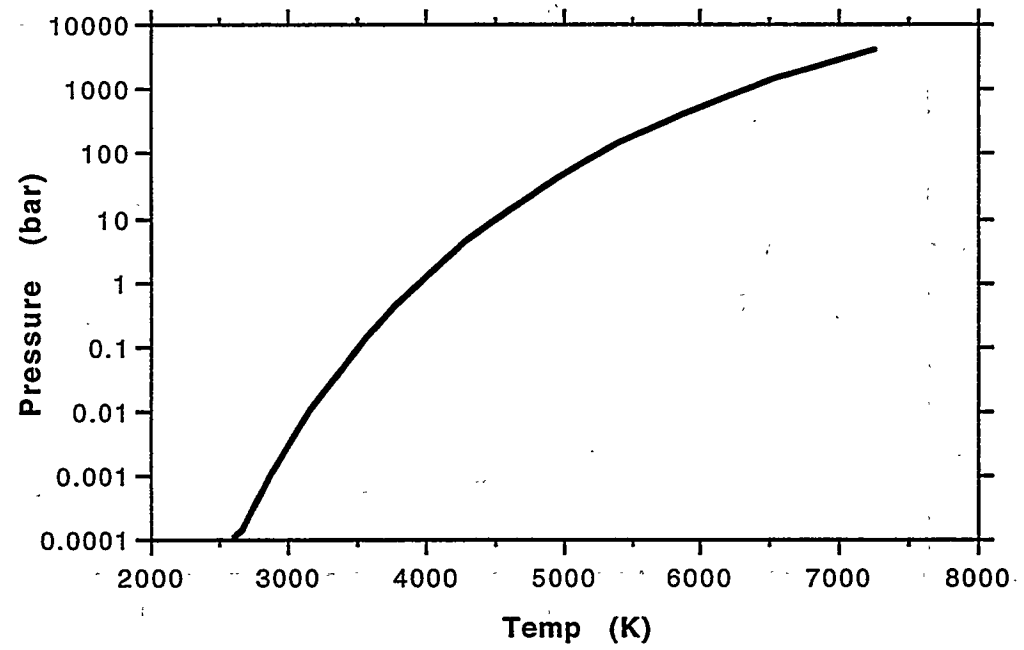

Figure 5-57: Equilibrium alumina vapor pressure as a function of temperature.

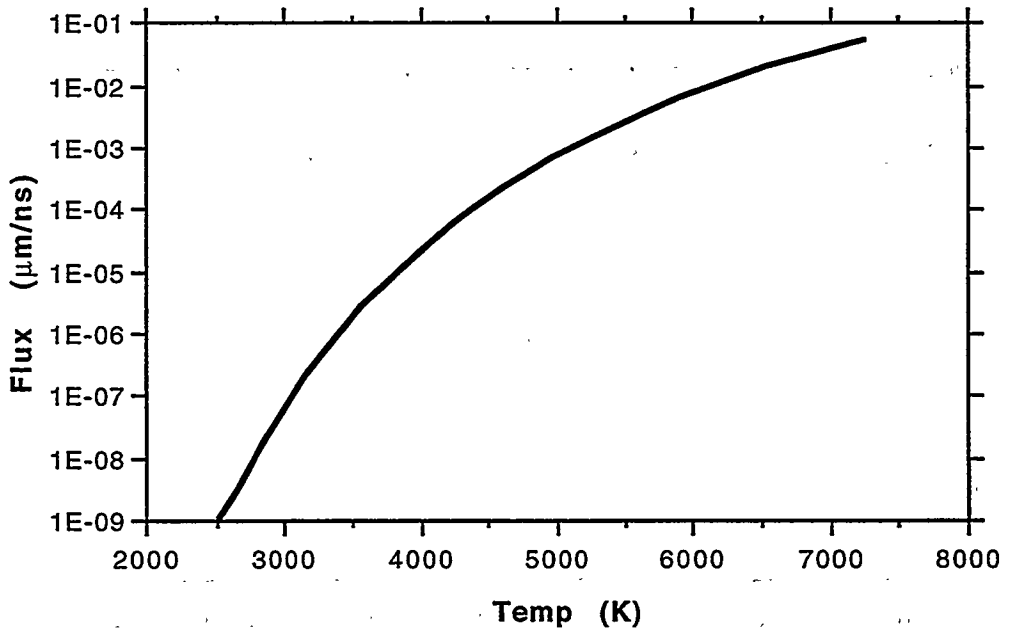

Figure 5-58: Evaporation flux from aluminum oxide based on equilibrium rate with no recondensation.

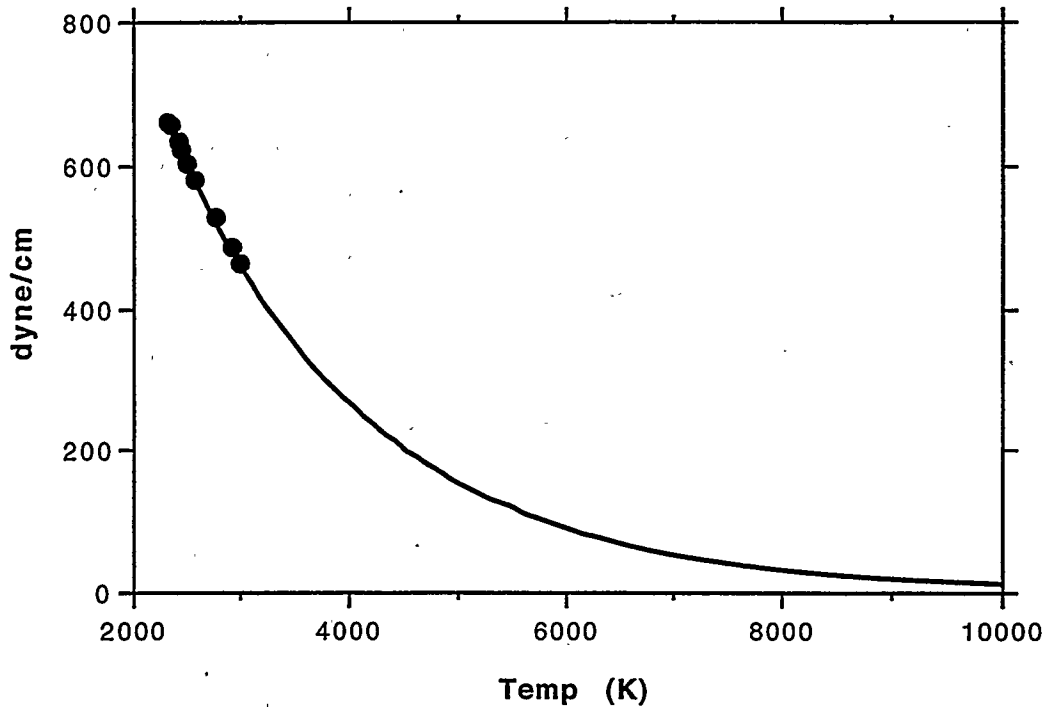

Figure 5-59: Aluminum oxide surface tension, with exponential curve fit to data from Shpil'rain.[23]

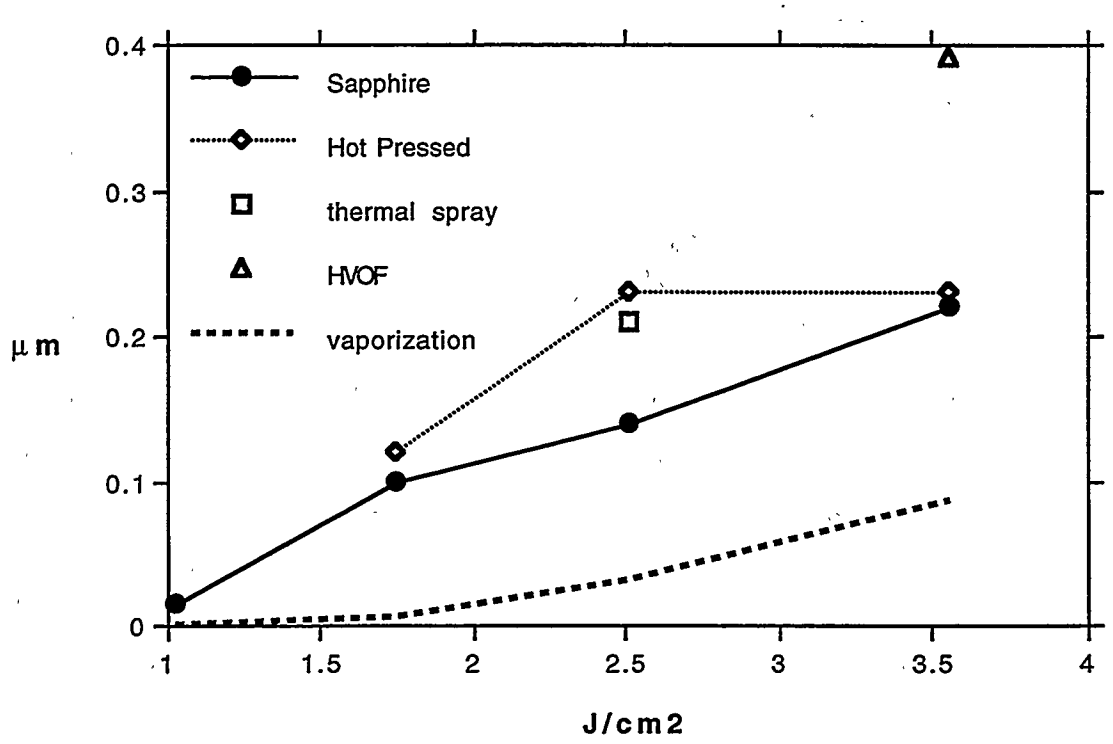

Figure 5-60: Response of aluminum oxide to x-ray deposition with a 200-eV blackbody spectrum in a 2.2-ns square pulse. ABLATOR's vaporization prediction accounts for less than one third of the mass loss.

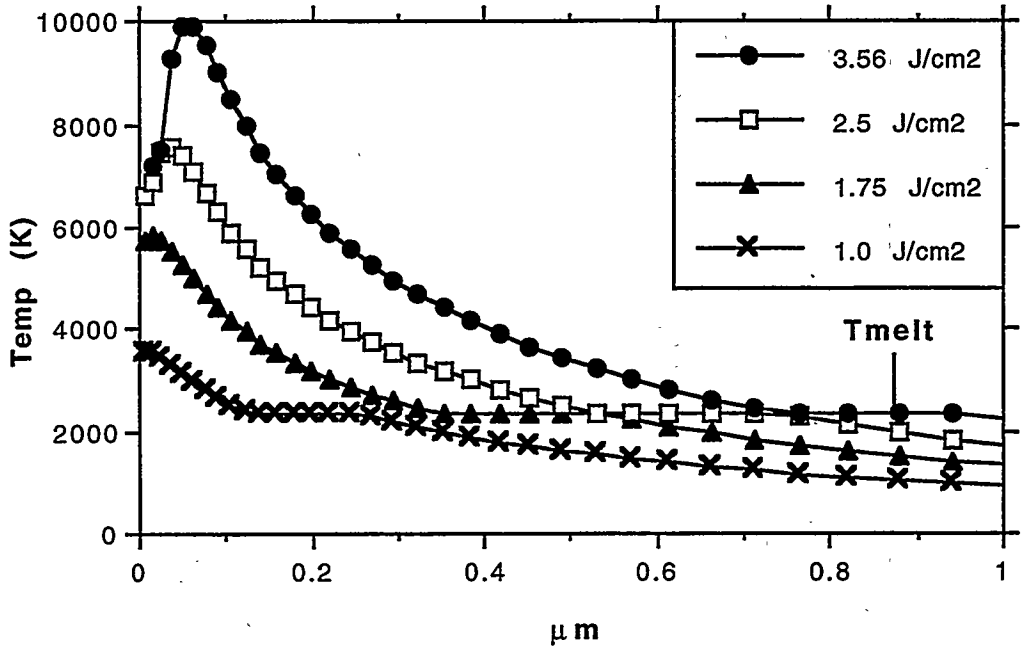

Figure 5-61: Temperature profiles in aluminum oxide after 2.2-ns pulse of 200-eV blackbody x rays at fluences of 3.56, 2.5, 1.75, and 1.0 J/cm^2. Effects of front surface vaporization are visible at higher fluences.

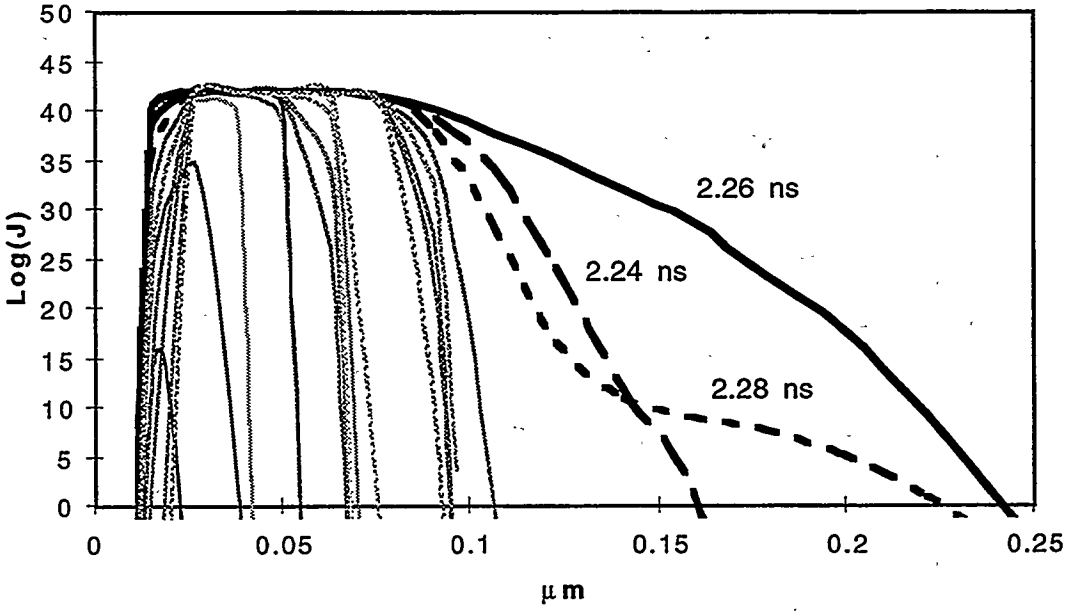

Figure 5-62: Nucleation rate profiles for aluminum oxide exposed to 2.5 J/cm2 of 200-eV BB x rays in a 2.2-ns pulse. J is in units of m^{-3} s^{-1}. Profiles from 1.5 to 2.4 ns.

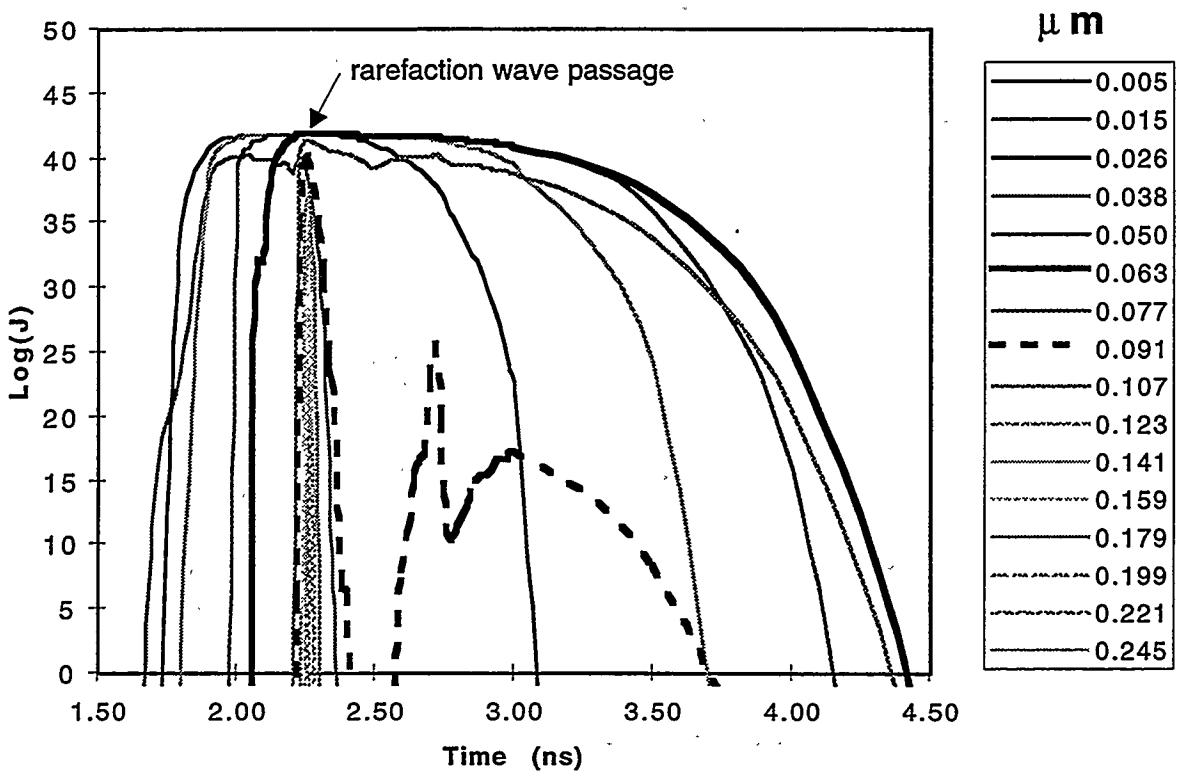

Figure 5-63: Nucleation rate time histories for aluminum oxide exposed to 2.5 J/cm2 of 200-eV BB x rays in a 2.2-ns pulse. J is in units of m^{-3} s^{-1}. Substantial nucleation before and after rarefaction wave passes.

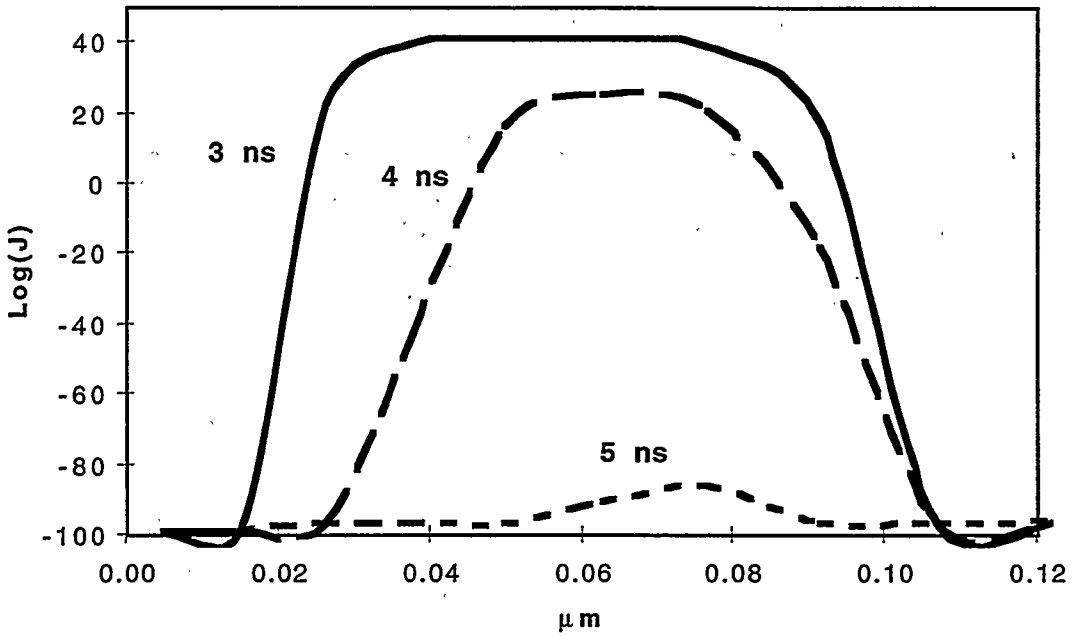

Figure 5-64: "Thermal" nucleation rate profiles for aluminum oxide exposed to 2.5 J/cm2 of 200-eV BB x rays in a 2.2-ns pulse. J is in units of m^{-3} s^{-1}.

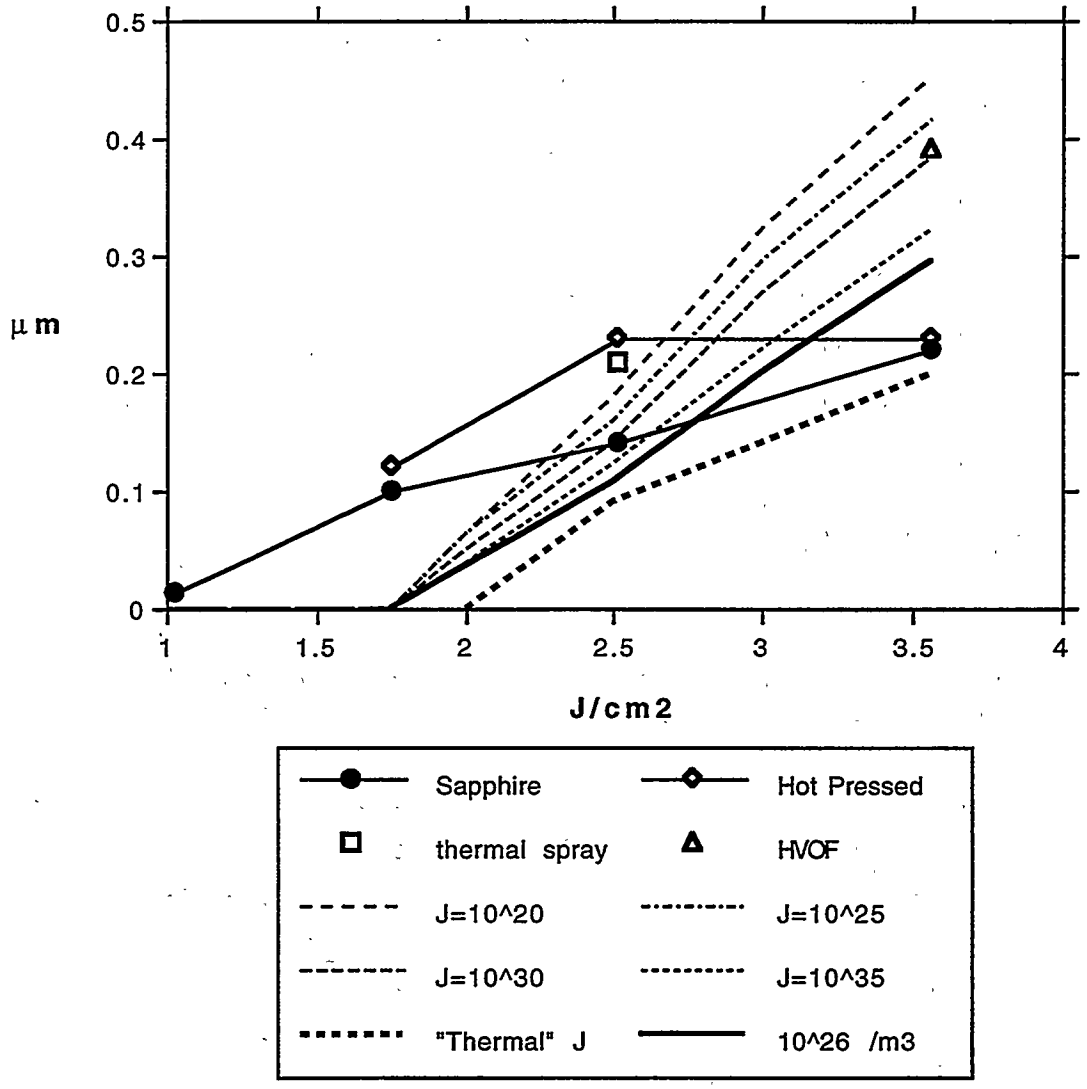

Figure 5-65: Comparison of maximum nucleation rate depth profiles to measured aluminum oxide removal depths. X-ray source is a 200-eV blackbody in a 2.2-ns pulse. "Thermal" cutoff at 10^{25} $m^{-3}s^{-1}$. Final curve is where J integrated over time reaches 10^{26} bubbles/m^3, about a 40% volume fraction.

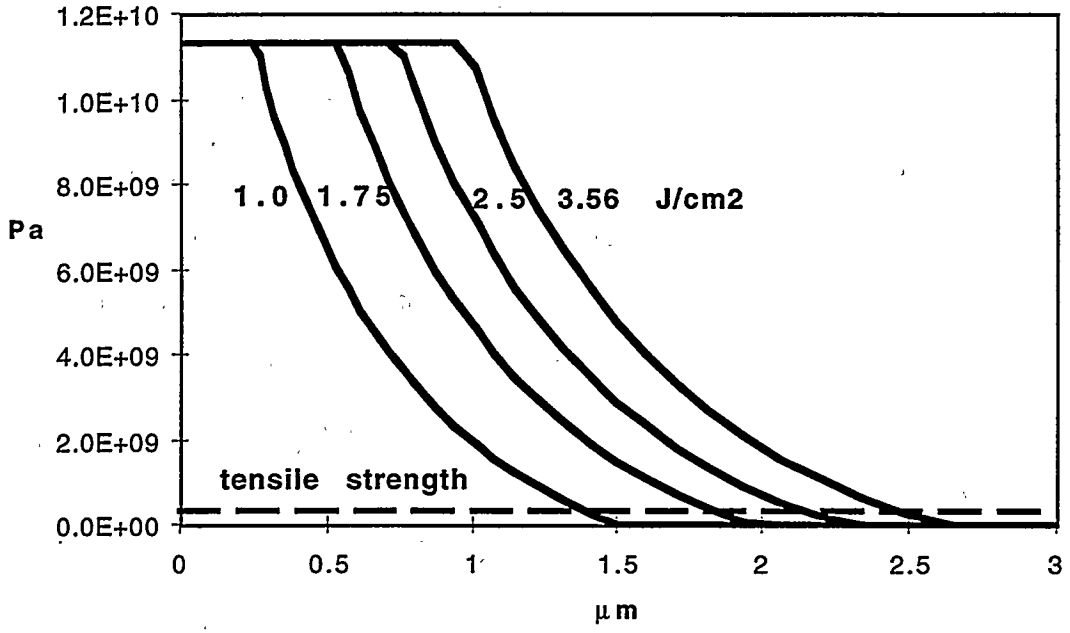

Figure 5-66: Thermal stress profiles in aluminum oxide based on peak temperature profiles of Figure 8 and a linear softening model.

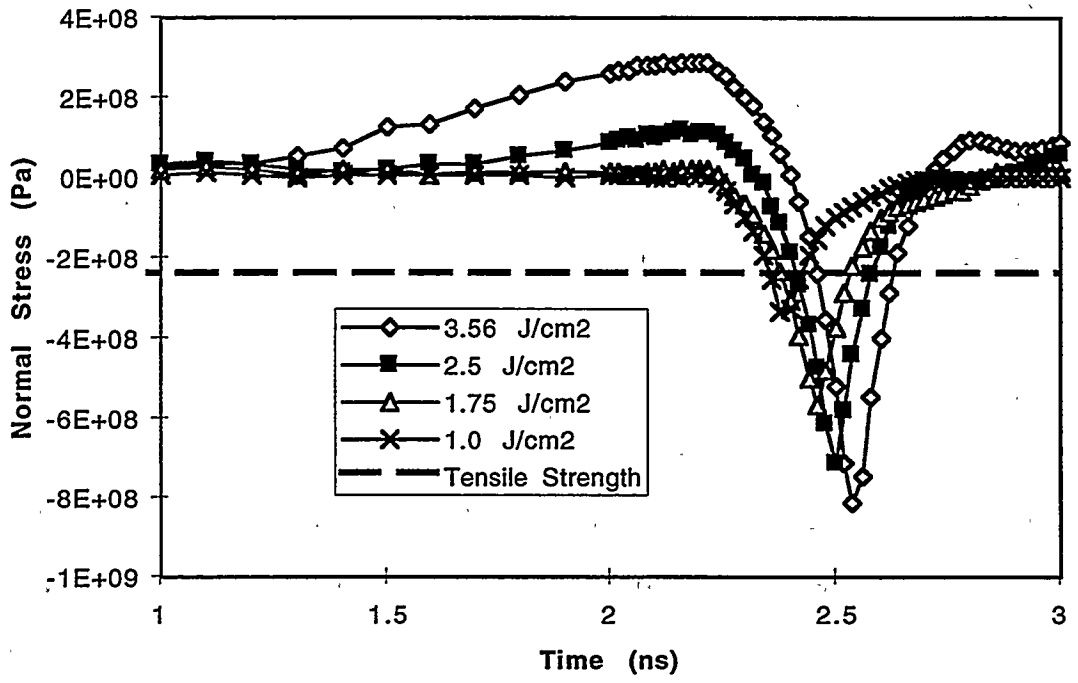

Figure 5-67: Pressure history in alumina at depth of maximum thermal stress crack for four x-ray fluences of 200-eV blackbody spectrum in 2.2-ns pulse. Depths from analysis plotted in Figure 13. Tensile stress is exceeded briefly at all tested fluences.

6. Conclusions

6.1 X-ray Source Description

The x-ray source calculations were performed to fulfill two purposes: to examine the specific target designs envisioned for the NIF; and to investigate issues of output scaling with target yield and hohlraum wall thickness. Prior to this study, predictions for ICF target x-ray outputs were based on general trends developed for a variety of target types. For example, it was assumed that the non-neutron energy (the laser energy plus 20% of the yield) was evenly divided among x rays and target debris. The results obtained with this series of simulations indicate an x-ray fraction of 60 - 75% of the non-neutron energy, rather than 50%. This represents a considerable improvement in the prediction for the NIF target chamber. The scaling studies may prove useful in optimizing either NIF or IFE targets to reduce their impacts on the target chamber.

6.2 Nova Experiments

One goal of the x-ray exposure testing on Nova was an "engineering" goal to expose candidate first wall materials to a range of x-ray fluences and measure removal depths. This provides a basis for selection of the "best" first wall material and an estimate of its ablation rate. The work of Chapter 2 on the expected x-ray sources gave the relevant fluences to test. Fluences were selected to overstress the materials, so that conversion to NIF conditions would not involve extrapolations in fluence, but rather modifications of spectral and pulse parameters. The development of modeling tools has now shown, as in the previous section, that the Nova test conditions did in fact cover the range of expected NIF conditions (and somewhat beyond). The

removal data for this range of materials represents important new information in the study of x-ray ablation.

The other goal of the Nova experiments was more "scientific," as a search for the underlying physical phenomena which govern x-ray ablation. Observations of surface topology were made in the x-ray exposed regions with optical microscopy, as well as atomic force microscopy and scanning electron microscopy. These observations provided the basis for identification of several different damage mechanisms in the tested materials. Knowledge of the various mechanisms permitted realistic models of materials response to be developed. When combined with removal depth measurements, the experimental data provided valuable benchmarks for the ABLATOR code performance.

6.3 Modeling Material Removal

6.3.1 Surface Vaporization

The surface vaporization model incorporated into the ABLATOR code represents one of the key findings of this work. For materials that were identified from Nova experiments as ablating primarily through vaporization (fused silica and silicon nitride), the code provides an excellent fit to the measured removal data. Since the model uses a definite mass flux relation at the ablating surface, it performs much better than previous ablation predictions based solely on peak specific energy profiles.

Some general observations can be made about cases in which surface vaporization is significant. One obvious fact is that the peak surface temperature is more relevant to vaporization removal than the total depth of

deposition (like a melt thickness). Another observation is that high vapor pressures are required for significant removal depths, since thermal conduction cools the front surface in a matter of nanoseconds to tens of nanoseconds. Only high vapor pressures (over a kilobar) can drive the vaporizing flux high enough (above 0.1 μm/ns, or 100 m/s) to remove measurable material in this short time. Finally, since all hot surfaces will evolve material at some rate, the predictions of vaporization removal for a particular material represent the minimum removal depth under some set x-ray exposure conditions.

6.3.2 Sub-Surface Boiling

Rapid and massive bubble nucleation initiated in a hot liquid layer by the passing rarefaction wave can be used as an indicator of material removal depth, as it was with aluminum. Conditions that generate high nucleation rates are assumed to also favor rapid growth of the bubbles, so that a vapor explosion occurs under the liquid surface. This removes the overlying material and leaves behind a very rough surface.

Calculations of bubble nucleation rates (J) are very sensitive to the value used for surface tension, which appears as the exponential of σ^3. Variations in σ of 20% can change the nucleation rate by orders of magnitude. Unfortunately, there is only very scarce data available for surface tension, particularly at temperatures significantly above the melt point. Results of the maximum nucleation depth calculations, however, turn out to be rather insensitive to changes in surface tension. This is because the steep spatial gradients of temperature are even more significant.

Another case in which high nucleation rates are predicted is when temperatures get high enough that the saturation vapor pressure greatly exceeds the local pressure, even without the influence of the rarefaction wave. I have called this mechanism "thermal" as opposed to the "tensile" mechanism described above. The thermal nucleation rates rise slowly in the material as it is heated by the x rays, and the high nucleation rate conditions can persist for up to about 10 ns. This is in contrast to the "tensile" case where the nucleation rates rise and fall in well under a nanosecond's time.

The usefulness of the "thermal" nucleation rate depths for prediction of material removal is questionable, at least when used without detailed bubble growth models. This method offers somewhat better correlation to the aluminum oxide data than does the "tensile" rate model. However when applied to silica, where the smooth, flat exposed surfaces point to little contribution of sub-surface explosions, the "thermal" model would predict double the observed removal depth. The conclusion is that any removal process that results from the "thermal" nucleation rate conditions requires a much more sophisticated analysis, including bubble growth and the resulting changes to the hydrodynamics and thermodynamics. Note that this would include 2-D or 3-D effects that might be difficult to incorporate into a 1-D model. Therefore if the ABLATOR model indicates that high "thermal" nucleation rates will exist at a particular set of conditions, the best that can be said is that there will be some material removal due to surface or sub-vaporization, but the amount cannot yet be quantified. If only the high "tensile" rates are found, however, the code's simple "rate switch" can be expected to produce a reasonable removal depth estimate.

6.3.3 Thermal Stress/Spall

For brittle materials subject to thermal stress damage, the models in the code can provide a prediction of the thermal crack depth and an indication of whether or not the hydrodynamic shock loading will be sufficient to remove some of the damaged flakes. The results for boron carbide largely validated this predictive capability, both in the depth of removal pits and for a threshold of material removal. The missing aspect of the model is a detailed accounting of the growth of the cracks in response to both hydrodynamic and thermal stress loadings. Crack growth combined with some statistical means of computing the fraction of damaged surface that spalls off would be required to make quantitative predictions of removal depths. Without this sophisticated analysis, the code is best used to judge if a spall threshold has been exceeded from a given x-ray pulse.

6.3.4 Other models

6.3.4.1 Tensile Spall

This model was developed to handle the fracture of liquids by the passing of the tensile rarefaction waves found after the end of the x-ray pulse. Further investigation revealed that for very short pulses, liquids have nearly the same tensile strength as a solid and further that these tensile strengths were significantly higher than those generated in the typical x-ray exposure. Therefore this technique was dropped in favor of the bubble nucleation approach that is more relevant at the lower tensile stresses.

6.3.4.2 Rayleigh-Taylor Instability

The possibility was considered that material removal in aluminum was due to a Rayleigh-Taylor instability in the melt layers. The driving

acceleration was the stopping of the expansion of the condensed material at the end of the x-ray pulse (the rarefaction wave). The analysis showed that, at least for single pulses, the sub-nanosecond duration of the tensile wave is far too short to significantly amplify any surface irregularities in the thin liquid layers. Laser ablation experiments conducted with repeated short pulses on metals have shown the instability effect to be important.[1] These laser studies were like the x-ray exposures, with short-lived, shallow melt depths and little destabilizing force. Thousands of shots were required to produce the rough topology that releases isolated droplets. It is reasonable to expect that Rayleigh-Taylor instability might also be important for roughened surfaces, particularly at lower x-ray fluences where other removal mechanisms do not exist. This would likely be a slow process, however.

6.3.5 Sensitivity to X-ray Characteristics

Some general comments can be made about how material response to x rays varies with spectrum and pulse length. These comments apply to the fluence range studied in this work (near the vaporization threshold). At significantly higher fluences, such as those in ICF reactor chambers, these trends may not hold.

6.3.5.1 Spectrum

The material removal mechanism most strongly affected by the x-ray spectrum is surface vaporization. A colder (lower energy photons) spectrum will deposit energy in a thinner surface layer, increasing the temperature at and very near the surface. The vaporization rate depends exponentially on surface temperature, and so is significantly increased. A damage mechanism like thermal stress cracking depends more on the melt depth, so is sensitive

to the amount of energy deposited, and less on the details of how it is distributed.

6.3.5.2 Pulse Length

Pulse length is most significant to the damage mechanisms related to peak tensile stresses. These are the spall of thermally cracked material and the initiation of "tensile-induced" sub-surface boiling. The reason is that pressure information travels at speeds on the order of the sound speed in a material, a few km/sec (or μm/ns). If the x-ray pulse length is about one nanosecond, significant pressures can build in the front micron or so where most of the energy is deposited. Much longer x-ray pulses give time for the pressures of material expansion to spread, which reduces the strength of the rarefaction wave at the end of the pulse.

Pulse length can also be significant for materials with high thermal conductivity. A longer pulse will give sufficient time for heat to conduct into the bulk of the material, reducing peak surface temperatures. However, for poor conductors like silica, the pulse length has only a relatively minor effect.

6.4 Applications to the NIF Chamber

6.4.1 Integrated Analysis

A primary goal of the modeling work undertaken in this dissertation is to predict the x-ray response of materials that will be used in the NIF target chamber. Chapter 2 provides the necessary information on the expected NIF x-ray threat: fluence, spectrum, and pulse length. The experiments described in Chapter 4 reveal x-ray damage mechanisms for various materials, which serves to guide the modeling. The models of Chapter 3, which were applied

to these experimental data in Chapter 5, combine the new NIF x-ray sources with the material response models to give predictions for the NIF chamber environment. Two important components of the NIF chamber are the first wall protective panels, made from boron carbide, and the fused silica covers for the unconverted laser light beam dumps.

6.4.2 NIF First Wall X-Ray Response

The aluminum walls of the NIF target chamber will be covered with protective panels of a refractory material, most likely boron carbide. These panels will minimize ablation of chamber materials by the x rays generated in the targets at the center of the chamber. The first wall will be at a distance of five meters from the targets. The highest fluence of x-ray energy will come from a 20-MJ yield shot, where the first wall near the poles of the chamber will receive in excess of 2.6 J/cm^2. The ABLATOR code was used to predict boron carbide response to the x-ray characteristics of this case, where the spectrum and pulse parameters were obtained from the results of Chapter 2.

X-ray damage to boron carbide is primarily a thermal shock/spall phenomenon. The important results from the ABLATOR model are therefore the melt depth and the strength of the rarefaction (tensile) wave. The melt depth provides an indication of the likely depth of thermal stress cracking in the material. The peak strength of the tensile wave, compared to the tensile strength, shows if spall of thermally damaged flakes is likely to occur. The melt depth was found to be 0.27 μm, which is comparable to a fluence of 2.5 J/cm^2 under the Nova exposure conditions. Using the thermal stress profiles from Figure 5-32 as a guide, the expected thermal crack depth would be about 0.6 - 0.7 μm.

As in Chapter 5, the normal stress history at the maximum crack depth was computed. Figure 6-1 shows a peak tensile stress of about 5 MPa, lasting for a few nanoseconds. This compares to a tensile strength in boron carbide of 155 MPa (at room temperature), so that spall from this tensile wave is not likely to occur. There may still be some material removal by repeated thermal stressing of the material. Note that Figure 5-35, giving the stress histories for the Nova exposures, shows a peak tensile stress of 500 MPa at 2.3 J/cm^2. Therefore in this respect, Nova exposures represent a severe overtest of the conditions expected in the NIF chamber.

6.4.3 X- Ray Response of Fused Silica Beam Dump Covers

Approximately 60% of the total 1.06-μm laser energy put into the NIF chamber will be frequency-tripled to the 0.35-μm light that enters the hohlraum and drives capsule implosion. The remaining unconverted light will miss the target and hit the far side chamber wall. At these locations, beam dumps composed of high-damage-threshold doped glass will absorb most of this unwanted laser energy. Fused silica covers will protect the absorbing glass from the x rays and debris in the chamber, and protect the chamber from possible damage particles generated in the absorbing glass under the fused silica cover. These fused silica plates will cover 10-15% of the first wall area at this five meter radius, and so represent an important component of the NIF chamber wall.

The ABLATOR model, using the x-ray source terms from Chapter 2, was used to predict material removal from the silica beam dump covers for several different NIF shots. Because of variations in x-ray emission with the angle from the hohlraum axis, two locations (23.5° and 47°) were analyzed to

correspond to the locations of "cones" of beams used to drive hohlraums. Figure 1-1 shows these beam line orientations in the NIF chamber. Table 6-1 shows the predicted vaporized depth in the silica for each shot, along with a total mass removal for all beam dump covers in the chamber. As a point of reference, the gold hohlraums weigh about 150 mg and are expected to contribute less than half of the total debris mass from any shot. The table shows that it is only for high-yield shots that significantly larger quantities of silica will be ablated, and so may be an issue for the chamber operation. Note that the peak removal depth of 0.9 μm is about the same as measured in the second highest x-ray fluence in the Nova experiments.

Table 6-1: Predicted removal of fused silica by x rays in various NIF exposures from beam dump covers at two angles from hohlraum axis.

Shot	Depth @ 23.5°	Depth @ 47°	ΣMass vaporized
1.8 MJ disk	0.005 μm	<0.001 μm	150 mg
100 kJ hohlraum	<0.001 μm	<0.001 μm	0.6 mg
5 MJ hohlraum	0.010 μm	0.006 μm	560 mg
20 MJ hohlraum	0.092 μm	0.062 μm	5,700 mg

6.5 Untested Materials

The final issue to address is whether enough has been learned about the ablation process through the various mechanisms to be able to predict the x-ray response of a new material without performing the Nova testing. Surface vaporization is the one mechanism that will occur for any hot material, so any removal predicted will be the minimum expected for a given material and set of x-ray conditions. For some refractory, low vapor pressure materials, this may be a very small amount of ablation. Brittle materials will be subject to thermal stress cracking because of the steep temperature

gradients. The code's hydrodynamic response results can serve as an indication of whether the spall threshold is likely to be exceeded. If not, then little additional material removal (beyond vaporization) would be expected from thermal spall. If the ABLATOR analysis for a material shows high bubble nucleation cause by the passage of the tensile wave (but not by high temperatures alone), then the maximum depth of these high rates can serve as a quantitative estimate of material removal. However, if the high nucleation rates are caused just by high temperatures, then nothing quantitative can be said beyond the statement that a damage threshold has been exceeded. To summarize, the code predictions for a new material can be used to determine a minimum ablation depth and to indicate if other, additional mechanisms may contribute to removal as well.

Reference

1) Kelley R, Rothenberg JE., "Laser Sputtering: Part III. The Mechanism of the Sputtering of Metals (at) Low Energy Densities", Nucl Inst & Meth, B7/8 p755-763, 1985.

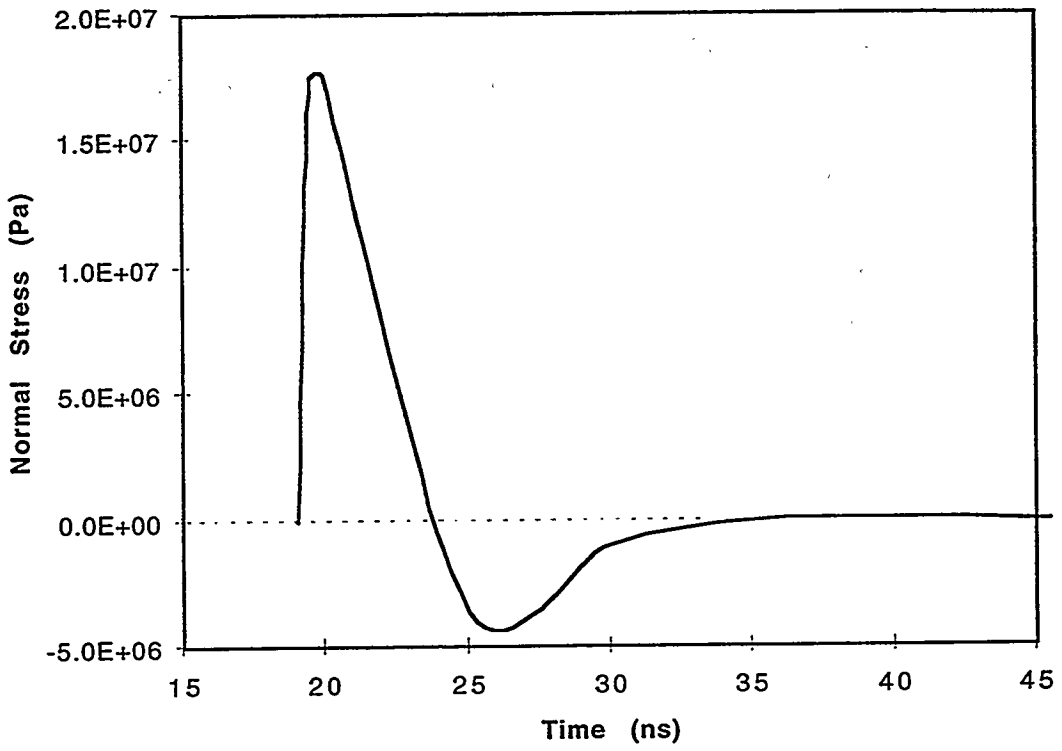

Figure 6-1: Normal stress history in boron carbide first wall at a depth of 0.65 μm in response to x-ray emission from a 20-MJ yield shot. Peak tensile stress is about 5 MPa, while the tensile strength is about 155 MPa.

Appendix A: ABLATOR Code

ABLATOR is a new code developed specifically for this study of x-ray ablation and this dissertation serves as its initial documentation. The models used in the code to predict material response are described in Chapter 3. This appendix provides the information necessary to run problems with various materials and x-ray fluence conditions. Program setup procedures, input commands, and output descriptions are given. Some example problems illustrate these procedures for different materials. Finally, the program listing is provided to complete the code documentation.

Program input is specified through a combination of external data files, "hardwired" parameters built into the code, and run time input from the terminal. Two external files are used to provide the code with all material properties. X-ray opacities are given in the OPACDATA file for each of the photon energy groups. Each line of the data file has average group energy, bin width, and opacity in a D13.6,TAB,D13.6,TAB,D13.6 format. (TAB is ASCII character 9.) The units are keV for energies and m^{-1} for the opacities. The other material data file, MATDATA, contains the thermomechanical properties of the material. These include density, melting temperature, temperature coefficients for thermal conductivity, temperature/energy correlations, vapor pressure curve fit parameters, equation of state data, Poisson's ratio, material strength, and surface tension curve fits, if available. This file is read with the READMAT routine in the code, which puts the data into several COMMON blocks. The units in the MATDATA file can be somewhat arbitrary, provided the READMAT routine is modified to convert the data to SI units. OPACDATA and MATDATA files are available for each of the materials discussed in this dissertation. They are listed separately in

Appendix B. Similar files for other materials can be generated by following the example of the given files.

The mesh parameters are currently "hardwired" into the code. The routine ZONESET is called early in the run to establish initial zone boundary locations and zone masses. Note that with the Lagrangian technique used in the code, zone mass does not change through the run. The default geometry uses a first zone thickness of 0.01 μm, and a geometric increase in thickness by 6% per zone. For 100 zones, this gives a total problem depth of 56 μm, effectively at infinity for the thermal response of these short runs. (This is not true for shock propagation, which requires the use of non-reflecting boundary conditions, described in Chapter 3.) To change the number of zones used in the problem, the parameters N and NP1 (N+1) must be changed throughout the code.

Several control parameters are also hardwired into the code. These include constants for the thermal and hydrodynamic time step stability, and for the artificial viscosity. Any of these numbers can be changed, either before the code is compiled, or by modifying the code to prompt the user for values at run time.

The energy input is determined at run time through user input to the terminal. One can select either a standard NIF target emission sequence (45 MJ, 20 MJ, 5 MJ, 100kJ yields) or a simple square or gaussian x-ray pulse. The pulse shapes, spectra, and energies are built-in for the NIF simulations, while these must be entered for the square and gaussian options. The user must also provide the distance from the target and the angle from the axis of

the target. The angle is necessary because hohlraum emissions from the laser entrance holes have a Lambertian distribution, making the fluence and spectra angle-dependent. The square and gaussian pulses are assumed to have a Lambertian distribution as well, which correlates well to emission from a simple disk target. Note that for these pulses, the energy which is entered is the total emitted into 4π steradians, again useful for disk target simulations. If response at a particular fluence is desired, this value in J/cm^2 can be entered at the prompt for energy in MJ, then specifying a radius of 2.821m and an angle to the hohlraum axis of 60°.

Another energy deposition option is available for use with either the square or gaussian pulse shapes. Some energy sources, such as a laser beam or single-line x-ray emission, deposit in a purely exponential depth profile, controlled by a single absorption coefficient. The user selects this option at run time by choosing the "laser" source, and then providing the absorption coefficient. The code then puts this same coefficient into all of the photon energy bins, giving the pure exponential deposition profile desired. Note that the OPACDATA file is not necessary when this option is selected.

The other information provided at run time is the stop time for the problem. The start time is automatically set to be just before the start of the x-ray pulse. Note that this is not zero for the NIF shots, where time is referenced to the start of the 20ns laser pulse, and not to the start of the x rays. Time of flight for these x rays from the target to the selected material distance is not included.

Output from an ABLATOR code run is in three forms. First is an intermittent print out of some temperatures, melt depth, and absorbed energy at given numbers of cycles and at certain time intervals. The second output is the summary information produced at the end of the runs giving depths for vapor and spall removal, and for total and incipient melting. Energy balance, time step ranges, and peak temperatures and energies are also given. The third form of output is a series of files giving the value of a particular variable at each zone at certain time intervals. Such files are produced for pressure, normal stress, temperature, specific energy, velocity, and others. The files are simply text files formatted with tabs to allow importing to standard plotting packages, such as Igor or Excel on a Macintosh.

The ABLATOR code has potential to be used as a starting point for a chamber gas dynamics code (see TSUNAMI reference to X.M. Chen in Chapter 3). This would permit accurate initialization of transport calculations for material vaporized from ICF chamber surfaces. ABLATOR would be run out in time to the point where vaporization is essentially stopped. The velocity, location, energy, and density data for the zones that had vaporized could be taken at the end of the run and mapped onto a fine Eulerian grid. The TSUNAMI code would then continue the vapor expansion into a 2-D geometry.

Example Problem #1

The first problem is the exposure of fused silica to the x-ray emission from a 20-MJ NIF shot. This scenario relates to the ablation from a beam dump cover located on the NIF chamber wall at an angle of 23.5° from the hohlraum axis. This case was examined at the end of Chapter 6.

In the listing below, ABLATOR prompts are in plain text, user input is in bold, and any comments are italicized.

```
> mv Silica.matdata matdata                    set up external data files
> mv Silica.opacdata opacdata

> ab                                  start the code, here compiled as "ab"
 X-ray or laser source? (1=Laser)
2
 fused silica                        code echos material type from data files
 fused silica w/ new Psat curve
 H-MELT-I (cal/g) =  353.404196432544
 H-MELT-T (cal/g) =  355.2743674226672
  PLANAR

Choose source term by number
1 = 45 MJ shot
2 = 20 MJ shot
3 = 5 MJ shot
4 = 100 kJ shot
5 = square pulse
6 = Gaussian pulse
2                                          choose 20-MJ NIF shot
 Closing(1) or Open(2) LEH Model?
2                                   choose open LEH model for source
Enter radius (m)
5                                   silica to be located on chamber wall
Enter angle in degrees
23.5                                        angle from hohlraum axis
 Enter Tstop (ns)
200                                                    stop time

   time    step size     temperatures for first 5 surface zones          melt depth
  19.002  .111E-11  303.580  303.580  303.580  303.580  303.580    .000
  21.000  .154E-11 1968.145 1961.406 1947.596 1928.211 1904.126    .141
  23.002  .164E-11 3615.655 3613.539 3595.889 3565.056 3522.868    .878
  25.001  .164E-11 4153.506 4215.878 4294.596 4346.235 4371.767   1.232
  27.001  .164E-11 4233.907 4246.017 4377.084 4485.631 4570.943   1.405

 ISURFvapor = 1                     first zone has completely vaporized
 TIME = 27.94735092237893
 CYCLE = 6003
  29.001  .174E-11 4248.439 4330.171 4462.937 4575.367 4666.740   1.499
```

skip to the end of the run

```
 181.001  .246E-11  3275.421  3276.245  3278.877  3281.208  3283.159    1.936
 191.002  .246E-11  3245.592  3246.192  3248.290  3250.089  3251.513    2.063
TIME 198.6006674187698
```

velocity, pressure, and temperatures for first 5 zones

```
U    3.08027E-02 3.06812E-02 3.05503E-02 3.04094E-02 3.02578E-02
P    4.84367E+05 4.84037E+05 4.84028E+05 4.84018E+05 4.84008E+05
T    3.22399E+03 3.22446E+03 3.22622E+03 3.22769E+03 3.22878E+03

Energy present & input (J/cm2) =     2.555     2.463
Total fluence (J/cm2) =     2.464
Maximum melt depth (micron) =     2.063
Maximum total melt depth (micron) =     2.063
Spalled depth (micron) =     .084     total original thickness of spalled zones
Maximum front surface temp =    15545.80
Maximum front surface enthalpy (cal/g) =  15357.6753
Minimum and maximum time steps =   2.257E-13  2.464E-12
Maximum enthalpy change (cal/g) =   1915.7539
Maximum heat flux (W/cm2) =   3.3142E+06
Fraction vaporized in surface zone    .50763
Energy present & input (J/cm2) =     2.554     2.464
Vaporized depth (micron) =     .092
J-depths (35,30,25,20) =     .000     .000     .000     .000
Bubble-depths (27,26,25,24) =     .000     .000     .000     .000
                                   all bubble nucleation was below threshold
```

Example Problem #2

The second problem is the exposure of aluminum to a 1.65 J/cm^2 x-ray pulse with a 200 eV blackbody spectrum and a 2.2 ns pulse length. This case was studied in section 5.5. The vaporization depth is seen to be very small compared to the depths for sub-surface boiling. The files Jprofile and BUBprofile should be plotted to find time history of the high nucleation rates.

> mv Al.matdata matdata *set up external data files*
> mv Al.opacdata opacdata

```
> ab                                          start the code, here compiled as "ab"
 X-ray or laser source? (1=Laser)
2
  aluminum
  aluminum
 H-MELT-I (cal/g) =  159.3087890991078
 H-MELT-T (cal/g) =  254.1556418044774
  PLANAR

Choose source term by number
1 = 45 MJ shot
2 = 20 MJ shot
3 = 5 MJ shot
4 = 100 kJ shot
5 = square pulse
6 = Gaussian pulse
5                                                   choose a square pulse
Enter pulse duration (ns)
2.2
Enter total energy into 4Pi (MJ)
1.65                                        this is desired fluence (J/cm 2)
Enter blackbody temperature (keV)
.2
Enter radius (m)
2.821                                  this radius and angle give correct fluence
Enter angle in degrees
60
 Enter Tstop (ns)
100

    time    step size      temperatures for first 5 surface zones              melt depth
    .000   .419E-12   298.373   298.373   298.371   298.370   298.369    .000
   2.001   .913E-12  5087.775  5094.258  5095.494  5090.961  5077.338   1.817
   4.001   .103E-11  3873.557  3873.530  3874.519  3874.712  3873.953   1.705
   6.001   .109E-11  3372.385  3372.351  3372.261  3371.695  3370.567   1.705
   8.001   .114E-11  3079.488  3079.465  3079.207  3078.609  3077.609   1.817
 ISURFvapor = 1                          first zone has completely vaporized
 TIME = 8.97881421792784
 CYCLE = 8630

    skip to the end of the run

 TIME 95.78547102172142
U      1.41988E+00 1.41549E+00 1.41084E+00 1.40592E+00 1.40069E+00
P      8.55662E+04 6.72783E+04 6.63398E+04 6.53435E+04 6.42856E+04
T      1.37368E+03 1.37366E+03 1.37362E+03 1.37355E+03 1.37346E+03
```

Energy present & input (J/cm2) = 1.701 1.650
100.001 .145E-11 1352.750 1352.732 1352.692 1352.628 1352.536 2.488

Total fluence (J/cm2) = 1.650
Maximum melt depth (micron) = 2.488
Maximum total melt depth (micron) = 2.488
Spalled depth (micron) = .010 *only one zone vaporized*
Maximum front surface temp = 7566.03
Maximum front surface enthalpy (cal/g) = 4268.2138
Minimum and maximum time steps = 5.016E-14 1.482E-12
Maximum enthalpy change (cal/g) = 853.6194
Maximum heat flux (W/cm2) = 8.9875E+07
Fraction vaporized in surface zone .01466
Energy present & input (J/cm2) = 1.700 1.650
Vaporized depth (micron) = .010
J-depths (35,30,25,20) = .452 .489 .570 .570
Bubble-depths (27,26,25,24) = .353 .417 .417 .452
significant depths for high bubble nucleation rates
(see Figures 5-53 and 5-54)

```
      PROGRAM ABLATOR
C ENERGY-BASED WALL RESPONSE MODEL
C 1-D TRANSIENT HEAT CONDUCTION
C 1-D FINITE DIFFERENCE WAVE PROPAGATION
C TEMPERATURE-DEPENDENT MATERIAL PROPERTIES
C HEAT GENERATION FROM X-RAY DEPOSITION
C  IN A DOUBLE EXPONENTIAL PULSE
C  OR IN SQUARE OR GAUSSIAN PULSES
C USES A 45 BIN APPROXIMATION TO SPECTRUM
C SUPPLY COLD OPACITIES IN INVERSE METERS
C EXPLICT SCHEME
C SIMPLE RATIO ZONING
C UNITS: SI, KEV FOR BBT STUFF

      IMPLICIT DOUBLE PRECISION(A-H,O-Z)
      PARAMETER (N=100,NP1=101,NBIN=45,NSAVE=5)
      DIMENSION H(N), HG(N), T(0:NP1), TNEW(0:NP1), ZMASS(NP1)
      DIMENSION EFRAC(N,NBIN), OPAC(NBIN), BIN(NBIN), BINW(NBIN)
      DIMENSION EWALL(NBIN), ELEAK(NBIN), EWALLOLD(NBIN)
      DIMENSION EIN(NBIN), ELEAKOLD(NBIN), EZONE(N)
      DIMENSION FBBWALL(NBIN), FBBLEAK(NBIN), XLOC(NP1)
      DIMENSION ACOND(13), AH2T(10), EOSCOEF(10), SIGMACOEF(7)
      DIMENSION A(0:N), U(0:NP1), X(0:NP1), X0(0:NP1), XC(NP1)
      DIMENSION XNEW(0:N),SX(0:NP1),SXNEW(0:NP1), P(0:N)
      DIMENSION SXD(N),SXDNEW(N),SZD(N),SZDNEW(N), PHI(0:NP1)
      DIMENSION RHO(0:NP1), RHONEW(0:NP1), Q(0:NP1), C(N)
      DIMENSION XQUAL(NP1),VOLF(NP1)
      DIMENSION RATEJ(N),TNUC(N), BUBBLE(N)
      DIMENSION QP1(N), QP2(N), SURFCSTUFF(10)
      INTEGER GEOM,QFLAG
      CHARACTER*1 TAB
      CHARACTER*1 JUNK
      CHARACTER*50 MATNAME

      EXTERNAL TSURF, PSURF, ZBRENT, CONDSURF, QIWO

      COMMON/MATDAT/TMELT,HMELTI,HMELTT,ACOND,AH2T
      COMMON/EOSDAT/RHO0,EOSCOEF,ABOIL,BBOIL,PRNU,YIELD0
      COMMON/EINTEGRAL/EWALLOLD,ELEAKOLD,EWALL,ELEAK,EIN
      COMMON/OPACBINS/BIN,BINW
      COMMON/SURFT/HGSURF,QUALSURFT
      COMMON/SURFP/RHOSURF,QUALSURFP,HGVSURF,HGLSURF,TEMPSURF
      COMMON/SURFC/SURFCSTUFF
      COMMON/SURFTEN/SIGMACOEF

C DEFINITION OF ARRAY VARIABLES
C   H           TOTAL INTERNAL ENERGY IN ZONE
C   HG          SPECIFIC INTERNAL ENERGY FOR A ZONE
C   T           TEMPERATURE IN A ZONE
C   TNEW        NEW TEMPERATURE (TO BE APPLIED NEXT TIME STEP)
C   ZMASS       MASS IN A ZONE (CONSTANT THROUGH PROBLEM)
C   EFRAC       FRACION OF INCIDENT BIN ENERGY EIN(J) ABSORBED
C                 IN A ZONE
C   OPAC        OPACITY IN INVERSE METERS AT A GIVEN PHOTON ENERGY
```

```
C   BIN          CENTRAL ENERGY (IN KEV) OF A PHOTON BIN
C   BINW         PHOTON BIN WIDTH
C   EWALL        RUNNING SUM OF WALL ENERGY IN A BIN
C   ELEAK        RUNNING SUM OF LEAK ENERGY IN A BIN
C   EWALLOLD     SUM FROM LAST TIME STEP
C   ELEAKOLD     SUM FROM LAST TIME STEP
C   EIN          TOTAL ENERGY ADDED THIS STEP IN A BIN
C   EZONE        FRACTION OF EIN DEPOSITED IN A ZONE
C   FBBWALL      FRACTION OF WALL ENERGY IN A BIN
C   FBBLEAK      FRACTION OF LEAK ENERGY IN A BIN
C   XLOC         CENTER OF ORIGINAL ZONE (MICRONS)
C   ACOND        COEFFICIENTS FOR THERMAL CONDUCTIVITY VS TEMP
C   AH2T         COEFFICIENTS FOR TEMPERATURE-ENTHALPY RELATIONS
C   EOSCOEF      COEFFICIENTS FOR EQUATION OF STATE
C   SIGMACOEF    COEFFICIENTS FOR SURFACE TENSION (AKA SIGMA)
C   A            ACCELERATION OF A NODE
C   U            VELOCITY OF A NODE
C   X            LOCATION OF A NODE
C   X0           ORIGINAL LOCATION OF A NODE
C   XC           CURRENT CENTER LOCATION OF A ZONE
C   XNEW         NEW NODE LOCATION (TO BE APPLIED NEXT TIME STEP)
C   SX           NORMAL STRESS
C   SXNEW        NEW NORMAL STRESS (TO BE APPLIED NEXT TIME STEP)
C   P            PRESSURE
C   SXD          DEVIATORIC STRESS
C   SXDNEW       NEW DEVIATORIC STRESS (TO BE APPLIED NEXT TIME STEP)
C   SZD          DEVIATORIC STRESS (FOR CYLINDRICAL GEOMETRIES)
C   SZDNEW       NEW DEVIATORIC STRESS (TO BE APPLIED NEXT TIME STEP)
C   PHI          DIFFERENCE BETWEEN LONGITUDINAL AND TRANSVERSE STRESS
C   RHO          DENSITY
C   RHONEW       NEW DENSITY (TO BE APPLIED NEXT TIME STEP)
C   Q            ARTIFICIAL VISCOSITY
C   C            LOCAL SOUND SPEED
C   XQUAL        QUALITY (VAPOR MASS FRACTION) IN ZONE
C   VOLF         VAPOR VOLUME FRACTION IN ZONE
C   RATEJ        LOG OF BUBBLE NUCLEATION RATE
C   TNUC         LOG OF INDUCTION TIME FOR NUCLEATION RATE DEVELOPMENT
C   BUBBLE       LOG OF CUMULATIVE NUMBER OF BUBBLES PER UNIT VOLUME
C   QP1          QUANTITIY FOR MOSS & WHITE ARTIFICIAL VISCOSITY
C   QP2          QUANTITIY FOR MOSS & WHITE ARTIFICIAL VISCOSITY
C   SURFCSTUFF   QUANTITIES FOR SURFACE ZONE CONDUCTION ITERATIONS


C DEFINE A BLACKBODY FUNCTION
   BBE(JBB,TBB) = BINW(JBB) * ((BIN(JBB)/TBB)**3) /
     &       (DEXP(BIN(JBB)/TBB)-1.)

   TAB = CHAR(9)
   PI = 4.*ATAN(1.)

   WRITE(*,*) 'X-ray or laser source? (1=Laser)'
   READ(*,*) LASERFLAG

   IF (LASERFLAG .NE. 1) THEN
```

```
      OPEN(UNIT=8,FILE="opacdata",STATUS="OLD")
      READ(8,130) MAINAME
      WRITE(*,*) MAINAME
      DO 2, J=1,NBIN
         READ(8,101) BIN(J), JUNK, BINW(J), JUNK, OPAC(J)
c        write(*,101) BIN(J), JUNK, BINW(J), JUNK, OPAC(J)
  2   CONTINUE
      CLOSE(8)
      ELSE
         WRITE(*,*) 'Enter absorption coefficient (m-1)'
         READ(*,*) OPACLASER
         DO 3, J=1,NBIN
            BIN(J) = DBLE(J)/20.
            BINW(J) = 0.05
            OPAC(J) = OPACLASER
  3      CONTINUE
      END IF

C READ IN MATERIAL PROPERTIES
      CALL READMAT
      GAMMA = EOSCOEF(9)
      RBAR = EOSCOEF(10)

C SHEAR MODULUS COEFFICIENT, BASED ON POISSON'S RATIO
      GNU = (1. - 2. * PRNU) / (2. * (1. - PRNU))
C SOUND SPEED COEFFICIENT, BASED ON POISSON'S RATIO
      SNU = SQRT(3. * (1. - PRNU) / (1. + PRNU))

C CHOOSE ARTIFICIAL VISCOSITY MEIHOD
c     WRITE(*,*) 'Artificial viscosity method'
c     WRITE(*,*) '     1 = VNR'
c     WRITE(*,*) '     2 = M&W'
c     READ(*,*) QFLAG
      QFLAG = 1

C INITIALIZE ARTIFICIAL VISCOSITY COEFFICIENTS
C B1,B2 ARE FOR SOLID, B3 IS FOR SPALLED MATERIAL (NOT USED)
      B1 = 1.000
      B2 = 0.30
C     B3 = 0.060
C     WRITE(*,*) 'Enter B2 (suggest 0.3)'
C     READ(*,*) B2

C INITIALIZE TIME STEP CONTROL COEFFICIENTS
      CT1 = 0.9
      CT2 = 1.10
C     WRITE(*,*) 'Enter CFL (must be < 0.5)'
C     READ(*,*) CFL
      CFL = 0.40

C SET SPALL STRESS (FOR REMOVAL OF MELTED MATERIAL) (in Pa)
      SPALL = -1.0D+10

C SET UP ZONES
```

```
C GEOM IS FLAG FOR PLANAR (1), CYLINDRICAL (2), OR SPHERICAL (3)
   CALL ZONESET(RHO0,X0,XC,XLOC,ZMASS,GEOM)
   IF (GEOM .EQ. 1) WRITE(*,*) 'PLANAR'
   IF (GEOM .EQ. 2) WRITE(*,*) 'CYLINDRICAL'
   IF (GEOM .EQ. 3) WRITE(*,*) 'SPHERICAL'
   IF (GEOM .LT. 1 .OR. GEOM .GT. 3) THEN
      WRITE(*,*) 'GEOM = ',GEOM
      STOP
   END IF

C CHOOSE SOURCE TERM
  7   CONTINUE
   WRITE(*,'(A)') 'Choose source term by number'
   IF (LASERFLAG .NE. 1) THEN
      WRITE(*,'(A)') '1 = 45 MJ shot'
      WRITE(*,'(A)') '2 = 20 MJ shot'
      WRITE(*,'(A)') '3 = 5 MJ shot'
      WRITE(*,'(A)') '4 = 100 kJ shot'
   END IF
   WRITE(*,'(A)') '5 = square pulse'
   WRITE(*,'(A)') '6 = Gaussian pulse'
   READ(*,*) ISOURCE
   IF(ISOURCE .GT. 6 .OR. ISOURCE .LT. 1) GOTO 7

C SET UP FOR ENERGY DEPOSITION BASED ON ISOURCE CHOICE
   CALL XSOURCE(ISOURCE,LASERFLAG,FBBWALL,FBBLEAK,TSTART)

   WRITE(*,'(A)') 'Enter radius (m)'
   READ(*,*) RADIUS
   AREA = 4. * PI * RADIUS**2

C  WRITE(*,'(A)') 'Hydro? (1=yes)'
C  READ(*,*) LHYDRO
   LHYDRO = 1

C ENTER ANGLE FROM TARGET AXIS IN DEGREES, CONVERT TO RADIANS
   WRITE(*,110)
   READ(*,*) THETA
   COSTH = COS(THETA * PI / 180.)

   HG0 = 0.0
   TINF = AH2T(1)

C DETERMINE INITIAL TIME STEP SIZE
C ROOM TEMPERATURE MATERIAL PROPERTIES, TO GET THINGS STARTED
C FIRST GET HEAT CAPACITY AT ROOM TEMP
   CALL H2T(HG0,T0)
   H1 = HG0 + 0.1
   CALL H2T(H1,T1)
   CVS = (H1 - HG0) / (T1 - T0)
C NOW GET HEAT CAPACITY OF LIQUID
   CVL = 1. / AH2T(8)
C CHOOSE MINIMUM FOR USE IN TIME STEP CALCULATION
   CV0 = MIN(CVS,CVL)
```

```
C      J/kg.K
       CALL CONDVST(TINF,0.0,COND)
C      W/m.K
       ALPHA = COND / (RHO0 * CV0)
C      m2/sec

       DIHEAT = CFL * (X0(1)-X0(0))**2 / ALPHA

C SET PROBLEM TIME (sec) AND FLAGS FOR OCCASSIONAL DATA DUMPS (ns)
       WRITE(*,*) 'Enter Tstop (ns)'
       READ(*,*) TSTOP
       TM = TSTART * 1.0D-09
       TSTOP = TSTOP * 1.0D-09 + 2.*DIHEAT
       TFRONT = TSTART - 1.0D-13
       TSCREEN = TSTART - 1.0D-13

       XMELTMAX = 0.
       XIMELTMAX = 0.
       TFMAX = TINF
       HGFMAX = HG0
       DHGMXMAX = 0.0

C INITIALIZE ENERGIES AND TEMPERATURES
C ZONE ENERGY STORED IN H( ), SPECIFIC ENERGY STORED IN HG( )
       DO 13, I=1,N
          H(I) = HG0 * ZMASS(I)
          HG(I) = HG0
          T(I) = TINF
  13   CONTINUE
       T(0) = TINF
       T(NP1) = TINF

C INITIALIZE HYDRO-MOTION VARIABLES
       CALL EOSF(RHO0,F1,F2)
       P0 = F1 + F2 * HG0
       CALL SOUND(HG0,RHO0,P0,F2,C0)
C CONVERT SOUND TO ELASTIC FROM HYDRODYNAMIC MATERIAL
       C0 = C0 * SNU
       DO 221, I = 1,N
          A(I) = 0.00D+00
          U(I) = 0.00D+00
          X(I) = X0(I)
          RHO(I) = RHO0
          Q(I) = 0.00D+00
          P(I) = P0
          SX(I) = 0.00D+00
          SXD(I) = 0.00D+00
          PHI(I) = 0.00D+00
          C(I) = C0
          XQUAL(I) = 0.00D+00
          VOLF(I) = 0.00D+00
          QP1(I) = 0.0D+00
          QP2(I) = 0.0D+00
          BUBBLE(I) = 0.0D+00
```

```
 221  CONTINUE

C ASSUME FREE BOUNDARY AT FRONT
    U(0) = 0.00D+00
    X(0) = X0(0)
    RHO(0) = 0.00D+00
    RHONEW(0) = 0.00D+00
    SX(0) = 0.00D+00
    P(0) = 0.00D+00
    PHI(0) = 0.00D+00
    Q(0) = 0.00D+00
C ASSUME NON-REFLECTING BOUNDARY AT BACK
    U(NP1) = 0.00D+00
    UNOLD = 0.00D+00
    X(NP1) = X0(NP1)
    RHO(NP1) = 0.00D+00
    SX(NP1) = 0.00D+00
    PHI(NP1) = 0.00D+00
    Q(NP1) = 0.00D+00
    XQUAL(NP1) = 0.00D+00
    VOLF(NP1) = 0.00D+00

C INITIALIZE LIQUID DENSITY (FOR SURFACE VAPORIZATION)
    RHOLSURF = RHO0

C SET INITIAL SPALL ZONE AND FRONT SURFACE ZONE
    ISPALL = 0
    ISURF = 1

C SET MIN QUALITY FOR SURFACE ZONE TO BE CONSIDERED W/O VAPOR
    QMIN = 1.0D-06

C SET INITIAL TIME STEP SIZE
    DIHYDRO = (X0(1)-X0(0))/C0
    DT = MIN(DIHEAT,DIHYDRO)
    IF (LHYDRO .NE. 1) DT = DIHEAT
    DTOLD = DT

C SET UP SOURCE ENERGY MULTIPLIERS
C WILL GIVE FRACTION OF ENERGY IN EACH ZONE, IN EACH BIN
C  OF THE TOTAL INCIDENT FROM WALL AND LEAK X RAYS
C SCALE LEAK ENERGY WITH LAMBERTIAN DISTRIBUTION
    DO 15, J=1,NBIN
        FRACIN = 1.
        DO 14, I=1,N
       FRACOUT = EXP(-X(I) * OPAC(J))
       EFRAC(I,J) = FRACIN - FRACOUT
       FRACIN = FRACOUT
  14       CONTINUE

C INITIALIZE ENERGIES/BIN FOR FIRST TIME STEP
        EWALLOLD(J) = 0.
        ELEAKOLD(J) = 0.
  15  CONTINUE
```

```
C SAVE ENERGY FRACTION IN EACH ZONE
   DO 17, I=1,N
       EZONE(I) = 0.0D+00
       DO 16, J=1,NBIN
      EZONE(I) = EZONE(I) + EFRAC(I,J)
  16      CONTINUE
  17  CONTINUE

C FOR LASER SOURCE, RECORD ENERGY DEPOSITION PROFILE
   IF (LASERFLAG .EQ. 1) THEN
       OPEN(UNIT=10,FILE='ldepfrac')
       DO 18, I=1,N
         WRITE(10,111) I, X0(I)*1.0D+06, EFRAC(I,1)
  18      CONTINUE
       CLOSE(10)
   END IF

   OPEN(UNIT=10,FILE='Pfront')
   OPEN(UNIT=11,FILE='Pprofile')
      OPEN(UNIT=13,FILE='SXprofile')
   OPEN(UNIT=14,FILE='SXDprofile')
   OPEN(UNIT=15,FILE='Uprofile')
   OPEN(UNIT=16,FILE='Xprofile')
   OPEN(UNIT=17,FILE='RHOprofile')
   OPEN(UNIT=18,FILE='QUALprofile')
   OPEN(UNIT=19,FILE='Tprofile')
   OPEN(UNIT=20,FILE='HGprofile')
   OPEN(UNIT=21,FILE='spall')
   OPEN(UNIT=22,FILE='VOLFprofile')
   OPEN(UNIT=24,FILE='TNUCprofile')
   OPEN(UNIT=25,FILE='Jprofile')
C  OPEN(UNIT=26,FILE='dh1')
C  OPEN(UNIT=27,FILE='dhvap')
C  OPEN(UNIT=33,FILE='iinstab')
c  OPEN(UNIT=34,FILE='dt')
   OPEN(UNIT=35,FILE='BUBprofile')

   EINMAX = 0.
   DIMIN = 100.
   DIMAX = 0.0
   HEASIMAX = 0.0
   DHGMXMAX = 0.0
   IF(GEOM .GT. 1 .AND. X0(0) .EQ. 0.0) THEN
      IFLAGAXIS = 1
   ELSE
      IFLAGAXIS = 0
   END IF

C INITIALIZE MAX BUBBLE NUCLEATION DEPTHS AND ZONE NUMBERS
   I35 = 1
   I30 = 1
   I25 = 1
   I20 = 1
```

```
      X35 = 0.0
      X30 = 0.0
      X25 = 0.0
      X20 = 0.0
      IB27 = 1
      IB26 = 1
      IB25 = 1
      IB24 = 1
      XB27 = 0.0
      XB26 = 0.0
      XB25 = 0.0
      XB24 = 0.0

C SET UP TO PRINT INFO TO SCREEN EVERY NCYCLEPRINT CYCLES
      NCYCLEPRINT = 10000
      NCYCLE = 1
      TPRESS = TM * 1.0D+09

C *******************************************************
C START MARCHING IN TM
   20 CONTINUE
      TM = TM + DT
      IF (TM.GT.TSTOP) GOTO 95

C SET UP MAGNITUDE OF ENERGY PULSES
C RETURNS ENERGY IN EACH BIN FOR THIS TIME STEP, EIN(J) IN COMMON
      CALL XPULSE(TM,ISOURCE,COSTH,AREA,FBBWALL,FBBLEAK)

C ADD THE TOTAL ENERGY DEPOSITED THIS STEP TO RUNNING TOTAL
      DO 39, J=1,NBIN
         EINMAX = EINMAX + EIN(J)
   39 CONTINUE

C RESET MAX SPECIFIC ENERGY CHANGE
      DHGMAX = 0.0
C RESET SPALL FLAG
      ISPALLFLAG = 0

C SET UP THERMAL CONDUCTIVITIES FOR FIRST ZONE
      VFLAG = VOLF(1)
      IF (ISURF .EQ. 1) VFLAG = 0.0D+00
      CALL CONDVST(T(1),VFLAG,CONDE)
      CALL BETAGEOM(GEOM,X(0),X(1),BETAC)
      AE = CONDE * BETAC / (X(1) - X(0))
C INSULATED FRONT SURFACE (CONDUCTION BETWEEN ZONES 0 AND 1)
      HEAST = 0.0D+00

      IF (LHYDRO .EQ. 1) THEN
C SET UP FOR FINDING NEW HYDRO-BASED MAXIMUM DT
         DTHYDRO = 100.
         IF (ISURF .EQ. 1 .AND. XQUAL(ISURF) .GT. QMIN) THEN
C        DETERMINE LEFT NODE MOTION OF ISURF ZONE W/O F=MA
          TRIGHT = T(1)
          PRIGHT = P(1)
```

```
      PLEFT = P(0)
      CALL USURFIX(TRIGHT,PRIGHT,PLEFT,UNEW)
      A(0) = (UNEW - U(0)) / DT
      U(0) = UNEW
      XNEW(0) = X(0) + DT * U(0)

     ELSE
      IF (GEOM .EQ. 1) THEN
C DETERMINE ACCELERATION, VELOCITY, LOCATION FOR LEFT EDGE
         A(0) = 2. * ( 0.0 - (SX(1)+Q(1))) /
     &       ( RHO(1)*(X(1)-X(0)) + 0.0 )
           U(0) = U(0) + A(0) * (DT + DTOLD)/2.
         XNEW(0) = X(0) + DT * U(0)
      ELSE
C        CHECK IF INNER RADIUS HAS ALREADY HIT AXIS
         IF (IFLAGAXIS .EQ. 0) THEN
           A(0) = 2. * ( 0.0 - (SX(1)+Q(1))) /
     &          ( RHO(1)*(X(1)-X(0)) + 0.0 ) +
     &          2. * (GEOM - 1) * (PHI(1) + PHI(0)) /
     &          ( RHO(1)*(X(1)+X(0)) + 0.0 )
          UNEW = U(0) + A(0) * (DT + DTOLD)/2.
          XNEW0 = X(0) + DT * UNEW
C     CHECK IF SURFACE HAS PASSED THROUGH AXIS
          IF (XNEW0 .LE. 0.0) THEN
C KEEPING SAME ACCELERATION, FIGURE DT TO WHEN STUFF HITS AT CENTER
             CALL AXIS(X(0),U(0),A(0),DTOLD,DTNEW)
             DT = DTNEW
             XNEW(0) = 0.0
             U(0) = 0.0
             IFLAGAXIS = 1
          ELSE
             U(0) = UNEW
             XNEW(0) = XNEW0
          END IF
               END IF
      END IF
     END IF
   END IF

C %%%%%%%%%%%%% START OF LOOP THROUGH ZONES %%%%%%%%%%%%%%
C FRONT BC IS THERMALLY INSULATED
C REAR BC IS AT FIXED TEMPERATURE
C FRONT SURFACE IS FREE TO MOVE
C REAR SURFACE IS NON-REFLECTING

   DO 50, I=1,N

   IF (LHYDRO .EQ. 1) THEN
C COMPUTE ACCELERATION, VELOCITY, LOCATION

   IF (I .EQ. (ISURF-1) .AND. XQUAL(ISURF) .GT. QMIN .AND.
     &      VOLF(I) .GT. 0.99) THEN
C DETERMINE RIGHT NODE MOTION OF ISURF ZONE W/ ADJUSTED PRESSURE
      PRIGHT = P(ISURF)
```

```
      DXSURF = (X(ISURF)-X(I)) * (1.0D+00-VOLF(ISURF))
      XINTERNAL = X(ISURF) - DXSURF
      DXC1 = XINTERNAL - XC(I)
      DX1 = XINTERNAL - X(I)
      CALL PLEFTCALC(PRIGHT,P(I),DXC1,DX1,RHOVSURF,
     &            XQUAL(ISURF),T(ISURF),PLEFT)

      A(I) = 2. * ( (SX(I)+Q(I)) - (PLEFT+Q(I+1))) /
     &     ( RHO(I+1)*(X(I+1)-X(I)) + RHO(I)*(X(I)-X(I-1)) ) +
     &      2. * (GEOM - 1) * (PHI(I) - PHI(I+1)) /
     &      ( RHO(I+1)*(X(I+1)+X(I)) + RHO(I)*(X(I-1)+X(I)) )
          U(I) = U(I) + A(I) * (DT + DTOLD)/2.

   ELSE IF (I .LT. N) THEN
      A(I) = 2. * ( (SX(I)+Q(I)) - (SX(I+1)+Q(I+1))) /
     &      ( RHO(I+1)*(X(I+1)-X(I)) + RHO(I)*(X(I)-X(I-1)) ) +
     &      2. * (GEOM - 1) * (PHI(I) - PHI(I+1)) /
     &      ( RHO(I+1)*(X(I+1)+X(I)) + RHO(I)*(X(I-1)+X(I)) )
          U(I) = U(I) + A(I) * (DT + DTOLD)/2.

      ELSE
C NON-REFLECTING BOUNDARY CONDITION (NRBC)
C BASED ON HALPERN, 1982
          DXNRBC = X(N) - X(N-1)
          TNRBC0 = 2.*((C(N)*DT)**2)/(C(N)*DT+DXNRBC)
          TNRBC1 = (-1./DXNRBC) + (DXNRBC/(C(N)*DT)**2)
          TNRBC2 = (C(N)*DT-DXNRBC)/(2.*(C(N)*DT)**2)
          TNRBC3 = 1. / DXNRBC
          UNNEW = TNRBC0*(U(N)*TNRBC1+UNOLD*TNRBC2+U(N-1)*TNRBC3)
          UNOLD = U(N)
          U(N) = UNNEW
          A(N) = U(N) / DT
      END IF

   XNEW(I) = X(I) + DT * U(I)

C COMPUTE NEW DENSITY FROM ZONE MASS
   CALL DENGEOM(GEOM,XNEW(I-1),XNEW(I),RDEN)
   RHONEW(I) = ZMASS(I) / ((XNEW(I) - XNEW(I-1)) * RDEN)
   RHOBAR = (RHONEW(I)+RHO(I)) / 2.
   DELRHO = 0.5*(RHONEW(I)-RHO(I))/RHOBAR**2
   RHODOT = (RHONEW(I)-RHO(I))/(DT*RHOBAR)

C COMPUTE FACTORS FOR LINEAR (IN ENERGY) EOS
   RHOEOS = RHONEW(I)
   IF (I .EQ. ISURF) THEN
C SPECIAL TREATMENT FOR VAPORIZING SURFACE ZONE
       CALL FSURF(RHOEOS,RHOLSURF,XQUAL(ISURF),QMIN,F1,F2)
   ELSE IF (I .GT. ISPALL) THEN
C SOLID/LIQUID ZONE
       CALL EOSF(RHOEOS,F1,F2)
   ELSE IF (VOLF(I) .LT. 0.001) THEN
       CALL EOSF(RHOEOS,F1,F2)
   ELSE IF (VOLF(I) .GT. 0.999) THEN
```

```
          CALL FVAPOR(RHOEOS,F1,F2)
       ELSE
          XQ2 = XQUAL(I)
          CALL F2PHASE(RHOEOS,HG(I),XQ2,F1,F2)
       END IF

C COMPUTE ARTIFICIAL VISCOSITY
       XXXX = (XNEW(I) - XNEW(I-1) + X(I) - X(I-1)) / 2.
       QLIN = RHOBAR * B2 * XXXX * C(I) * RHODOT
          QQUAD = RHOBAR * (B1 * XXXX)**2 * RHODOT * ABS(RHODOT)
C CHOOSE VON NEUMANN & RICHTMEYER OR MOSS & WHITE FORM
       IF (QFLAG .EQ. 2) THEN
C SET CRITERION FROM MOSS & WHITE
          QP = SX(I) * (U(I)-U(I-1))/XXXX
          QPTEST = QP1(I) + (QP1(I)-QP2(I)) * DT/DTOLD
          QF1 = 0.0
          QF2 = 0.0
          IF(QP .GT. 0.) QF1=1.
          IF(QP .GT. QPTEST) QF2=1.
          Q(I) = (QQUAD + QLIN) * (QF1 + QF2)
       ELSE
C VON NEUMANN & RICHTMEYER
          IF (RHODOT .GT. 0.) THEN
            Q(I) = QLIN + QQUAD
          ELSE
            Q(I) = 0.0D+00
          END IF
       END IF
C TURN OFF ART VISC FOR SURFACE ZONE
       IF (I .EQ. (ISURF)) THEN
          Q(I) = 0.0D+00
       END IF

C COMPUTE DEVIATORIC STRESSES AND ENERGIES IF SOLID
       IF (T(I) .LT. TMELT .AND. I .GT. ISPALL) THEN
          DXD = (U(I) - U(I-1)) / XXXX + RHODOT / 3.
          G = GNU * RHO(I) * C(I)**2
C COMPUTE CURRENT YIELD STRENGTH USING LINEAR RAMP OF
C YIELD STRENGTH FROM YIELD0 @ TINF DOWN TO 0 @ TMELT
          YBIG = YIELD0 * (TMELT-T(I))/(TMELT-TINF)
          SIGMAXD = SXD(I) + 2. * DT * G * DXD

C SPLIT BASED ON GEOMETRY
          IF (GEOM .EQ. 1 .OR. GEOM .EQ. 3) THEN
C PLANAR OR SPHERICAL
            YIELDTEST = YBIG * 2. / 3.
            IF (ABS(SIGMAXD) .GT. YIELDTEST) THEN
             SXDNEW(I) = ABS(SIGMAXD)/SIGMAXD * YIELDTEST
            ELSE
             SXDNEW(I) = SIGMAXD
            END IF
          PHI(I) = 1.5 * SXDNEW(I)
            DELED = 0.75*DT*DXD*(SXDNEW(I)+SXD(I)) / RHOBAR
          ELSE
```

```
C CYLINDRICAL
        DZD = RHODOT / 3.
      SIGMAZD = SZD(I) + 2. * DT * G * DZD
      FY = 2.*(SIGMAXD**2 + SIGMAXD*SIGMAZD + SIGMAZD**2)
      YIELDTEST = (2./3.) * YBIG**2
      IF (FY .GT. YIELDTEST) THEN
          FSQ = SQRT(YIELDTEST/FY)
          SXDNEW(I) = SIGAMAXD * FSQ
          SZDNEW(I) = SIGAMAZD * FSQ
      END IF

   DELED=(DT/(2.*RHOBAR))*((SXDNEW(I)+SXD(I))*(2.*DXD+DZD)+
     &          (SZDNEW(I)+SZD(I))*(2.*DZD+DZD))
         PHI(I) = 2.*SXDNEW(I) + SZDNEW(I)
       END IF
   ELSE
C MELTED OR SPALLED MATERIALS
       DELED = 0.0D+00
       PHI(I) = 0.0D+00
       SXDNEW(I) = 0.0D+00
       SZDNEW(I) = 0.0D+00
  END IF
   IF (I .LE. ISPALL) SXDNEW(I) = 0.0

C COMPUTE STRESS ENERGY CHANGE IN J/M2
   HSTRESS = (F1 + P(I) + 2.*Q(I)) * DELRHO * ZMASS(I)

C COMPUTE DEVIATORIC CONTRIBUTION IN J/M2
   HDEV = DELED * ZMASS(I)

   END IF
C END IF FOR LHYDRO-ONLY STEPS

C SET UP SOURCE ENERGY
C SUM TO GET NET ENERGY/ZONE
C NET ENERGY HAS UNITS OF J/M2
   HIN = 0.
   DO 48, J=1,NBIN
       HIN = HIN + EFRAC(I,J) * EIN(J)
  48  CONTINUE

C HEAT CONDUCTION BALANCE ((I-1) TO EAST = -(I TO WEST))
   HWEST = HEAST
C SET CONDUCTION COEFFICIENT FOR THIS ZONE
   CONDP = CONDE
   VFLAG = VOLF(I+1)
   IF (I .EQ. (ISURF-1)) VFLAG = 0.0D+00
   CALL CONDVST(T(I+1),VFLAG,CONDE)
   CONDEI = 2. * CONDP * CONDE / (CONDP + CONDE)

C BASE HEAT CONDUCTION ON TEMP, LOCATIONS, PROPERTIES FROM PREVIOUS TM

   IF (I .EQ. ISURF) THEN
C ADJUST CONDUCTION DISTANCE TO REFLECT ONLY REMAINING LIQUID
```

```
C   AND SOLVE IMPLICITLY
      DXSURF = (X(I)-X(I-1)) * (1.0D+00-VOLF(I))
      XINTERNAL = X(I) - DXSURF
      CALL BETAGEOM(GEOM,XINTERNAL,X(I),BETAC)
      DXP1 = XC(I+2) - XC(I+1)
C FIGURE WHAT WILL BE HEAT COND BETWEEN (I+1) AND (I+2)
      CALL CONDVST(T(I+2),VOLF(I+2),CONDE2)
      CONDEI1 = 2. * CONDE * CONDE2 / (CONDE + CONDE2)
      CALL BETAGEOM(GEOM,XC(I+1),XC(I+2),BETAC1)
      AE1 = CONDEI1 * BETAC1 / DXP1
      HEAST1 = AE1*(T(I+1)-T(I+2))
C SET TEMPORARY ENERGIES IN ZONE ISURF AND ISURF+1
      HTEMPP = H(ISURF) + HWEST * DT + HSTRESS + HIN
      HTEMPE = H(ISURF+1) - HEAST1*DT + HIN*EZONE(I+1)/EZONE(I)
      HGTEMPP = HTEMPP / ZMASS(ISURF)
      HGTEMPE = HTEMPE / ZMASS(ISURF+1)
C ENHANCE CONDUCTIVITY TO REDUCE SURFACE TEMPERATURE VARIATIONS
      CONDP = CONDP * (1.0D+00 + 4. * XQUAL(ISURF)**2)
C FILL UP COMMON BLOCKS FOR ITERATION ROUTINE
      SURFCSTUFF(1) = HTEMPP
      SURFCSTUFF(2) = HTEMPE
      SURFCSTUFF(3) = ZMASS(ISURF)
      SURFCSTUFF(4) = ZMASS(ISURF+1)
      SURFCSTUFF(5) = DT
      SURFCSTUFF(6) = QMIN
      SURFCSTUFF(7) = CONDP
      SURFCSTUFF(8) = DXSURF
      SURFCSTUFF(9) = BETAC
      SURFCSTUFF(10) = T(I)
      QUALSURFT = XQUAL(I)
C SET UP BRACKETING INITIAL GUESSES FOR HEAST BASED ON CURRENT TEMPS
      HEAST = CONDP * BETAC * (T(I)-T(I+1)) / DXSURF
      CALL BRACKET(CONDSURF,HEAST,HE1,HE2)
      TOL = 1.0D-05
      HEAST = ZBRENT(CONDSURF,HE1,HE2,TOL)

   ELSE
      CALL BETAGEOM(GEOM,XC(I),XC(I+1),BETAC)
      DXC = XC(I+1) - XC(I)
      AE = CONDEI * BETAC / DXC
      HEAST = AE*(T(I)-T(I+1))
   END IF

   IF (HEAST .GT. HEASTMAX) HEASTMAX = HEAST
C COMPUTE NET ENERGY CHANGE FROM CONDUCTION
   HCOND = (HWEST - HEAST) * DT

C UPDATE TOTAL ZONE AND SPECIFIC ENERGIES
   DH = (HIN+HCOND+HDEV+HSTRESS) / (1.D+00 - F2*DELRHO)
   IF (LHYDRO .NE. 1) DH = HIN + HCOND
   H(I) = H(I) + DH
   HG(I) = H(I) / ZMASS(I)

C CHECK FOR MAXIMUM CHANGE IN ZONE ENERGY/KG
```

```
      DHG = DH / ZMASS(I)
      IF(DABS(DHG) .GT. DHGMAX) THEN
            DHGMAX = DABS(DHG)
            IDHGMAX = I
            IF(DHGMAX .GT. DHGMXMAX) THEN
               DHGMXMAX = DHGMAX
               IDHGMXMAX = I
            END IF
      END IF

C APPLY EOS INFORMATION TO GET PRESSURE, TEMP, SOUND SPEED
C DIFFERENT TREATMENTS DEPENDING ON EXPECTED STATE

C SPECIAL TREATMENT FOR SURFACE ZONE (PRESCRIBED QUALITY
C     FROM SURFACE VAPORIZATION ROUTINE)
      IF(I .EQ. ISURF) THEN
         TEMPSURF = T(I)
         HGSURF = HG(I)
         QUALSURFT = XQUAL(I)
         RHOSURF = RHONEW(I)
         QUALSURFP = XQUAL(I)
         PM1 = P(I-1)
         CALL EOSURF(RHOLSURF,RHOVSURF,RHONEW(I+1),QMIN,
     &           PM1,P(I),VOLF(I),C(I))
         TNEW(I) = TEMPSURF
         IF(TNEW(I) .LT. 0.0) THEN
            WRITE(*,*) 'ERROR IN SURF TEMP'
            WRITE(*,*) 'T = ',TNEW(I)
            WRITE(*,*) 'I = ',I
            WRITE(*,*) 'TIME = ',TM*1.0D+09
            WRITE(*,*) 'HG (cal/g) = ',HT
            STOP
         END IF

C USE SOLID/LIQUID EOS FOR UNSPALLED MATERIAL
      ELSE IF(I .GT. ISPALL) THEN
C DETERMINE WHAT THE NEW TEMPERATURE WILL BE
         HT = HG(I)
         CALL H2T(HT,TNEW(I))
         IF(TNEW(I) .LT. 0.0) THEN
            WRITE(*,*) 'ERROR IN SOLID/LIQUID TEMP'
            WRITE(*,*) 'T = ',TNEW(I)
            WRITE(*,*) 'I = ',I
            WRITE(*,*) 'TIME = ',TM*1.0D+09
            WRITE(*,*) 'HG (cal/g) = ',HT
            STOP
         END IF

C COMPUTE NEW PRESSURE FROM EOS
         P(I) = F1 + F2 * HG(I)

C COMPUTE NEW SOUND SPEED
         HEOS = HG(I)
         REOS = RHONEW(I)
```

```
        PEOS = P(I)
        CALL SOUND(HEOS,REOS,PEOS,F2,CEOS)
        IF (TNEW(I) .LT. TMELT) THEN
C APPLY CORRECTION FOR ELASTIC MATERIAL
          C(I) = SNU * CEOS
        ELSE
          C(I) = CEOS
        END IF

C USE "SPALL" OR "VAPOR" EOS FOR SPALLED MATERIAL
    ELSE
        TS = T(I)
      IF(HG(I) .GT. 0.0 .AND. HG(I) .LT. 1.0D+15) THEN
       CALL EOSPALL(HG(I),RHONEW(I),TS,P(I),XQUAL(I),VOLF(I),C(I))
        TNEW(I) = TS
        IF(TNEW(I) .LT. 0.0) THEN
          WRITE(*,*) 'ERROR IN SPALL TEMP'
          WRITE(*,*) 'T = ',TNEW(I)
          WRITE(*,*) 'I = ',I
          WRITE(*,*) 'TIME = ',TM*1.0D+09
          WRITE(*,*) 'HG (cal/g) = ',HG(I)
          WRITE(*,*) 'RHO = ',RHONEW(I)
          STOP
        END IF
      ELSE
          WRITE(*,*) 'ERROR IN ZONE ENERGY'
          WRITE(*,*) 'HG (cal/g)= ',HG(I)/4184.
          WRITE(*,*) 'I = ',I
          WRITE(*,*) 'TIME = ',TM*1.0D+09
          WRITE(*,*) 'T = ',T(I)
          WRITE(*,*) 'RHO = ',RHONEW(I)
          WRITE(*,*) 'QUAL = ',XQUAL(I)
          STOP
      END IF

    END IF

C COMPUTE NEW SIGMA-X
    SXNEW(I) = P(I) - SXDNEW(I)

C COMPUTE MAXIMUM HYDRO TIME STEP FOR THIS ZONE
    DELTAX = XNEW(I)-XNEW(I-1)
    DTI = CT1 * DELTAX /
     &       (B2*C(I) + 2.*B1**2 * ABS(RHODOT) * DELTAX +
     &       SQRT((B2*C(I) + 2.*B1**2 * ABS(RHODOT) * DELTAX)**2 +
     &       C(I)**2))
    IF (DTI .LT. DTHYDRO) THEN
          DTHYDRO = DTI
       IHYDRO = I
    END IF

    TNS = TM * 1.0D+09

C UPDATE POWERS FOR ARTIFICIAL VISCOSITY SWITCH
```

```
      QP2(I) = QP1(I)
      QP1(I) = QP

      IF (LHYDRO .EQ. 1) THEN
C CHECK FOR SPALLED ZONE (LIQUID AT NEGATIVE STRESS)
         TTEST = TMELT + 1.0D-5
         IF (TNEW(I) .GE. TTEST .AND. I .GT. ISPALL) THEN
         IF (SXNEW(I) .LT. SPALL) THEN
                ISPALL = I
                WRITE(*,*) 'ISPALL melt= ',ISPALL
                WRITE(21,134) TM*1.0D+09,TAB,ISPALL,TAB,
     &              X0(ISPALL)*1.0D+06
                ISURF = ISPALL+1
                ISPALLFLAG = 1
         END IF
         END IF
      END IF

   50  CONTINUE
C %%%%%%%%%%%%% END OF LOOP THROUGH ZONES %%%%%%%%%%%%%%

C UPDATE OLD T, X, XC, RHO, AND SIGMA VALUES
      X(0) = XNEW(0)
      T(0) = T(1)
      DTEMPMAX = 0.0
      DO 57, I=1,N
C STORE FOR LIMITING TIME STEP
         DTEMP = ABS(T(I)-TNEW(I))
         IF(DTEMP .GT. DTEMPMAX) THEN
           DTEMPMAX = DTEMP
           ITEMPMAX = I
         END IF
         T(I) = TNEW(I)
         X(I) = XNEW(I)
         XC(I) = (X(I) + X(I-1)) / 2.
         RHO(I) = RHONEW(I)
         SX(I) = SXNEW(I)
         SXD(I) = SXDNEW(I)
   57  CONTINUE
      T(N) = TINF

C DETERMINE MELT DEPTH, IF ANY
      TMLOW = TMELT - 0.1
      TMHIGH = TMELT + 0.1
      IF(T(1) .GE. TMLOW) THEN
         DO 64, I=ISPALL+1,N
         IF(T(I).LT.TMLOW.AND.T(I-1).GE.TMLOW) THEN
            XMELT = XLOC(I-1)
         END IF
         IF(T(I).LT.TMHIGH.AND.T(I-1).GE.TMHIGH) THEN
            XTMELT = XLOC(I-1)
         END IF
   64       CONTINUE
         IF(XMELT .GT. XMELTMAX) XMELTMAX = XMELT
```

```
          IF(XIMELT .GT. XIMELTMAX) XIMELTMAX = XIMELT
       ELSE
          XMELT = 0.0
          XIMELT = 0.0
       END IF

C SURFACE VAPORIZATION SECTION
C COMPUTE VAPORIZED MASS AND ENERGY IN THIS TIME STEP
C FIRST SET AMBIENT PRESSURE
       IF (ISURF .EQ. 1) THEN
          PAMB = 1.33D-04
       ELSE
          PAMB = P(ISURF-1)
       END IF
       DTVAP = 100.
       CALL SURFVAP(GEOM,PAMB,TNEW(ISURF),XNEW(ISURF),DT,
     &          DVAPMASS,DHVAP)

C GET NEW QUALITY (MASS FRACTION OF VAPOR) IN SURFACE ZONE
       DXQ = DVAPMASS / ZMASS(ISURF)
       XQ = XQUAL(ISURF) + DXQ

       IF (XQ .LT. 1.0D+00) THEN
          XQUAL(ISURF) = XQ
       ELSE
C SPALL OFF THIS ZONE AND ADVANCE ISURF
          DQI = 1.0D+00 - XQUAL(ISURF)
          XQUAL(ISURF) = 1.0D+00
          VOLF(ISURF) = 1.0D+00
          DVAPMASS = ZMASS(ISURF) * (XQ - 1.0D+00)
          ISPALL = ISURF
          ISURF = ISURF + 1
          WRITE(*,*) 'ISURFvapor =',ISPALL
          WRITE(*,*) 'TIME =',TM*1.0D+09
          WRITE(*,*) 'CYCLE =',NCYCLE
          WRITE(21,134) TM*1.0D+09,TAB,ISPALL,TAB,
     &             X0(ISPALL)*1.0D+06

C SET UP NEXT SURFACE ZONE PROPERLY
          DXQ = DVAPMASS / ZMASS(ISURF)
          XQUAL(ISURF) = DXQ
          RHOV = P(ISURF) / (RBAR * T(ISURF))
          VOLF = QUAL * RHO / RHOV

          RHOLSURF = RHO(ISURF)
          ISPALLFLAG = 1
       END IF
C END OF SURFACE VAPORIZATION SECTION

C SET NEW TIME STEP TO PREVENT EXCESSIVE VAPORIZATION NEXT STEP
       IF(ISPALLFLAG .EQ. 1) THEN
          CALL SURFVAP(GEOM,PAMB,TNEW(ISURF),XNEW(ISURF),DT,
     &             DVMNEXT,DHVAPN)
          VAPRATIO = DVMNEXT / ZMASS(ISURF)
```

```
        IF(VAPRATIO .GT. 0.02) THEN
       DIVAP = DT * 0.02 / VAPRATIO
        END IF
    END IF

C KEEP TRACK OF MAXIMUM FRONT SURFACE ENERGY
    IF(HG(1) .GT. HGFMAX) THEN
       TFMAX = T(1)
       HGFMAX = HG(1)
    END IF

C WRITE SURFACE ZONE PRESSURE TO A FILE FOR A WHILE
    TNS = TM * 1.0D+09
    IF(TNS .LT. 3.) THEN
        WRITE(10,155) TNS,TAB,ISURF,TAB,P(ISURF),
     &        TAB,T(ISURF),TAB,T(ISURF+1)
    END IF

C CHECK ENERGY BALANCE
    HSUM = 0.0
    EKIN = 0.0
    DO 92, I=1,N
       HSUM = HSUM + H(I)
       UBAR = (U(I) - U(I-1)) / 2.
       EKIN = EKIN + 0.5 * ZMASS(I) * UBAR**2
   92  CONTINUE
    ESUM = HSUM + EKIN

C OUTPUT FOR DIAGNOSTIC PURPOSES
    NCYMOD = MOD(NCYCLE,NCYCLEPRINT)
    IF(NCYMOD .EQ. 0) THEN
       TNS = TM * 1.0D+09
       WRITE(*,*) 'TIME', TM*1.0E+09
       K1 = ISPALL + 1
       K2 = ISPALL + NSAVE
       WRITE(*,139) 'U      ', (U(K),K=K1,K2)
       WRITE(*,139) 'P      ', (P(K),K=K1,K2)
       WRITE(*,139) 'T      ', (T(K),K=K1,K2)
       WRITE(*,136) ESUM/10000.0, EINMAX/10000.0
    END IF
    NCYCLE = NCYCLE + 1

C DETERMINE NEW HEAT TIME STEP FROM CFL CONSTRAINT
    DTHEAT = 1.0D+02
    DO 70, I=1,N
       IF(T(I) .LT. 0.0) THEN
          WRITE(*,*) 'cfl T = ',T(I)
          WRITE(*,*) 'I = ',I
          WRITE(*,*) 'ISURF = ',ISURF
          WRITE(*,*) 'CYCLE = ',NCYCLE
          WRITE(*,*) 'HG = ',HG(I)
          STOP
       END IF
       VFLAG = VOLF(I)
```

```
      IF (I .EQ. ISURF) VFLAG = 0.0D+00
      CALL CONDVST(T(I),VFLAG,COND)
      CALL HEATCAP(VOLF(I),T(I),HG(I),CV)
      ALPHA = COND /(RHO(I) * CV)
      DXHEAT = X(I) - X(I-1)
      DTI = CFL * DXHEAT**2 / ALPHA
      IF(DTI .LT. DTHEAT) THEN
         DTHEAT = DTI
      END IF
   70 CONTINUE

C LIMIT TIME STEP IF MAX TEMP CHANGE IN LAST TIME STEP WAS TOO BIG
    TEMPBIG = 200.0
    IF(DTEMPMAX .GT. TEMPBIG) THEN
       DTTEMP = DT * TEMPBIG / DTEMPMAX
    ELSE
       DTTEMP = 100.
    END IF

C SET NEXT TIME STEP FROM HYDRO AND THERMAL CONSTRAINTS
    DTOLD = DT
    DT = MIN(DTHEAT,DTHYDRO,CT2*DT,DTVAP,DTTEMP)
    IF (LHYDRO .NE. 1) DT = DTHEAT
    IF(DT .GT. DTMAX) DTMAX = DT
    IF(DT .LT. DTMIN) THEN
       DTMIN = DT
    END IF

C TIME STEP DIAGNOSTIC SECTION
    IF (DT .LT. 1.0D-17) THEN
        WRITE(*,153) DT,DTHEAT,DTHYDRO,DTVAP,DTTEMP,DTEMPMAX
    END IF

C COMPUTE NUCLEATION RATE (LOG10(J)=RATEJ)
    DO 87, K=1,N
        IF (K .GT. ISURF .AND. T(K) .GT. TMELT) THEN
          CALL NUCLEATE(T(K),RHO(K),P(K),RAWJ,RAWINUC)
          RATEJ(K) = DLOG10(RAWJ)
          TNUC(K) = DLOG10(RAWINUC)
          RAWBUB = 10.**BUBBLE(K) + RAWJ*DT
          BUBBLE(K) = DLOG10(RAWBUB)
C TEST VARIOUS MAXIMUM THRESHOLD DEPTHS
          IF (RATEJ(K) .GT. 35. .AND. K .GT. I35) THEN
              I35 = K
              X35 = XLOC(K)
          END IF
          IF (RATEJ(K) .GT. 30. .AND. K .GT. I30) THEN
              I30 = K
              X30 = XLOC(K)
          END IF
          IF (RATEJ(K) .GT. 25. .AND. K .GT. I25) THEN
              I25 = K
              X25 = XLOC(K)
          END IF
```

```
      IF (RATEJ(K) .GT. 20. .AND. K .GT. I20) THEN
            I20 = K
            X20 = XLOC(K)
         END IF
      IF (BUBBLE(K) .GT. 27. .AND. K .GT. IB27) THEN
            IB27 = K
            XB27 = XLOC(K)
         END IF
      IF (BUBBLE(K) .GT. 26. .AND. K .GT. IB26) THEN
            IB26 = K
            XB26 = XLOC(K)
         END IF
      IF (BUBBLE(K) .GT. 25. .AND. K .GT. IB25) THEN
            IB25 = K
            XB25 = XLOC(K)
         END IF
      IF (BUBBLE(K) .GT. 24. .AND. K .GT. IB24) THEN
            IB24 = K
            XB24 = XLOC(K)
         END IF
       ELSE
         RATEJ(K) = -99.
       END IF
   87  CONTINUE

C WRITE PRESSURE AND STUFF TO FILES EVERY DTPRESS NANOSECONDS
    TNS = TM * 1.0D+09
    IF(TNS .LT. 3.0) THEN
       DTPRESS = 0.05
    ELSE IF(TNS .LT. 20.0) THEN
       DTPRESS = 0.5
    ELSE
       DTPRESS = 5.0
    END IF

    IF(TNS.GT.TPRESS) THEN
        WRITE (11,105) TNS,(TAB,P(K),K=1,N)
        WRITE (13,105) TNS,(TAB,SXNEW(K),K=1,N)
        WRITE (14,105) TNS,(TAB,SXDNEW(K),K=1,N)
        WRITE (15,145) TNS,(TAB,U(K),K=0,N)
        WRITE (16,145) TNS,(TAB,XNEW(K),K=0,N)
        WRITE (17,105) TNS,(TAB,RHONEW(K),K=1,N)
        WRITE (18,105) TNS,(TAB,XQUAL(K),K=1,N)
        WRITE (19,105) TNS,(TAB,T(K),K=1,N)
        WRITE (20,105) TNS,(TAB,HG(K)/4184.,K=1,N)
        WRITE (22,105) TNS,(TAB,VOLF(K),K=1,N)
        WRITE (24,105) TNS,(TAB,TNUC(K),K=1,N)
        WRITE (25,105) TNS,(TAB,RATEJ(K),K=1,N)
        WRITE (35,105) TNS,(TAB,BUBBLE(K),K=1,N)
        TPRESS = TPRESS + DTPRESS
    END IF

C WRITE SOME INFO TO SCREEN EVERY FEW NS
    DTSCREEN = 2.
```

```
      IF (TNS .GT. 50.) DTSCREEN = 10.
      IF(TNS.GT.TSCREEN) THEN
         K1 = ISURF
         K2 = ISURF + 4
         WRITE(*,137) TNS, DT, (T(K),K=K1,K2), XMELT
         TSCREEN = TSCREEN + DTSCREEN
      END IF

      GOTO 20
C ***********************************************************
C TIME LIMIT HAS BEEN REACHED
   95 CONTINUE

      CLOSE(10)
      CLOSE(11)
      CLOSE(13)
      CLOSE(14)
      CLOSE(15)
      CLOSE(16)
      CLOSE(17)
      CLOSE(18)
      CLOSE(19)
      CLOSE(20)
      CLOSE(21)
      CLOSE(22)
      CLOSE(25)
C     CLOSE(26)
C     CLOSE(27)
C     CLOSE(28)
C     CLOSE(29)
C     CLOSE(33)
C     CLOSE(34)
      CLOSE(35)

      XOM1 = XO(ISURF-1)
      VAPDEPTH = 1.0D+06*(XOM1+XQUAL(ISURF)*(XO(ISURF)-XOM1))
      OPEN(UNIT=23,FILE='summary')
      EINMAX = EINMAX / 10000.
      WRITE(*,112) EINMAX
      WRITE(*,113) XMELTMAX
      WRITE(*,119) XTMELTMAX
      WRITE(*,120) XO(ISPALL) * 1.0D+06
      WRITE(*,114) TFMAX
      WRITE(*,115) HGFMAX / 4184.
      WRITE(*,117) DTMIN, DTMAX
      WRITE(*,118) DHGMXMAX / 4184.
      WRITE(*,122) HEASTMAX/10000.
      WRITE(*,135) XQUAL(ISURF)
      WRITE(*,136) ESUM/10000.0, EINMAX
      WRITE(*,148) VAPDEPTH
      WRITE(*,157) X35,X30,X25,X20
      WRITE(*,158) XB27,XB26,XB25,XB24
      WRITE(23,112) EINMAX
      WRITE(23,113) XMELTMAX
```

```
      WRITE(23,119) XIMELTMAX
      WRITE(23,120) X0(ISPALL) * 1.0D+06
      WRITE(23,114) TFMAX
      WRITE(23,115) HGFMAX / 4184.
      WRITE(23,117) DIMIN, DIMAX
      WRITE(23,118) DHGMXMAX / 4184.
      WRITE(23,122) HEASTMAX/10000.
      WRITE(23,135) XQUAL(ISURF)
      WRITE(23,136) ESUM/10000.0, EINMAX
      WRITE(23,148) VAPDEPTH
      WRITE(23,157) X35,X30,X25,X20
      WRITE(23,158) XB27,XB26,XB25,XB24

      CLOSE(23)

   99 CONTINUE

  101 FORMAT(D13.6,2(A1,D13.6))
  102 FORMAT('TIME =',2F12.3)
  103 FORMAT(F10.5,A1,F10.2,A1,F12.3,A1,F12.4)
  104 FORMAT('TIME =',F12.5)
  105 FORMAT(F10.5,100(A1,E11.5))
  106 FORMAT(F10.5,F10.2,F10.3)
  107 FORMAT(F12.5,F12.3,F12.5)
  108 FORMAT(F12.3,35(A1,F12.5))
  109 FORMAT(4E12.4)
  110 FORMAT('Enter angle in degrees')
  111 FORMAT(I5,F10.4,E14.5)
  112 FORMAT('Total fluence (J/cm2) =',F12.3)
  113 FORMAT('Maximum melt depth (micron) =',F12.3)
  114 FORMAT('Maximum front surface temp =',F12.2)
  115 FORMAT('Maximum front surface enthalpy (cal/g) =',F12.4)
  117 FORMAT('Minimum and maximum time steps =',2(1PE12.3))
  118 FORMAT('Maximum enthalpy change (cal/g) = ',F12.4)
  119 FORMAT('Maximum total melt depth (micron) =',F12.3)
  120 FORMAT('Spalled depth (micron) =',F12.3)
  122 FORMAT('Maximum heat flux (W/cm2) = ',1PE12.4)
  130 FORMAT(A)
  131 FORMAT(D12.4)
  133 FORMAT(D13.6,2(A3,D15.6))
  134 FORMAT(F10.4,A1,I5,A1,F10.4)
  135 FORMAT('Fraction vaporized in surface zone',F10.5)
  136 FORMAT('Energy present & input (J/cm2) =',2F12.3)
  137 FORMAT(F11.3,E11.3,6F11.3)
  138 FORMAT(I8,F8.3,2E12.3,F12.5,I5)
  139 FORMAT(A7,5(1PE12.5))
  141 FORMAT(F12.4,5(A1,1PE12.4))
  145 FORMAT(F10.5,101(A1,E11.5))
  146 FORMAT(F10.5,A1,I5,2(A1,F12.5))
  147 FORMAT(F12.7,4(A1,1PE12.5))
  148 FORMAT('Vaporized depth (micron) =',F12.3)
  149 FORMAT(F12.7,5(A1,1PE12.5))
  153 FORMAT('low DT  ',6E12.4)
  154 FORMAT(F12.7,A1,1PE12.5)
```

```
 155   FORMAT(F12.7,A1,I5,3(A1,E12.5))
 157   FORMAT('J-depths (35,30,25,20) =',4F10.3)
 158   FORMAT('Bubble-depths (27,26,25,24) =',4F10.3)

       STOP
       END


C ***************************************************
C READ IN MATERIAL PROPERTY DATA
C UNITS INPUT AS CONVENIENT, BUT CONVERT TO SI IN THIS SUBROUTINE

       SUBROUTINE READMAT
       IMPLICIT DOUBLE PRECISION (A-H,O-Z)
       DIMENSION ACOND(13),AH2T(10),EOSCOEF(10),SIGMACOEF(7)
       CHARACTER*50 MATNAME, COMMENT

       COMMON/MATDAT/TMELT,HMELTI,HMELTT,ACOND,AH2T
       COMMON/EOSDAT/RHO0,EOSCOEF,ABOIL,BBOIL,PRNU,YLD0
       COMMON/SURFTEN/SIGMACOEF

       OPEN(UNIT=12,FILE="matdata",STATUS="OLD")
       READ(12,130) MATNAME
       WRITE(*,*) MATNAME
       READ(12,130) COMMENT
C DENSITY IN kg/m**3
       READ(12,*) RHO0
       READ(12,130) COMMENT
C MELT TEMPERATURE IN K
       READ(12,*) TMELT
       READ(12,130) COMMENT
C CURVE FIT COEFFICIENTS FOR THERMAL COND VS TEMP
C FIFTH-ORDER POLYNOMIALS FOR SOLID AND LIQUID
C AND ONE PARAMETER FOR VAPOR
C UNITS: cal/m.s.K and K
       DO 4, K=1,6
         READ(12,*) ACOND(K)
  4    CONTINUE
       READ(12,130) COMMENT
       DO 5, K=7,12
          READ(12,*) ACOND(K)
  5    CONTINUE
       READ(12,130) COMMENT
       READ(12,*) ACOND(13)
C CONVERT TO SI UNITS (W/m.K)
       DO 20 K=1,13
          ACOND(K) = ACOND(K) * 4.184
  20   CONTINUE

C CURVE FIT COEFFICIENTS FOR TEMPERATURE VS ENTHALPY
C   FIRST 6 FOR SOLID, THEN 2 EACH FOR LIQUID AND VAPOR
C UNITS: K and cal/g
       READ(12,130) COMMENT
       DO 6, K=1,6
```

```
      READ(12,*) AH2T(K)
   6  CONTINUE
      READ(12,130) COMMENT
      READ(12,*) AH2T(7)
      READ(12,*) AH2T(8)
      READ(12,130) COMMENT
      READ(12,*) AH2T(9)
      READ(12,*) AH2T(10)
C CONVERT TO SI UNITS (J/kg)
      DO 25, K=2,6
         AH2T(K) = AH2T(K) / (4184.**(K-1))
  25  CONTINUE
      AH2T(8) = AH2T(8) / 4184.
      AH2T(10) = AH2T(10) / 4184.

C Tboil vs. P COEFFICIENTS
C FROM DUSHMAN: LOG(P) = A - B/T
C UNITS: P in microns, T in K
      READ(12,130) COMMENT
      READ(12,*) ABOIL
      READ(12,*) BBOIL
C CONVERT TO SI UNITS (Pa)
      ABOIL = ABOIL - DLOG10(7.50D+00)

C EQUATION-OF-STATE COEFFICIENTS
      READ(12,130) COMMENT
      DO 216, K=1,10
         READ(12,*) EOSCOEF(K)
 216  CONTINUE

C POISSON'S RATIO
      READ(12,130) COMMENT
      READ(12,*) PRNU

C YIELD STRENGTH
      READ(12,130) COMMENT
      READ(12,*) YLD0

C SURFACE TENSION PARAMETERS
      READ(12,130) COMMENT
      DO 217, K=1,7
         READ(12,*) SIGMACOEF(K)
 217  CONTINUE

      CLOSE(12)

C COMPUTE ENTHALPIES FOR INCIPIENT AND TOTAL MELT
C START BY ASSUMING A LINEAR FIT FOR LIQUID T VS. H
C UNITS ARE J/kg and K
      HMELTT = (TMELT - AH2T(7)) / AH2T(8)
C NOW GET INCIPIENT MELT ENERGY VIA NEWTON'S METHOD
      HM = 0.6 * HMELTT
      AH2TZERO = AH2T(1) - TMELT
      DO 218, K=1,6
```

```
      HM = HM - (AH2TZERO + HM*(AH2T(2) + HM*(AH2T(3) + HM*
     &       (AH2T(4) + HM*(AH2T(5) + HM*AH2T(6))))) /
     &       (AH2T(2) + HM*(2.*AH2T(3) + HM*(3.*AH2T(4) + HM*
     &       (4.*AH2T(5) + HM*5.*AH2T(6)))))
  218 CONTINUE
    HMELTI = HM
    WRITE(*,*) 'H-MELT-I (cal/g) = ',HM/4184.
    WRITE(*,*) 'H-MELT-T (cal/g) = ',HMELTT/4184.

  130  FORMAT(A)

    RETURN
    END


C ***************************************************
C SET UP ZONE EDGE LOCATIONS, ZONE CENTERS, AND ZONE MASSES
C GEOM IS FLAG FOR PLANAR (1), CYLINDRICAL (2), OR SPHERICAL (3)
    SUBROUTINE ZONESET(RHO0,X0,XC,XLOC,ZMASS,GEOM)
    IMPLICIT DOUBLE PRECISION (A-H,O-Z)
    INTEGER GEOM
    PARAMETER(NP1=101)
    DIMENSION X0(0:NP1),XC(NP1),XLOC(NP1),ZMASS(NP1)

C PLANAR GEOMETRY
    GEOM = 1
C FIRST ZONE GRID SIZE DX METERS
    DX = 1.0E-08
    RATIO = 1.06
C THESE PARAMETERS GIVE TOTAL X = 56 microns FOR 100 ZONES
C ZONE MASS IN kg/m2
C ZONE LOCATIONS IN meters
C INITIAL ZONE CENTER LOCATIONS IN XLOC ARRAY IN microns
    X0(0) = 0.00D+00
    DO 207, I=1,NP1
       X0(I) = X0(0) + DX * (RATIO**I - 1.)/(RATIO - 1.)
       CALL DENGEOM(GEOM,X0(I-1),X0(I),RDEN)
       ZMASS(I) = RHO0 * (X0(I) - X0(I-1)) * RDEN
       XC(I) = (X0(I) + X0(I-1)) / 2.
       XLOC(I) = XC(I) * 1.0D+06
  207 CONTINUE

    RETURN
    END

C ***************************************************
C RETURN GEOMETRY FACTOR TO GET CORRECT ZONE MASSES

    SUBROUTINE DENGEOM(GEOM,R1,R2,RDEN)
    IMPLICIT DOUBLE PRECISION (A-H,O-Z)
    INTEGER GEOM

    PI = 4.0 * ATAN(1.)
```

```
      IF (GEOM .EQ. 1) THEN
         RDEN = 1.0D+00
      ELSE IF (GEOM .EQ. 2) THEN
         RDEN = PI * (R1 + R2)
      ELSE
         RDEN = (4./3.) * PI * (R1**2 + R1*R2 + R2**2)
      END IF

      RETURN
      END

C *****************************************************
C RETURN GEOMETRY FACTOR TO GET CORRECT HEAT CONDUCTION
C Q = BETAC * K * ΔT / ΔX
C FOR W/m2 planar, W/m cylindrical, and W sherical

      SUBROUTINE BETAGEOM(GEOM,R1,R2,BETAC)
      IMPLICIT DOUBLE PRECISION (A-H,O-Z)
      INTEGER GEOM

      PI = 4.0 * ATAN(1.)

      IF (GEOM .EQ. 1) THEN
         BETAC = 1.0D+00
      ELSE IF (GEOM .EQ. 2) THEN
         BETAC = PI * (R1 + R2)
      ELSE
         BETAC = PI * (R1 + R2)**2
      END IF

      RETURN
      END
C *****************************************************
C RETURN AREA AT A GIVEN RADIUS DEPENDING ON GEOMETRY
      SUBROUTINE AREAGEOM(GEOM,R,AREA)
      IMPLICIT DOUBLE PRECISION(A-H,O-Z)
      INTEGER GEOM

      PI = 4.0 * ATAN(1.0)

      IF (GEOM .EQ. 1) THEN
         AREA = 1.0D+00
      ELSE IF (GEOM .EQ. 2) THEN
         AREA = 2.0D+00 * PI * R
      ELSE
         AREA = 4.0D+00 * PI * R**2
      END IF

      RETURN
      END

C *****************************************************
C FIND NEW TIME STEP SIZE TO HAVE X0 POINT JUST HIT AXIS
C FOR CYLINDRICAL AND SPHERICAL GEOMETRIES
```

```
C ** CAUTION!! UNTESTED ROUTINE **

      SUBROUTINE AXIS(X0,U0,A0,DTOLD,DTNEW)
      IMPLICIT DOUBLE PRECISION (A-H,O-Z)

      A = A0 / 2.0
      B = U0 + A0 * DTOLD / 2.0
      C = X0
      B24AC = B**2  - 4.*A*C
      IF (B24AC .LT. 0.) THEN
         WRITE(*,*) 'ERROR IN AXIS ROUTINE'
         STOP
      END IF
      DTP = (-B + SQRT(B24AC)) / (2.*A)
      DTM = (-B - SQRT(B24AC)) / (2.*A)

C CHOOSE NEW TIME STEP AS SMALLEST POSITIVE ROOT
      IF (DTM .LE. 0.0) THEN
          IF (DTP .GT. 0.0) THEN
            DTNEW = DTP
          ELSE
         WRITE(*,*) 'ERROR IN AXIS ROUTINE'
         STOP
          END IF
      ELSE
          DTMIN = DTM
      END IF

      RETURN
      END

C ****************************************************
C SET UP FOR ENERGY DEPOSITION BASED ON ISOURCE CHOICE

      SUBROUTINE XSOURCE(ISOURCE,LASERFLAG,FBBWALL,FBBLEAK,TSTART)
      IMPLICIT DOUBLE PRECISION (A-H,O-Z)
      PARAMETER(NBIN=45)
      DIMENSION BIN(NBIN),BINW(NBIN),FBBWALL(NBIN),FBBLEAK(NBIN)

      COMMON/PULSE/AWALL,BWALL,CWALL,T0WALL,ALEAK,BLEAK,CLEAK,
     &      T0LEAK, TSQ, ESQ, EGAUSS, SC, FWHM
      COMMON/OPACBINS/BIN,BINW

C DEFINE A BLACKBODY FUNCTION
      BBE(JBB,TBB) = BINW(JBB) * ((BIN(JBB)/TBB)**3) /
     &      (EXP(BIN(JBB)/TBB)-1.)

      IF(ISOURCE .EQ. 1) THEN
C 45 MJ YIELD, CLOSING LEH MODEL
C DOUBLE EXPONENTIAL EXTRAPOLATIONS TO LEAK AND WALL FLUX PULSES
C WALL FIT TO INTEGRAL OF PULSE FOR 20 MJ SHOT
C TIMES IN UNITS = ns
          AWALL = 3.88872D+05
          BWALL = 0.0616607
```

```
        CWALL = 0.785557
        TOWALL = 22.3283

        ALEAK = 1.32328D+06
        BLEAK = 0.38682
        CLEAK = 4.5486
        TOLEAK = 20.51

C BLACKBODY EXTAPOLATIONS TO X-RAY EMISSION DATA
C FIT WALL WITH 3 BBT (HOT, WARM, COLD)
        BBIWH = 0.200
        BBIWW = 0.125
        BBIWC = 0.018
        WFH = 0.000
        WFW = 1.000
        WFC = 0.000
        BBILEAK = 0.400

    ELSE IF(ISOURCE .EQ. 2) THEN

C DOUBLE EXPONENTIAL FITS TO LEAK AND WALL FLUX PULSES
C WALL FIT TO INTEGRAL OF PULSE FOR 20 MJ SHOT
C TIMES IN UNITS = ns

        WRITE(*,*) 'Closing(1) or Open(2) LEH Model?'
        READ(*,*) MODEL

        IF(MODEL .EQ. 1) THEN
C CLOSING LEH MODEL
        AWALL = 1.4774D+05
        BWALL = 0.0503353
        CWALL = 0.641271
        TOWALL = 22.3283

        ALEAK = 7.4086D+05
        BLEAK = 0.3684
        CLEAK = 4.332
        TOLEAK = 20.51

C BLACKBODY FITS TO AA202 X-RAY EMISSION DATA
C FIT WALL WITH 3 BBT (HOT, WARM, COLD)
        BBIWH = 0.200
        BBIWW = 0.089
        BBIWC = 0.018
        WFH = 0.000
        WFW = 0.925
        WFC = 0.075
        BBILEAK = 0.400

    ELSE
C OPEN LEH MODEL
        AWALL = 8.66534D+04
        BWALL = 0.0446395
        CWALL = 0.240587
```

```
      TOWALL = 20.495

      ALEAK = 1.354317D+06
      BLEAK = 0.28911
      CLEAK = 1.02102
      TOLEAK = 19.065

C BLACKBODY FITS TO AA202 X-RAY EMISSION DATA
C FIT WALL WITH 3 BBT (HOT, WARM, COLD)
      BBIWH = 0.200
      BBIWW = 0.081
      BBIWC = 0.015
      WFH = 0.000
      WFW = 0.870
      WFC = 0.130
      BBILEAK = 0.320
       END IF

   ELSE IF(ISOURCE .EQ. 3) THEN

C DOUBLE EXPONENTIAL FITS TO LEAK AND WALL FLUX PULSES
C WALL FIT TO INTEGRAL OF PULSE FOR 5 MJ SHOT (AA206)
C TIMES IN UNITS = ns

       WRITE(*,*) 'Closing(1) or Open(2) LEH Model?'
       READ(*,*) MODEL

       IF(MODEL .EQ. 1) THEN
C CLOSING LEH MODEL
      AWALL = 4.2916D+04
      BWALL = 0.034722
      CWALL = 0.146738
      TOWALL = 43.9112

      ALEAK = 7.3947D+05
      BLEAK = 0.287161
      CLEAK = 0.449518
      TOLEAK = 16.2683

C BLACKBODY FITS TO AA206 X-RAY EMISSION DATA
C FIT WALL WITH 3 BBT (HOT, WARM, COLD)
      BBIWH = 0.200
      BBIWW = 0.075
      BBIWC = 0.018
      WFH = 0.00
      WFW = 0.84
      WFC = 0.16
      BBILEAK = 0.290

   ELSE
C OPEN LEH MODEL
      AWALL = 7.823D+03
      BWALL = 0.0172618
      CWALL = 1.56811
```

```
      TOWALL = 53.2955

      ALEAK = 2.357273D+05
      BLEAK = 0.133414
      CLEAK = 3.57782
      TOLEAK = 16.7587

C BLACKBODY FITS TO AA206 X-RAY EMISSION DATA
C FIT WALL WITH 3 BBT (HOT, WARM, COLD)
      BBIWH = 0.200
      BBIWW = 0.058
      BBIWC = 0.013
      WFH = 0.00
      WFW = 0.65
      WFC = 0.35
      BBILEAK = 0.240
       END IF

   ELSE IF(ISOURCE .EQ. 4) THEN

C DOUBLE EXPONENTIAL FITS TO LEAK AND WALL FLUX PULSES
C BOTH FIT TO AA204 TIME HISTORY W/ ADJUSTED A's
C TIMES IN UNITS = ns
      AWALL = 1.0901D+04
      BWALL = 0.0229719
      CWALL = 0.153419
      TOWALL = 68.7083

      ALEAK = 6.1098D+05
      BLEAK = 0.300598
      CLEAK = 0.466202
      TOLEAK = 15.9443

C BLACKBODY FITS TO AA205 X-RAY EMISSION DATA
C FIT WALL WITH 3 BBT (HOT, WARM, COLD)
      BBIWH = 0.200
      BBIWW = 0.052
      BBIWC = 0.012
      WFH = 0.00
      WFW = 0.61
      WFC = 0.39
      BBILEAK = 0.255


   ELSE IF(ISOURCE .EQ. 5) THEN

   WRITE(*,'(A)') 'Enter pulse duration (ns)'
   READ(*,*) TSQ
   WRITE(*,'(A)') 'Enter total energy into 4Pi (MJ)'
   READ(*,*) ESQ
C CONVERT TO JOULES
   ESQ = ESQ * 1.0D+06
   IF (LASERFLAG .NE. 1) THEN
      WRITE(*,'(A)') 'Enter blackbody temperature (keV)'
```

```
      READ(*,*) BBTLEAK
   ELSE
      BBTLEAK = .3
   END IF

   ELSE IF(ISOURCE .EQ. 6) THEN

   WRITE(*,'(A)') 'Enter pulse FWHM (ns)'
   READ(*,*) FWHM
   WRITE(*,'(A)') 'Enter total energy into 4Pi (MJ)'
   READ(*,*) EGAUSS
C CONVERT TO JOULES
   EGAUSS = EGAUSS * 1.0D+06
   IF (LASERFLAG .NE. 1) THEN
      WRITE(*,'(A)') 'Enter blackbody temperature (keV)'
      READ(*,*) BBTLEAK
   ELSE
      BBTLEAK = .3
   END IF

   SC = 2. * SQRT(-2. * LOG(0.5)) / FWHM

   ELSE
       WRITE(*,*) 'Invalid source term number entered'
       STOP
   END IF

C FRACTION OF BLACKBODY ENERGY IN EACH BIN
   IF(ISOURCE .LE. 4) THEN

      SUMWH = 0.
      SUMWW = 0.
      SUMWC = 0.
      SUMLEAK = 0.
      DO 8, J=1,NBIN
         SUMWH = SUMWH + BBE(J,BBIWH)
         SUMWW = SUMWW + BBE(J,BBIWW)
         SUMWC = SUMWC + BBE(J,BBIWC)
         FBBLEAK(J) = BBE(J,BBTLEAK)
         SUMLEAK = SUMLEAK + FBBLEAK(J)
 8       CONTINUE

C NORMALIZE TO MAKE THESE FRACTIONS OF TOTAL ENERGY
      DO 9, J=1,NBIN
         FBBWALL(J) = (WFH * BBE(J,BBIWH) / SUMWH +
     &              WFW * BBE(J,BBIWW) / SUMWW +
     &              WFC * BBE(J,BBIWC) / SUMWC )
         FBBLEAK(J) = FBBLEAK(J) / SUMLEAK
 9       CONTINUE

   ELSE
C ASSUME SQUARE AND GAUSSIAN PULSES ARE PURE LAMBERTIAN
      SUMLEAK = 0.
      DO 10, J=1,NBIN
```

```
          FBBLEAK(J) = BBE(J,BBTLEAK)
          SUMLEAK = SUMLEAK + FBBLEAK(J)
  10      CONTINUE

C NORMALIZE TO MAKE THESE FRACTIONS OF TOTAL ENERGY
        DO 11, J=1,NBIN
          FBBWALL(J) = 0.0
          FBBLEAK(J) = FBBLEAK(J) / SUMLEAK
  11      CONTINUE

     END IF

C SET PROBLEM START TIME, TSTART IN NS
     IF (ISOURCE .LE. 4) THEN
         TMINNS = DMIN1(T0WALL,T0LEAK)
         TSTART = DINT(TMINNS)
     ELSE
         TSTART = 0.0
     END IF

     RETURN
     END

C ***************************************************
C SET UP MAGNITUDE OF ENERGY PULSES
C RETURNS ENERGY IN EACH BIN FOR THIS TIME STEP

     SUBROUTINE XPULSE(TM,ISOURCE,COSTH,AREA,FBBWALL,FBBLEAK)
     IMPLICIT DOUBLE PRECISION (A-H,O-Z)
     PARAMETER(NBIN=45)
     DIMENSION EWALL(NBIN), ELEAK(NBIN), EWALLOLD(NBIN)
     DIMENSION EIN(NBIN), ELEAKOLD(NBIN), BIN(NBIN), BINW(NBIN)
     DIMENSION FBBWALL(NBIN), FBBLEAK(NBIN)

     COMMON/PULSE/AWALL,BWALL,CWALL,T0WALL,ALEAK,BLEAK,CLEAK,
       &       T0LEAK, TSQ, ESQ, EGAUSS, SC, FWHM
     COMMON/EINTEGRAL/EWALLOLD,ELEAKOLD,EWALL,ELEAK,EIN
     COMMON/OPACBINS/BIN,BINW

     TNS = TM * 1.0D+09
     IF(ISOURCE .LE. 4) THEN
C FROM DOUBLE EXPONENTIAL FITS
C TIME IN NS FOR THESE CURVE FITS
        TW = DMAX1((TNS - T0WALL),0.0D+00)
        TL = DMAX1((TNS - T0LEAK),0.0D+00)
        FTMWALL = ((AWALL/BWALL)*(1.-EXP(-BWALL*TW)) -
       +          (AWALL/CWALL)*(1.-EXP(-CWALL*TW)))
           FTMLEAK = ((ALEAK/BLEAK)*(1.-EXP(-BLEAK*TL)) -
       +          (ALEAK/CLEAK)*(1.-EXP(-CLEAK*TL)))

        ELSE IF(ISOURCE .EQ. 5) THEN
C SQUARE PULSE, STARTS AT TIME = 0
C USE A 2% RAMP AT START AND END
       TRAMP = TSQ * 0.02
```

```
      FIMWALL = 0.0
         IF (TNS .LT. TRAMP) THEN
         FIMLEAK = ESQ * TNS**2 / (2. * TSQ * TRAMP)
      ELSE IF(TNS .LT. TSQ) THEN
            FIMLEAK = ESQ * (TNS-TRAMP/2.) / TSQ
         ELSE IF(TNS .LT. (TSQ+TRAMP)) THEN
         TAU = TNS - TSQ
         FIMLEAK=(ESQ/TSQ)*(TSQ-TRAMP/2.+TAU-TAU**2 /(2.*TRAMP))
      ELSE
            FIMLEAK = ESQ
         END IF


   ELSE
C GAUSSIAN PULSE
          FIMWALL = 0.0
          TSTAR = (TNS - 1.5 * FWHM) * SC / SQRT(2.)
       FIMLEAK = 0.5 * (1. + ERF(TSTAR)) * EGAUSS
   END IF

C SET UP INCIDENT ENERGY IN EACH BIN IN THIS TIME STEP
C EIN(J) IS IN J/M2;  EWALL,ELEAK ARE IN JOULES
      DO 33, J=1,NBIN
      EWALL(J) = FBBWALL(J) * FIMWALL
      ELEAK(J) = FBBLEAK(J) * FIMLEAK
      EWNET = EWALL(J) - EWALLOLD(J)
      ELNET = ELEAK(J) - ELEAKOLD(J)
      EIN(J) = (ELNET*2.*COSTH + EWNET) / AREA
      EWALLOLD(J) = EWALL(J)
      ELEAKOLD(J) = ELEAK(J)
  33  CONTINUE

   RETURN
   END

C ***************************************************
C DEFINE THERMAL CONDUCTIVITY VS TEMPERATURE
C USE UP TO A FIFTH-ORDER POLYNOMIAL
C UNITS ARE W/m.K AND K IN CURVE FITS

   SUBROUTINE CONDVST(T,VOLF,COND)
   IMPLICIT DOUBLE PRECISION (A-H,O-Z)
   DIMENSION AS(0:5), AL(0:5), AH2T(10)
   COMMON/MATDAT/TMELT,HMELTI,HMELTT,AS,AL,AV,AH2T

   IF(T .LT. 0.0) THEN
      WRITE(*,*) 'T = ',T
      STOP
   END IF

   CONDS = AS(0) + T*(AS(1) + T*(AS(2) + T*(AS(3) +
     &       T*(AS(4) + T*AS(5)))))
   CONDL = AL(0) + T*(AL(1) + T*(AL(2) + T*(AL(3) +
     &       T*(AL(4) + T*AL(5)))))
```

```
C MONATOMIC GAS CONDUCTIVITY
   CONDV = AV * SQRT(T)

   IF (VOLF .LE. 1.0D-01) THEN
       IF(T .LT. (TMELT-.1)) THEN
         COND = CONDS
          ELSE IF(T .GT. (TMELT+.1)) THEN
         COND = CONDL
       ELSE
C TWO PHASE LIQUID/SOLID REGION
         COND = 2. * CONDS * CONDL / (CONDS + CONDL)
       END IF
   ELSE IF (VOLF .GE. 0.99) THEN
       COND = CONDV
   ELSE
C TWO PHASE LIQUID/VAPOR REGION
       COND = CONDV
   END IF

      RETURN
      END

C ****************************************************
C CONVERT ENTHALPY TO A TEMPERATURE
C FOR BOTH SOLID AND LIQUID
C USE UP TO FIFTH-ORDER POLYNOMIALS
C UNITS ARE J/kg AND K IN CURVE FITS

   SUBROUTINE H2T(HJKG,T)
   IMPLICIT DOUBLE PRECISION (A-H,O-Z)
   DIMENSION ACOND(13), AS(0:5)
   COMMON/MATDAT/TMELT,HMELTI,HMELTT,ACOND,AS,AL0,AL1,AV0,AV1

   H = HJKG
   TS = AS(0) + H*(AS(1) + H*(AS(2) + H*(AS(3) +
     &       H*(AS(4) + H*AS(5)))))
   TL = AL0 + H*AL1

      IF(TL .GT. TMELT) THEN
      T = TL
   ELSE IF(TS .LT. TMELT) THEN
      T = TS
   ELSE
      T = TMELT
      END IF

      RETURN
      END

C ****************************************************
C DETERMINE HEAT CAPACITY (Cv) FOR SOLID, LIQUID, VAPOR
C VAPOR IS BASED ON IDEAL GAS, USING GAMMA & RBAR
C LIQUID AND SOLID USE T vs. ENTHALPY RELATIONS(Cp~Cv)
C DECIDE STATE BASED ON VOLUME FRACTION VAPOR (VOLF)
```

```
C USE UP TO FIFTH-ORDER POLYNOMIALS
C UNITS ARE J/kg AND K IN CURVE FITS

      SUBROUTINE HEATCAP(VOLF,T,HG,CV)
      IMPLICIT DOUBLE PRECISION (A-H,O-Z)
      DIMENSION ACOND(13), AS(0:5), EOSCOEF(10)
      COMMON/MATDAT/TMELT,HMELTI,HMELTT,ACOND,AS,AL0,AL1,AV0,AV1
      COMMON/EOSDAT/RHO0,EOSCOEF,ABOIL,BBOIL,PRNU,YLD0

      GAMMA = EOSCOEF(9)
      RBAR = EOSCOEF(10)

      CVVAPOR = RBAR / (GAMMA - 1.0D+00)
      CVLIQUID = 1.0D+00 / AL1
      CVSOLID = 1.0D+00 / ( AS(1) + HG*(2.*AS(2) +
     &          HG*(3.*AS(3) + HG*(4.*AS(4) + HG*5.*AS(5)))))

      IF (VOLF .GT. 0.999999) THEN
C        VAPOR
         CV = CVVAPOR
      ELSE IF (VOLF .LT. 0.001) THEN
         IF (T .GT. TMELT) THEN
C           LIQUID
            CV = CVLIQUID
         ELSE IF (T .LT. TMELT) THEN
C           SOLID
            CV = CVSOLID
            ELSE
C           TWO-PHASE SOLID/LIQUID
            CV = MIN(CVLIQUID,CVSOLID)
            END IF
         ELSE
C        TWO-PHASE VAPOR/LIQUID
         CV = MIN(CVLIQUID,CVVAPOR)
      END IF

         RETURN
         END


C ******************************************************
C APPROXIMATION TO ERF(X) FROM ABRAMOWITZ & STEGUN
      DOUBLE PRECISION FUNCTION ERF(XIN)
      IMPLICIT DOUBLE PRECISION (A-H,O-Z)

      A1 = 0.278393
      A2 = 0.230389
      A3 = 0.000972
      A4 = 0.078108

      X = DABS(XIN)

      ERF = DSIGN((1. - 1. / (1. + X * (A1 + X *
     &      (A2 + X * (A3 + X * A4))))**4), XIN)
```

```
      RETURN
      END

C ***************************************************
C COMPUTE EQUATION OF STATE COEFFICIENTS
C F1 = F1(RHO) AND F2 = F2(RHO)
C FOR LINEAR EOS:  PRESSURE = F1 + F2 * ENERGY

      SUBROUTINE EOSF(RHO,F1,F2)
      IMPLICIT DOUBLE PRECISION (A-H,O-Z)
      DIMENSION EOSCOEF(10), C(0:6)
      COMMON/EOSDAT/RHO0,EOSCOEF,ABOIL,BBOIL,PRNU,YLD0

      U = RHO/RHO0 - 1.0D+00
C EOS TYPE
      ITYPE = NINT(EOSCOEF(1))

      IF (ITYPE .EQ. 1) THEN
C STIENBERG'S MODEL (DYNA2D EOS #4)
         C0 = EOSCOEF(2)
         S1 = EOSCOEF(3)
         S2 = EOSCOEF(4)
         S3 = EOSCOEF(5)
         G0 = EOSCOEF(6)
         B  = EOSCOEF(7)
         IF (U .LE. 0.) THEN
        F1 = RHO0 * C0**2 * U
         ELSE
        F1 = RHO0 * C0**2 * U *
     &       (1. + (1. - G0/2.) * U + B/2. * U**2) /
     &       (1. - (S1-1.)*U - S2*U**2/(U+1.) - S3*U**3/(U+1.)**2)
         END IF
         F2 = (G0 + B * U) * RHO
      ELSE IF (ITYPE .EQ. 2) THEN
C LINEAR POLYNOMIAL MODEL (DYNA2D EOS #1 AND #6)
         DO 20, K=0,6
           C(K) = EOSCOEF(K+2)
  20       CONTINUE
         IF (U .LE. 0.) THEN
        F1 = C(0) + C(1)*U + C(3)*U**3
        F2 = (C(4) + C(5)*U) * RHO
         ELSE
        F1 = C(0) + C(1)*U + C(2)*U**2 + C(3)*U**3
        F2 = (C(4) + C(5)*U + C(6)*U**2) * RHO
         END IF

      ELSE
         WRITE(*,*) 'NOT A VALID EOS NUMBER'
         STOP
      END IF

      RETURN
      END
```

```
C ***************************************************
C COMPUTE EQUATION OF STATE COEFFICIENT DERIVATIVES
C F1 = F1(RHO) AND F2 = F2(RHO)
C FOR LINEAR EOS:  PRESSURE = F1 + F2 * ENERGY

      SUBROUTINE EOSDF(RHO,DF1,DF2)
      IMPLICIT DOUBLE PRECISION (A-H,O-Z)
      DIMENSION EOSCOEF(10), C(0:6)
      COMMON/EOSDAT/RHO0,EOSCOEF,ABOIL,BBOIL,PRNU,YLD0

      U = RHO/RHO0 - 1.0D+00
C EOS TYPE
      ITYPE = NINT(EOSCOEF(1))

      IF (ITYPE .EQ. 1) THEN
C STIENBERG'S MODEL (DYNA2D EOS #4)
         C0 = EOSCOEF(2)
         S1 = EOSCOEF(3)
         S2 = EOSCOEF(4)
         S3 = EOSCOEF(5)
         G0 = EOSCOEF(6)
         B  = EOSCOEF(7)
         IF (U .LE. 0.) THEN
        DF1 = C0**2
         ELSE
           XNUMER = C0**2*RHO*(2*RHO**3 + 4.*(1.-G0/2.)*RHO**3*U +
     1        3.*B*RHO**3*U**2 - 2.*(1.-G0/2.)*(S1-1.)*RHO**3*U**2 +
     2        2.*RHO**2*RHO0*S2*U**2 - 2.*B*(S1-1.)*RHO**3*U**3 -
     3        2.*RHO*RHO0**2*S2*U**3 + 4.*RHO*RHO0**2*S3*U**3 -
     4        B*RHO**2*RHO0*S2*U**4 -
     5        2.*(1.-G0/2.)*RHO*RHO0**2*S2*U**4 +
     6        2.*(1.-G0/2.)*RHO*RHO0**2*S3*U**4 -
     7        4.*RHO0**3*S3*U**4 - B*RHO*RHO0**2*S2*U**5 -
     8        4.*(1.-G0/2.)*RHO0**3*S3*U**5 - 2.*B*RHO0**3*S3*U**6)
           XDENOM = 2.*(-RHO**2 + (S1-1.)*RHO**2*U +
     &        RHO*RHO0*S2*U**2 + RHO0**2*S3*U**3)**2
         DF1 = XNUMER / XDENOM
        END IF
        DF2 = G0 - B + 2. * B * RHO / RHO0

      ELSE IF (ITYPE .EQ. 2) THEN
C LINEAR POLYNOMIAL MODEL (DYNA2D EOS #1 AND #6)
        DO 20, K=0,6
          C(K) = EOSCOEF(K+2)
 20       CONTINUE
        IF (U .LE. 0.) THEN
          DF1 = (C(1) + 3.*C(3)*U**2) / RHO0
          DF2 = C(4) - C(5) + 2. * C(5) * RHO / RHO0
        ELSE
          DF1 = (C(1) + 2.*C(2)*U + 3.*C(3)*U**2) / RHO0
          DF2 = C(4) - C(5) + 2.*C(5)*RHO/RHO0 +
     &          C(6)*(1.0D+00+RHO/RHO0*(-4.0D+00+3.*RHO/RHO0))
        END IF
```

```
      ELSE
          WRITE(*,*) 'NOT A VALID EOS NUMBER'
          STOP
      END IF

      RETURN
      END

C *****************************************************
C COMPUTE EQUATION OF STATE COEFFICIENTS FOR PURE VAPOR
C F1 = F1(RHO) AND F2 = F2(RHO)
C FOR LINEAR EOS:  PRESSURE = F1 + F2 * ENERGY
C ASSUMES IDEAL GAS EOS:  P = RHO * RBAR * T

      SUBROUTINE FVAPOR(RHO,F1,F2)
      IMPLICIT DOUBLE PRECISION (A-H,O-Z)
      DIMENSION ACOND(13), AH2T(10), EOSCOEF(10)
      COMMON/MATDAT/TMELT,HMELTI,HMELTT,ACOND,AH2T
      COMMON/EOSDAT/RHO0,EOSCOEF,ABOIL,BBOIL,PRNU,YLD0

      AV0 = AH2T(9)
      AV1 = AH2T(10)
      GAMMA = EOSCOEF(9)

      F1 = 0.0
      F2 = (GAMMA - 1.0D+00) * RHO

      RETURN
      END

C *****************************************************
C COMPUTE SOUND SPEED IN SOLID/LIQUID
C USING DERIVATIVES OF EQUATION OF STATE COEFFICIENTS
C F1 = F1(RHO) AND F2 = F2(RHO)
C FOR LINEAR EOS:  PRESSURE = F1 + F2 * ENERGY

      SUBROUTINE SOUND(HG,RHO,P,F2,C)
      IMPLICIT DOUBLE PRECISION (A-H,O-Z)
      DIMENSION EOSCOEF(10)
      COMMON/EOSDAT/RHO0,EOSCOEF,ABOIL,BBOIL,PRNU,YLD0

      CALL EOSDF(RHO,DF1,DF2)

      C = SQRT(DF1 + HG*DF2 + P*F2/RHO**2)

      RETURN
      END

C *****************************************************
C EQUATION OF STATE COEFFICIENTS FOR SPALLED MATERIAL
C     (LIQUID AND/OR VAPOR)
C P = F1(RHO) + F2(RHO) * HG
C FOR LIQUID PART, USE SOLID (UNSPALLED) EOS
```

```
C FOR VAPOR PART, USE IDEAL GAS RELATION
C BASE TWO-PHASE FITTING ON Tsat vs. Psat CURVE
C UNITS: AL,AV COEFFICIENTS IN J/KG, PRESSURE IN Pa

      SUBROUTINE F2PHASE(RHO,HG,QUAL,F1,F2)
      IMPLICIT DOUBLE PRECISION (A-H,O-Z)

C CALL EOS ROUTINE TWICE WITH SLIGHTLY DIFFERENT ENERGIES
      HG1 = HG
      DELTAHG = HG * 0.01
      HG2 = HG + DELTAHG
      CALL EOSPALL(HG1,RHO,T,P1,QUAL,VOLF,CSOUND)
      CALL EOSPALL(HG2,RHO,T,P2,QUAL,VOLF,CSOUND)
      F2 = (P2 - P1) / DELTAHG
      F1 = P1 - F2 * HG1

      RETURN
      END

C ******************************************************
C EQUATION OF STATE FOR SPALLED MATERIAL (LIQUID AND/OR VAPOR)
C ALSO COMPUTE SOUND SPEED
C FOR LIQUID PART, USE SOLID (UNSPALLED) EOS
C FOR VAPOR PART, USE IDEAL GAS RELATION
C BASE TWO-PHASE FITTING ON Tsat vs. Psat CURVE
C NOTE THAT QUAL (OLD VALUE) IS SENT AS AN INITIAL GUESS
C UNITS: AL,AV COEFFICIENTS IN J/KG, PRESSURE IN Pa

      SUBROUTINE EOSPALL(HG,RHO,T,P,QUAL,VOLF,CSOUND)
      IMPLICIT DOUBLE PRECISION (A-H,O-Z)
      DIMENSION ACOND(13),AH2T(10), EOSCOEF(10)

      EXTERNAL QIWO

      COMMON/MATDAT/TMELT,HMELTI,HMELTT,ACOND,AH2T
      COMMON/EOSDAT/RHO0,EOSCOEF,ABOIL,BBOIL,PRNU,YLD0
      COMMON/QIWODAT/HGIWO,RHOIWO,RHOV,RHOL,TIWO,HGL

C MINIMUM PRESSURE IN CHAMBER IS 10^-6 TORR
      PMIN = 1.33D-04
      GAMMA = EOSCOEF(9)
      RBAR = EOSCOEF(10)

      TINF = AH2T(1)
      AL0 = AH2T(7)
      AL1 = AH2T(8)
      AV0 = AH2T(9)
      AV1 = AH2T(10)

C FIRST SEE IF LIQUID STATE WORKS OUT FOR LOW-QUALITY ZONE
      TL = AL0 + HG * AL1
      CALL EOSF(RHO,F1,F2)
      PL = F1 + F2 * HG
      PSAT = 10.**(ABOIL-BBOIL/TL)
```

```
   IF (PL .GT. PSAT .AND. QUAL .LT. 0.05) THEN
C PURE LIQUID
       P = PL
       T = TL
       CALL SOUND(HG,RHO,PL,F2,CSOUND)
       QUAL = 0.0
       VOLF = 0.0

   ELSE

C SEE IF PURE VAPOR WORKS FOR HIGH-QUALITY ZONE
       TV = AV0 + HG * AV1
       PV = RHO * RBAR * TV
       PSAT = 10.**(ABOIL-BBOIL/TV)
       IF (PV .LT. PSAT .AND. QUAL .GT. 0.95) THEN
C PURE VAPOR WORKS
         T = TV
         P = PV
      CSOUND = SQRT(RBAR*GAMMA*T)
      QUAL = 1.0
      VOLF = 1.0

       ELSE

C TWO-PHASE REGION
C SEE IF TWO-PHASE BASED ON CURRENT QUALITY WILL WORK
         HGIWO = HG
         RHOIWO = RHO
         QLOW = MAX(0.0,QUAL-0.05)
         QHIGH = MIN(1.0,QUAL+0.05)
         TESTLOW = QIWO(QLOW)
         TESTHIGH = QIWO(QHIGH)
         TESTPROD = TESTLOW * TESTHIGH
         IF(TESTPROD .LT. 0.0) THEN

C EQUILIBRIUM TWO-PHASE REGION
C ITERATE ON QUALITY USING BRENT'S ROUTINE
          TOL = 1.0D-08
          QUAL = ZBRENT(QIWO,QLOW,QHIGH,TOL)

          ELSE

C TWO-PHASE BRACKET FAILED, BASED ON LATEST QUALITY
C NON-EQUILIBRIUM REGION
          IF(ABS(TESTHIGH) .LT. ABS(TESTLOW)) THEN
            QUAL = QHIGH
          ELSE IF(ABS(TESTHIGH) .GT. ABS(TESTLOW)) THEN
            QUAL = QLOW
          ELSE
            QUAL = QUAL
          END IF
C USE TIWO AND HGL FROM QIWO
          TEST = QIWO(QUAL)
          PSAT = 10.**(ABOIL-BBOIL/TIWO)
```

```
C GET RHOL FROM ITERATIONS ON NONLINEAR FUNCTIONS F1,F2
          RHOL = RHO0
          CALL NEWTP(HGL,PSAT,RHOL)
C DETERMINE NON-EQUILIBRIUM VAPOR DENSITY
          IF(QUAL .GT. 0.0) THEN
            RHOV=RHOL/(1.0D+00-(1.0D+00-(RHOL/RHO))/QUAL)
          ELSE
            RHOV = PSAT / (RBAR * TIWO)
          END IF
          WRITE(*,*) 'NONEQUIL: HG,HGL,RHO,RHOL,QUAL',
     &          HG,HGL,RHO,RHOL,QUAL
           END IF

C COMPUTE THE REST OF THE TWO-PHASE PROPERTIES
      T = TIWO
C ZONE PRESSURE WILL BE SATURATION PRESSURE
      P = (10.**(ABOIL - BBOIL/T))
      VOLF = QUAL * RHO / RHOV
      IF(QUAL .GT. 0.999) THEN
         VOLF = MIN(VOLF,1.0D+00)
      END IF
      IF(VOLF .GE. 0.0D+00 .AND. VOLF .LE. 1.0D+00) THEN
C NOW COMPUTE SOUND SPEED
         CALL EOSF(RHOL,F1,F2)
         CALL SOUND(HGL,RHOL,P,F2,CLIQ)
         CVAP = SQRT(RBAR*GAMMA*T)
C VOLUME FRACTION OF VAPOR FOR CRUDE INITIAL GUESS AT SOUND SPEED
         CSOUND = VOLF*CVAP + (1.-VOLF)*CLIQ
      ELSE
C THERE IS A PROBLEM WITH VOLF
         WRITE(*,*) 'PROBLEM WITH VOLF IN EOSTWO'
         WRITE(*,*) 'VOLF = ', VOLF
         WRITE(*,*) 'QUAL = ', QUAL
         WRITE(*,*) 'RHO = ', RHO
         WRITE(*,*) 'RHOV = ', RHOV
         STOP
      END IF
       END IF
   END IF

   RETURN
   END

C ************************************************
C EQUATION OF STATE FOR 2-PHASE SPALLED MATERIAL (LIQUID AND VAPOR)
C FOR LIQUID PART, USE CURRENT LIQUID/SOLID EOS
C FOR VAPOR PART, USE IDEAL GAS RELATION
C BASE TWO-PHASE FITTING ON Tsat vs. Psat CURVE
C UNITS: AL,AV COEFFICIENTS IN J/KG, PRESSURE IN Pa

   FUNCTION QIWO(QUAL)
   IMPLICIT DOUBLE PRECISION (A-H,O-Z)
   DIMENSION ACOND(13),AH2T(10),EOSCOEF(10)
   COMMON/MATDAT/TMELT,HMELTI,HMELTT,ACOND,AH2T
```

```
      COMMON/EOSDAT/RHO0,EOSCOEF,ABOIL,BBOIL,PRNU,YLD0
      COMMON/QIWODAT/HG,RHO,RHOV,RHOL,T,HGL

      AL0 = AH2T(7)
      AL1 = AH2T(8)
      AV0 = AH2T(9)
      AV1 = AH2T(10)
      GAMMA = EOSCOEF(9)
      RBAR = EOSCOEF(10)

C DETERMINE TEMPERATURE BASED ON ENERGY BALANCE
      Z1 = HG + QUAL*AV0/AV1 + (1.0D+00-QUAL)*AL0/AL1
      Z2 = (QUAL/AV1) + ((1.0D+00-QUAL)/AL1)
      T = Z1 / Z2
C ENTHALPIES FOLLOW DIRECTLY
      HGV = (T - AV0) / AV1
      HGL = (T - AL0) / AL1
C ZONE PRESSURE WILL BE SATURATION PRESSURE
      PSAT = (10.**(ABOIL - BBOIL/T))
C VAPOR DENSITY FROM IDEAL GAS RELATION
      RHOV = PSAT / (RBAR * T)
C GET RHOL FROM ITERATIONS ON NONLINEAR FUNCTIONS F1,F2
      RHOL = RHO0
      CALL NEWTP(HGL,PSAT,RHOL)

C GET QUALITY IMPLIED BY MASS BALANCE
      QUALRHO = (1.0D+00-RHOL/RHO) / (1.0D+00-RHOL/RHOV)

C QUALITIES MUST BE EQUAL IN CONVERGED SOLUTION
      QIWO = QUAL - QUALRHO

      RETURN
      END

C ***************************************************
C NEWTON'S METHOD ITERATION TO FIND DENSITY,
C GIVEN PRESSURE AND SPECIFIC ENERGY
C F1 = F1(RHO) AND F2 = F2(RHO)
C FOR LINEAR EOS:  PRESSURE = F1 + F2 * ENERGY

      SUBROUTINE NEWTP(HG,P,RHO)
      IMPLICIT DOUBLE PRECISION (A-H,O-Z)

      TOL = 1.0D-6
      K = 0
      RHONEW = RHO

   10 CONTINUE

      RHO = RHONEW
      CALL EOSF(RHO,F1,F2)
      CALL EOSDF(RHO,DF1,DF2)
      F = F1 + F2*HG - P
      FP = DF1 + HG*DF2
```

```
      RHONEW = RHO - F/FP

      K = K+1
      IF (K .GT. 10) THEN
         WRITE(*,*) 'TOO MANY NEWTON ITERATIONS ON RHOL'
         STOP
      END IF

      IF(ABS(RHONEW-RHO) .GT. TOL) GOTO 10
      RHO = RHONEW

      RETURN
      END

C ***************************************************
C CALCULATION OF SURFACE EVAPORATION MASS AND ENERGY LOSS
C FOR NOW CRUDE ESTIMATE USING MAXIMUM FLUX (PAMB = 0)
C LIMIT FROM KELLEY & ROTHENBERG, NUC INST & METH, 1985, p 755

      SUBROUTINE SURFVAP(GEOM,PAMB,TSAT,X,DT,DVAPMASS,DHVAP)
      IMPLICIT DOUBLE PRECISION (A-H,O-Z)
      INTEGER GEOM
      DIMENSION ACOND(13),AH2T(10),EOSCOEF(10)
      COMMON/MATDAT/TMELT,HMELTI,HMELTT,ACOND,AH2T
      COMMON/EOSDAT/RHO0,EOSCOEF,ABOIL,BBOIL,PRNU,YLD0

      PI = 4.0 * ATAN(1.0)
      RBAR = EOSCOEF(10)

C VAPOR PRESSURE FUNCTION FROM DUSHMAN, PRESSURE IN Pa
      PSAT = (10.**(ABOIL - BBOIL/TSAT))
C FLUX IN kg/m2.sec
      FLUX = PSAT / SQRT(2. * PI * RBAR * TSAT)

      IF (GEOM .EQ. 1) THEN
         AREA = 1.0D+00
      ELSE IF (GEOM .EQ. 2) THEN
         AREA = 2.0 * PI * X
      ELSE
         AREA = 4.0 * PI * X**2
      END IF
      DVAPMASS = FLUX * DT * AREA

C ENERGY IN THIS MASS
C ASSUME VAPOR AT CURRENT ZONE TEMPERATURE
C USES LINEAR FIT TO T VS. H CURVE (in K vs. J/kg)
      HG = (TSAT - AH2T(9)) / AH2T(10)
      HL = (TSAT - AH2T(7)) / AH2T(8)
      DHVAP = (HG - HL) * DVAPMASS

      RETURN
      END
```

```
C ***************************************************
C COMPUTE EQUATION OF STATE COEFFICIENTS FOR SURFACE ZONE
C F1 = F1(RHO) AND F2 = F2(RHO)
C FOR LINEAR EOS:  PRESSURE = F1 + F2 * ENERGY
C ASSUMES IDEAL GAS EOS:  P = (GAMMA-1)*RHO*HG
C OR JUST USE SOLID EOS FOR LOW VAPOR FRACTION

   SUBROUTINE FSURF(RHO,RHOL,QUAL,QMIN,F1,F2)
   IMPLICIT DOUBLE PRECISION (A-H,O-Z)

   IF (QUAL .LE. QMIN) THEN
C JUST LIQUID/SOLID IN ZONE, SO IGNORE VAPOR
      CALL EOSF(RHO,F1,F2)
   ELSE
C APPROXIMATION BASED ON CONSTANT RHOL FROM LAST TIME STEP
      RHOV = QUAL / ((1./RHO) + (QUAL - 1.0D+00)/RHOL)
      CALL FVAPOR(RHOV,F1,F2)
   END IF

   RETURN
   END

C ***************************************************
C ROUTINE TO DETERMINE NEW VELOCITY OF OUTER NODE
C BASED ON PSEUDO-STEADY ISENTROPIC IDEAL GAS FLOW RELATIONS
C ASSUME VAPORIZING SURFACE IS STATIONARY
C VAPORIZING SURFACE AT P0=Psat, OUTER SURFACE AT P=P(0)

   SUBROUTINE USURFIX(T,P0,P,UNEW)
   IMPLICIT DOUBLE PRECISION (A-H,O-Z)
   DIMENSION EOSCOEF(10)

   COMMON/EOSDAT/RHO0,EOSCOEF,ABOIL,BBOIL,PRNU,YLD0

   GAMMA = EOSCOEF(9)
   RBAR = EOSCOEF(10)
   GM1 = GAMMA - 1.0D+00

   C0 = SQRT(RBAR*GAMMA*T)

   UNEW = C0*SQRT((2./GM1)*DABS((1.0D+00-(P/P0)**(GM1/GAMMA))))
C KEEP WITH SIGN CONVENTION
   IF (P .LT. P0) THEN
      UNEW = -UNEW
   END IF

   RETURN
   END

C ***************************************************
C ROUTINE TO DETERMINE NEW PRESSURE AT OUTER NODE OF ISURF
C BASED ON ISENTROPIC IDEAL GAS FLOW RELATIONS
C C/C0 = 1 - B*X  LINEAR ACROSS EXPANSION FAN
C BUT ASYMPTOTE TO IDEAL GAS PRESSURE IN SPALLED ZONE
```

```
      SUBROUTINE PLEFTCALC(PSAT,PC,DXC1,DX1,RHOV,QUAL,T,PLEFT)
      IMPLICIT DOUBLE PRECISION (A-H,O-Z)
      DIMENSION EOSCOEF(10)
      COMMON/EOSDAT/RHO0,EOSCOEF,ABOIL,BBOIL,PRNU,YLD0

      GAMMA = EOSCOEF(9)
      GM1 = GAMMA - 1.0D+00
      RBAR = EOSCOEF(10)
      N = 4

C ASSUME AVERAGE DROP ACROSS SONIC KNUDSEN LAYER (KNIGHT)
C  P0 = 0.235 * PSAT
C ASSUME NO DROP ACROSS KNUDSEN LAYER
      P0 = PSAT
      B = (1.0D+00-(PC/P0)**(GM1/(2.*GAMMA)))/DXC1
      PEXP = P0 * (1.0D+00 - B * DX1)**(2.*GAMMA/GM1)
      PEXP = MAX(PEXP,PC)

C AVERAGE VAPOR PRESSURE
      PVAP = RHOV * RBAR * T

C INTERPOLATE BEIWEEN THESE PRESSURES WITH Nth ORDER FUNCTION
      QSTAR = (1.0D+00 - QUAL)**N
      PLEFT = PEXP * QSTAR + (1.0D+00 - QSTAR) * PVAP

      RETURN
      END

C ***************************************************
C EQUATION OF STATE FOR (IN GENERAL) 2-PHASE SURFACE ZONE
C FOR LIQUID PART, USE CURRENT LIQUID/SOLID EOS
C FOR VAPOR PART, USE IDEAL GAS RELATION
C UNITS: AL,AV COEFFICIENTS IN J/KG, PRESSURE IN Pa
C NOTE THAT T PROVIDES BOTH AN INITIAL TEMPERATURE GUESS
C     AND RETURNS THE FINAL TEMPERATURE RESULT

      SUBROUTINE EOSURF(RHOL,RHOV,RHOP1,QMIN,PM1,P,ALPHA,CSOUND)
      IMPLICIT DOUBLE PRECISION (A-H,O-Z)
      DIMENSION ACOND(13),AH2T(10),EOSCOEF(10)

      EXTERNAL TSURF,PSURF

      COMMON/MATDAT/TMELT,HMELTI,HMELTT,ACOND,AH2T
      COMMON/EOSDAT/RHO0,EOSCOEF,ABOIL,BBOIL,PRNU,YLD0
      COMMON/SURFT/HGSURF,QUALSURFT
      COMMON/SURFP/RHOSURF,QUALSURFP,HGV,HGL,T

      AL0 = AH2T(7)
      AL1 = AH2T(8)
      AV0 = AH2T(9)
      AV1 = AH2T(10)
      GAMMA = EOSCOEF(9)
      RBAR = EOSCOEF(10)
```

```
      QUAL = QUALSURFT
      HG = HGSURF
      RHO = RHOSURF

C ITERATE ON TEMPERATURE CHOICE TO MATCH VALUES
C OBTAINED FOR LIQUID AND VAPOR
C SOLVE USING BRENT'S METHOD (SEE NUMERICAL RECIPES)
C HG1 AND HG2 MUST BRACKET THE ROOT TO Tvapor-Tliquid=0,
C WHICH IS IN THE EXTERNAL FUNCTION TSURF(HGV)
C WHERE HGV IS THE SPECIFIC ENERGY OF THE VAPOR PHASE
C FIRST GET TWO HGV VALUES THAT BRACKET FUNCTION ZERO
      HGNOM = (T - AV0) / AV1
      CALL BRACKET(TSURF,HGNOM,HG1,HG2)
      TOL = 1.0D-05
      HGV = ZBRENT(TSURF,HG1,HG2,TOL)
      HGL = (HG - QUAL*HGV) / (1.00D+00 - QUAL)
      TV = AV0 + AV1 * HGV
c     IF(ABS(T-TV) .GT. 30.) WRITE(*,*) 'DIvapor =',(TV-T)
      CALL H2T(HGL,TL)
      TRATIO = 2.*ABS(TV-TL)/(TV+TL)
      IF (TRATIO .GT. 0.01) THEN
         WRITE(*,*) 'PROBLEM IN ISURF TEMP MATCH'
         WRITE(*,*) 'TL, TV =', TL,TV
         STOP
      ELSE
         T = (TL + TV) / 2.00D+00
      END IF

C NOW DETERMINE PRESSURE IN THE SURFACE ZONE
C FOR SMALL VAPOR CONTENT, ASSUME FULLY LIQUID/SOLID AS IN FSURF
C OTHERWISE, FIX PRESSURE AT Psat
      IF (QUAL .LE. QMIN) THEN
          RHOL = RHO
          CALL EOSF(RHO,F1,F2)
          P = F1 + F2 * HG
          CALL SOUND(HG,RHO,P,F2,CSOUND)
          ALPHA = 0.0D+00
          RHOV = P / (RBAR * T)
      ELSE

C SET PRESSURE EQUAL TO THE SATURATION VAPOR PRESSURE
C OR THE PRESSURE IN THE NEXT VAPOR ZONE, WHICHEVER IS HIGHER
      PSAT = (10.**(ABOIL - BBOIL/T))
      P = MAX(PSAT,PM1)
C UPDATE LIQUID DENSITY BASED ON THIS PRESSURE
C MUST ITERATE WITH BRENT'S METHOD (SEE NUMERICAL RECIPIES)
C FIRST GET TWO RHOL VALUES THAT BRACKET FUNCTION ZERO
      RNOM = RHOL
      CALL BRACKET(PSURF,RNOM,RL1,RL2)
      TOL = 1.0D-05
      RHOL = ZBRENT(PSURF,RL1,RL2,TOL)
C UNDER SOME CONDITIONS,
C    RHOL MAY CALCULATE TO BE LESS THAN RHO
C    SET A FLOOR DENSITY ON WHICH TO BASE A RHOV CALCULATION
```

```
C   ADJUST ZONE PRESSURE ACCORDINGLY
    IF(RHOL .LT. RHO) THEN
        IF(RHOP1 .GT. RHO) THEN
          RHOL = RHOP1
        ELSE
          RHOL = RHO + 1.0
        END IF
        CALL EOSF(RHOL,F1,F2)
        P = F1 + F2 * HGL
    END IF

C COMPUTE VOLUME FRACTION VAPOR
    RHOV = QUAL / ((1./RHO) + (QUAL - 1.0D+00)/RHOL)
    ALPHA = QUAL * RHO / RHOV
C NOW COMPUTE SOUND SPEED
    CALL EOSF(RHOL,F1,F2)
    CALL SOUND(HGL,RHOL,P,F2,CLIQ)
    CVAP = SQRT(RBAR*GAMMA*T)
C VOLUME FRACTION OF VAPOR FOR CRUDE INITIAL GUESS AT SOUND SPEED
    CSOUND = ALPHA*CVAP + (1.-ALPHA)*CLIQ

    END IF

    RETURN
    END

C ***************************************************
C TEMPERATURE ITERATION FOR 2-PHASE SURFACE ZONE
C NOTE THAT T PROVIDES BOTH AN INITIAL TEMPERATURE GUESS
C      AND RETURNS THE FINAL TEMPERATURE RESULT

    SUBROUTINE EOSURFT(QMIN,T)
    IMPLICIT DOUBLE PRECISION (A-H,O-Z)
    DIMENSION ACOND(13),AH2T(10),EOSCOEF(10)

    EXTERNAL TSURF

    COMMON/MATDAT/TMELT,HMELTI,HMELTT,ACOND,AH2T
    COMMON/EOSDAT/RHO0,EOSCOEF,ABOIL,BBOIL,PRNU,YLD0
    COMMON/SURFT/HG,QUAL

    AL0 = AH2T(7)
    AL1 = AH2T(8)
    AV0 = AH2T(9)
    AV1 = AH2T(10)
    GAMMA = EOSCOEF(9)
    RBAR = EOSCOEF(10)

    IF (QUAL .LT. QMIN) THEN
C ALL LIQUID OR SOLID
        CALL H2T(HG,T)
    ELSE IF(QUAL .GT. 0.99999) THEN
C ESSENTIALLY ALL VAPOR
        T = AV0 + AV1 * HG
```

```
      ELSE
C ITERATE ON TEMPERATURE CHOICE TO MATCH VALUES
C OBTAINED FOR LIQUID AND VAPOR
C SOLVE USING BRENT'S METHOD (SEE NUMERICAL RECIPES)
C HG1 AND HG2 MUST BRACKET THE ROOT TO Tvapor-Tliquid=0,
C WHICH IS IN THE EXTERNAL FUNCTION TSURF(HGV)
C WHERE HGV IS THE SPECIFIC ENERGY OF THE VAPOR PHASE
C FIRST GET TWO HGV VALUES THAT BRACKET FUNCTION ZERO
         HGNOM = (T - AV0) / AV1
         CALL BRACKET(TSURF,HGNOM,HG1,HG2)
         TOL = 1.0D-05
         HGV = ZBRENT(TSURF,HG1,HG2,TOL)
         HGL = (HG - QUAL*HGV) / (1.00D+00 - QUAL)
         TV = AV0 + AV1 * HGV
         CALL H2T(HGL,TL)
         TRATIO = 2.*ABS(TV-TL)/(TV+TL)
         IF (TRATIO .GT. 0.01) THEN
        WRITE(*,*) 'PROBLEM IN ISURF TEMP MATCH'
        WRITE(*,*) 'TL, TV =', TL,TV
        STOP
         ELSE
        T = (TL + TV) / 2.00D+00
         END IF
      END IF

      RETURN
      END

C ***************************************************
C TEMP MATCHING FUNCTION FOR (IN GENERAL) 2-PHASE SURFACE ZONE
C FORM IS TSURF = Tvap - Tliq -> 0 WITH BRENT'S METHOD
C TSURF IS A FUNCTION OF VAPOR ENERGY (HGV)
C ROOT SOLVER WILL VARY ENERGY PARTITION VAPOR/LIQUID TO MATCH TEMPS

      FUNCTION TSURF(HGV)
      IMPLICIT DOUBLE PRECISION (A-H,O-Z)
      DIMENSION ACOND(13),AH2T(10)
      COMMON/MATDAT/TMELT,HMELTI,HMELTT,ACOND,AH2T
      COMMON/SURFT/HG,QUAL

      AV0 = AH2T(9)
      AV1 = AH2T(10)

      HGL = (HG - QUAL*HGV) / (1.0D+00 - QUAL)
      TV = AV0 + AV1 * HGV
      CALL H2T(HGL,TL)
      TSURF = TV - TL

      RETURN
      END

C ***************************************************
C PRESSURE MATCHING FUNCTION FOR 2-PHASE SURFACE ZONE
C FORM IS PSURF = Psat - Pliq -> 0 WITH BRENT'S METHOD
```

```
C PSURF IS A FUNCTION OF LIQUID DENSITY (RHOL)
C ROOT SOLVER WILL VARY LIQUID DENSITTY TO MATCH PRESSURES

      FUNCTION PSURF(RHOL)
      IMPLICIT DOUBLE PRECISION (A-H,O-Z)
      DIMENSION EOSCOEF(10)
      COMMON/EOSDAT/RHO0,EOSCOEF,ABOIL,BBOIL,PRNU,YLD0
      COMMON/SURFP/RHO,QUAL,HGV,HGL,T

      PSAT = (10.**(ABOIL - BBOIL/T))

      CALL EOSF(RHOL,F1L,F2L)
      PL = F1L + F2L * HGL

      PSURF = PSAT - PL

      RETURN
      END

C ******************************************************
C BRENT'S METHOD TO FIND THE ROOT OF A FUNCTION FUNC KNOWN TO
C LIE BETWEEN X1 AND X2.  THE ROOT, ZBRENT, WILL BE REFINED UNTIL
C ITS ACCURACY IS TOL.
C PARAMETERS: MAX # OF ITERATIONS, MACHINE FLOATING-POINT PRECISION
C REFERENCE:  NUMERICAL RECIPES, SECTION 9.3

      FUNCTION ZBRENT(FUNC,X1,X2,TOL)
      INTEGER ITMAX
      DOUBLE PRECISION ZBRENT,TOL,X1,X2,FUNC,EPS
      EXTERNAL FUNC
      PARAMETER (ITMAX=100, EPS=1.0D-15)
      INTEGER ITER
      DOUBLE PRECISION A,B,C,D,E,FA,FB,FC,P,Q,R,S,TOL1,XM

      A = X1
      B = X2
      FA = FUNC(A)
      FB = FUNC(B)
      IF((FA.GT.0. .AND. FB.GT.0.) .OR.
     &      (FA.LT.0. .AND. FB.LT.0.)) THEN
        WRITE(*,*) 'ROOT MUST BE BRACKETED FOR ZBRENT'
        WRITE(*,*) 'X1,X2=',X1,X2
        WRITE(*,*) 'F(X1),F(X2)=',FA,FB
        STOP
      END IF
      C = B
      FC = FB
      DO 11, ITER=1,ITMAX
        IF((FB.GT.0. .AND. FC.GT.0.) .OR.
     &        (FB.LT.0. .AND. FC.LT.0.)) THEN
          C = A
          FC = FA
          D = B - A
          E = D
```

```
        END IF
        IF(ABS(FC).LT.ABS(FB)) THEN
            A = B
            B = C
            C = A
            FA = FB
            FB = FC
            FC = FA
        END IF
C CONVERGENCE CHECK
        TOL1 = 2. * EPS * ABS(B) + 0.5 * TOL
        XM = 0.5 * (C - B)
        IF(ABS(XM) .LE. TOL1 .OR. FB.EQ.0.) THEN
            ZBRENT = B
      RETURN
        END IF
        IF(ABS(E).GE.TOL1 .AND. ABS(FA).GT.ABS(FB)) THEN
C ATTEMPT INVERSE QUADRATIC INTERPOLATION
      S = FB / FA
      IF(A.EQ.C) THEN
          P = 2. * XM * S
          Q = 1.0D+00 - S
      ELSE
          Q = FA / FC
          R = FB / FC
          P = S * (2.*XM*Q*(Q-R) - (B-A)*(R-1.0D+00))
          Q = (Q-1.0D+00) * (R-1.0D+00) * (S-1.0D+00)
      END IF
      IF(P.GT.0.) Q = -Q
C CHECK WHETHER IN BOUNDS
      P = ABS(P)
      IF(2.*P .LT. MIN(3.*XM*Q-ABS(TOL1*Q),ABS(E*Q))) THEN
C ACCEPT INTERPOLATION
          E = D
          D = P / Q
      ELSE
C INTERPOLATION FAILED, USE BISECTION
          D = XM
          E = D
      END IF
       ELSE
C BOUNDS DECREASING TOO SLOWLY, USE BISECTION
      D = XM
      E = D
        END IF
C MOVE LAST BEST GUESS TO A
        A = B
        FA = FB
C EVALUATE NEW TRIAL ROOT
        IF(ABS(D) .GT. TOL1) THEN
          B = B + D
        ELSE
          B = B + DSIGN(TOL1,XM)
        END IF
```

```
      FB = FUNC(B)

   11 CONTINUE

    WRITE(*,*) 'ZBENT EXCEEDED MAXIMUM ITERATIONS'
    ZBRENT = B

    RETURN
    END

C ***************************************************
C ROUTINE TO BRACKET ROOT OF FUNCTIONS, TO GIVE INPUT TO
C BRENT'S METHOD TO FIND THE ROOT OF A FUNCTION FUNC
C SINGLE-SIDED SEARCH, WITH XMIN AS LOWER LIMIT ALLOWED

    SUBROUTINE BRKTMIN(FUNC,XMIN,XNOM,X1,X2)
    DOUBLE PRECISION XMIN,XNOM,X1,X2,FUNC
    EXTERNAL FUNC
    DOUBLE PRECISION A,B,FA,FB

    A = MAX(XMIN,XNOM*.85)
    B = A * 1.02
    FA = FUNC(A)

    DO 10, ICNT=1,20
    FB = FUNC(B)
    IF((FA.GT.0. .AND. FB.LT.0.) .OR.
     &       (FA.LT.0. .AND. FB.GT.0.)) THEN
          X1 = A
          X2 = B
          RETURN
       END IF
    B = B * 1.02

   10 CONTINUE
    WRITE(*,*) 'TOO MANY BRACKET ITERATIONS WITH XMIN'
    B = A * 1.02
    FB = FUNC(B)
    WRITE(*,*) 'A,B=',A,B
    WRITE(*,*) 'FA,FB=',FA,FB
    STOP
    END

C ***************************************************
C ROUTINE TO BRACKET ROOT OF FUNCTIONS, TO GIVE INPUT TO
C BRENT'S METHOD TO FIND THE ROOT OF A FUNCTION FUNC
C BASED ON USING A NOMINAL X AS STARTING POINT

    SUBROUTINE BRACKET(FUNC,XNOM,X1,X2)
    DOUBLE PRECISION XNOM,X1,X2,FUNC
    EXTERNAL FUNC
    DOUBLE PRECISION A,B,C,FA,FB,FC

    IFLAG = 0
```

```
      IF (XNOM .EQ. 0.0) THEN
          A = -1.0
          B =  1.0
      ELSE
          A = XNOM * 0.9999
          B = XNOM * 1.02
      END IF
      FA = FUNC(A)
      FB = FUNC(B)
     20  CONTINUE
      IF((FA.GT.0. .AND. FB.LT.0.) .OR.
        &       (FA.LT.0. .AND. FB.GT.0.)) THEN
            X1 = B
            X2 = A
            RETURN
         END IF
C PICK A NEW POINT WITH LINEAR INTERPOLATION + 2%
      DO 10, ICNT=1,20
      C = B - 1.02 * (A-B) * FB / (FA-FB)
      FC = FUNC(C)
      IF((FA.GT.0. .AND. FC.LT.0.) .OR.
        &       (FA.LT.0. .AND. FC.GT.0.)) THEN
            IF(ABS(A-C) .LT. ABS(B-C)) THEN
              X1 = C
              X2 = A
              RETURN
            ELSE
              X1 = C
              X2 = B
              RETURN
            END IF
         END IF
C THROW AWAY POINT FARTHEST FROM NEW POINT, AND TRY AGAIN
         IF(ABS(A-C) .LT. ABS(B-C)) THEN
               B = C
               FB = FC
         ELSE
               A = C
               FA = FC
         END IF

      IF(IFLAG .EQ. 1)THEN
         WRITE(*,*) A,FA
         WRITE(*,*) B,FB
      END IF

     10  CONTINUE

C TOO MANY BRACKET ITERATIONS
      A = XNOM * 10.000
      B = XNOM * -10.00
      FA = FUNC(A)
      FB = FUNC(B)
      IFLAG = IFLAG+1
```

```
      IF(IFLAG.EQ.1) THEN
         GOTO 20
      ELSE
         WRITE(*,*) 'TOO MANY BRACKET ITERATIONS'
         WRITE(*,*) 'A,B=',A,B
         WRITE(*,*) 'FA,FB=',FA,FB
         STOP
      END IF

      RETURN
      END

C ***************************************************
C FUNCTION FOR IMPLICIT HEAT CONDUCTION BETWEEN ZONES
C ISURF AND (ISURF+1), TO BE SOLVED WITH BRENT'S METHOD
C RETURNS DIFFERENCE BETWEEN HEAT CONDUCTION (INPUT)
C AND FOURIER CONDUCTION BASED ON TEMPS AT END OF TIME STEP
C HPN & HEN ARE ENERGIES AT STEP N, REST OF H & T AT N+1

      FUNCTION CONDSURF(HEAST)
      IMPLICIT DOUBLE PRECISION (A-H,O-Z)
      COMMON/SURFC/HPN,HEN,ZMP,ZME,DT,QMIN,CONDP,DX,BETAC,TP
      COMMON/SURFT/HGP,QUAL

C COMMPUTE NEW ZONE ENERGIES BASED ON CURRENT HEAST
      HP = HPN - HEAST * DT
      HE = HEN + HEAST * DT
      HGP = HP / ZMP
      HGE = HE / ZME
C UPDATE TEMPERATURES
      CALL EOSURFT(QMIN,TP)
      CALL H2T(HGE,TE)
C COMPUTE FOURIER CONDUCTION BASED ON NEW TEMPS
      HEASTNEW = (TP - TE) * CONDP * BETAC / DX

      CONDSURF = HEASTNEW - HEAST

      RETURN
      END

C ***************************************************
C BUBBLE NUCEATION RATE ROUTINE
C FROM CAREY, EQN 5.74
C MATERIAL PROPERTIES HARDWIRED FOR AL,ALUMINA,SILICA
C UNITS: J in m-3.s-1, SIGMA in N/m

      SUBROUTINE NUCLEATE(T,RHO,P,J,TSTAR)
      IMPLICIT DOUBLE PRECISION (A-H,O-Z)
      DOUBLE PRECISION J,ISTAR
      DIMENSION ACOND(13),AH2T(10),EOSCOEF(10),SIGMACOEF(7)

      COMMON/MATDAT/TMELT,HMELTI,HMELTT,ACOND,AH2T
      COMMON/EOSDAT/RHO0,EOSCOEF,ABOIL,BBOIL,PRNU,YLD0
      COMMON/SURFTEN/SIGMACOEF
```

```
      RBAR = EOSCOEF(10)
      JFLAG = NINT(SIGMACOEF(1))

      IF (JFLAG .EQ. 0) THEN
C NO MATERIAL SURFACE TENSION INFORMATION -- SKIP J CALCULATION
          J = 2.0D-97
          TSTAR = 0.1
      ELSE

          IF(JFLAG .EQ. 1) THEN
C FIT PARAMETERS FOR FIT TO MURR (CUBIC EQUATION)
          A = SIGMACOEF(2)
          TCRIT = SIGMACOEF(3)
          SIGMA0 = SIGMACOEF(4)
          ASIG = SIGMACOEF(5)
          BSIG = SIGMACOEF(6)
          CSIG = SIGMACOEF(7)

          ELSE IF(JFLAG .EQ. 2) THEN
C FIT PARAMETERS FOR EXPONENTIAL EQUATION
          A = SIGMACOEF(2)
          TCRIT = SIGMACOEF(3)
          AEXP = SIGMACOEF(4)
          BEXP = SIGMACOEF(5)

          ELSE
          WRITE(*,*) 'INVALID MATERIAL (NUCLEATE)'
          STOP
          END IF

          AVOGADRO = 6.022D+26
          GAMMAE = 0.5772
          BOLTZ = 1.38D-23
          PI = 4.*ATAN(1.)

          IF (T .LT. TMELT) THEN
          WRITE(*,*) 'TEMP OUTSIDE RANGE FOR NUCLEATE'
          J = 1.0D-98
          TSTAR = 0.1
          ELSE IF (T .GE. TCRIT) THEN
          IF(P .GT. 0.) THEN
             J = 1.0D-96
             TSTAR = 0.1
          ELSE
             J = 1.0D+43
             TSTAR = 1.0D-19
          END IF
          ELSE

C COMPUTE SATURATION PRESSURE
          PSAT = (10.**(ABOIL - BBOIL/T))

          IF (P .GT. PSAT) THEN
```

```
            J = 1.0D-96
            TSTAR = 0.1
        ELSE

C COMPUTE SURFACE TENSION
          IF(JFLAG .EQ. 2) THEN
C USE EXPONENTIAL FIT EQUATION
              SIGMA = AEXP * 10.**(BEXP * T)
          ELSE
C CUBIC SPLINE FIT TO DATA AT MELT TEMP AND ZERO AT CRIT
              T1 = (T - TMELT)
            SIGMA = SIGMA0 + T1*(ASIG+T1*(BSIG+T1*CSIG))
          END IF

            ETA = DEXP((P-PSAT)/(RHO*RBAR*T))
            X1 = -1.8195D+24 * (SIGMA**3)/(T*(ETA*PSAT-P)**2)
            X2 = SQRT(RHO**2 * SIGMA / A)

            J = 1.44D+40 * X2 * DEXP(X1)
            J = MAX(J,1.0D-97)
          END IF

C COMPUTE INDUCTION TIME REQUIRED TO REACH STEADY J-VALUE
C FROM MODIFICATION OF VAPOR CONDENSATION MEMO BY WILEMSKI
C RSTAR IS THE CRITICAL BUBBLE RADIUS (meters)
          RSTAR = 2. * SIGMA / (ETA*PSAT - P)
          IF (RSTAR .LE. 0.) THEN
              TSTAR = 1.0D-02
          ELSE
           U = SQRT(8.*RBAR*T/PI)
           RHOV = PSAT / (RBAR * T)
           SMALLM = A / AVOGADRO
           SMALLN = ETA * PSAT / (BOLTZ * T)
           ISTAR = (4./3.) * PI * RSTAR**3 * RHOV / SMALLM
         WSTAR=(16.*PI/2.)*SIGMA**3/(BOLTZ*T*(ETA*PSAT-P)**2)
         TSTAR = RSTAR*ISTAR*RHOV / (U*SMALLM*SMALLN*WSTAR) *
     &              (DLOG(WSTAR/3.) + GAMMAE)
           IF(TSTAR .LE. 0.) TSTAR = 1.0D-18

          END IF
        END IF
      END IF

  101  FORMAT(7(1PE12.3))
      RETURN
      END
```

Appendix B: External Material Data Files

The ABLATOR code takes all material property data from two external data files. X-ray opacities are given in the OPACDATA file for each of the photon energy groups. The units are keV for energies and m^{-1} for the opacities. The other material data file, MATDATA, contains the thermomechanical properties of the material. Sets of these data files have been generated for each of the five materials examined in this study. This appendix contains a listing of each of these files.

Silica.matdata

```
fused silica
# density kg/m3
2.20D+03
# T melt  K
1696.0
# k vs. T, solid, cal/m.k.s
0.5731
-9.884D-04
1.123D-06
0.000D+00
0.0D+00
0.0D+00
# k vs. T, liquid, cal/m.k.s
1.500
0.00D+00
0.0
0.0
0.0
0.0
# k vs. T, vapor, cal/m.k.s
1.00D-04
# T vs. H, solid, K & cal/g
303.58
5.0301
-5.2407D-03
6.1012D-06
0.0
0.0
# T vs. H, liquid, K & cal/g
585.3768
3.1261
# T vs. H, vapor, K & cal/g
-963.7
1.075
# coeff for log(P) = A - B/T, micron & K
14.2299
26286.2452
# Gruneisen EOS coeff & gamma & Rbar in J/kg.K
1.0
4350.
0.300
0.0
0.0
0.039
0.00
0.0
1.3
210.
# Poissons's Ratio
0.16
# Yield strength (Pa)
6.90E+08
# Surface tension (flag + 6 coefficients)
1.
64.08
11605.
0.30
3.10D-05
-9.276D-09
3.1203D-13
```

Silica.opacdata

fused silica

1.259000D-03	6.520000D-04	3.104587D+07
1.995000D-03	9.270000D-04	3.104587D+07
3.162000D-03	1.469000D-03	3.104587D+07
5.012000D-03	2.329000D-03	3.104587D+07
7.943000D-03	3.690000D-03	3.104587D+07
1.259000D-02	5.850000D-03	1.121220D+07
1.995000D-02	9.270000D-03	4.850431D+07
3.162000D-02	1.469000D-02	5.211945D+07
5.012000D-02	2.329000D-02	2.669526D+07
7.943000D-02	3.690000D-02	1.282589D+07
1.259000D-01	5.850000D-02	1.488247D+07
1.995000D-01	9.270000D-02	8.192421D+06
3.162000D-01	1.469000D-01	2.942232D+06
5.012000D-01	2.329000D-01	1.056272D+06
7.943000D-01	3.690000D-01	1.171862D+06
1.055000D+00	1.130000D-01	5.922726D+05
1.175000D+00	1.260000D-01	4.439687D+05
1.308000D+00	1.410000D-01	3.332442D+05
1.456000D+00	1.560000D-01	2.501608D+05
1.621000D+00	1.740000D-01	1.877141D+05
1.804000D+00	1.940000D-01	1.410027D+05
2.009000D+00	2.150000D-01	3.854086D+05
2.236000D+00	2.400000D-01	2.860712D+05
2.489000D+00	2.670000D-01	2.122701D+05
2.771000D+00	2.980000D-01	1.574608D+05
3.085000D+00	3.310000D-01	1.168069D+05
3.435000D+00	3.690000D-01	8.662606D+04
3.824000D+00	4.100000D-01	6.428108D+04
4.257000D+00	4.570000D-01	4.770492D+04
4.739000D+00	5.090000D-01	3.540631D+04
5.525000D+00	1.105000D+00	2.272258D+04
6.746000D+00	1.350000D+00	1.260982D+04
8.238000D+00	1.648000D+00	6.995946D+03
1.006000D+01	2.007000D+00	3.879316D+03
1.228000D+01	2.460000D+00	2.107494D+03
1.500000D+01	3.000000D+00	1.142688D+03
1.831000D+01	3.670000D+00	6.209232D+02
2.236000D+01	4.470000D+00	3.339310D+02
2.730000D+01	5.460000D+00	1.784291D+02
3.334000D+01	6.670000D+00	9.527036D+01
4.071000D+01	8.140000D+00	5.089748D+01
4.971000D+01	9.950000D+00	2.719232D+01
6.070000D+01	1.214000D+01	1.438304D+01
7.411000D+01	1.483000D+01	7.609043D+00
9.050000D+01	1.810000D+01	4.023155D+00

SiN.matdata

```
silicon nitride
# density kg/m3
3.16D+03
# T melt K
1800.0
# k vs. T, solid, cal/m.k.s
13.022
-2.1655D-02
2.1690D-05
-1.0429D-08
1.8882D-12
0.0
# k vs. T, liquid, cal/m.k.s
3.00
0.00D+00
0.0
0.0
0.0
0.0
# k vs. T, vapor, cal/m.k.s
0.05
# T vs. H, solid, K & cal/g
316.62
4.7375
-3.2837D-03
2.1307D-06
0.0
0.0
# T vs. H, liquid, K & cal/g
562.1229
3.1391
# T vs. H, vapor, K & cal/g
-5337.9796
3.7708
# coeff for log(P) = A - B/T, micron & K
16.3856
22615.4451
# Gruneisen EOS coeff & gamma & Rbar in J/kg.K
1.0
8530.
0.0
0.0
0.0
0.24
0.00
0.0
1.40
119.
# Poissons's Ratio
0.27
# Yield strength (Pa)
4.5E+08
# Surface tension (flag + 6 coefficients)
0
0
0
0
0
0
0
```

SiN.opacdata

silicon nitride

1.259000D-03	6.520000D-04	6.188586D+08
1.995000D-03	9.270000D-04	6.188586D+08
3.162000D-03	1.469000D-03	6.188586D+08
5.012000D-03	2.329000D-03	6.188586D+08
7.943000D-03	3.690000D-03	6.188586D+08
1.259000D-02	5.850000D-03	3.749718D+08
1.995000D-02	9.270000D-03	1.439430D+08
3.162000D-02	1.469000D-02	7.805009D+07
5.012000D-02	2.329000D-02	2.516297D+07
7.943000D-02	3.690000D-02	1.062464D+07
1.259000D-01	5.850000D-02	2.272778D+07
1.995000D-01	9.270000D-02	1.339471D+07
3.162000D-01	1.469000D-01	4.869807D+06
5.012000D-01	2.329000D-01	4.026164D+06
7.943000D-01	3.690000D-01	1.255657D+06
1.055000D+00	1.130000D-01	6.062574D+05
1.175000D+00	1.260000D-01	4.525282D+05
1.308000D+00	1.410000D-01	3.382551D+05
1.456000D+00	1.560000D-01	2.528786D+05
1.621000D+00	1.740000D-01	1.889819D+05
1.804000D+00	1.940000D-01	1.413870D+05
2.009000D+00	2.150000D-01	6.218852D+05
2.236000D+00	2.400000D-01	4.624270D+05
2.489000D+00	2.670000D-01	3.437441D+05
2.771000D+00	2.980000D-01	2.554426D+05
3.085000D+00	3.310000D-01	1.898276D+05
3.435000D+00	3.690000D-01	1.410282D+05
3.824000D+00	4.100000D-01	1.048338D+05
4.257000D+00	4.570000D-01	7.793576D+04
4.739000D+00	5.090000D-01	5.794351D+04
5.525000D+00	1.105000D+00	3.727184D+04
6.746000D+00	1.350000D+00	2.074282D+04
8.238000D+00	1.648000D+00	1.154040D+04
1.006000D+01	2.007000D+00	6.416796D+03
1.228000D+01	2.460000D+00	3.494008D+03
1.500000D+01	3.000000D+00	1.898748D+03
1.831000D+01	3.670000D+00	1.034048D+03
2.236000D+01	4.470000D+00	5.573173D+02
2.730000D+01	5.460000D+00	2.984224D+02
3.334000D+01	6.670000D+00	1.596718D+02
4.071000D+01	8.140000D+00	8.547799D+01
4.971000D+01	9.950000D+00	4.575892D+01
6.070000D+01	1.214000D+01	2.424260D+01
7.411000D+01	1.483000D+01	1.284525D+01
9.050000D+01	1.810000D+01	6.802279D+00

B4C.matdata

```
boron carbide
# density kg/m3
2.50D+03
# T melt
2743.
# k vs. T, solid, cal/m.k.s
5.8642
-6.3475E-03
3.2643E-06
-5.3776E-10
0.00D+00
0.00D+00
# k vs. T, liquid, cal/m.k.s
1.9120
0.0D+00
0.0D+00
0.0D+00
0.0D+00
0.0D+00
# k vs. T, vapor, cal/m.k.s
0.1
# T vs. H, solid, K & cal/g
305.37
3.0327
-3.2045D-03
4.3275D-06
-2.9961D-09
7.8814D-13
# T vs. H, liquid, K & cal/g
-275.6752
1.7000
# T vs. H, vapor, K & cal/g
-32406.16
2.9618
# coeff for log(P) = A - B/T, micron & K
13.4172
29722.5202
# Gruneisen EOS coeff & gamma & Rbar in J/kg.K
1.0
9630.
1.0
0.0
0.0
1.46
0.00
0.0
1.50
630.
# Poissons's Ratio
0.19
# Yield strength (Pa)
1.55E+08
# Surface tension (flag + 6 coefficients)
0
0
0
0
0
0
0
```

B4C.opacdata

boron carbide

1.259000E-03	6.520000E-04	4.372495E+08
1.995000E-03	9.270000E-04	4.372495E+08
3.162000E-03	1.469000E-03	4.372495E+08
5.012000E-03	2.329000E-03	4.372495E+08
7.943000E-03	3.690000E-03	4.372495E+08
1.259000E-02	5.850000E-03	2.758531E+08
1.995000E-02	9.270000E-03	1.098610E+08
3.162000E-02	1.469000E-02	4.373263E+07
5.012000E-02	2.329000E-02	1.740633E+07
7.943000E-02	3.690000E-02	6.930430E+06
1.259000E-01	5.850000E-02	2.609818E+06
1.995000E-01	9.270000E-02	1.354320E+07
3.162000E-01	1.469000E-01	6.632787E+06
5.012000E-01	2.329000E-01	2.283640E+06
7.943000E-01	3.690000E-01	6.553077E+05
1.055000E+00	1.130000E-01	3.005332E+05
1.175000E+00	1.260000E-01	2.198593E+05
1.308000E+00	1.410000E-01	1.610744E+05
1.456000E+00	1.560000E-01	1.180211E+05
1.621000E+00	1.740000E-01	8.643703E+04
1.804000E+00	1.940000E-01	6.337703E+04
2.009000E+00	2.150000E-01	4.633970E+04
2.236000E+00	2.400000E-01	3.327861E+04
2.489000E+00	2.670000E-01	2.388871E+04
2.771000E+00	2.980000E-01	1.714131E+04
3.085000E+00	3.310000E-01	1.229924E+04
3.435000E+00	3.690000E-01	8.821738E+03
3.824000E+00	4.100000E-01	6.331163E+03
4.257000E+00	4.570000E-01	4.543959E+03
4.739000E+00	5.090000E-01	3.261359E+03
5.525000E+00	1.105000E+00	2.009000E+03
6.746000E+00	1.350000E+00	1.062095E+03
8.238000E+00	1.648000E+00	5.612529E+02
1.006000E+01	2.007000E+00	2.964883E+02
1.228000E+01	2.460000E+00	1.550630E+02
1.500000E+01	3.000000E+00	8.092105E+01
1.831000E+01	3.670000E+00	4.232332E+01
2.236000E+01	4.470000E+00	2.196318E+01
2.730000E+01	5.460000E+00	1.134765E+01
3.334000E+01	6.670000E+00	5.858024E+00
4.071000E+01	8.140000E+00	3.025696E+00
4.971000E+01	9.950000E+00	1.562720E+00
6.070000E+01	1.214000E+01	8.036948E-01
7.411000E+01	1.483000E+01	4.134659E-01
9.050000E+01	1.810000E+01	2.125762E-01

Al.matdata

```
aluminum
# density kg/m3
2.707D+03
# T melt  K
933.45
# k vs. T, solid, cal/m.k.s
46.46
6.262D-02
-1.092D-04
5.021D-08
0.0D+00
0.0D+00
# k vs. T, liquid, cal/m.k.s
15.06
7.170D-03
0.0
0.0
0.0
0.0
# k vs. T, vapor, cal/m.k.s
2.60D-04
# T vs. H, solid, K & cal/g
298.36
4.5495
-3.5338D-03
0.0
0.0
0.0
# T vs. H, liquid, K & cal/g
29.7742
3.5556
# T vs. H, vapor, K & cal/g
-15405.5
5.382
# coeff for log(P) = A - B/T, micron & K
11.755
15891.5
# Gruneisen EOS coeff & gamma & Rbar in J/kg.K
1.0
5386.
1.339
0.0
0.0
1.97
0.48
0.0
1.666667
308.
# Poissons's Ratio
0.33
# Yield strength (Pa)
4.0E+07
# Surface tension (flag + 6 coefficients)
1.
26.98
5726.
0.866
-5.0D-04
1.33104D-07
-1.38714D-11
```

Al.opacdata

aluminum

1.259000D-03	6.520000D-04	3.239731D+07
1.995000D-03	9.270000D-04	3.239731D+07
3.162000D-03	1.469000D-03	3.239731D+07
5.012000D-03	2.329000D-03	3.239731D+07
7.943000D-03	3.690000D-03	3.239731D+07
1.259000D-02	5.850000D-03	3.239731D+07
1.995000D-02	9.270000D-03	3.239731D+07
3.162000D-02	1.469000D-02	3.239731D+07
5.012000D-02	2.329000D-02	3.239731D+07
7.943000D-02	3.690000D-02	3.239731D+07
1.259000D-01	5.850000D-02	2.718165D+07
1.995000D-01	9.270000D-02	1.421092D+07
3.162000D-01	1.469000D-01	5.063376D+06
5.012000D-01	2.329000D-01	1.800533D+06
7.943000D-01	3.690000D-01	5.578696D+05
1.055000D+00	1.130000D-01	2.691360D+05
1.175000D+00	1.260000D-01	2.018905D+05
1.308000D+00	1.410000D-01	1.516474D+05
1.456000D+00	1.560000D-01	1.139194D+05
1.621000D+00	1.740000D-01	1.097791D+06
1.804000D+00	1.940000D-01	8.339986D+05
2.009000D+00	2.150000D-01	6.320478D+05
2.236000D+00	2.400000D-01	4.718028D+05
2.489000D+00	2.670000D-01	3.520496D+05
2.771000D+00	2.980000D-01	2.625955D+05
3.085000D+00	3.310000D-01	1.958626D+05
3.435000D+00	3.690000D-01	1.460398D+05
3.824000D+00	4.100000D-01	1.089458D+05
4.257000D+00	4.570000D-01	8.127645D+04
4.739000D+00	5.090000D-01	6.063539D+04
5.525000D+00	1.105000D+00	3.910091D+04
6.746000D+00	1.350000D+00	2.179378D+04
8.238000D+00	1.648000D+00	1.214223D+04
1.006000D+01	2.007000D+00	6.759979D+03
1.228000D+01	2.460000D+00	3.680086D+03
1.500000D+01	3.000000D+00	1.999302D+03
1.831000D+01	3.670000D+00	1.088431D+03
2.236000D+01	4.470000D+00	5.848412D+02
2.730000D+01	5.460000D+00	3.115420D+02
3.334000D+01	6.670000D+00	1.658218D+02
4.071000D+01	8.140000D+00	8.830378D+01
4.971000D+01	9.950000D+00	4.702128D+01
6.070000D+01	1.214000D+01	2.481828D+01
7.411000D+01	1.483000D+01	1.310134D+01
9.050000D+01	1.810000D+01	6.911816D+00

Alumina.matdata

```
aluminum oxide
# density kg/m3
3.97D+03
# T melt  K
2327.0
# k vs. T, solid, cal/m.k.s
17.95
-4.681D-02
5.533D-05
-3.368D-08
1.038D-11
-1.278D-15
# k vs. T, liquid, cal/m.k.s
1.400
0.00D+00
0.0
0.0
0.0
0.0
# k vs. T, vapor, cal/m.k.s
0.2
# T vs. H, solid, K & cal/g
307.44
4.1892
-2.4429D-03
1.8465D-06
0.0
0.0
# T vs. H, liquid, K & cal/g
426.1951
2.2165
# T vs. H, vapor, K & cal/g
542.3
1.0689
# coeff for log(P) = A - B/T, micron & K
13.8318
31615.1267
# Gruneisen EOS coeff & gamma & Rbar in J/kg.K
1.0
7916.
1.897
0.0
0.0
1.53
0.00
0.0
1.55
267.5
# Poissons's Ratio
0.3
# Yield strength (Pa) (Compressive Strength)
2.1E+09
# Surface tension (flag + 6 coefficients)
2.
102.
16000.
2.3609
-2.366D-04
0.0
0.0
```

Alumina.opacdata

alumina

1.259000D-03	6.520000D-04	2.476688D+07
1.995000D-03	9.270000D-04	2.476688D+07
3.162000D-03	1.469000D-03	2.476688D+07
5.012000D-03	2.329000D-03	2.476688D+07
7.943000D-03	3.690000D-03	2.476688D+07
1.259000D-02	5.850000D-03	2.476689D+07
1.995000D-02	9.270000D-03	9.835363D+07
3.162000D-02	1.469000D-02	8.785649D+07
5.012000D-02	2.329000D-02	6.421366D+07
7.943000D-02	3.690000D-02	4.340113D+07
1.259000D-01	5.850000D-02	2.760899D+07
1.995000D-01	9.270000D-02	1.330071D+07
3.162000D-01	1.469000D-01	4.667299D+06
5.012000D-01	2.329000D-01	1.636624D+06
7.943000D-01	3.690000D-01	1.825318D+06
1.055000D+00	1.130000D-01	9.210890D+05
1.175000D+00	1.260000D-01	6.897975D+05
1.308000D+00	1.410000D-01	5.172738D+05
1.456000D+00	1.560000D-01	3.879389D+05
1.621000D+00	1.740000D-01	1.064657D+06
1.804000D+00	1.940000D-01	8.066552D+05
2.009000D+00	2.150000D-01	6.096388D+05
2.236000D+00	2.400000D-01	4.529688D+05
2.489000D+00	2.670000D-01	3.364574D+05
2.771000D+00	2.980000D-01	2.498418D+05
3.085000D+00	3.310000D-01	1.855307D+05
3.435000D+00	3.690000D-01	1.377382D+05
3.824000D+00	4.100000D-01	1.023175D+05
4.257000D+00	4.570000D-01	7.601409D+04
4.739000D+00	5.090000D-01	5.647795D+04
5.525000D+00	1.105000D+00	3.624578D+04
6.746000D+00	1.350000D+00	2.009264D+04
8.238000D+00	1.648000D+00	1.113515D+04
1.006000D+01	2.007000D+00	6.167500D+03
1.228000D+01	2.460000D+00	3.343969D+03
1.500000D+01	3.000000D+00	1.809483D+03
1.831000D+01	3.670000D+00	9.812760D+02
2.236000D+01	4.470000D+00	5.255528D+02
2.730000D+01	5.460000D+00	2.791894D+02
3.334000D+01	6.670000D+00	1.481990D+02
4.071000D+01	8.140000D+00	7.870886D+01
4.971000D+01	9.950000D+00	4.180207D+01
6.070000D+01	1.214000D+01	2.201142D+01
7.411000D+01	1.483000D+01	1.159267D+01
9.050000D+01	1.810000D+01	6.101902D+00